ABSTRACT

Title of Thesis:	INTEGRATED GEOCHEMICAL STUDIES OF THE SHURAM EXCURSION IN SIBERIA AND SOUTH CHINA
	Matthew G. Pedersen Master of Science in Geology 2024
Thesis Directed By:	Distinguished University Professor Alan Jay Kaufman (Chair, Advisor): University of Maryland, Department of Geology

The Ediacaran Period Shuram Excursion (SE) is a globally-distributed and highly controversial phenomenon where over millions of years, sedimentary carbonates record $\delta^{13}C$ values of -10‰ and lower. This carbon cycle anomaly may reflect disequilibrium in the world's oceans, driven by the oxidation of a large pool of dissolved organic carbon (DOC), with the oxidants sourced from the intense weathering of the continents, forcing major changes to ocean chemistry through the ventilation of the deep ocean, evidenced by a positive shift in carbonate uranium isotope values, and invoking the onset of early animal biomineralization. This study utilizes high-resolution carbonate Li isotopes from two SE-successions, U isotopes, REE abundances and Ce anomalies which reveal the dynamic interplay between intensified continental weathering associated with tectonic reconfiguration and the subsequent environmental and ecological response that may have been amplified by the ecosystem-engineering abilities of a newly discovered sponge-grade animal.

INTEGRATED GEOCHEMICAL STUDIES OF THE SHURAM EXCURSION IN SIBERIA AND SOUTH CHINA

by

Matthew G. Pedersen

Thesis submitted to the Faculty of the Graduate School of the
University of Maryland, College Park, in partial fulfillment
of the requirements for the degree of
Master of Science
2024

Advisory Committee:
Distinguished University Professor Alan Jay Kaufman, Chair
Professor Michael Evans
Associate Professor Geoffrey Gilleaudeau

© Copyright by
Matthew G. Pedersen
2024

Acknowledgements

I would like to thank my advisor, Dr. Alan Jay Kaufman, for his mentorship and support throughout the duration of this thesis. I would also like to thank Dr. Geoffrey Gilleaudeau from George Mason University and Dr. Tian Gan from the University of Maryland for their assistance with this all aspects of this project. I would like to thank Andrew Doerrler and Jenna Wollney for aiding in measurements and sample preparation.

This work would not have been possible without our Russian collaborators from the Trofimuk Institute of Petroleum Geology and Geophysics, Dr. Dimitry Grazhdankin and Vadim Maximenko. I would also like to thank Dr. Natalia Bykova from the University of Missouri who went through great risks by flying out of Russia amidst the ongoing conflict in Ukraine to deliver 190 sample powders in the name of progressing science. Lastly, I would like to thank my parents, Greg and Janine, Grandparents, Jim and Pat, siblings, Christopher, Molly (and Bandit), Thomas, and girlfriend, Grace, as without their support I would not have made it this far.

Table of Contents

Acknowledgements ii
Table of Contents iii
List of Tables iv
List of Figures vi
Chapter 1: Introduction 1
1.1: Molecular Oxygen 1
1.3: The Shuram Excursion 4
1.5: Strontium Isotopes 12
1.6: Uranium Isotopes 13
Chapter 2: Methodology 27
2.1: Sample Selection 27
2.2: Sample Processing and Export 27
2.3: Electron Probe Microanalyzer Analysis and Elemental Mapping 29
2.4: Carbon and Oxygen Isotope Analysis 30
2.5: Lithium Isotopes 32
2.6: Strontium Isotopes 33
Chapter 3: A Lithium Isotope Study of the Shuram Excursion in Siberia and South China 38
3.1: Abstract 38
3.2: Introduction 38
3.3: Results 42
3.3.1: Patom Uplift 43
3.3.2: Doushantuo Formation 51
3.5: Discussion 59
3.5.1: Diagenesis 59
3.5.1.1: Patom Uplift 59
3.5.1.2: Doushantuo Formation 70
3.5.2: An Alkalinity Anomaly 79
3.6: Conclusions 85
Chapter 4: A Multi-Proxy Redox Study of the Shuram Excursion in Siberia 86
4.1: Abstract 86
4.2: Introduction 87
4.3: Results 91
4.4: Discussion 94
4.4.1: The Case for a Primary U Signal 94
4.4.2: The Case for a Primary REE Signal 104
4.4.3: Global Redox Conditions 108
4.4.4: Local Redox Conditions 110
4.4.5: Was the Shuram Excursion a True Oxygenation Event? 113
4.5: Conclusions 115
Chapter 5: Research Conclusions 118
Appendix I 124
Appendix II 138
Bibliography 145

List of Tables

Table 2.1: Data table containing analytical uncertainties for isotopic measurements ($\delta^{13}C$, $\delta^{18}O$, $\delta^{7}Li$, $^{87}Sr/^{86}Sr$, $\delta^{88}Sr$, and $\delta^{238}U$). Uncertainties are reported as 1σ for the C and O measurements and 2σ for the other isotopic measurements **31**

Table 2.2: Data table containing analytical uncertainties for elemental measurements (Li, Mg, Al, P, Ca, Mn, Rb, Sr, Y, Ce, Pr, Nd, Ho, and U). Uncertainties reported as 1sd and RSD for ASU and RSD for Carnegie Institution for Science **34**

Table 3.1: Data table containing element concentration averages from the Li leach (Li, Mg, Al, P, Ca, Mn, Fe, Rb, and Sr) for both the Zhuya Group and Doushantuo Formation samples **58**

Table 3.2: Data table containing element ratio averages (Mg/Ca, Mn/Sr, Rb/Sr Li/(Mg+Ca), Al/(Mg+Ca), P/(Mg+Ca), Mn/(Mg+Ca), Rb/(Mg+Ca), and Sr/(Mg+Ca)) for both the Zhuya Group and Doushantuo Formation samples from the Li leach (*cf.* Gan et al., *in-preparation*)..... .....**58**

Table 3.3: Data table of averages for percent carbonate, isotopic averages (for $\delta^{13}C$, $\delta^{18}O$, $\delta^{7}Li$, $\delta^{7}Li_{SW}$, $\delta^{88}Sr$, and $^{87}Sr/^{86}Sr$) and average uncertainties for both the Zhuya Group and Doushantuo Formation (*cf.* Gan et al., *in-preparation)* **58**

Table 4.1: Data table of averages the U leach ($\delta^{238}U$ with average 2σ, Mn, Fe, Sr, Mo, Re, U, Mg/Ca, Mn/Sr, U/Al, Mo/(Mg+Ca), and U/(Mg+Ca)) for the Zhuya Group.....**93**

Table 4.2: Data table of averages from the REE leach (Mn, Sr, U, Mg/Ca, Mn/Sr, Ce/Ce*, Y/Ho, Eu/Eu*, MREE/MREE*, and ∑REE) for the Zhuya Group.....**93**

Table A1: Data table containing elemental concentrations from the Li leach (Li, Mg, Al, P, Ca, Mn, Fe, Rb, and Sr) for the Zhuya Group.....**124**

Table A2: Data table containing elemental ratios from the Li leach (X/(Mg+Ca)) from the Li leach (Mg/Ca, Mn/Sr, Rb/Sr, Li, Al, P, Mn, Rb, Sr) for the Zhuya Group.....**125**

Table A3: Data table of isotopic data ($\delta^{13}C$, $\delta^{18}O$, $\delta^{7}Li$, $\delta^{7}Li_{SW}$, $\delta^{88}Sr$, $^{87}Sr/^{86}Sr$ and associated uncertainties) for the Zhuya Group. Note, red means interpret with caution **126**

Table A4: Data table containing elemental concentrations from the Li leach (Li, Mg, Al, P, Ca, Mn, Fe, Rb, and Sr) for the Doushantuo Formation **127**

Table A5: Data table of isotopic data ($\delta^{13}C$, $\delta^{18}O$, $\delta^{7}Li$, $\delta^{7}Li_{SW}$, and associated uncertainties) and elemental ratio data (X/(Mg+Ca)) from the Li leach (Mg/Ca, Mn/Sr, Rb/Sr, Li, Al, P, Mn, Rb, and Sr) for the Doushantuo Formation. Note, red means interpret with caution..... **127**

Table A6: Data table containing elemental concentrations from the U leach (Li, Mg, Al, P, Ca, V, Cr, Mn, Fe, Rb, Sr, Zr, Mo, Re, Th, and U) for the Zhuya Group..... **129**

Table A7: Data table containing % carbonate, isotopic data ($\delta^{13}C$, $\delta^{18}O$, $\delta^{238}U$ and associated uncertainties) and elemental ratios from the U leach (Mg/Ca, Mn/Sr, Sr/Ca, Rb/Sr, U/Th, U/Al, Mo/(Mg+Ca), U/(Mg+Ca), Sr/(Mg+Ca), Mn/(Mg+Ca)) for the Zhuya Group..... **131**

Table A8: Data table containing % carbonate and elemental concentrations from the REE leach (Li, Mg, Al, Ca, Ti, Mn, Fe, Rb, Sr, Zr, and U) for the Zhuya Group. Note red means interpret with caution..... **134**

Table A9: Data table containing elemental ratios from the REE leach (Mn/Sr, Mg/Ca, Sr/Ca, Mn/Fe, Y/Ho, Ce/Ce*, Eu/Eu*, MREE/MREE*, Nd/Yb, and ∑REE) for the Zhuya Group. Note red means interpret with caution..... **136**

List of Figures

Figure 1.1: Figure 1.1: (A) Carbon isotope composition of marine carbonates from the Neoproterozoic to the present day, the Precambrian is characterized by extreme positive and negative swings in the carbon cycle, with the Shuram Excursion representing one of the largest negative anomalies in all of Earth history (modified from Shields et al., 2019). (B) Normalized composite of $\delta^{13}C$ data from four geographically distant successions that host the Ediacaran Shuram Excursion: Sonora, NW Mexico (Li et al., 2020); Oman (Fike et al., 2006); South China (McFadden et al., 2008); and South Australia (Calver, 2000). The extreme depletion in the $\delta^{13}C$ values coupled with the anomalous behavior of several other geochemical proxies has made the SE perhaps one of the most controversial events in the entire Neoproterozoic Era **4**

Figure 1.2: Chemostratigraphic observations of the Ediacaran Period before and after the SE. The SE is a prominent event, insofar as it stands out amongst Ediacaran successions, highlighted by the gray shaded region. The data collected is based on (McFadden et al., 2008; Husson et al., 2015; Narbonne et al., 2012; Li et al., 2020) as well as the data collected in herein. Note the stippled curve in the C and O plots represents EN2, a large negative carbon isotope excursion represented only in the Krol Formation of India and the Doushantuo Formation in South China (Kaufman et al., 2006; McFadden et al., 2008) **5**

Figure 1.3: Simple steady-state box model illustrating the Li budget in the modern ocean. The riverine and hydrothermal input are the two main sources, though subduction refluxed Li does contribute to the seawater Li inventory. The dominant removal mechanism is through the formation of MAACs and low T hydrothermal alteration (modified after Misra and Froelich, 2012; Weldeghebriel and Lowenstein, 2023) **11**

Figure 1.4: Simplified mass balance for seawater U. The two dominant sinks for U are euxinic/reducing sediments, which preferentially incorporate the isotopically heavy U(IV) species, and carbonates which form calcium-uranyl complexes with the aqueous U(IV) (after Tissot and Dauphas, 2015) **14**

Figure 1.5: Sedimentological indicators of high carbonate saturation found within the Patom Uplift. (A) Biomineralized remains of a sponge-grade organisms found within a reef complex in the Khopych Formation. (B) Massive grapestones and ooids (average diameter ~250 μm), some of which have been neomorphosed from aragonite to calcite and others appear bimineralic, and grapestones. (C) Vertical sheet crack cements. (D) Plate breccias formed from a storm event ripping up the seafloor which was rapidly cemented. (E) Aragonite precipitate cements that resemble blades of grass growing from the seafloor **17**

Figure 1.6: (A) Geological and geographical maps illustrating the location of the studied Khapchagai Rock Section in the Patom Highlands of Sibieria. The sampled outcrops are exposed

along the Lena River approximately 130 km east of Lensk, Russia (60°19'01.74" N, 116°55'11.07" E). (B) Composite of the Patom Supergroup which is predominantly comprised of Ediacaran successions, but also includes the Cryogenian Bol'shoi Patom Formation and the Cambrian Zherba and Tinnaya formations. Timeseries carbon isotope trends, the presence of acanthomorphic acritacrchs in the Ura Formation, and Pb-Pb dates correlate the large negative carbon isotope excursion spanning the Zhuya Group to other SE successions. The Zhuya Group is truncated by two erosional surfaces at the Khapchagai Section, one at the base of the Nikol'skoe Formation and the other at the top of the Khopych Formation above the reef complex (modified after Moczydłowska & Nagovitsin, 2011) **19**

Figure 1.7: Geographical map indicating the location of the Doushantuo Formation at the Three Gorges region. The formation is subdivided into four members, spanning roughly 160 m and composed of mixed limestone, dolostone, and shaly intervals. The unit overlies the Nantuo Diamictite, corroborating the lower Ediacaran age constraint. The overlying Dengying Formation marks the last Ediacaran unit just prior to the BACE Event. Based on the carbon isotope chemostratigraphy, there are several prominent carbon isotope excursions, both positive and negative, preserved in the Doushantuo Formation, though the largest, EN3, is considered to be the SE based on the very negative $\delta^{13}C$, the presence of the novel Doushantuo-Pertatataka acritarch assemblage in units below the excursion, and the rough age constraints (modified after McFadden et al., 2008) **24**

Figure 3.1: Stratigraphy and chemostratigraphy of the Zhuya Group at Khapchagai Section. (B) Li concentrations steadily decline from the basal Nikol'skoe Formation to a nadir in the Alyanch Formation before steadily rising at the Alyanch-Khopych boundary where they rise to a maximum in the Khopych Formation reef. (C) P concentrations remain consistently below 100 ppm and broadly follow the Li trend with a decease to minimum values from the Nikol'skoe to Alyanch formations before rising to about 40 ppm in the Khopych Formation. (C, D) Sr and Mn display an inverse trend where Sr starts from a nadir of 250 ppm in the basal Nikol'skoe Formation and rises to a maximum of 2650 ppm in the Khopych Formation while Mn starts at a maximum of 3000 ppm in the basal Nikol'skoe Formation and steadily decreases to a minimum through the Alyanch Formation, before rising and falling in the Khopych Formation. (F, G) Al and Rb serve as detrital proxies with all but 3 samples falling below 125 ppm and all samples below 0.5 ppm, respectively **47**

Figure 3.2: Stratigraphy and chemostratigraphy of the Zhuya Group at Khapchagai Section. (A) from Fig. 3.1. (B) Li/(Mg+Ca) ratios. (C) P/(Mg+Ca) or CAP ratios. (D) Sr/(Mg+Ca) ratios. (E) Mn/(Mg+Ca) ratios. (F) Al/(Mg+Ca) ratios, the stippled line represents the boundary beyond which aluminosilicate contamination may have compromised the leachate. (G) Rb/(Mg+Ca) ratios are all consistently below the 3×10^{-5} ppm/ppm cutoff indicating aluminosilicate contamination (*cf.* Gan et al., *in-preparation*) **48**

Figure 3.3: Stratigraphy and chemostratigraphy of the Zhuya Group at Khapchagai Section. (A, B) Ultra low $\delta^{13}C$ and $\delta^{18}O$ values that are notably coupled (R^2=0.74, P<0.001). (C) Mg/Ca is consistent between all three leach methods. (D) Mn/Sr is consistent across all three leach methods, decreasing from a maximum in the Nikol'skoe Formation to below 1 for the remaining 450 m of stratigraphy. (E) Rb/Sr is consistent across all three leaches, though the U leach does show slightly

higher values in several points, indicating more Rb was leached in the bulk solution whereas the REE and Li leach were much gentler **49**

Figure 3.4: Stratigraphy and chemostratigraphy of the Zhuya Group at Khapchagai Section. (A) Percent carbonate. (B, C) $\delta^{13}C$ and $\delta^{18}O$ from 3.3, characterized by an extreme depletion and smooth covariance in the basal 300 m of the study section. (D) Sr isotopes decrease sharply in the first 150 m from highly radiogenic values, before a monotonous rise towards the typical $^{87}Sr/^{86}Sr$ for Ediacaran seawater. Average uncertainty is ±4 x 10^{-6} (2σ). (E) $\delta^{88}Sr$ values sharply rise throughout the Nikol'skoe Formation before plateauing around 0.4‰. Average uncertainty is ±0.01‰ (2σ). (F) Li isotopes climb from a nadir at ~150 m coincident with the rise in $^{87}Sr/^{86}Sr$ and $\delta^{88}Sr$. Average uncertainty is ±0.3‰ **50**

Figure 3.5: Stratigraphy and chemostratigraphy of the Doushantuo Formation at Jiulongwan Section. (B) Li concentrations are notably higher around 1.0 ppm in the dolostone intervals before and after the SE while the [Li] during the SE is at a nadir of roughly 0.2 ppm. (C) P broadly follow the Li concentrations, decreasing to a minimum in the SE interval before rising to pre-SE values in the post-SE interval. (D, E) Sr and Mn display an inverse trend where Sr values start at a minimum in the pre-SE before rising to a maximum during the SE while Mn starts at a maximum in the pre-SE and falls to a minimum during the SE. (F,G) Aluminum is elevated throughout the section with 8 samples falling off-axis while 2 samples plot off-axis for Rb (3 ppm and 1.3 ppm) **54**

Figure 3.6: Stratigraphy and chemostratigraphy of the Doushantuo Formation at Jiulongwan Section. (B) Li/(Mg+Ca) ratios. (C) P/(Mg+Ca) or CAP ratios show a broad consistency with those reported in Dodd et al. (2023). (D) Sr/(Mg+Ca) ratios. (E) Mn/(Mg+Ca) ratios. (F) Al/(Mg+Ca) ratios, the stippled line represents the boundary beyond which aluminosilicates may have compromised the leachate. 8 samples from the dolostone section plot above the line. (G) Rb/(Mg+Ca) ratios are all consistently below the 3 x 10^{-5} ppm/ppm cutoff indicating a potential siliciclastic influence.....**55**

Figure 3.7: Stratigraphy and chemostratigraphy of the Doushantuo Formation at Jiulongwan Section. (A, B) Ultra low $\delta^{13}C$ and $\delta^{18}O$ values that are notably coupled (r^2=0.67, p<0.001). (C) Mg/Ca is elevated in the pre- and post-SE intervals, consistent with the dolostone units while the SE interval has low Mg/Ca, indicating limestone. (D) Mn/Sr is elevated in the pre- and post-SE intervals, consistent with the dolostone units while the SE interval has an Mn/Sr consistently below 3. (E) Rb/Sr is elevated in the dolostone units, attributable to a loss of Sr during the process of dolomitization **56**

Figure 3.8: Stratigraphy and chemostratigraphy of the Doushantuo Formation at Jiulongwan Section. (A) % carbonate is >80% for the 22 samples it was determined on (McFadden et al., 2022). (B, C) Ultra low $\delta^{13}C$ and $\delta^{18}O$ values that are notably coupled (r^2=0.67, p<0.001) throughout the SE interval and decoupled in the intervals before and after the event. (D) $^{87}Sr/^{86}Sr$ normalized to this study (Wei et al., 2022). (E) $\delta^{7}Li$ trend of the entire SE interval. Dolostone units exhibit enrichment in ^{7}Li while the limestone samples are near crustal values. Associated uncertainties are ±0.3‰ based on replicate analyses. (F, G) $\delta^{34}S_{py.}$ and $\delta^{34}S_{CAS}$ values decrease

throughout the SE interval, consistent with the growth of the sulfate reservoir (McFadden et al., 2008) **57**

Figure 3.9: Three distinct ooid morphotypes present throughout the Zhuya Group. (A, D) Ooids approximately 250 μm in diameter in the Nikol'skoe Formation. The radial internal structure indicates high carbonate saturation paired with a slightly quieter environment permitted the development of a radial internal fabric (Davies et al., 1978). (E, H) Representative ooids from the basal Khopych Formation. The average diameter is 300 to 350 μm in diameter. The inner cortex in the ooids has been partially recrystallized, likely the result of neomorphism from an original aragonite mineralogy to low-Mg calcite. The tangential cortex indicates a high energy shoaling environment subject to constant agitation. (I, L) The final ooids from the Khopych Formation immediately above the reef complex that consist of blocky neomorphosed ooids, some of which were replaced by a singular grain, and bimineralic ooids with the inner nucleus retained and the inner cortex recrystallized. Samples are photographed under crossed-polarized light and at 5x, 10x, 20x, and 50x magnification from left to right..... **62**

Figure 3.10: (A) Thin section scan of sample 2101-39.02 from the basal Nikol'skoe Formation. (B) Si maps reveal high density in the micritic half and heterogenous distribution in the intraclast cements of the ooid section. (C) Al has the same distribution as Si, suggesting a co-occurrence of aluminosilicate minerals. (D) The distribution of Mg broadly matches that of Si and Al indicating the presence of magnesian clay minerals, predominantly in the micrite. (E) Mn is concentrated in the intraclast cements, indicating transport of the ooids downslope where they were cemented under reduced conditions. (F) S map did not return any discernable information **63**

Figure 3.11: (A) Thin section scan of sample 2102-39.15 from the Nikol'skoe Formation. (B) Si maps reveal high density distributions primarily around the outer cortex of the ooids with some very high signatures indicating minor silicification (arrows point to high density points). (C) Al is distributed around the ooids, coincident with Si, but the ooids appear to contain minor amounts of Al inside the cortex. (D) The distribution of Mg matches that of Si and Al indicating the presence of magnesian clay minerals. The ooids appear to have higher Mg than the surrounding cements, though the co-occurrence with Al suggests authigenic clays are present (E) Mn is slightly more concentrated in the cements relative to the ooids, though the distribution is muted due to lower concentrations. (F) Sr is highly concentrated with Si, Mg, and Al, indicating that Sr may have absorbed onto the negatively charged surface of any clay minerals precipitating **64**

Figure 3.12: (A) Thin section scan of sample 2102-78.85 from the Nikol'skoe Formation. (B, D) Si, Al, and Mg maps reveal high density point distributions though the abundance is minor relative to the two underlying samples indicating a lack of abundant clay minerals present. (E, F) Mn and Sr are homogenously distributed throughout the map. Mn appears to be concentrated around the opaque phases consisting of pyrrhotite with pyrite rims **65**

Figure 3.13: (A) Thin section scan of sample 2103-171 from the Khopych Formation. (B, C) Si, Al, and Mg maps reveal high concentration along the boundaries of the several stylolites (arrows indicate high concentration areas around the stylolites). (E, F) The Sr and Mn maps are relatively homogenous and thus cannot be interpreted..... ..... **66**

Figure 3.14: (A) Thin section scan of sample 2103-280 from the Khopych Formation. (B, C) Al and Mg maps reveal high concentration along the outer cortices of the ooids (white arrows point to neomorphosed single-crystal ooids and yellow arrows point to bimineralic ooids). (D) Sr is distributed primarily in the cements with two bright spots corresponding to a Sr-sulfide. (E, F) The Mn and P maps are fairly muted and do not exhibit a clear discernable distribution within a specific phase **67**

Figure 3.15: Cross-plots of δ^7Li versus other elemental ratios and conventional indicators of diagenesis for the Zhuya Group. (A) δ^7Li versus Li/(Mg+Ca). (B) δ^7Li versus P/(Mg+Ca). (C) δ^7Li versus Sr/(Mg+Ca). (D) δ^7Li versus Mn/Sr. (E) δ^7Li versus δ^{13}C. (F) δ^7Li versus δ^{18}O. (G) δ^7Li versus Al/(Mg+Ca). (H) δ^7Li versus Rb/(Mg+Ca). (I) δ^7Li versus Mg/(Mg+Ca). Note, black line is the regression line, blue stippled line is 95% confidence interval, and red stippled line is the 95% predicted confidence interval..... **69**

Figure 3.16: Plate of thin section photos from sample SSFT-8.3 from the Doushantuo Formation. (A) Thin section scan. (B, E) Plane-polarized light images of microspar with small, euhedral dolomite rhombs and clays (white arrows point to dolomite grains). (F, G) Crossed-polarized light images. (H, I) Reflected light images. Magnifications are 5x, 10x, 20x, and 50x from right to left, respectively **72**

Figure 3.17: Plate of thin section photos from sample HND-26.6 from the Doushantuo Formation. (A) Thin section scan. (B, E) Plane-polarized light images of dolomite rhombs in the dolostone half (white arrows), clay horizon (red arrows), and the limestone half. (F, G) Crossed-polarized light images. (H, I) Reflected light images. Magnifications are 5x, 10x, 20x, and 50x from right to left, respectively..... **73**

Figure 3.18: (A) Thin section scan of sample SSFT-8.3 from the Doushantuo Formation. (B, C) Al and Mg co-occur in interlayered regions of high and low density (white arrows point to high density regions and yellow arrows point to lower density regions). (D) Sr is relatively homogenously distributed but there is some faint interlayering similar to Al and Mg. (E, F) Mn and Fe are muted and thus cannot be reliably interpreted **74**

Figure 3.19: (A) Thin section scan of sample HND-26.6 from the Doushantuo Formation. (B, D) Al, Mg, and Sr maps reveal high concentration along the clay horizon separating the limestone from dolostone. Though there is a clear boundary, some small dolomite grains are present within the limestone. (E, F) The Mn and Fe maps are fairly muted and do not exhibit a clear discernable distribution within a specific phase..... **75**

Figure 3.20: Cross-plots of δ^7Li versus other elemental ratios and conventional indicators of diagenesis for the Doushantuo Formation. (A) δ^7Li versus Li/(Mg+Ca). (B) δ^7Li versus P/(Mg+Ca). (C) δ^7Li versus Sr/(Mg+Ca). (D) δ^7Li versus Mn/Sr. (E) δ^7Li versus δ^{13}C. (F) δ^7Li versus δ^{18}O. (G) δ^7Li versus Al/(Mg+Ca). (H) δ^7Li versus Rb/(Mg+Ca). (I) δ^7Li versus Mg/(Mg+Ca). Note, orange represents dolostone and black represents limestone samples. Note,

black line is the regression line, blue stippled line is 95% confidence interval, and red stippled line is the 95% predicted confidence interval **78**

Figure 3.21: Stratigraphy and chemostratigraphy of the Zhuya Group and Doushantuo Formation. (A) $\delta^{13}C$ and reconstructed seawater $\delta^{7}Li$ of the Zhuya Group. (B) $\delta^{13}C$ and reconstructed seawater $\delta^{7}Li$ of the Doushantuo Formation..... **80**

Figure 3.22: (A) Cross-plot of $\delta^{13}C$ versus $\delta^{18}O$ to highlight the coupling in the lower 300 m (r^2=0.66; p<0.001) of the Zhuya Group and de-coupling in the upper 300 m ((r^2=0.02; p=0.18). (B) Cross-plot of $\delta^{13}C$ versus $\delta^{18}O$ to highlight the coupling in the limestones (r^2=0.85; p<0.001) of the Doushantuo Formation and the decoupling in the dolostones (r^2=0.06; p=0.30)..... ..... **84**

Figure 4.1: Zhuya Group chemostratigraphy. (A) Carbon isotopes measured relative to V-PDB. (B) High [U] signifies excellent preservation and a more aragonite-dominated mineralogy. (C) $\delta^{238}U$ values are consistently around -0.20‰, indicative of a global oceanic ventilation and a reduction in the euxinic reservoir. (D) Y/Ho consistently >36, indicative of an authigenic seawater signal. The Y/Ho may also be interpreted as the rocks having been deposited in an open marine setting, rather than a restricted basin. (E) Ce/Ce* highlights local redox variations with suboxic to anoxic conditions in the first ~400 m of the stratigraphic section, followed by a brief pulse of oxygenation for ~100 m, around 500 m conditions oscillate between anoxic and oxic before shifting back to anoxic in the upper ~30 m. (F) [Mn] exhibits a sharp decline from ~3000 ppm to ~100 ppm at the Nikol'skoe-Chencha Boundary, before slowly climbing to approximately 300 ppm in the middle Chencha Formation, then slowly declines to ~100 ppm..... **92**

Figure 4.2: Plate of thin section photos from sample 2102-39.15 from the Patom Uplift. (A) Thin section scan. (B, E) Plane-polarized light images of representative ooids from the Nikol'skoe Formation with blocky intraclastic cements, highlighting the overall retention of original fabrics. (F, G) Crossed-polarized light images. (H, I) Reflected light images. Magnifications are 5x, 10x, 20x, and 50x from right to left, respectively..... **97**

Figure 4.3: Plate of thin section photos from sample 2103-M4 from the Patom Uplift. (A) Thin section scan. (B, E) Plane-polarized light images of the boundary between the micrite and grainstone. (F, G) Crossed-polarized light images. (H, I) Reflected light images. Magnifications are 5x, 10x, 20x, and 50x from right to left, respectively..... **98**

Figure 4.4: Plate of thin section photos from sample 2103-171 from the Patom Uplift. (A) Thin section scan. (B, E) Plane-polarized light images of representative ooids from the Khopych Formation below the reef complex. The ooids are roughly 300 μm in diameter with tangential fabrics and evidence of recrystallization, likely neomorphism of metastable aragonite to low-Mg Ca, though the primary depositional fabrics have been retained. (F, G) Crossed-polarized light images. (H, I) Reflected light images. Magnifications are 5x, 10x, 20x, and 50x from right to left, respectively..... **99**

Figure 4.5: Plate of thin section photos from sample 2103-280 from the Patom Uplift. (A) Thin section scan. (B, E) Plane-polarized light images of the diverse ooid assemblage: Single crystal

neomorphosed ooids (white arrows); bimineralic ooids (red arrows); and a large grapestone (green arrows). The 10x and 20x photos also highlight the dogtooth cements that surround some of the ooids (blue arrow). (F, G) Crossed-polarized light images. (H, I) Reflected light images. Magnifications are 5x, 10x, 20x, and 50x from right to left, respectively..... **100**

Figure 4.6: Cross-plots of $\delta^{238}U$ versus various proxies for diagenesis. (A) $\delta^{238}U$ versus $\delta^{18}O$. (B) $\delta^{238}U$ versus $\delta^{13}C$. (C) $\delta^{238}U$ versus Mn/Sr. (D) $\delta^{238}U$ versus Mg/Ca. (E) $\delta^{238}U$ versus [Mn]. (F) $\delta^{238}U$ versus [U]. (G) $\delta^{238}U$ versus [Mo]. (H) $\delta^{238}U$ versus [Re]. (I) $\delta^{238}U$ versus U/(Mg+Ca). (J) $\delta^{238}U$ versus Mo/(Mg+Ca). (K) $\delta^{238}U$ versus [Al]. (L) $\delta^{238}U$ versus U/Al. Note, black line is the regression line, blue stippled line is 95% confidence interval, and red stippled line is the 95% predicted confidence interval..... **103**

Figure 4.7: Cross-plots of Ce/Ce* and Y/Ho versus various proxies for alteration. (A) Ce/Ce* versus Y/Ho. (B) Ce/Ce* versus % carbonate. (C) Ce/Ce* versus [Al]. (D) Ce/Ce* versus [Ti]. (E) Ce/Ce* versus [Mn]. (F) Ce/Ce* versus [Fe]. (G) Y/Ho versus [Zr]. (H) Y/Ho versus [Rb]. (I) MREE/MREE* versus ∑REE. Note, black line is the regression line, blue stippled line is 95% confidence interval, and red stippled line is the 95% predicted confidence interval..... **106**

Figure 4.8: (A) REE Spider plot of the average Zhuya Group versus the average Olenek Uplift ($^{+++}$Cherry et al., 2022); Average Brak Section (Nama Group; $^{\wedge}$Tostevin et al., 2017); Average Pleistocene platform carbonate ($^{+}$Liu et al., 2019); and average N. Pacific Seawater from 400 m (*Alibo and Nozaki, 1999). (B) Ce/Ce* versus $\delta^{238}U$ divided by formation..... **107**

Figure 4.9: Global correlation between 6 different U isotope studies on 5 geographically distant SE successions. All of the successions exhibit a similar step-wise increase of roughly +0.4‰ towards a steady $\delta^{238}U$ signal of roughly -0.25‰ within the SE-interval before shifting back to near pre-SE values **108**

Figure 4.10: Cross-sectional interpretation of the local redox profile. The upwelling of ventilated waters coupled with the high productivity in the shallower ramp settings may have promoted the formation of a low oxygen wedge along the distal ramp and shelf settings, while enhanced organic matter loading in the restricted back lagoonal setting promoted suboxic to anoxic conditions **112**

Figure 4.11: Results of the 2-sink model calculation. With the three offsets (-0.13‰, -0.27‰, and -0.41‰) applied to the average Zhuya Group $\delta^{238}U$ values, the minimum extent of seafloor anoxia is 0.09% and the maximum is 1%..... **113**

Figure 4.12: Alternate cross-sectional interpretation of the local redox profile where the increased export efficiency of organic matter restricted the redox boundary to the sediment-water interface, where cementation occurred under anoxic conditions. Further up in the Khopych Formation, the constant wave agitation likely aerated the sediments, efficiently capturing a primary seawater signal during cementation. The low oxygen back lagoon may still have been the result of enhanced organic matter loading and a general restriction from the open ocean..... **115**

Figure 5.1: A synthesizing conceptual model, combining both the long-term and short-term carbon cycle, highlighting the various pathways in which the depleted $\delta^{13}C$ values preserved in SE-bearing strata could have been generated and promoted the subsequent environmental and biological changes observed throughout the anomaly. Each pathway is not mutually exclusive and was likely a combination of all components. Flux and reservoir values adapted from Wallman and Aloisi, (2012) and Shields and Mills, (2017).....**119**

Figure A1: Plate of thin section photos from sample 2102-78.85 from the Patom Uplift. (A) Thin section scan. (B, E) Plane-polarized light images of microspar with the interspersed opaque phases. (F, G) Crossed-polarized light images. (H, I) Reflected light images highlighting the presence of pyrrhotite (blue arrow) with pyrite rims (red arrow) indicating that pyritization was abruptly ended through a lack of sufficient sulfide. Magnifications are 5x, 10x, 20x, and 50x from right to left, respectively .....
.....**138**

Figure A2: Plate of thin section photos of an alternate view of sample 2103-171 from the Patom Uplift. (A) Thin section scan. (B, E) Plane-polarized light images. (F, G) Crossed-polarized light images. (H, I) Reflected light images (red arrows point to pyrrhotite and the blue arrows point to the pyrite rims). Magnifications are 5x, 10x, 20x, and 50x from right to left, respectively139

Figure A3: Plate of thin section photos of an alternate view of sample 2103-280 from the Patom Uplift. (A) Thin section scan. (B, E) Plane-polarized light images. (F, G) Crossed-polarized light images. (H, I) Reflected light images. Magnifications are 5x, 10x, 20x, and 50x from right to left, respectively **140**

Figure A4: Plate of thin section photos of an alternate view of sample 2103-280 from the Patom Uplift. (A) Thin section scan. (B, E) Plane-polarized light images. (F, G) Crossed-polarized light images. (H, I) Reflected light images. Magnifications are 5x, 10x, 20x, and 50x from right to left, respectively **141**

Figure A5: Plate of thin section photos of sample HND-10.0 from the Doushantuo Formation. (A) Thin section scan. (B, E) Plane-polarized light images. (F, G) Crossed-polarized light images. (H, I) Reflected light images. Magnifications are 5x, 10x, 20x, and 50x from right to left, respectively **142**

Figure A6: Plate of thin section photos of sample HND-23.55 from the Doushantuo Formation at the dolostone-limestone boundary. (A) Thin section scan. (B, E) Plane-polarized light images. (F, G) Crossed-polarized light images. (H, I) Reflected light images. Magnifications are 5x, 10x, 20x, and 50x from right to left, respectively.....**143**

Figure A7: Plate of thin section photos of sample HND-44.4 from the Doushantuo Formation. (A) Thin section scan. (B, E) Plane-polarized light images. (F, G) Crossed-polarized light images. (H, I) Reflected light images. Magnifications are 5x, 10x, 20x, and 50x from right to left, respectively **144**

Chapter 1: Introduction

1.1: Molecular Oxygen

Molecular oxygen is a basic requirement for animal respiration and life. For example, the synthesis of collagen, which represents over 25% of the proteins in mammals, requires roughly 13% of the Present Atmospheric Level (or PAL) although the minimum level is still poorly constrained and is likely dependent on the size and complexity of the organism (Cole et al., 2020). Considering this metabolic requirement, Nursall (1959) coined the 'Oxygen Control Hypothesis' suggesting that a rise in atmospheric oxygen in the late Neoproterozoic prompted the emergence of early metazoans. Berkner and Marshall (1965) further elaborated by arguing that during the Neoproterozoic, atmospheric oxygen levels had eclipsed the minimum 1% present atmosphere levels (PAL), triggering aerobic metabolisms. However, the presence of iron oxides in stromatolites and banded-iron formations suggested that the atmosphere had reached the critical 1% threshold around 2 Ga (*cf.* Guo et al., 2009), leading Cloud (1968) to speculate that 1% PAL is insufficient to sustain animal life. Alternatively, he suggested that other biological innovations were needed to support metazoan activities, such as multicellularity and the development of specialized organelles, prior to the appearance of the earliest animals.

Recent laboratory studies reveal that some simple animals are tolerant of low oxygen conditions, notably modern sponges (Mills et al., 2014) and potentially the Ediacaran biota (Boag et al., 2018; Cherry et al. 2022) – an early failed experiment in multicellularity that perished around the Ediacaran-Cambrian boundary (ca. 538.8 Ma; Linnemann et al., 2019). Based on molecular clock studies (Peterson et al., 2004; Peterson and Butterfield, 2005) sponges are estimated to have first appeared during the Tonian Period. This is important insofar as a 1 kg sponge can filter

~24,000 L of water per day through their vast network of pores and channels, allowing them to survive in as little as 0.5-4% PAL (Mills et al. 2014), similar to the low oxygen conditions suggested for much of the Ediacaran Period (Canfield et al., 2007; Li et al., 2015; Sperling et al. 2015; Sahoo et al., 2016; Ding et al., 2022; Cherry et al., 2022). Through ecosystem engineering sponges have the potential to clarify the surrounding water column by removing particulate organic matter and dissolved metals, thereby channeling dissolved and particulate organic carbon from the overlying water column into the benthic ecosystem, thus linking the pelagic and benthic realms (Pile and Young, 2006; de Goeij et al., 2013; Cathalot et al., 2015). Furthermore, their ability to survive under low oxygen conditions would have profound implications for ocean chemistry. By removing photosynthetic carbon, their metabolic activities would have allowed oxygen to build up in seawater potentially driving the ventilation of the oceans just prior to the appearance of the Ediacaran biota and the oxidation of a large organic carbon pool (Rothman et al., 2003) that could explain major oscillations in the exogenic carbon cycle.

1.2: The Carbon Cycle Through Time

Coincident with the presumed rise in Neoproterozoic oxygen levels were major disturbances in the oceanic carbon cycle, which are tracked between depositional environments and through time by the ratio of stable carbon isotopes (^{13}C and ^{12}C) in sedimentary carbonates and organic matter. Carbon isotope data is critical in reconstructing secular (or temporal) shifts in the composition of seawater throughout Earth history. The isotope system is used for correlating between stratigraphic intervals locally and globally, allowing for the construction of chemostratigraphic age models (Saltzman and Thomas 2012; Nelson et al., 2021) and interpretation of environmental changes in the world oceans. The $\delta^{13}C$ values of carbonate rocks are reflective of dissolved inorganic carbon (DIC) in seawater, which may be shifted by the effects

of diagenetic and metamorphic alteration (Urey et al.,1951; Craig, 1953; Valley, 2001; Knauth and Kennedy, 2009; Derry, 2010). There are two primary processes that draw carbon out of seawater: the formation of carbonates and organic matter. Carbonates will take ^{12}C and ^{13}C in the same proportion as seawater. On the other hand, during the autotrophic fixation of CO_2, ^{12}C is preferentially incorporated relative to ^{13}C, determined by the kinetic properties of the CO_2-fixing enzyme and the availability of CO_2 at the molecular site of fixation (Park and Epstein, 1960; Emrich et al., 1970; Farquhar et al., 1989). Photosynthetic uptake of the isotopically light ^{12}C leaves the DIC of the surface ocean enriched in the isotopically heavy ^{13}C (Kaufman and Knoll, 1995). The difference in isotopic composition of carbonate and organic carbon is measured as a fractionation. Carbon isotope excursions (CIEs) occur when there is an imbalance between organic carbon oxidation and burial with negative CIEs representing periods of net organic carbon oxidation resulting from the conversion of DOM depleted in ^{13}C to bicarbonate via anaerobic processing. Conversely, positive CIEs occur when there is greater net organic carbon burial, leading to a seawater reservoir of carbon that is isotopically enriched in ^{13}C (Broecker, 1970; Hayes, 1983). The Neoproterozoic is characterized by wide swings in the carbon cycle where $\delta^{13}C$ values in carbonate rocks reach as high as +15‰ and as low as -13‰, likely reflecting periods of non-steady state conditions in the oceans (Fig. 1A). Of the numerous major CIEs in the Neoproterozoic, none have generated as much controversy as the enigmatic Shuram Excursion (henceforth SE), a profoundly negative CIE that preserves early evidence of carbonate biomineralization by animals, and largely precedes the appearance of the soft-bodied Ediacaran biota (Fig. 1B).

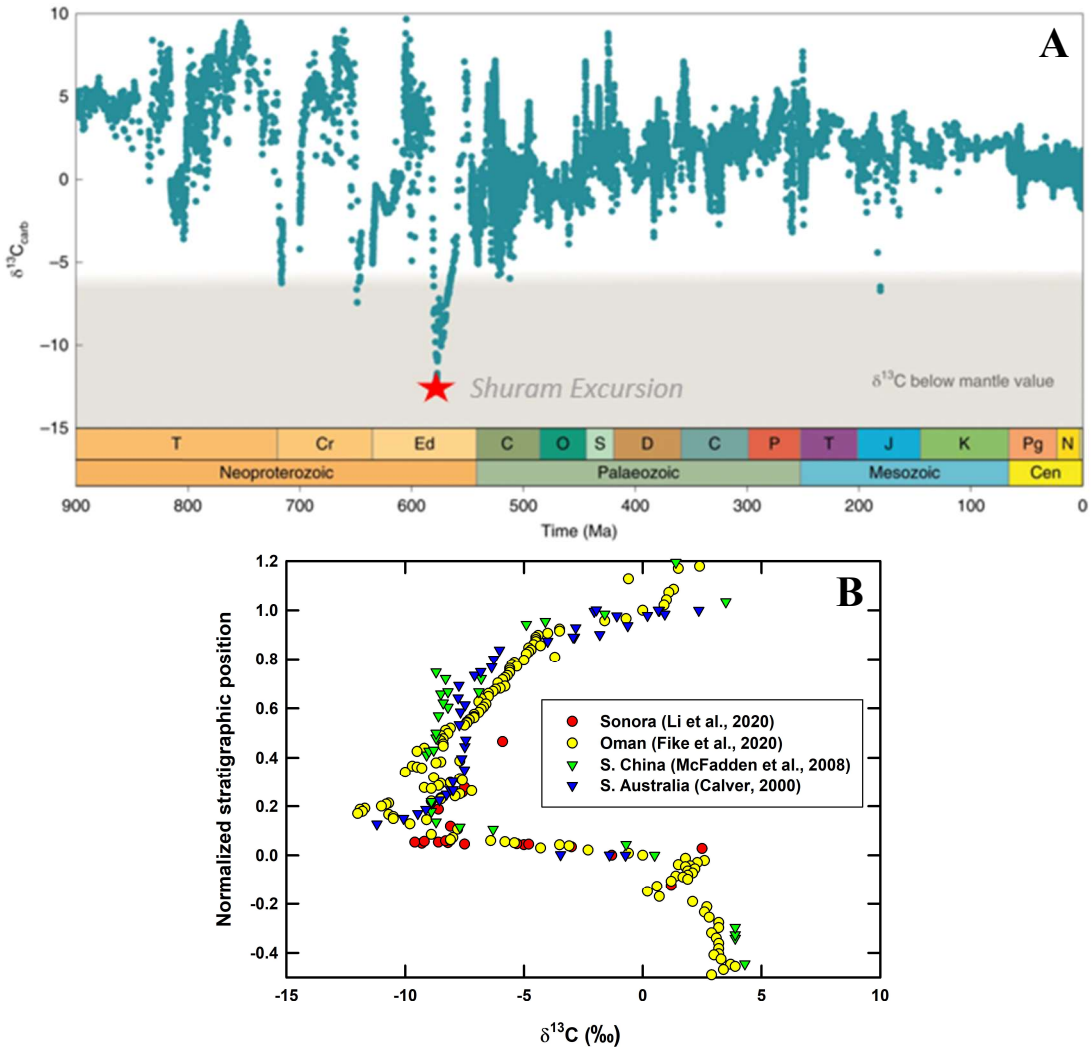


Figure 1.1: (A) Carbon isotope composition of marine carbonates from the Neoproterozoic to the present day, the Precambrian is characterized by extreme positive and negative swings in the carbon cycle, with the Shuram Excursion representing one of the largest negative anomalies in all of Earth history (modified from Shields et al., 2019). (B) Normalized composite of $\delta^{13}C$ data from four geographically distant successions that host the Ediacaran Shuram Excursion: Sonora, NW Mexico (Li et al., 2020); Oman (Fike et al., 2006); South China (McFadden et al., 2008); and South Australia (Calver, 2000). The extreme depletion in the $\delta^{13}C$ values coupled with the anomalous behavior of several other geochemical proxies has made the SE perhaps one of the most controversial events in the entire Neoproterozoic Era.

1.3: The Shuram Excursion

The middle Ediacaran SE is a globally-distributed event preserved on multiple continents across a wide range of shallow marine, carbonate-dominated lithofacies where: (1) $\delta^{13}C$ values reach a nadir of -10‰ or less, well below the canonical mantle input of -6‰ (Fig. 2A; Burns and Matter, 1993; Blank et al. 1999; Rothman et al., 2003; Fike et al., 2006; Kaufman et al., 2007;

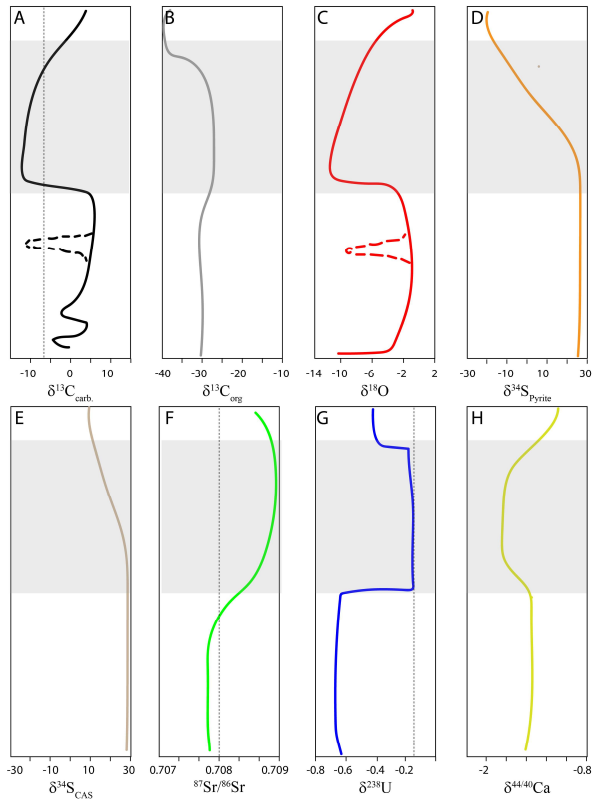


Figure 1.2: Chemostratigraphic observations of the Ediacaran Period before and after the SE. The SE is a prominent event, insofar as it stands out amongst Ediacaran successions, highlighted by the gray shaded region. The data collected is based on (McFadden et al., 2008; Husson et al., 2015; Narbonne et al., 2012; Li et al., 2020) as well as the data collected in herein. Note the stippled curve in the C and O plots represents EN2, a large negative carbon isotope excursion represented only in the Krol Formation of India and the Doushantuo Formation in South China (Kaufman et al., 2006; McFadden et al., 2008).

McFadden et al., 2008; Grotzinger et al., 2011; Husson et al., 2015; Busch et al., 2022); (2) Organic and inorganic carbon isotope compositions are decoupled, arising from the $\delta^{13}C_{org}$ values preserving a stable signal from surface ocean primary productivity, while the $\delta^{13}C_{carb}$ values reflect whole-ocean changes (Fig. 2B; Fike et al., 2006; McFadden et al., 2008; Cañadas et al., 2022); (3) $\delta^{18}O$ values exhibit depletion, and are generally coupled with the $\delta^{13}C$ values, serving as the foundation of the diagenetic argument (see below) (Fig 2C; Knauth and Kennedy, 2009; Derry et al., 2010; Grotzinger, 2011); (4) Up section negative $\delta^{34}S$ excursions are reported for both pyrite and carbonate-associated sulfate (CAS), argued as the product of exposure and weathering of Tonian evaporites or the growth of the global sulfate reservoir (Fig. 2D, E; Fike et al., 2006; Kaufman et al., 2007; McFadden et al., 2008; Cui et al., 2017; Shields et al., 2019); (5) Increasing radiogenic strontium isotope compositions are reported, resulting from increased tectonic collisions and the weathering of exposed igneous and metamorphic continental cores (Fig. 2F; Melezhik et al., 2009; Cui et al., 2015); (6) A step-wise increase in $\delta^{238}U$ values, attributed to

a reduction of the global euxinic pool and an expansion in either oxic or ferruginous conditions (Fig 2G; Zhang et al., 2019; Li et al., 2020; Cao et al., 2020; Gong et al., 2023); and (7) A negative $\delta^{44/40}Ca$ excursion (Husson et al., 2015; Busch et al., 2022) potentially related to carbonate mineralogy (aragonite vs. calcite) or to high precipitation rates associated with a higher seawater carbonate saturation state (Lemarchand et al., 2004; Fantle and DePaolo, 2007; Tang et al., 2008; Nielsen et al., 2011) (Fig. 2H). The observed trends in the various geochemical proxies highlight the unique features of the SE relative to the rest of the Ediacaran Period. Uranium isotope data suggests that the oceans were more ventilated, while the $^{87}Sr/^{86}Sr$ and S isotopic data reflect enhanced continental weathering, which would have trafficked limiting nutrients (like P and N), salts (like Ca^{2+}), ions (like HCO_3^- and CO_3^{2-}), oxidants (like SO_4^{2-}, NO_3^-, Mn(III/IV) oxides, or ferric iron), and sediments into the oceans.

Given the anomalous nature of the SE (ca. 579-564 Ma; Rooney et al., 2020), its global synchroneity based on astrochronologic and magnetostratigraphic records (Minguez and Kodama, 2017), and the uncertainty as to why this non-steady state period in the carbon cycle reaches such negative extremes, numerous hypotheses on its origin have been argued. Despite the many proposed SE origin hypotheses, they can be boiled down to two main arguments: a diagenetic insult or a primary oceanographic event. If associated with later diagenetic or metamorphic processes (e.g., Knauth and Kennedy, 2009; Derry, 2010) all the time-series isotope variations need to be explained by a common process that would affect numerous successions in varying facies, spread globally. Knauth and Kennedy (2009) use the covariation of $\delta^{13}C$ and $\delta^{18}O$ values in SE-bearing successions to explain that the depleted C/O isotopic values of SE carbonates are a result of meteoric fluids rich in decayed terrestrial plant matter flushing through marine platforms and altering or overprinting pre-existing carbonates. This is problematic insofar as younger

Phanerozoic successions that accumulated after the advent of known land plants do not reveal similar C/O isotope excursions, and such processes should have mineralogical and petrographic signposts that have not been observed. Furthermore, meteoric diagenesis is an inherently local process and is typically identified by negative $\delta^{13}C$ shifts near the top of exposure surfaces, which have not been observed in the SE (Allan and Matthews, 1982; Swart and Kennedy, 2012; Husson et al., 2012). Alternatively, Derry (2010) suggests the carbon isotope anomaly worldwide was a result of deep burial diagenesis. However, the smooth and cohesive nature of the C/O isotopes suggests otherwise, and would not explain all of the other systematic isotope system changes observed during the event. The burial diagenesis hypothesis was dismissed by Husson et al. (2012) who used an isotope conglomerate test on SE strata in South Australia to show that the C/O isotope compositions were depositional and not diagenetic. Bergmann (2013) similarly concluded (from clumped carbon isotope compositions that monitor equilibration temperatures of SE carbonates in the western USA) that deep burial and thermal alteration was unlikely. Lastly, Busch et al. (2022) argued that low $\delta^{44/40}Ca$ and high Sr/Ca ratios in SE successions worldwide were inconsistent with late-stage diagenesis. If early diagenetic in origin, the SE might be explained by an authigenic mixing model in which calcite strongly depleted in ^{13}C formed in unconsolidated sediments through the buildup of alkalinity in pore fluids by the anaerobic oxidation of methane (Schrag et al., 2013; Cui et al., 2017). This would suggest varying degrees of authigenic calcite mineralization, likely in the sulfate-methane transition zone (SMTZ), which could explain the time-series carbon isotope trend recorded in the SE globally.

If the SE was an oceanographic phenomenon, seawater dissolved inorganic carbon (DIC) would either require an additional source of ^{12}C or that the fractionation between carbonate ion and mineral carbonate would need to increase to record such low $\delta^{13}C$ values in marine carbonates

insofar as the mantle input to surface environments has a value of -6‰ (Blank et al., 1993). The sudden increase in ^{12}C in DIC may have resulted from disequilibrium in SE oceans with pre-Shuram conditions characterized by anoxic seawater containing a high percentage of dissolved organic carbon (DOC). During the SE, the DOC pool could have been subsequently remineralized to dissolved inorganic carbon (DIC) (requiring anaerobic processing since aerobic remineralization only releases CO_2) resulting in the formation of carbonates strongly depleted in ^{13}C (Rothman et al., 2003; Fike et al., 2006; Kaufman et al., 2007; McFadden et al., 2008; Cui et al., 2017). The oxidation of this large DOC pool requires a massive source of oxidants to sustain such a long-lived excursion. According to Bristow and Kennedy (2008), the flux of oxidants available in the late Neoproterozoic oceans were insufficient to support the SE DOC model. However, throughout the Neoproterozoic and into the Cambrian Period, the surface of the planet was undergoing profound tectonic reconfiguration associated with the formation of the Gondwana supercontinent and the rise of an equatorial chain of Trans-Gondwanan super mountains and globally distributed suture zones (Squire, 2006; Schmidt et al., 2018). The increasingly radiogenic $^{87}Sr/^{86}Sr$ coupled with the increase in carbonate-associated sulfate during the event is consistent with enhanced tectonic uplift and weathering triggered by Pan-African orogenesis (Meert, 2003; Fike et al., 2006; Melezhik et al., 2009; Osburn et al., 2015). Enhanced weathering of the continents would result in the pulsed delivery of oxidants to the oceans, providing the accelerant needed to remineralize the large DOC pool. Furthermore, the added delivery of salts to the oceans would have resulted in the supersaturation of carbonate ions, potentially providing an alternative explanation for the covariation of C/O isotopes. Experimental studies by Spero et al. (1997) on biogenic carbonates found that with increasing carbonate saturation and pH, an isotope effect takes place in foraminifera that is expressed by a notable depletion and co-variation amongst C/O

isotopes. A follow up study by Zeebe (1999) found that the effect of [CO_3^{2-}] on O isotopes of inorganic calcite is virtually indistinguishable from that of the planktonic foraminifer *Orbulina universa*.

Numerous supporting lines of evidence corroborate an oceanographic origin for the enigmatic SE. The growth of the CAS reservoir during the SE may have resulted from the dissolution of exposed Tonian evaporite lithologies, delivering sulfate to the oceans. Reduction of the newly delivered sulfate would produce pyrite that, once buried, would promote the oxygenation of the ocean, allowing for the oxidation of the large DOC pool (Shields et al., 2019). The initiation of the oxygenation event occurred shortly after the onset of the SE and was terminated at the end of the event, plunging the Ediacaran oceans back to a predominantly anoxic or ferruginous state (Canfield et al., 2008; Zhang et al., 2018; Kendall et al., 2015; Tostevin et al., 2019; Cherry et al., 2022). Several lines of evidence support the SE ventilation model, including sulfate triple oxygen isotopes ($\Delta^{17}O$), which reveal ^{17}O-depleted atmospheric O_2 in marine sulfate minerals or CAS, attributed to the oxidative weathering of pyrite on land delivering sulfate to the oceans and the oxidation of reduced sulfur species in the deep ocean caused by the invasion of atmospheric O_2 (Wang et al., 2023). Furthermore, the enhanced delivery of key limiting nutrients (like P) through continental weathering to the oceans would have stimulated a biological turnover, spurring photosynthetic reactions, which when combined with enhanced sedimentation rates and increased organic matter burial, could oxygenate previously anoxic or euxinic water masses (Van Cappellen and Ingall, 1996). Carbonate-associated phosphate (CAP) data reported by Dodd et al. (2023) reveals two pronounced spikes during the initial and final stages of the SE, suggesting a period of non-steady state conditions in which enhanced weathering on land delivered sulfate to the predominantly anoxic oceans. This would result in the oxidation of the large DOC pool, releasing

organic-bound C and P, driving the negative downturn of the $\delta^{13}C$ values and subsequent oxygenation of the oceans, reflected in the positive shift in $\delta^{238}U$ values.

The potential drivers for the increase in productivity and the sudden onset of oxygenation associated with the SE all share one common process: intensified continental weathering. During the Ediacaran Period, the $^{87}Sr/^{86}Sr$ record is characterized by a notable rise to increasingly radiogenic values during the SE, corresponding to the tectonic uplift and weathering triggered by Pan-African orogenesis (Melezhik et al., 2009; Cui et al., 2017). However, the Sr record is complicated insofar as it reflects sources rather than overall weathering rate with increasingly radiogenic values corresponding to continental collision and the weathering of exposed igneous and metamorphic cores. On the other hand, non-radiogenic values could correspond to rifting periods and increased hydrothermal input (Kısakűrek et al., 2005), or to alteration by fluid flow through flood basalts (Cui et al., 2019). For this reason, an independent monitor of continental weathering that is unaffected by the source terrain is required to better understand potential terrestrial drivers of the SE. An emerging proxy that provides a means of quantifying the intensity and style of weathering on the continents is the lithium isotope system.

1.4: Lithium Isotopes

Lithium isotopes serve as an excellent proxy for assessing terrestrial weathering rates because the isotopic composition of marine carbonates (recorded as $\delta^{7}Li$) is determined by the fractionation between solution, secondary mineral formation (primarily clays), and the intensity of weathering, rather than bedrock lithology (Pogge van Strandmann et al., 2010). Lithium has two stable isotopes, the minor ^{6}Li and the major ^{7}Li, the mass difference between which is large, imparting a considerable fractionation when subject to low temperature geochemical processes. Because of its long residence time (~1 Myr), lithium is homogenously distributed throughout the

ocean (Penniston-Dorland et al., 2017; Cao et al., 2022). There are three main sources for seawater lithium, hydrothermal input from mid-ocean ridges (~13.7 ± 2.8 Gmol/yr), riverine input via silicate weathering of continental rock (~10 Gmol/yr), and subduction refluxed Li (6 Gmol/yr; Misra and Froelich, 2012). The two sinks include low-temperature hydrothermal alteration and marine authigenic aluminosilicate clay formation (MAACs; ~28 Gmol/yr) which remove Li from seawater, imparting a large fractionation of Li isotopes (Fig. 1.3; Misra and Froelich, 2012; Cao et al., 2022; Weldeghebriel and Lowenstein, 2023). The modern ocean has a δ^7Li of ~31‰, with the hydrothermal sources characterized δ^7Li values of ~8.3‰, dissolved Li from rivers containing a δ^7Li composition of ~23‰, and subduction refluxed Li matching that of the subducted sediments (~15‰; Hathorne and James, 2006). In sedimentary environments, Li is preferentially incorporated, relative to other soluble elements like Na^+ and Ca^{2+}, during the alteration and

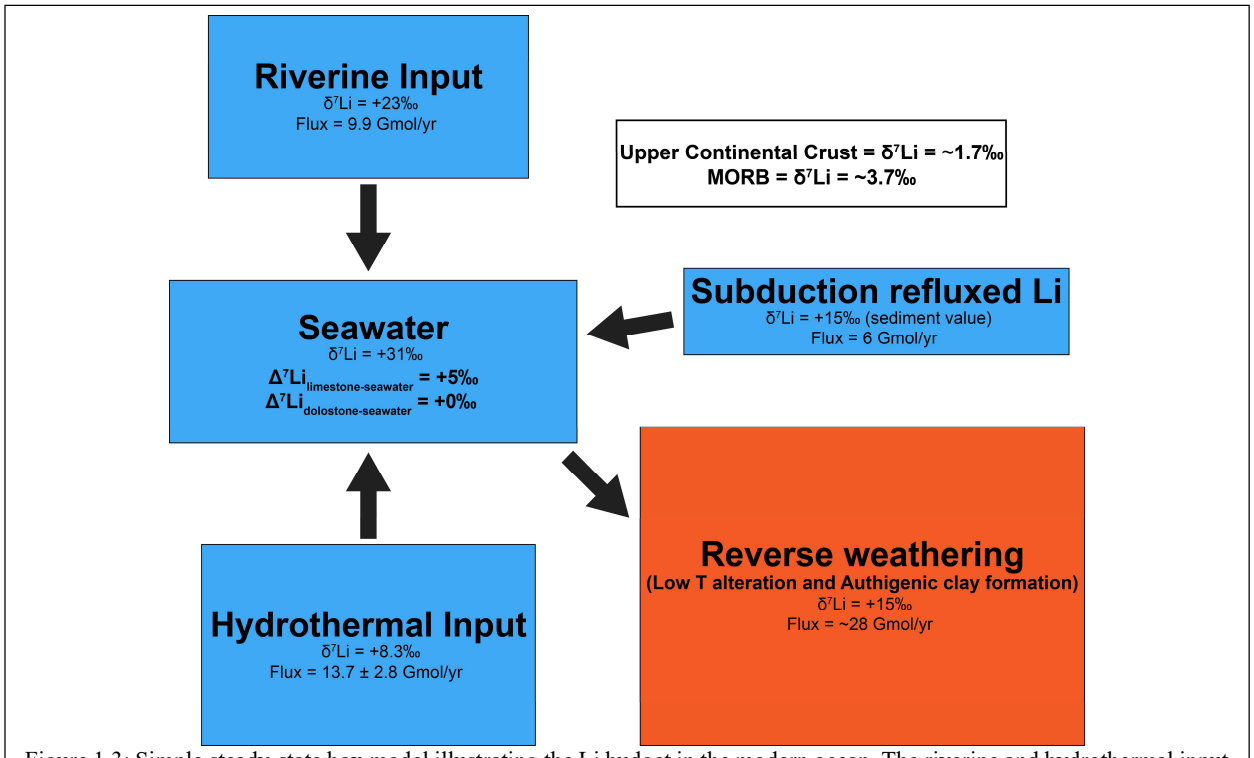


Figure 1.3: Simple steady-state box model illustrating the Li budget in the modern ocean. The riverine and hydrothermal input are the two main sources, though subduction refluxed Li does contribute to the seawater Li inventory. The dominant removal mechanism is through the formation of MAACs and low T hydrothermal alteration (modified after Misra and Froelich, 2012; Weldeghebriel and Lowenstein, 2023).

formation of clay minerals like kaolinite, illite, smectite, sepiolite, and the micas (Starkey, 1982). There are two primary weathering processes that can affect seawater δ^7Li, congruent weathering, where primary mineral dissolution results in a high dissolved riverine Li flux characterized by a low isotopic composition (approaching the average crustal value of 0‰; Teng et al., 2004), and incongruent weathering, where the formation of secondary clay minerals preferentially incorporate ^{6}Li, imparting a large fractionation and thus resulting in a suspended riverine flux rich in Li and a dissolved flux with low [Li] and a high isotopic composition (Pogge von Strandmann et al., 2022). For inorganically precipitated and biogenically secreted carbonates, lithium has a constant isotopic fractionation of approximately 5 ± 5‰ from seawater, and thus, the relatively small fractionations (<1.5‰) imparted by the effects of temperature and salinity, which control Li uptake into secondary minerals, are negligible (Marriott et al., 2004a; Mariott et al., 2004b; Misra and Froelich, 2012; Pogge von Strandmann et al., 2013, 2019). Therefore, δ^7Li of marine carbonates serve as an excellent proxy for assessing differences in weathering regimes and by extension, major perturbations to the ocean-atmosphere system that may have been promoted by the intense physical and chemical weathering of the continents.

1.5: Strontium Isotopes

Like lithium isotopes, radiogenic strontium isotope (^{87}Sr/^{86}Sr) compositions have been used to track periods of orogenesis and rifting, due to the long residence time (~2.5 Ma) and homogenous distribution of strontium in seawater (Broecker and Peng, 1982). In the ocean, Sr has two sources, the weathering of exposed terrestrial rocks, including igneous and metamorphic cores rich in ^{87}Rb, and hydrothermal input, lacking ^{87}Sr due to the absence of Rb in basalts. Thus, variations in ^{87}Sr/^{86}Sr have been interpreted to reflect varying proportions of Sr input from riverine and hydrothermal sources (Faure, 1986; Veizer et al., 1999), with increasingly radiogenic

compositions corresponding to mountain-building events and non-radiogenic signatures during LIP emplacement or rifting events (Goldstein and Jacobsen, 1987).

In addition to radiogenic Sr isotopes, stable strontium ($\delta^{88}Sr$) has recently emerged as a promising proxy to track carbonate precipitation rates. During carbonate precipitation, the lighter ^{86}Sr is preferentially incorporated, leaving seawater enriched in ^{88}Sr, with the fractionation between carbonate and seawater ($\Delta^{88}Sr$) growing with increasing precipitation rates (Böhm et al., 2012; Wang et al., 2023). However, while this holds true on a local scale, the rapid removal of ^{86}Sr will drive the $\delta^{88}Sr$ of precipitating carbonates towards heavier values, creating a 'lost reservoir' which may be preserved in authigenic carbonates precipitating from high alkalinity pore waters (Wang et al., 2023).

1.6: Uranium Isotopes

In the modern ocean, uranium has a concentration of roughly 3.2 ppb and a residence time of approximately 500 kyr. The typical thermohaline mixing cycle in the ocean is approximately 1-2 kyr resulting in $\delta^{238}U$ compositions that are homogenous and globally distributed in an oxidized open ocean (Zhang et al., 2018), thus serving as an excellent indicator for tracing global redox changes. Additionally, uranium exists in two natural redox states, the soluble U(VI), which is responsible for forming calcium-uranyl-bicarbonate structures under oxidized conditions. Under euxinic conditions, U(VI) is reduced to the insoluble U(IV), imparting a large, relative to the degree of mass difference, fractionation caused by the nuclear volume effect (NVE) as well as mass-dependent effects, in which the reduced phase preferentially sequesters ^{238}U (Bigeleisen, 1996; Nomura et al., 1996; Schauble, 2007; Zhang et al., 2020). The rate of U removal to sediments ultimately places a control on the direction of fractionation, where fast removal is determined by

kinetic effects that favor the light isotope while slow removal favors the heavy isotope (Brown et al., 2018; Zhang et al., 2020).

Among the various sinks for seawater uranium, reducing sediments impart the fractionation through the preferential sequestration of ^{238}U (Fig. 1.4). Carbonate sediments represent a second uranium sink that would impart a smaller fractionation, but during specific events when the carbonate rain rate appears elevated, these may be volumetrically more significant than reducing sediments. However, because the reducing sediments pull the heavier ^{238}U from seawater more effectively, the carbonate sediments in equilibrium with seawater are also depleted with respect to ^{238}U, thus recording strong negative $\delta^{238}U$ compositions (Stirling et al., 2015, Lau et al., 2017). Conversely, under oxygenated (or ventilated) conditions, a decrease in the size of the euxinic pool by seemingly insignificant amounts has the ability to impart a notable fractionation on the $\delta^{238}U$ values of seawater, reflected by a positive shift in carbonate $\delta^{238}U$ values (Kipp and Tissot, 2022). Uranium reduction also occurs through biotic means via the enzymatic activities of sulfate or other dissimilatory reducing bacteria, which is the dominant cause of U reduction in natural environments today (Barnes and Cochran, 1993; Rademacher et al., 2006; Basu et al., 2014; Stylo et al., 2015; Zhang et al., 2020). Despite the overly simplified model of the controls over the isotopic composition and fractionating behavior of U in the oceanic reservoir, the extent of

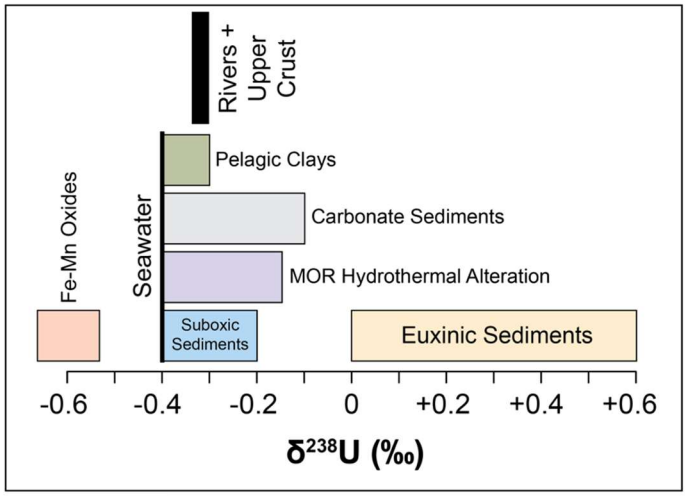


Figure 1.4: Simplified mass balance for seawater U. The two dominant sinks for U are euxinic/reducing sediments, which preferentially incorporate the isotopically heavy U(IV) species, and carbonates which form calcium-uranyl complexes with the aqueous U(IV) (after Tissot and Dauphas, 2015).

reducing conditions in marine environments has the largest influence on seawater U isotopic compositions, serving as a reliable proxy to track changes in the proportion of oxic and anoxic seafloor on a global scale. However, the effect of high carbonate saturation cannot be overlooked. Precipitation experiments under various pH, [Ca^{2+}], [Mg^{2+}], and [CO_3^{2-}] revealed that relatively small U isotope fractionations occur during coprecipitation with aragonite, although when fractionations were observed, Rayleigh-type behavior occurred with ^{238}U preferentially incorporated into aragonite at pH 8.5 (Chen et al., 2017).

1.7: Rare Earth Elements (REEs)

To investigate local redox conditions, the use of Rare Earth Element (REE) abundances in carbonates has been successfully employed in many recent Ediacaran studies. One element, cerium, is unique amongst the other REE because it can exist in both the trivalent and tetravalent oxidation states. Under oxic conditions, Ce(III) is partially oxidized to Ce(IV) and absorbed onto the surface of Mn oxides, where it no longer participates in solid solution exchange reactions, depleting the residual seawater in Ce relative to the other REE (Tostevin et al., 2016). In this study, cerium anomalies are calculated by comparing the Post Archean Australian Shale (PAAS)-normalized concentrations of Ce to its neighboring REE using the following equation:

$$\frac{Ce_{SN}}{Ce^*_{SN}} = \frac{[Ce]_{SN}}{(\frac{[Pr]^2_{SN}}{[Nd]_{SN}})} \quad \text{(eq. 1.1)}$$

Negative Ce anomalies are ubiquitous in the modern, well-oxygenated ocean, although the magnitude of the anomaly varies within and between ocean basins (De Baar et al., 1985; De Baar, 1991), and can respond to changes in water column redox on a meter scale (De Carlo and Green, 2002). Under anoxic conditions, Ce remains in the trivalent state and is not removed from the

water column which results in a Ce/Ce* ratio that is greater than or equal to 0.9. However, positive Ce-anomalies can be generated under manganous conditions in which the tetravalent Ce contacts an anoxic or manganous fluid (or redoxcline) and is reduced to the trivalent state. Additionally, the preferential stabilization and formation of carbonato-Ce(IV)-complexes under alkaline conditions may also bring about a positive Ce/Ce* (Möller and Bau, 1993; Pourret et al., 2008; Wu et al., 2018). Another powerful proxy, yttrium to holmium (Y/Ho) ratios, can be used validate a primary seawater signal within carbonates as Ho is scavenged rapidly from seawater relative to Y due to differences in surface complexation, thus a higher Y/Ho (>36) indicates a primary seawater signal (Liu and Byrne, 1995; Nozaki et al., 1997; Nothdurft et al., 2004; Tostevin et al., 2016).

1.8: Geology

1.8.1: Siberia

A recent discovery of a SE reef complex in Siberia containing the biomineralized remains of early animals (Kaufman et al., 2023) supports the view that the carbon cycle anomaly was oceanographic rather than diagenetic in origin. In the Patom Uplift of Siberia, bioclasts with external calcium carbonate coatings and scales, along with internal chambers and channels, interpreted as the remains of a sponge-grade animal, were found in the reef complex of the Khopych Formation (Fig. 1.5A). The discovery of biomineralized animals is consistent with elevated levels of nutrients, salts (including Ca^{2+}), and ions (bicarbonate and carbonate) in the SE oceans. Because calcium is highly regulated by animals with its excess used to form bones, teeth, shells, or excreted with other waste (Simkiss, 1977), the sudden appearance of biomineralized animal fossils implies that the flux of salts like Ca^{2+} and dissolved carbonate ion into the oceans

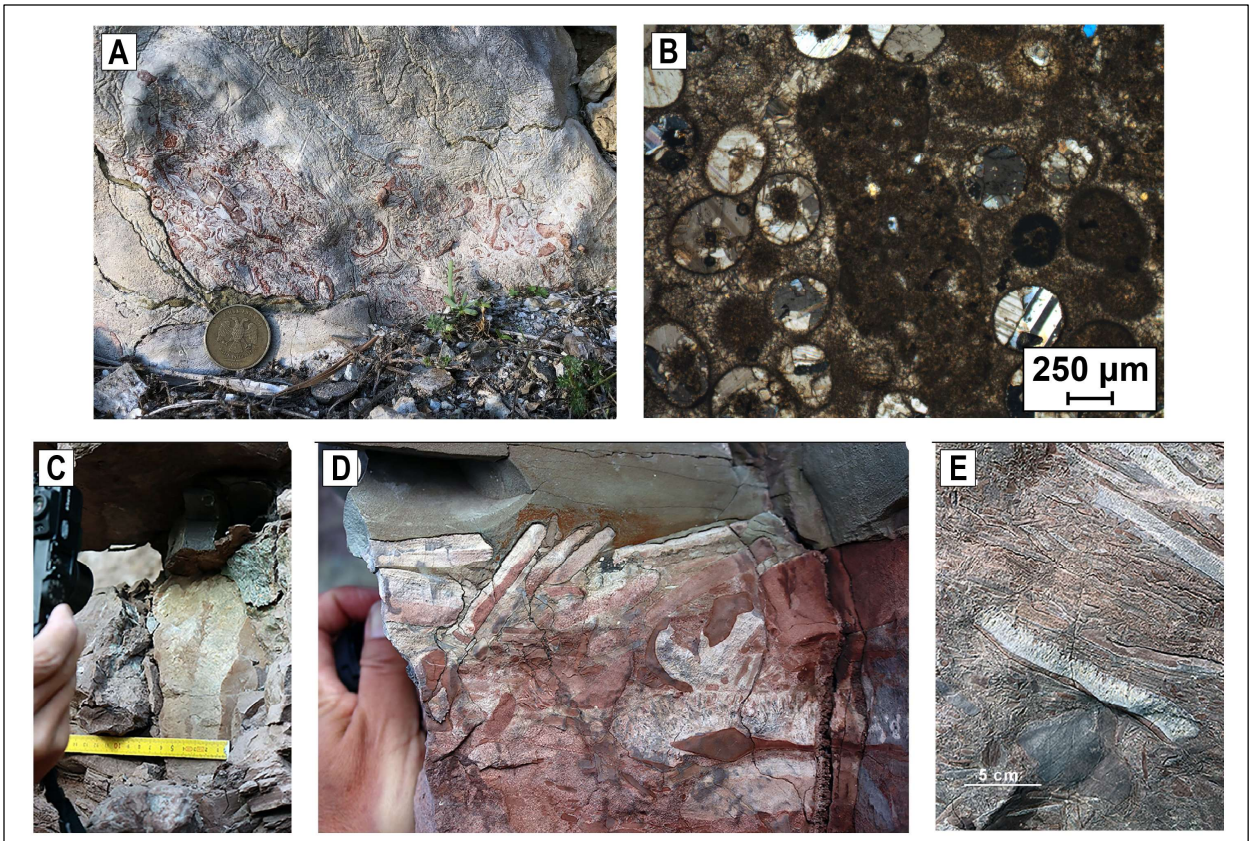


Figure 1.5: Sedimentological indicators of high carbonate saturation found within the Patom Uplift. (A) Biomineralized remains of a sponge-grade organisms found within a reef complex in the Khopych Formation. (B) Massive grapestones and ooids (average diameter ~250 µm), some of which have been neomorphosed from aragonite to calcite and others appear bimineralic, and grapestones. (C) Vertical sheet crack cements. (D) Plate breccias formed from a storm event ripping up the seafloor which was rapidly cemented. (E) Aragonite precipitate cements that resemble blades of grass growing from the seafloor.

were so high that animals living in the oceans were forced to form shells to regulate calcium concentrations in their cells. Sedimentological indicators in the SE succession of Siberia also support increased seawater carbonate saturation through the presence of large ooids and grapestones, vertical sheet crack cements, plate breccias containing clasts of former seafloor that had been ripped up during storm events and rapidly lithified, and aragonite precipitates (Fig. 1.5B, D). It is plausible that the enhanced delivery of salts, sediments, oxidants, ions, and nutrients would have been transported to the oceans via an intense weathering flux during the SE associated with tectonic uplift and erosion of exposed continents.

The Patom/Ura Uplift is part of the broader Patom Supergroup, a late Neoproterozoic succession, located in central Siberia, which is comprised of thick (~5-7 km) siliciclastic and carbonate successions that have been folded and uplifted (Fig. 1.6A). It is divided into the Dal'nyaya Taiga, Zhuya, and Trehversta groups (Fig. 1.6B). The Dal'nyaya Taiga Group is subdivided into the Bol'shoy Patom, Barakun, Ura, and Kalancha formations. The basal Bol'shoy Patom Formation forms the interior of two NW-trending anticlines, consisting of dark gray massive and faintly bedded diamictites and conglo-breccias (with striated clasts and dropstones in laminated facies), considered correlative to the Marinoan glacial diamictites (Chumakov et al., 2011). Deposited over the Bol'shoy Patom Formation is a 5-7 m thick 'cap dolostone' with $\delta^{13}C$ values approaching -5‰ before rising to +8‰, then gradually decreasing to 0‰ over a ~1500 m stratigraphic interval at the top of the Kalancha Formation (Fig. 1.5B; Pokrovskii et al., 2006; Petrov, 2018). The presence of acanthomorphic acritarchs in the Barakun Formation showing a marked resemblance to the lower Ediacaran Doushantuo-Pertatataka assemblage is consistent with Pb-Pb dates for the Barakun and Kalancha formations of 581 ± 16 Ma and 574 ± 20 Ma, respectively (Sergeev et al., 2011; Rud'ko et al., 2021; Moczydłowska and Nagovitsin, 2012; Vorob'eva and Petrov, 2020).

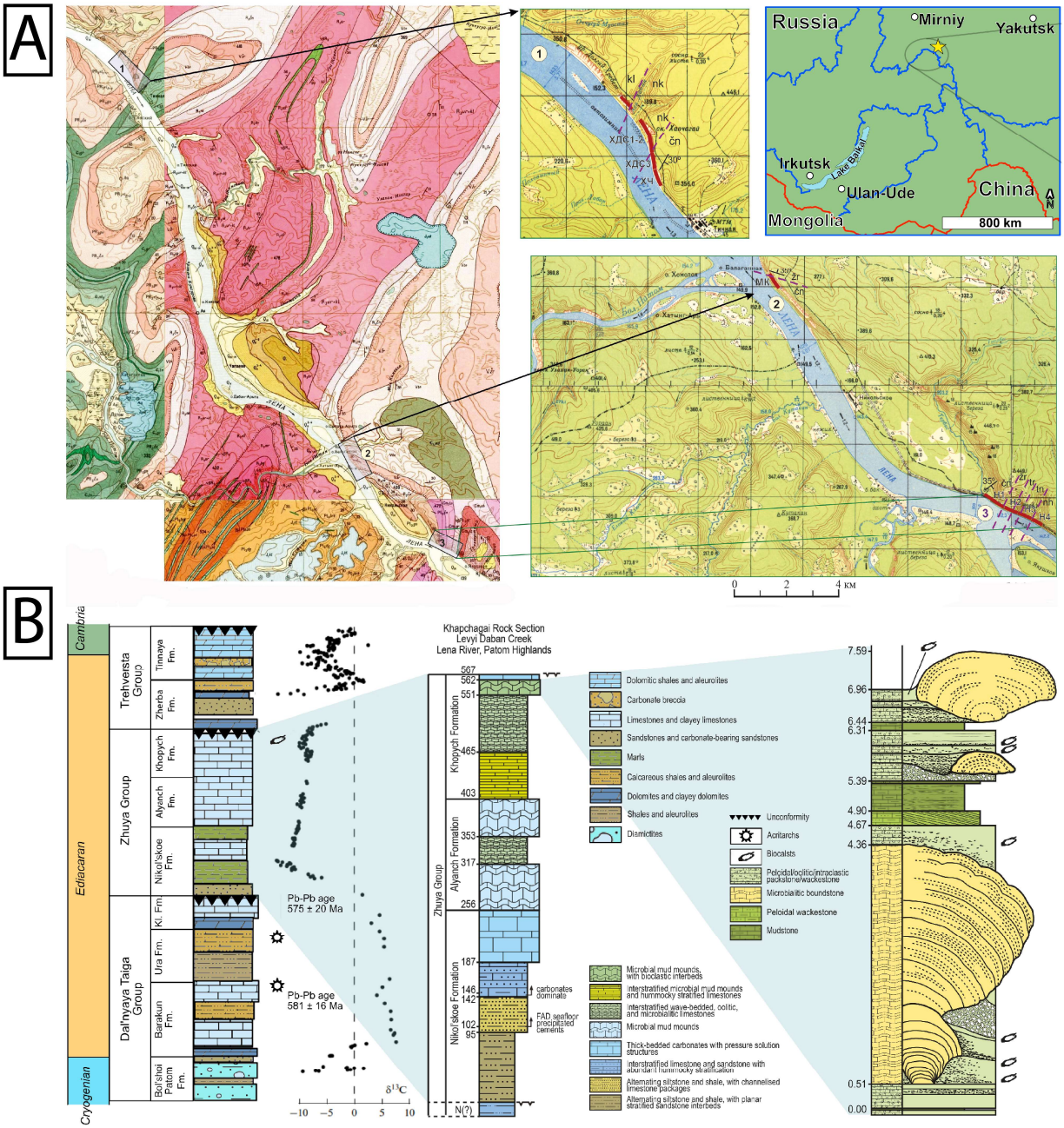


Figure 1.6: (A) Geological and geographical maps illustrating the location of the studied Khapchagai Rock Section in the Patom Highlands of Sibieria. The sampled outcrops are exposed along the Lena River approximately 130 km east of Lensk, Russia (60º19'01.74" N, 116º55'11.07" E). (B) Composite of the Patom Supergroup which is predominantly comprised of Ediacaran successions, but also includes the Cryogenian Bol'shoi Patom Formation and the Cambrian Zherba and Tinnaya formations. Timeseries carbon isotope trends, the presence of acanthomorphic acritacrchs in the Ura Formation, and Pb-Pb dates correlate the large negative carbon isotope excursion spanning the Zhuya Group to other SE successions. The Zhuya Group is truncated by two erosional surfaces at the Khapchagai Section, one at the base of the Nikol'skoe Formation and the other at the top of the Khopych Formation above the reef complex (modified after Moczydłowska & Nagovitsin, 2011).

Overlying the Dal'nyaya Taiga Group is the Zhuya Group, which, based on field observations, is dominated by subtidal carbonates that preserve a wide array of sedimentary textures indicative of elevated carbonate saturation. The basal layers of the Nikol'skoe Formation are dominated by aragonite precipitates, sheet-crack cements, seafloor plate breccias, and large (~250 μm) ooids with a radial internal fabric and very thin outer cortices. The basal ~150 m of the formation consists of alternating siltstone and shales with planar stratified sandstone interbeds that gradually shift to alternating siltstone and shale with channelized limestone packages. Around 150 m into the section carbonates begin to dominate with interstratified limestones and sandstones with abundant hummocky stratification. Above this section are thickly bedded carbonates that represent the top of the Nikol'skoe Formation forming a sharp contact with the overlying Alyanch Formation. The base of the Alyanch Formation is characterized by large wavelength and massive microbial mud mounds that dominate for approximately 200 m before contacting the overlying Khopych Formation. The Khopych Formation was deposited in an upper ramp to reef setting, evidenced by the interstratified microbial mudmounds, hummocky stratified limestone, oolitic and microbialitic limestone, and a reef complex with bioclastic interbeds at the top of the formation. The Khopych Formation contains two distinct ooid morphotypes, the first ~100 m is characterized by the presence of ooids with a tangential cortex and micritic to microspar and blocky nucleus, indicative of deposition in a shoaling environment and an original aragonite mineralogy. The second ooid morphotype occurs above the Khopych Formation reef and are defined by blocky and neomorphosed nuclei and tangential fabrics, some of which may have been bimineralic.

The reef complex is roughly 8 m thick, representing a diverse array of lithologies, highlighting the complexity of the Khopych depositional environment. The basal layers are an

amalgamation of limestones interbedded with mudstone, oolites, and siltstone with some cross-bedding structures indicating tidal motion. Roughly 1.5 m from the bottom of the reef complex, there appears to be the remains of an incised channel overlain by a layer of oolites and cross-bedded limestones and interbedded sandstones suggesting a shallower ocean setting. The remaining layers are composed of oolites and alternating beds of limestone and sandstone with mudstone interbeds and bioherms. The top of the 8 m section contains the biomineralized remains of potential sponge-grade organisms. The sedimentary structures preserved in the reef complex are consistent with the overarching interpretation that the Zhuya Group represents a shallow carbonate ramp-to-rim transition that was well-connected to the open ocean.

A distinct and profound negative carbon isotope excursion correlated to the Shuram Excursion worldwide is preserved in the very high Sr carbonates of the Nikol'skoe, Alyanch, and Khopych formations (Pokrovskii et al., 2006; Melezhik et al., 2009; Pokrovsky and Bujakaite, 2015) where the $\delta^{13}C$ values sharply decrease from near 0 to a nadir of -12‰ in the Nikol'skoe Formation and slowly climb to -7‰ in the Alyanch and Khopych formations where they are truncated by an unconformity. Thus the Patom Uplift succession represents only a portion of the entire SE (Fig. 1.6B on page 19). The equivalence of these units with the SE worldwide is supported by the presence of potential Nama Assemblage-type Ediacaran macrofossils in sandstones near the top of the Khopych and overlying Zherba formations (Kolesnikov et al., 2024). The top of the Khopych Formation is truncated by an erosional surface where it unconformably contacts the overlying Trehversta Group, consisting of the Zherba and Tinnaya formations (Pelechaty, 1998; Pokrovsky and Butjikite, 2015). The carbon isotope trend continues to rise above the sequence boundary to values of approximately -5‰, so the disconformity may represent only a brief temporal hiatus. In the upper Zherba and Tinnaya formations, the $\delta^{13}C$ trend (Pokrovsky

and Bujakaite, 2015) documents a second notable and well-defined negative CIE, conceivably representing the BACE event near the Ediacaran-Cambrian boundary (Knoll et al., 1995; Kaufman et al., 1996; Pelechaty et al., 1996; Zhu et al., 2006). This chemostratigraphic trend is also consistent with the preservation of Cambrian small shelly fossils in the upper Tinnaya Formation.

1.8.2: South China

The Doushantuo Formation is distributed throughout South China, deposited in a marine shelf environment on the Yangtze Block, a passive continental margin, with sedimentological evidence suggesting that the entire formation at the Jiulongwan section (the locality in this study) was deposited at or near wave base (Jiang et al., 2003; McFadden et al., 2008; Jiang et al., 2011). Subdivided into four members, the Doushantuo Formation at the Three Gorges area has been constrained between 635.2 ± 0.6 and 551 ± 0.7 Ma based on U-Pb dates, although the upper age constraint may be complicated by the presence of a major unconformity (Fig. 1.7; Condon et al., 2005; McFadden et al., 2008; An et al., 2015; Yang et al., 2016). Member I was deposited during one of three transgressive-regressive sequences, consisting of a 3-5 m cap carbonate that overlies the Cryogenian Nantuo glacial diamictite. It is comprised of thinly laminated and normally graded dolomite and limestone with tepee-like structures composed of cavities lined by cements and host dolomicrites, bedding parallel sheet cracks, and cemented breccias (Jiang et al., 2006). Member II is composed of organic-rich shales and dolostone beds containing abundant chert nodules, potential animal eggs and embryos, multicellular algae, filamentous and coccoidal cyanobacteria, and the enigmatic Doushantuo-Pertatataka acritarch assemblage (Zhou et al., 2007; McFadden et al., 2008). Member III is a 70 m section that consists of dolostone with bedded cherts that span approximately 40 m with the remaining 30 m comprised of ribbon limestone (Zhang et al., 2019). Member IV is the uppermost unit in the Doushantuo Formation, characterized by approximately

10 m of organic-rich shales with thin dolostone interbeds that contentiously forms an unconformable contact with the Dengying Formation (McFadden et al., 2008; An et al., 2015). Timeseries carbon isotope trends in the Doushantuo Formation, reported in McFadden et al. (2008), highlight 3 negative excursions (often referred to as EN1-3) separated by two positive excursions (EP1 and EP2). Member I hosts EN1 where $\delta^{13}C$ values drop to -5‰ before climbing to +5‰ in Member II, where the values remain relatively stable before EN2, which is a short, but profoundly negative excursion near the boundary between Members II/III. Members III/IV contain the profound EN3 or Shuram Excursion where the $\delta^{13}C$ values rapidly drop to roughly -10‰ and slowly rise to approximately 0‰ at the top of Member IV, although the abundant black shales present in this interval is problematic for interpreting the rise in $\delta^{13}C$ values.

The overlying Dengying Formation is subdivided into three members, including the Hamajing, Shibantan, and Baimatuo members. The Hamajing Member is composed of thick-bedded dolostones, overlain by the dark, bituminous limestones of the Shibantan Member which contains fossils of Ediacaran biota (Chen et al., 2014). The Baimatuo Member overlies the Shibantan Member and is composed of thickly-bedded massive dolostones. The $\delta^{13}C$ values reach a pinnacle of approximately +5‰ before a marked negative $\delta^{13}C$ excursion in the overlying Yanjiahe Formation, which, based on the presence of overlying small shelly fossils (or SSFs) above the excursion, is arguably related to the BACE event (Ishikawa et al., 2008; Jiang et al., 2012; An et al., 2015).

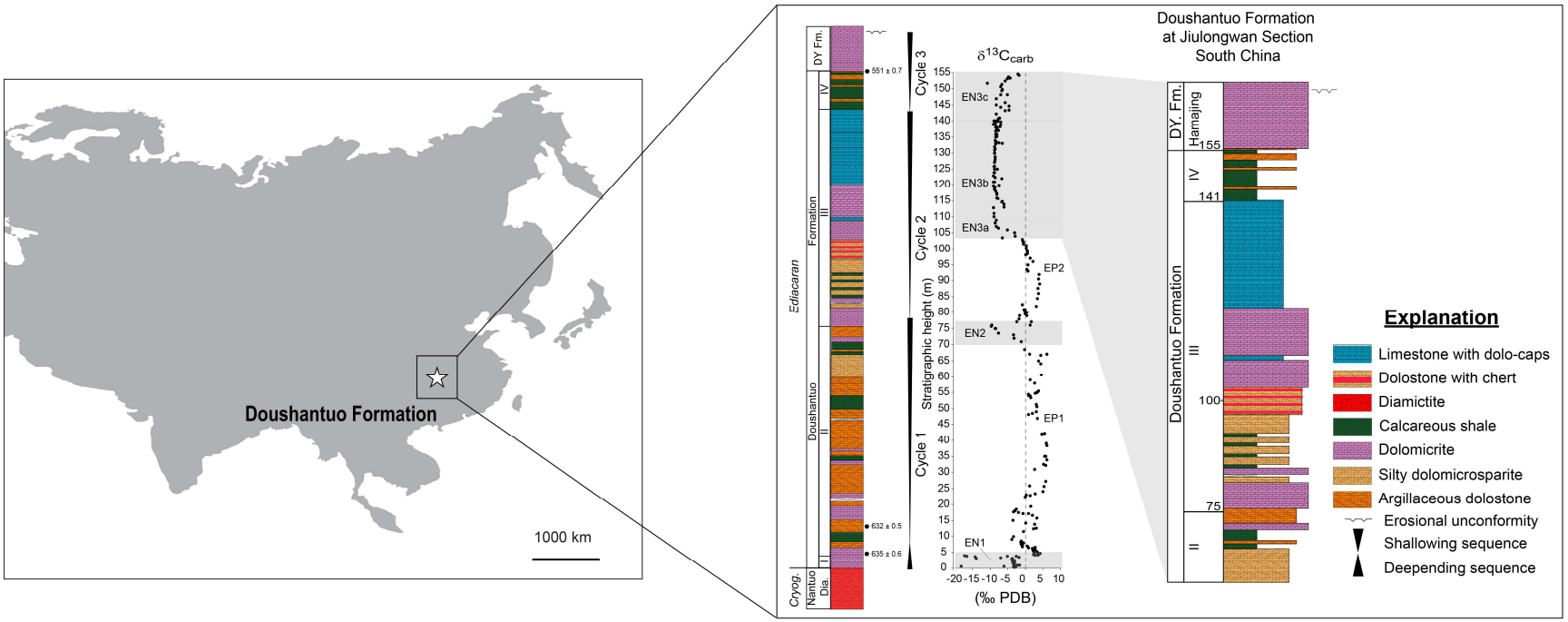


Figure 1.7: Geographical map indicating the location of the Doushantuo Formation at the Three Gorges region. The formation is subdivided into four members, spanning roughly 160 m and composed of mixed limestone, dolostone, and shaly intervals. The unit overlies the Nantuo Diamictite, corroborating the lower Ediacaran age constraint. The overlying Dengying Formation marks the last Ediacaran unit just prior to the BACE Event. Based on the carbon isotope chemostratigraphy, there are several prominent carbon isotope excursions, both positive and negative, preserved in the Doushantuo Formation, though the largest, EN3, is considered to be the SE based on the very negative $\delta^{13}C$, the presence of the novel Doushantuo-Pertatataka acritarch assemblage in units below the excursion, and the rough age constraints (modified after McFadden et al., 2008).

1.9: Research Goals

The goal of this study is to utilize various geochemical barometers to assess the environmental and biological drivers of the alkalinity and oxygenation events observed during the Shuram Excursion. The intense periods of tectonic reconfiguration associated with the formation of Gondwana and the physical weathering of freshly uplifted terrains, coupled with elevated CO_2 enhancing congruent silicate weathering would have delivered blanket of sediments, salts, and ions to the oceans. This flux of freshly weathered continental material would have contributed to the supersaturation of the oceans with respect to carbonate and promoted rapid sedimentation rates, evidenced by previous geochemical indicators of enhanced weathering ($^{87}Sr/^{86}Sr$), elevated carbonate saturation ($\delta^{44/40}Ca$, coupled C/O isotopes), and the numerous sedimentological indicators (giant ooids and grapestones, aragonite fans, seafloor plate breccias, biomineralized remains, and vertical sheet crack cements). For this reason, I predict that marine carbonate Li isotope values will shift towards crustal values during the SE. However, because the Patom Uplift only preserves the nadir and climbing limb of the SE, the Li isotope composition of carbonates from the Doushantuo Formation in South China will be measured to reconstruct the full Li isotope expression of the SE. I predict that the carbonate Li isotope values during the SE in South China will be consistent with the those observed in Siberia, indicating a highly congruent weathering regime.

The two key questions to be addressed in this thesis are: 1.) how might enhanced continental weathering explain the ^{13}C depletion of seawater DIC and carbonates, and what are the biological implications; and 2.) how might increased nutrient delivery through weathering drive an oceanic ventilation event as recorded in the $\delta^{238}U$ data for the SE worldwide? To evaluate the sponge ventilation hypothesis, I will be conducting time-series redox geochemistry of the

Nikol'skoe, Alyanch, and Khopych formations in the Patom Uplift of Siberia using the carbonate U isotope and REE compositions as global and local redox proxies, respectively. Based on a previous study of equivalent strata in Siberia (and worldwide), I predict that the U isotopes will be ^{238}U enriched in the study area, and there would be evidence for water column oxygenation based on REE abundances and Ce anomalies.

Chapter 2: Methodology

2.1: Sample Selection

During field work in Autumn of 2021, middle Ediacaran outcrops from the Zhuya Group along the Lena River were sampled at high resolution (roughly 3-5 m spacing) for geochemical analyses including carbonate carbon and oxygen isotopes, lithium isotopes, strontium isotopes, uranium isotopes, and major, minor, trace, and REE abundances. The collected samples cover the climbing-limb of the Shuram Excursion from the nadir in the Nikol'skoe Formation to the top of the exposed Khopych Formation. Overall, approximately 200 samples were collected from the Zhuya Group outcrop along the Lena River (60º19'01.74" N, 116º55'11.07" E). Collaborators Dr. Dimitry Grazhdankin and Vadim Maximenko provided detailed stratigraphic logging, sedimentological context, and created thin sections of the samples that were imaged at Trofimuk Institute of Petroleum Geology and Geophysics (henceforth Trofimuk) in Novosibirsk, Russia.

Samples from the Jiulongwan Section of the Doushantuo Formation that were previously analyzed for carbon and oxygen isotopes, uranium isotopes, sulfur isotopes, and elemental abundances were generously donated by Dr. Shuhai Xiao from Virginia Polytechnic Institute and State University (henceforth VPI) in Blacksburg, Virginia for lithium isotope analysis. Approximately 50 samples were provided for the study, of which, 32 samples spanning the SE interval were selected for paired trace element and Li, C, and O isotope analyses.

2.2: Sample Processing and Export

Initially, 21 Khopych Formation samples from the reef complex were exported to UMD by Dr. Alan Kaufman in November 2021. Hand samples were cut using an MK tile saw with a 10" diamond blade and polished on one side using a Labopol grinding wheel starting with 80 grit sand

paper, followed by 220, 320, and lastly 550 grit sandpaper. The textures of the samples were observed and micro-drilled for carbon and oxygen isotope analysis. Export of the remaining samples were delayed indefinitely due to the ongoing conflict in Ukraine. In November 2022, collaborator Natalia Bykova traveled to Toronto, Canada from Novosibirsk to deliver approximately 170 powders of samples from the entire Zhuya Group, and in November 2023, Dr. Dima Grazhdankin travelled to China where he was able to export an additional 15 samples and thin sections. One final trip by Natalia Bykova in January 2024 added another ~20 thin sections to the study.

The various isotopic and elemental analyses require that the samples selected are high purity carbonate (>80%). To determine which samples would be best suited for the various geochemical analyses, approximately 100 mg of sample powder was weighed out into clean individual 15 mL centrifuge tubes. The weight of the empty tube and cap and the powder weight was recorded prior to the addition of 5 mL of 3M hydrochloric acid (HCl) to each sample. The solutions were agitated and left to digest overnight (~16 hours). The following morning, samples were centrifuged using an IEC Centra MP4 at 5000 rpm for 10 minutes, decanted, and an additional 5 mL of 3M HCl was added for an additional 2 hours to ensure complete dissolution of the carbonate phases, after which, solutions were centrifuged, decanted, and the residues dried overnight at 80^{o}C in a drying oven. Once dry, samples were weighed and the weight percent carbonate was calculated.

The Jiulongwan Doushantuo and Dengying samples were delivered as ~50 g rock billets, allowing for visual and petrographic observations, subsampling, and polished eProbe section production. The billets were subsampled using a DREMEL® 3300 rotary tool with a 1/8” diamond tipped drill bit for ceramics, where approximately 500 mg of powder was extracted for subsequent

isotopic and elemental analyses. Insofar as the Jiulongwan succession has been extensively studied and the local redox geochemistry has been well documented, the geochemical analyses were limited to lithium, carbon, and oxygen isotopes and trace element abundances.

2.3: Electron Probe Microanalyzer Analysis and Elemental Mapping

Thin sections from both the Siberian and South China carbonate samples were observed using a Nikon LV100POL petrographic microscope connected to a Dell PC along with QCapturePro software for petrographic documentation of samples at UMD. Following the detailed petrographic analysis, 10 representative samples from both formations were selected for polishing by Grindstone Laboratory in Portland, Oregon. The polished thin sections were photographed at four different magnifications (5x, 10x, 20x, and 50x) utilizing three different polarizing filters (plane-polarized light, crossed-polarized light, and reflected light). Following the detailed petrographic analysis of the samples, the polished thin sections were coated with 200 to 300 Å of carbon to prepare for eProbe elemental mapping. A JEOL JXA-8900R WD/ED Microanalyzer at the University of Maryland's Advanced Imaging and Microscopy Laboratory (AIMLab) was used with the assistance of Dr. Philip Piccoli. During the production of WDS stage maps, the electron beam remains stationary while the stage below is moved. The resolution of the maps are 400 x 400 and have a step size of 10 μm, producing a 4 x 4 mm map. The dwell time of the beam at a given point was 50 milliseconds. The accelerating voltage of the beam was 15 kV, sample current was 500 nA, and the diameter of the beam was 10 μm. Five wavelength dispersive spectrometers (WDS) were utilized and optimized to detect relative element abundances in the map area. Insofar as the goal of the elemental mapping was to identify clay mineral phases, the elements selected were Mg, Al, Sr, Mn, and Si, with Fe instead of Si for the Doushantuo Formation samples. Magnesium is useful for evaluating the degree of dolomitization the rocks may have undergone

and identifying potential authigenic clay mineral phases present within the sample. Aluminum, iron, silicon (and magnesium) were used as proxies for clay minerals as their co-occurrences indicate the presence of clay mineral phases, providing a deeper understanding of how the lithium and strontium isotopes may have been affected by authigenic mineral formation. Strontium and manganese are useful for evaluating secondary alteration, as Mn is preferentially incorporated into carbonates during meteoric diagenesis, and Sr is simultaneously removed during mineral transformation from aragonite to calcite and dolomite. The elemental WDS stage maps that were generated from each sample are semi-quantitative as they reveal the abundance of an element relative to the area being analyzed using a color scale.

2.4: Carbon and Oxygen Isotope Analysis

Stable isotope analyses were carried out at the University of Maryland Paleoclimate Co-laboratory. For analysis, approximately 100 μg of carbonate powder was weighed and placed in a Labco Exetainer® sample vial sealed with a 16.5 mm screw cap with a pierceable rubber septum. Utilizing a Multiflow inlet system in-line with an Isoprime gas source mass spectrometer, samples were loaded into a sample tray where they were kept at a constant temperature of 65ºC. A two-hole needle was inserted through the septum to flush each vial with a stream of ultra-high purity He gas for 60 seconds. After 60 seconds, the flush needle was removed and ~1 mL of 103% phosphoric acid ($\rho > 1.89$ g/ml) heated to 80ºC was injected with a syringe and allowed to react with the sample powder for 60 minutes. After 60 minutes had passed, the two-hole needle was re-inserted into the vial to initiate a flow of UHP He carrier gas to push the analyte CO_2 to the Isoprime source for isotopic analysis. Typical peak amplitudes during analysis range from 2-10 nA. After the run, a series of corrections were applied to the data with the first being a spline correction to account for drift in the raw values across the run. Next, an amplitude correction was

applied to the data to account for varying purity of micro-drilled carbonate in each sample. Lastly, a two-point correction was applied to partially corrected data which converted the values to known (calibrated against IAEA-CO-1, LSVEC, JTB-1, and MCC1) compositions using the following equation:

$$X_{known} = a + b * X_{measured} \quad \text{(eq. 2.1)}$$

where a and b are coefficients calculated from the two-point regression of known values of JTB-1 and MCC1 relative to international standards IAEA-CO-1 and LSVEC on the V-PDB scale versus working standard values measured in the specific batch of analyses (Evans et al., 2016). Once a and b were estimated, the measured values were converted to the V-PDB scale. Reported uncertainties for the carbon and oxygen isotope analyses are based on replicate analyses of the MCC1 and JTB1 standards that were run interspersed with samples throughout the analytical sessions, with an average uncertainty (1σ) for $\delta^{13}C$ of ±0.07‰ and ±0.11‰ for $\delta^{18}O$ for the Patom Uplift samples and ±0.16‰ for $\delta^{13}C$ and ±0.14‰ for $\delta^{18}O$ for the Doushantuo Formation samples (Table 2.1).

Table 2.1: Data table containing analytical uncertainties for isotopic measurements ($\delta^{13}C$, $\delta^{18}O$, $\delta^{7}Li$, $^{87}Sr/^{86}Sr$, $\delta^{88}Sr$, and $\delta^{238}U$). Uncertainties are reported as 1σ for the C and O measurements and 2σ for the other isotopic measurements.

Average Analytical Uncertainties						
Location of Analysis	**$\delta^{13}C$**	**$\delta^{18}O$**	**$\delta^{7}Li$**	**$^{87}Sr/^{86}Sr$**	**$\delta^{88}Sr$**	**$\delta^{238}U$**
University of Maryland	±0.16	±0.14	±0.3			±0.07
Texas A&M				4.63E-06	±0.01	

2.5: Lithium Isotopes

Approximately 200 mg of sample powder was weighed and placed into clean 15 mL centrifuge tubes that had been pre-leached with 6M HCl. The samples then underwent a sequential leaching process following the procedure detailed in Cao et al. (2020; 2022; 2023). Sample powder was mixed with 10 mL of 1M ammonium acetate (NH_4Ac), ultrasonicated for 30 minutes, and centrifuged at 5000 rpm for 5 minutes. The leachate was discarded, and the powders were rinsed with 18.2 MΩ Milli-Q water before further treatment with 10 mL of 1M ammonium carbonate ($(NH_4)_2CO_3$), ultrasonicated for another 30 minutes, centrifuged at 5000 rpm for 5 minutes, and the leachate discarded. The leach procedures were repeated, and the residual samples were rinsed with Milli-Q water. Following the Milli-Q rinse, the samples were dissolved using 10 mL of 0.3M acetic acid (HAc), and the supernatant was filtered with a 0.2 μm Basix™ syringe filter and collected in a Teflon® PFA (perfluoroalkoxy alkanes) beaker for isotopic and elemental analyses. Samples were then dried down overnight and redigested in 2.1 mL of 0.7M HNO_3. A 0.1 mL aliquot was removed from the solution and diluted to 10 mL in 2% HNO_3 for trace element analysis and 1 mL of solution was sent to Texas A&M for stable and radiogenic Sr isotope analysis.

To separate and purify lithium, the other 1 mL of the leachate was passed through two rounds of column chemistry at the University of Maryland. Both columns use Bio-Rad™ AG50W (200-400) mesh resin. The first column dimensions are 1.5 cm internal diameter (ID), 10 cm tall, and filled with approximately 17 mL of resin. The second column is 0.6 cm ID, 20 cm tall, and filled with 3.4 mL of resin. Both columns follow the same procedure but utilize different acids at different concentrations to purify Li from the other matrix elements. Before and after the main collection step, three 2 mL pre-cuts and three 2 mL post-cuts were collected from each sample, the NIST standard, and a blank, and analyzed on the Thermo Scientific Neptune Plus MC-ICP-MS at

the University of Maryland to ensure a 100% recovery rate for Li. Once 100% Li recovery had been verified, the samples were dried down completely, redigested in 0.2M HCl, and passed through the second column to remove residual Na from the samples to prevent any interference with the isotopic measurements.

Lithium isotopes were measured with a 50 µL/min PFA nebulizer at low resolution using X skimmer and Jet sampler cones. The typical ^{7}Li signal intensity was 2–3 V for a 5 ppb Li solution. Samples and the international lithium standard LSVEC were diluted to 5 ng/g in 2% nitric acid, and $\delta^{7}Li$ values were analyzed using a standard-sample bracketing method relative to the LSVEC standard. Each sample was measured three separate times to report standard deviation (2s). Nitric acid (2%) was measured before each sample and standard for background subtraction. Accuracy and precision were also assessed from repeated measurements of a 2 ppb in-house standard (UMD-1), reporting $\delta^{7}Li$ 55.3‰ ± 0.4 (2σ, n = 22), in good agreement with the published values of $\delta^{7}Li$ 54.7 ± 1.0‰ (2σ, n = 31; Table 2.1 on page 31; Penniston-Dorland et al., 2012).

2.6: Strontium Isotopes

Aliquots for Sr isotope analysis were processed using Sr Spec resin filled columns to purify Sr from Ca and other matrix elements at Texas A& M University by collaborator Dr. Lucien Nana Yobo. The purified Sr cuts were loaded onto outgassed Re-filaments with TaF_5 and H_3PO_4 and measured using a Thermo Scientific Triton Plus TIMS using a multi-static measurement technique adapted following procedures in Nana Yobo et al. (2021). The $^{87}Sr/^{86}Sr$ ratios were corrected for instrumental mass fractionation using an $^{86}Sr/^{88}Sr$ ratio of 0.1194. The external precision for $^{87}Sr/^{86}Sr$ is better than ±5 ppm (2σ) based on repeated measurements of the SRM 987 standard yielding 0.710251± 0.000003 (n=30, ±2σ; Table 2.1 on page 31; *cf.* Gan et al., *in-preparation*).

2.7: Major, Minor, and Trace Element Preparation and Analysis

For elemental analysis, roughly 1.5 g of each sample powder from key intervals across the Zhuya Group were weighed and placed in clean, 6M HCl-leached centrifuge tubes. Samples digestion involved a three-step process of 20 mL of 1M trace metal grade (TMG) nitric acid (HNO_3), followed by 5 mL of concentrated TMG HNO_3, and a final 15 mL of 1M TMG HNO_3. Following acidification, the samples were vortexed for 30 seconds, and left to react overnight. The next morning, solutions were centrifuged in an International Equipment Company Centra-MP4 at 5000 rpm for 10 minutes, and the supernatant was decanted into a fresh 50 mL 6M HCl-leached centrifuge tube. A 200 µL aliquot of each sample was taken and added to individual fresh 15 mL centrifuge tubes which were diluted up to 10 mL with 2% TMG HNO_3. Major, minor, and trace elements, along with REE were analyzed at Arizona State University on the Thermo Scientific Quadrupole ICP-MS. Standards used were the Ca Leonard II standard which was run after every eight samples. Average standard deviation varies depending on the element analyzed. Reported uncertainties for the elements of interest are as follows: Li ±0.45 ppb (6% RSD); Mg ±21.3 ppb (11% RSD); Al ±20.2 ppb (11% RSD); Ca ±10823 ppb (5% RSD); Mn ±1.4 ppb (7% RSD); Sr ±0.46 ppb (3% RSD); U ±0.01 ppb (1% RSD). The average RSD across the entire elemental suit from the analytical session is reported as ±3% (Table 2.2).

Table 2.2: Data table containing analytical uncertainties for elemental measurements (Li, Mg, Al, P, Ca, Mn, Rb, Sr, Y, Ce, Pr, Nd, Ho, and U). Uncertainties reported as 1σ and RSD for ASU and RSD for Carnegie Institution for Science.

Average Analytical Uncertainties															
Location of Analysis		Li	Mg	Al	P	Ca	Mn	Rb	Sr	Y	Ce	Pr	Nd	Ho	U
Arizona State University	ppb (±)	0.45	21.28	20.24	9.47	10822.54	1.41	0.14	0.47	0.00	0.05	0.01	0.03	6.84E-04	0.01
	RSD	6%	11%	11%	11%	5%	7%	3%	3%	35%	1%	1%	1%	1%	1%
Carnegie Institution for Science	RSD	3%	7%	7%	10%	6%	5%	5%	6%	5%	6%	7%	10%	9%	8%

*Note only RSD is reported for CIS

2.8: *U Isotope Preparation and Analysis*

Following the determination of major, minor, and trace elements, the amount of $^{233}U/^{236}U$ double-spike for each sample and the amount of solution to dry down was calculated based on the concentration of U in each sample. Sample specific amounts of the 40 mL leach were dried town in Teflon® beakers on a hotplate at 180ºC to obtain 300 ng of U for the isotopic analysis. Following the initial dry down the samples were spiked with 0.48 mL of 10.7 ppb IRMM $^{233}U/^{236}U$ double-spike and subsequently dried. Following the dry-down, 6 mL of inverse aqua regia (3:1 mix of concentrated 2x Teflon® distilled HNO_3 and concentrated 2x Teflon® distilled HCl) was added to the beakers, which were capped and placed on the hotplate overnight at 180ºC and dried down until only a small (<0.5 mL) bead of liquid remained. This step was repeated until the entire sample was dissolved, after which 2 mL of concentrated 2x Teflon® distilled HNO_3 and 0.2 mL of 30% H_2O_2 was added to the beakers, which were capped and placed on the hotplate overnight. The following morning, samples were uncapped and partially dried down until only a small (<0.5 mL) bead of liquid remained, after which 2 mL of concentrated 2x Teflon® distilled HNO_3 was added to the beakers, which were then capped and left on the hotplate overnight. The next morning samples were partially dried down until only a small (<0.5 mL) bead of liquid remained, after which 10 mL of 3M HNO_3 was added to each beaker, which was capped and placed on the hotplate overnight. The following morning solutions were cooled and transported to George Mason University for two rounds of ion exchange chromatography in the clean laboratory of collaborator Dr. Geoffrey Gilleaudeau. The first column utilized Uranium and TetraValents Actinides (UTEVA) resin to extract uranium and thorium, the latter of which was removed upon addition of 5M HCl and 0.05M oxalic acid. Following the first column, samples were dried down completely, redigested in 2 mL concentrated HNO_3 and 0.2 mL 30% H_2O_2, capped, and left on the hotplate

overnight at 180ºC. The following morning, samples were dried down completely. This process was repeated and then samples were digested in 1 mL of 6M HNO_3. The second column used Diglycolamine (DGA) resin, which removes any excess calcium and sodium that would suppress uranium ionization during analysis. After the second column, samples were dried down completely and diluted to 40 ppb U with the appropriate amount of 2% HNO_3, capped and placed on the hotplate overnight. The following morning the samples were removed from the hot plate and once cool, were analyzed (n=3) on the Thermo Scientific Neptune Plus MC-ICP-MS at the University of Maryland. The standards used in the isotopic analysis were Certified Reference Material (CRM)-145 and CRM-129a. To analyze the U isotopes, the sample uptake straw is placed in a 40-ppb solution of the CRM-145 standard that had been spiked with the same amount of $^{233}U/^{236}U$ double-spike to achieve a ratio of U_{spike}/U_{sample} of ~1.7‰. The instrument was tuned to the maximum signal strength while up taking the CRM-145 solution starting with the sweep and sample gas, followed by the inlet system, source lens, and lastly, zoom optics. Once optimal tuning was achieved, a series of standards were run, with multiple iterations of the CRM-145 standard interspersed with the CRM-129a standard, which has a known isotopic offset with the CRM-145 standard of 1.7‰. Once the proper value of the CRM-129a standard bracketed with the CRM-145 standard had been measured at least five times, the sample analyses were able to proceed. The analytical session involved a CRM-145 standard run after every two samples with the isotopic composition of the samples calculated by bracketing with the CRM-145 standard run before and after. After every ten samples, a CRM-129a standard was also run, bracketed by two CRM-145 standards, to ensure that the signal was still at the optimal strength and to account for any drift throughout the analytical session. The average analytical uncertainty across an analytical session was ±0.07‰ (2σ; see Table 2.1 on page 31).

2.9: Rare Earth Elements (REEs)

Approximately 70 samples (>80 wt. % carbonate) from the Zhuya Group were selected for REE analysis. The REE procedure follows the protocol detailed in Tostevin et al. (2016). Approximately 25 mg of sample powder was weighed out and placed in fresh 2 mL disposable centrifuge tubes. The samples were rinsed with 18.2 MΩ Milli-Q water at 25ºC, agitated for 30 minutes, centrifuged at 5000 rpm for 10 minutes, and the water was discarded. Next, 312.5 µL of trace metal grade 2% HNO_3 was added to each sample, which were then agitated for 30 minutes and left to react for 12 hours overnight. The following morning samples were centrifuged at 5000 rpm for 10 minutes, and the supernantant was discarded. A final 625 µL of 2% HNO_3 was added to each sample, which were then agitated for 30 minutes, left to leach for 12 hours overnight, and centrifuged the following morning at 5000 rpm for 10 minutes. The supernatant from each sample was decanted into fresh 15 mL centrifuge tubes and diluted up to 10 mL with 2% HNO_3. Samples were then packaged and shipped off to Arizona State University where they were analyzed on the Thermo Scientific Quadrupole ICP-MS. Reported uncertainties for the REY of interest are as follows: Ce ±0.05 ppb (1% RSD); Pr ±0.01 ppb (1% RSD); Nd ±0.03 ppb (1% RSD); Ho ±0.001 ppb (1% RSD). The average RSD across the entire elemental suite from the analytical session is reported as ±3% (*Note, the REY samples were analyzed during the same analytical session as the major, minor, and trace elements see Table 2.2 on page 34).

Chapter 3: A Lithium Isotope Study of the Shuram Excursion in Siberia and South China

3.1: Abstract

Novel lithium isotope data from two Shuram Excursion (SE) successions in central Siberia and South China reveal a profound lithium isotope anomaly in limestone facies, broadly coincident with the nadir of carbon isotope values. The low δ^7Li values signify a highly congruent weathering regime where silicate dissolution is complete and coupled with the extremely rapid formation of authigenic clay minerals (i.e., reverse weathering) in the oceans. Intense terrestrial weathering appears to have driven the mass delivery of continental material to the ocean, stimulating an alkalinity anomaly through the supersaturation of the global oceans with respect to carbonate ion and dissolved calcium. Coincident with the near-crustal δ^7Li compositions is the appearance of sedimentological indicators of carbonate supersaturation (i.e., large ooids and other coated grains, aragonite seafloor precipitates, lower shoreface hardgrounds and plate breccias), as well as various geochemical indicators (coupling of carbon and oxygen isotopes, and low δ^{88}Sr compositions). The SE alkalinity event was likely driven by middle Ediacaran tectonic forces and climate that promoted the extreme weathering regime, and may have been the driving force for the origin of biomineralization by sponge-grade animals.

3.2: Introduction

Earth's climate is regulated through a series of feedback loops (e.g., temperature-ice line latitude-albedo positive feedback loop, temperature-weathering-CO_2 negative feedback loop) that are generally in a state of equilibrium. However, periods of non-steady state conditions can have profound impacts on the global climate and Earth's biogeochemical cycles. The most critical feedback keeping Earth's climate in balance is silicate weathering, which regulates atmospheric

CO_2 levels on timescales ranging between 10^4-10^6 years (Berner et al., 1983; Pogge von Strandmann et al., 2013). During silicate weathering reactions, atmospheric CO_2 combines with water vapor to form carbonic acid that reacts with silicate minerals acting as an effective sink for atmospheric CO_2. The dissolution of silicate minerals releases cations (like Ca^{2+}, Fe^{2+}, Mg^{2+}, and K^+) and anions (like HCO_3^- and H_2SiO4^-), which can form secondary clay minerals on land through incongruent chemical reactions (Equation 3.1):

$$XAl_2Si_2O_8 + 2CO_2 + 2H_2O \rightarrow X + Al_2Si_2O_5(OH)_4 + 2HCO_3^- + H_2O \quad \text{(eq. 3.1)}$$

Clay mineral formation can also occur in the oceans during reverse weathering, which is promoted by high dissolved silica concentrations (Mackenzie and Kump, 1995). This process serves to counteract the sequestration of CO_2 during the process of silicate weathering through the consumption of alkalinity, thereby creating acidity and releasing CO_2 through the dissolution of pre-existing carbonate minerals and subsequent formation of clays (e.g., saponite, sepiolite, minnesotaite, greenalite, and sudioite; Equation 3.2; Isson and Planavsky, 2018):

$$4X + Al_4Si_4O_{10}(OH)_8 + 8HCO_3^- \rightarrow X_4Al_4Si_2O_{10}(OH)_8 + 8CO_2 + 2H_4SiO_2 \quad \text{(eq. 3.2)}$$

Insofar as these processes are directly linked to the carbon cycle, understanding the degree of continental weathering congruency and secondary clay mineral formation in the oceans is imperative to understanding carbon cycle perturbations throughout Earth history (Rothman et al., 2003; Cui et al., 2015, 2017, 2020).

Several geochemical proxies have been used to indirectly evaluate the degree of continental weathering. One such proxy is the strontium (Sr) isotope system, which reflects a balance between continental sources rich in ^{87}Sr, based on the β^- decays of ^{87}Rb in exposed igneous and metamorphic rocks, and hydrothermal fluids that are lacking in ^{87}Sr due to the absence of Rb in basalts. Variations in $^{87}Sr/^{86}Sr$ have thus been interpreted to reflect changes in the proportion of Sr input from riverine sources and that from hydrothermal sources (Faure, 1986; Veizer et al., 1999), with increasingly radiogenic compositions consistent with periods of orogenesis and non-radiogenic signatures during rifting events or LIP emplacement (Goldstein and Jacobsen, 1987). During the middle Ediacaran Period, the $^{87}Sr/^{86}Sr$ composition of marine carbonates is characterized by a monotonic rise to increasingly radiogenic values during the SE (Burns et al., 1994), attributed to major tectonic uplift and intense continental weathering triggered by Pan-African orogenesis (Derry et al., 1992; Jacobsen and Kaufman, 1999; Meert, 2003; Melezhik et al., 2009). These increasingly radiogenic Sr values during the SE suggest the possibility that the carbon cycle anomaly was driven by the delivery of blankets of sediments, salts, ions, oxidants, and nutrients to the oceans, altering oceanic chemistry by supersaturating seawater with respect to CO_3^{2-} that is arguably related to the oxidation of a large DOC reservoir in anoxic seawater (Rothman et al., 2003). However, while the Sr isotope system has proven useful in identifying periods of increased continental collision and rifting, the system falls short in quantifying the flux associated with the periods of continental collision as it likely reflects sources more so than overall weathering intensity (Kısakűrek et al., 2005).

For this reason, lithium isotopes serve as a promising proxy to track processes that control the long-term carbon cycle, namely silicate weathering, because the isotopic composition (recorded as δ^7Li values) is determined by the fractionation between solution, secondary mineral

formation, and the degree of weathering, rather than bedrock lithology (Pogge van Strandmann et al., 2010). Lithium isotopes in river water delivered to the oceans respond to enhanced continental weathering (congruent) by exhibiting values near the crustal average (ca. 0‰), while higher δ^7Li values in rivers (ca. +23‰ in the modern) correspond to the partial weathering (incongruent) of continental material when clay minerals are formed. Weathering congruency is defined by silicate weathering intensity (W/D), which is the ratio of the chemical weathering rate (W) to the rate of total (D) denudation [erosion (E) + chemical weathering (W)], promoted by greater sediment surface area and high atmospheric pCO_2 (Dellinger et al., 2015). Both high and low W/D regimes are characterized by low δ^7Li compositions but the high W/D is the result of the dissolution of secondary clays driving a low Li riverine flux while low W/D regimes are driven by the dissolution of primary rock, resulting in a high Li riverine flux (Dellinger et al., 2015; Pogge von Strandmann et al., 2021). Intermediate W/D is generated through secondary clay mineral formation on land, resulting in a riverine flux defined by high δ^7Li values and low dissolved Li (Dellinger et al., 2015).

Carbonate sediments preserve seawater Li isotope compositions with minimal fractionation, and thus have proven reliable in tracking δ^7Li variations of seawater through time. Insofar as the SE is associated with the assembly of Gondwana and the formation of the massive Trans-Gondwanan super mountain ranges (Squire et al., 2006; Schmitt et al., 2018), stratigraphic variations in carbonate δ^7Li values hold the promise to assess weathering congruency during the pre-, syn-, and post-SE intervals. The null hypothesis states that the δ^7Li compositions of SE carbonates do not reflect a period of enhanced weathering congruency, so that an alternative mechanism is required to explain the onset of the SE. The rapid continental collision and uplift associated with the assembly of Gondwana as well as elevated atmospheric CO_2 levels during the middle Ediacaran would have promoted the intense physical and chemical weathering of the

continents. The massive flux of continental material would have delivered profound quantities of nutrients, salts, oxidants, sediments, and ions into the oceans, increasing the oceanic carbonate saturation state and thus promoting the rapid and widespread deposition of massive carbonate complexes along continental margins during the SE. The enhanced delivery of nutrients and oxidants would stimulate the anaerobic conversion of DOC to ^{13}C-depleted DIC, diluting the oceanic DIC inventory and driving the $\delta^{13}C_{carb.}$ to profoundly negative values.

The objective of this study is to determine time-series carbonate δ^7Li compositions of two SE successions, including the Patom Uplift (the Nikol'skoe, Alyanch, and Khopych formations) of Siberia and the upper Doushantuo and lower Dengying formations at Jiulongwan in South China, to understand how changes in weathering congruency may have influenced the carbonate saturation state of the Ediacaran oceans and promoted early animal biomineralization. This weathering-driven alkalinity anomaly during the SE is independently supported by a Macrostrat analysis indicating extreme carbonate accumulation at this time (Segessenman and Peters, 2024). High resolution stratigraphic sampling of these two successions provides a unique framework for novel δ^7Li isotope studies of the SE. Furthermore, by comparing the δ^7Li data from two widely separated successions, it can be determined whether the δ^7Li data is globally representative, or if it was locally influenced by early to late-stage diagenetic processes.

3.3: Results

The results of geochemical measurements, including % carbonate, major, minor, and trace elements and ratios, and isotope compositions for the Siberia and South China exposures are discussed and presented graphically below and numerically in the form of averages in tables 3.1 through 3.3 and in tables A1 through A5 in Appendix I, with emphasis on the stratigraphic position of samples.

3.3.1: Patom Uplift

For the Patom Uplift percent carbonate was determined on 161 samples with a range of average value of 83.9 ± 2.7% based on replicate acidifications. There are two notable intervals with lower % carbonate in both the Nikol'skoe and Khopych formations (Fig. 3.4A). Carbon and oxygen isotopes were measured on 193 samples, with average $\delta^{13}C$ of -10.06‰ and average $\delta^{18}O$ of -9.90‰. The carbon and oxygen isotope trends are characterized by a smooth covariance throughout the basal Nikol'skoe Formation and into the lower interval of the Alyanch Formation, until roughly 300 m above the base of the measured section where there is a decoupling seen by a plateau in the oxygen isotope values while those of the carbon isotopes continue to climb (Fig. 3.3B, C).

Elemental concentrations were calculated and plotted in figure 3.1 and the averages the are reported in Table 3.1. The average [Li] for the entire Zhuya Group is 0.52 ppm (n=46), characterized by a decline to a minimum in the Alyanch Formation and a slow rise to the maximum in the Khopych Formation reef. Insofar as phosphorous is a critical limiting bionutrient, P concentrations were determined for the Zhuya Group succession. The average [P] is 16 ppm (n=45), with the trend following that of Li, decreasing to a minimum in the Alyanch Formation and rising to a maximum in the Khopych Formation. Strontium concentrations sharply rise with increasing stratigraphic height, with an average [Sr] of 745 ppm (n=46). Nikol'skoe Formation represents the minimum with an average [Sr] of 430 ppm while the Khopych Formation reef contains nearly triple the average [Sr] with a concentration of 1290 ppm. Throughout the entire Zhuya Group, Mn oscillates starting with an average concentration of 645 ppm (n=46) in the Nikol'skoe Formation, before reaching a nadir in the Alyanch Formation, and gradually rising to 265 ppm before falling in the Khopych Formation. Aluminum and Rb concentrations were plotted

to assess detrital influence with [Al] consistently below 0.01 wt. % in all but 3 samples and [Rb] below 0.2 ppm in all but 1 sample.

In addition to absolute concentrations, elemental ratios are reported as averages in Appendix I Table A4 and plotted in figure 3.2 as [element]/(Mg + Ca), but for simplicity the data is reported as X/carbonate. The average Li/carbonate in the Zhuya Group is 1.96 x 10^{-6} ppm/ppm (n=46) with a minimum Li/carbonate in the Alyanch Formation, before a steady rise to a maximum in the Khopych Formation (Fig. 3.2B). Carbonate-associated phosphate (CAP; see Dodd et al., 2023) values were also determined for the Zhuya Group carbonates. The average CAP values for the Zhuya Group are 7.01 x 10^{-5} ppm/ppm with a notable decrease around the Nikol'skoe-Alyanch transition and a steady rise to maximum values in the Khopych Formation (Fig. 3.2C). Both Sr/carbonate and Mn/carbonate were plotted with the Sr/carbonate (average = 1.65 x 10^{-3} ppm/ppm; n=46) increasing with stratigraphic height and the Mn/carbonate (average = 9.89 x 10^{-4} ppm/ppm; n=46) decreasing with stratigraphic height through the upper Nikol'skoe and lower Alyanch formations before slightly rising in the Khopych Formation (Fig. 3.2D, E).

Several detrital and diagenetic proxies were also analyzed to assess the extent of diagenesis in the Patom Uplift. Aluminum/carbonate values across the entire Zhuya Group are on average 3.1 x 10^{-4} ppm/ppm, with the Nikol'skoe Formation averaging 3.3 x 10^{-4} ppm/ppm and the Alyanch and Khopych formations averaging 1.3 x 10^{-4} ppm/ppm and 2.5 x 10^{-4} ppm/ppm, respectively (Fig. 3.3F). The average Rb/carbonate value of the Zhuya Group samples is 3.1 x 10^{-7} ppm/ppm with the upper Nikol'skoe Formation containing slightly heavier values compared to the overlying Alyanch and Khopych formations (Fig. 3.3G). Magnesium/Calcium and Mn/Sr ratios were calculated and reported in this section using the data obtained from the Li leach. Across the entire Zhuya Group, the average Mg/Ca is 0.01, and remains consistently below 0.02 for the entire

stratigraphic interval while the average Mn/Sr for the entire Zhuya Group is 1.42 (Fig. 3.3C, D). The basal Nikol'skoe Formation is characterized by Mn/Sr values up to 11, with an average value of 2.7. Conversely, the Mn/Sr value of the Alyanch and Khopych formations are considerably lower with an average Mn/Sr of 0.16 and 0.26, respectively. The average Rb/Sr is 2.0×10^{-4} (n=46) with slightly elevated values in the first 150 m of the Nikol'skoe Formation before they fall to near 0 in the Alyanch and Khopych formations (Fig. 3.3E).

Lithium isotopes were measured on 46 samples with an average δ^7Li composition for the entire Zhuya Group of 7.4‰ (average 2σ = ±0.17‰; Table 3.3). The δ^7Li values exhibit a smooth trend throughout the 600 m interval, characterized by declining values in the basal 150 m of the Nikol'skoe Formation to a nadir of 2.9‰. Following the nadir, the values get heavier before reaching a maximum of 10.7‰ in the basal Alyanch Formation. Above this level, δ^7Li values oscillate between 8.6‰ and 10.1‰ in the upper Alyanch and entire Khopych formations (Fig. 3.4F).

Aliquots from the Li leach were analyzed for both $^{87}Sr/^{86}Sr$ and stable strontium (δ^{88}Sr) isotope compositions at Texas A&M by collaborator Dr. Lucien Nana Yobo. The average $^{87}Sr/^{86}Sr$ across the sampled Zhuya Group is 0.7082 (n=30; average 2σ = ±4.32E-6) with the Nikol'skoe Formation exhibiting more radiogenic values in the basal 150 m before decreasing to a low value of 0.7079 in the upper Nikol'skoe Formation (Fig. 3.4D). Upsection, the $^{87}Sr/^{86}Sr$ curve exhibits a monotonic rise towards more radiogenic values in the Alyanch and Khopych formations ending with a maximum value of 0.7084. The average δ^{88}Sr for the Zhuya Group samples was 0.34‰ (n=22; average 2σ = ±0.01‰). The δ^{88}Sr exhibits an inverse relationship with the $^{87}Sr/^{86}Sr$, as the lightest values (near 0‰) are found in the basal Nikol'skoe Formation, followed by a steady

increase to a plateau of values (up to 0.4) in the Alyanch and Khopych formations (Fig. 3.4E; (*cf.* Gan et al., *in-preparation*).

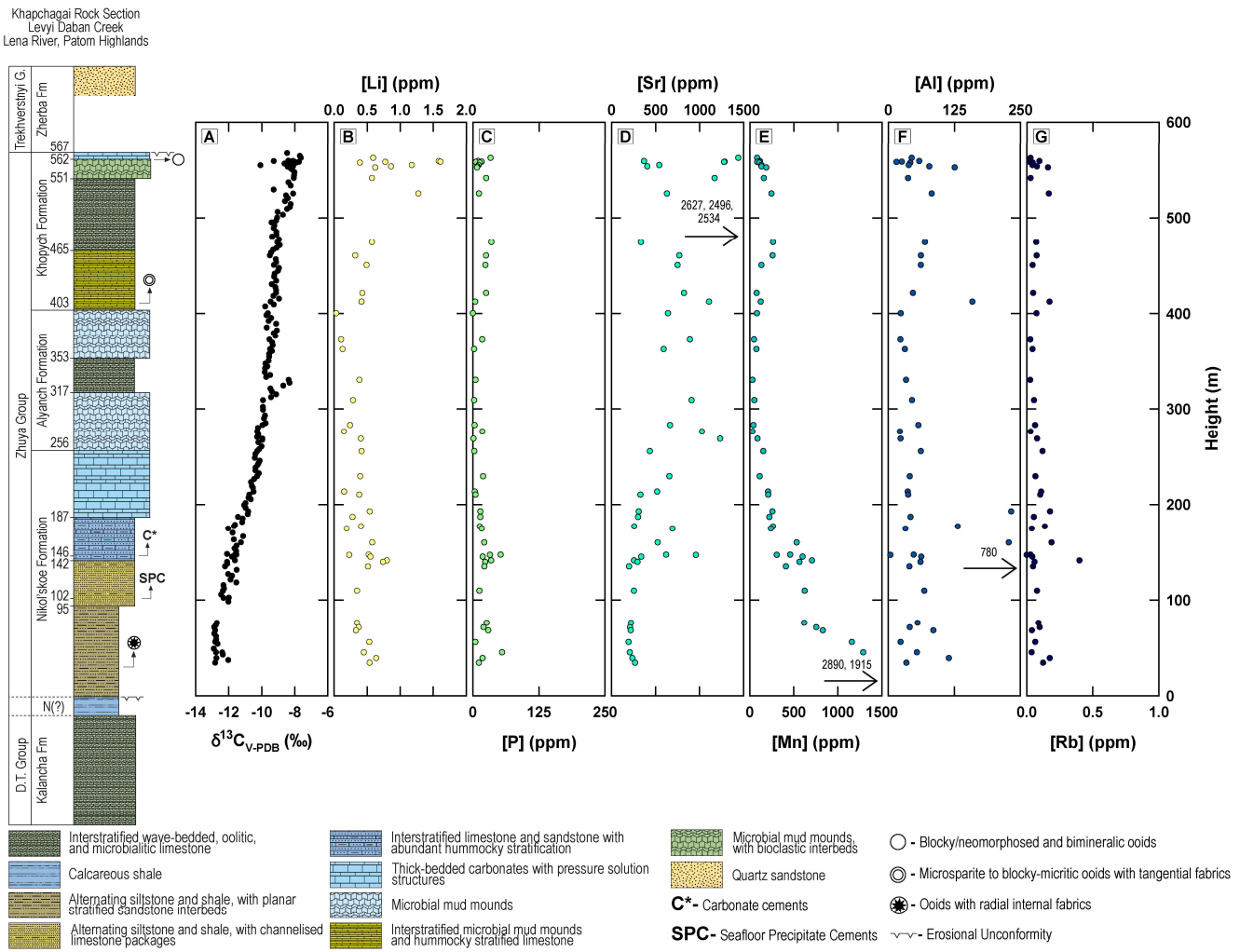


Figure 3.1: Stratigraphy and chemostratigraphy of the Zhuya Group at Khapchagai Section. (B) Li concentrations steadily decline from the basal Nikol'skoe Formation to a nadir in the Alyanch Formation before steadily rising at the Alyanch-Khopych boundary where they rise to a maximum in the Khopych Formation reef. (C) P concentrations remain consistently below 100 ppm and broadly follow the Li trend with a decease to minimum values from the Nikol'skoe to Alyanch formations before rising to about 40 ppm in the Khopych Formation. (C, D) Sr and Mn display an inverse trend where Sr starts from a nadir of 250 ppm in the basal Nikol'skoe Formation and rises to a maximum of 2650 ppm in the Khopych Formation while Mn starts at a maximum of 3000 ppm in the basal Nikol'skoe Formation and steadily decreases to a minimum through the Alyanch Formation, before rising and falling in the Khopych Formation. (F, G) Al and Rb serve as detrital proxies with all but 3 samples falling below 125 ppm and all samples below 0.5 ppm, respectively.

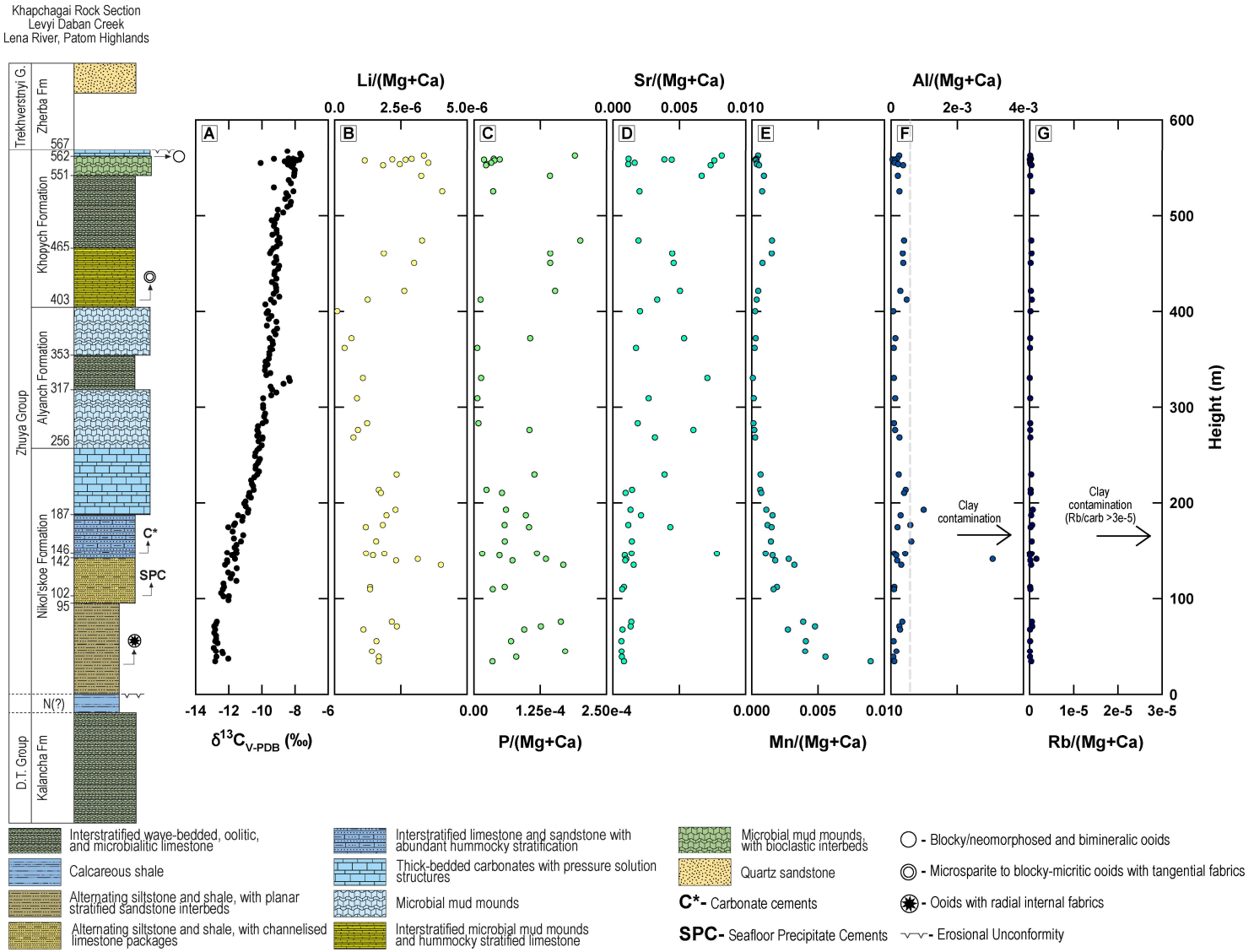


Figure 3.2: Stratigraphy and chemostratigraphy of the Zhuya Group at Khapchagai Section. (A) from Fig. 3.1. (B) Li/(Mg+Ca) ratios. (C) P/(Mg+Ca) or CAP ratios. (D) Sr/(Mg+Ca) ratios. (E) Mn/(Mg+Ca) ratios. (F) Al/(Mg+Ca) ratios, the stippled line represents the boundary beyond which aluminosilicate contamination may have compromised the leachate. (G) Rb/(Mg+Ca) ratios are all consistently below the 3 x 10^{-5} ppm/ppm cutoff indicating aluminosilicate contamination (*cf.* Gan et al., *in-preparation*).

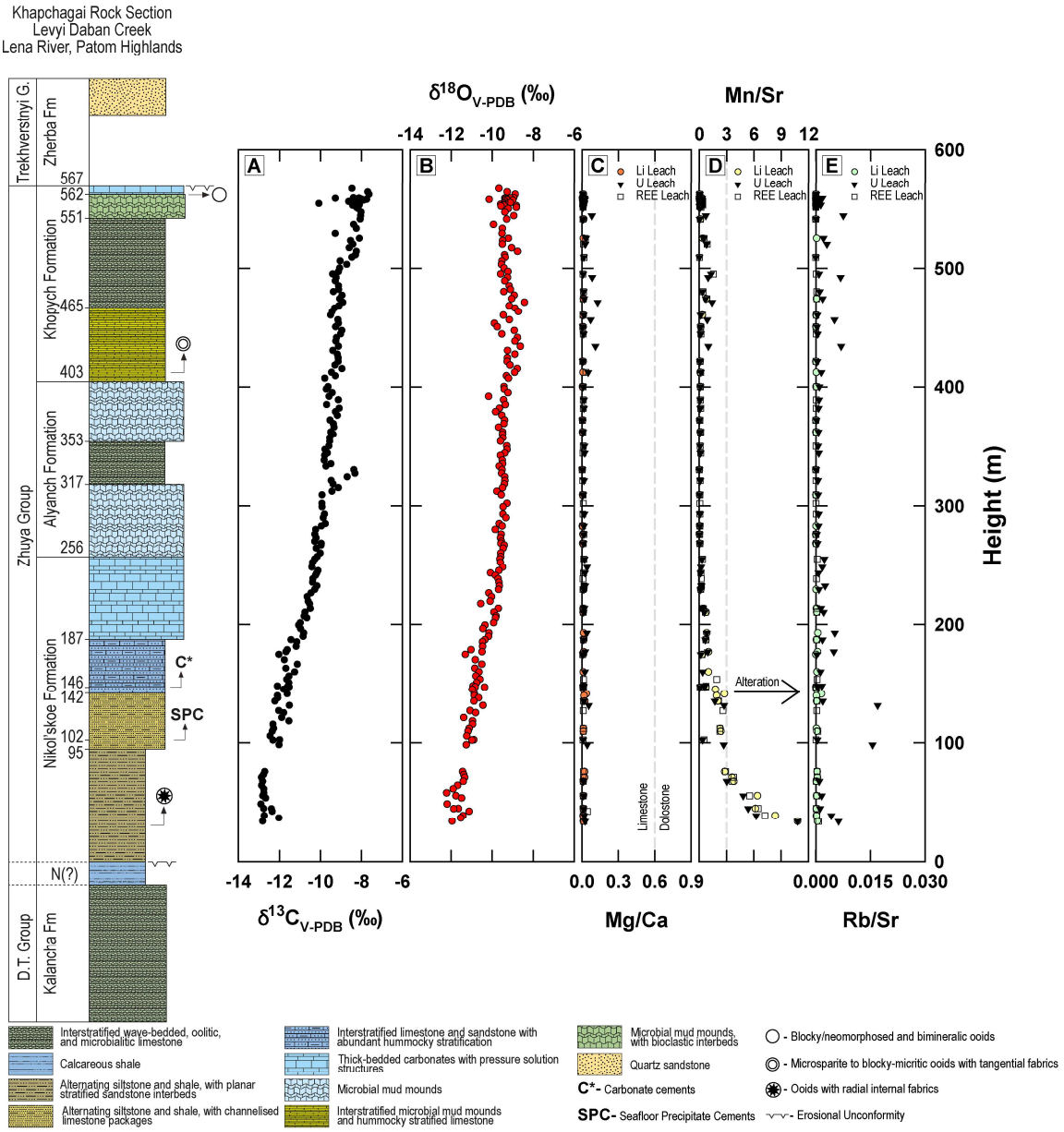


Figure 3.3: Stratigraphy and chemostratigraphy of the Zhuya Group at Khapchagai Section. (A, B) Ultra low $\delta^{13}C$ and $\delta^{18}O$ values that are notably coupled (R^2=0.74, P<0.001). (C) Mg/Ca is consistent between all three leach methods. (D) Mn/Sr is consistent across all three leach methods, decreasing from a maximum in the Nikol'skoe Formation to below 1 for the remaining 450 m of stratigraphy. (E) Rb/Sr is consistent across all three leaches, though the U leach does show slightly higher values in several points, indicating more Rb was leached in the bulk solution whereas the REE and Li leach were much gentler.

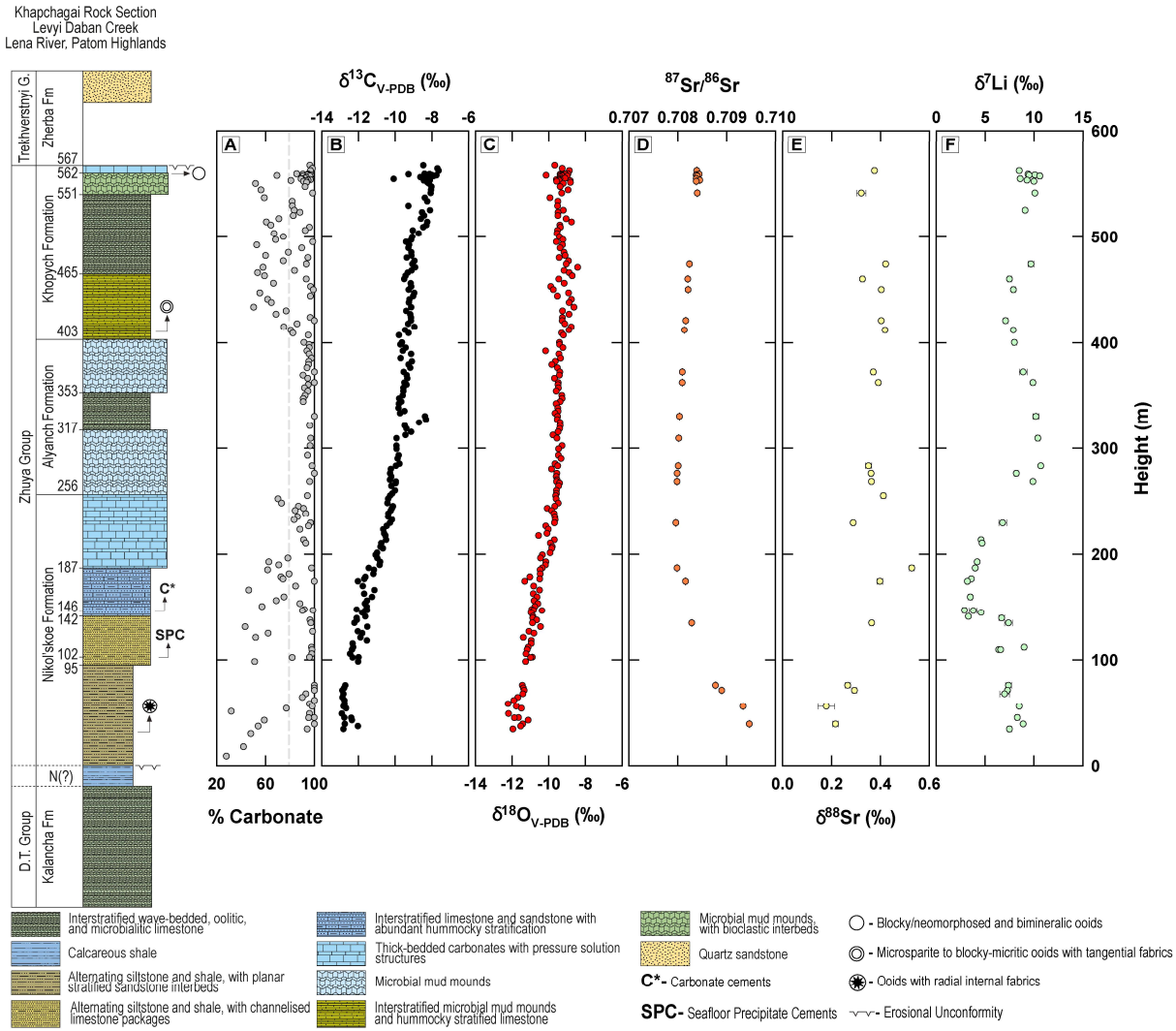


Figure 3.4: Stratigraphy and chemostratigraphy of the Zhuya Group at Khapchagai Section. (A) Percent carbonate. (B,C) $\delta^{13}C$ and $\delta^{18}O$ from 3.3, characterized by an extreme depletion and smooth covariance in the basal 300 m of the study section. (D) Sr isotopes decrease sharply in the first 150 m from highly radiogenic values, before a monotonous rise towards the typical $^{87}Sr/^{86}Sr$ for Ediacaran seawater. Average uncertainty is ±4 x 10^{-6} (2σ). (E) $\delta^{88}Sr$ values sharply rise throughout the Nikol'skoe Formation before plateauing around 0.4‰. Average uncertainty is ±0.01‰ (2σ). (F) Li isotopes climb from a nadir at ~150 m coincident with the rise in $^{87}Sr/^{86}Sr$ and $\delta^{88}Sr$. Average uncertainty is ±0.3‰ (*cf.* Gan et al., *in-preparation*).

3.3.2: Doushantuo Formation

Insofar as the 32 mixed dolostone and limestone Doushantuo and Dengying samples from the Jiulongwan succession span strata that encompass the entire SE, the average values for the elemental and isotopic data are reported for pre-SE, SE, and post-SE intervals, with the SE interval characterized by $\delta^{13}C$ values of 0‰ or less. For the Jiulongwan samples, percent carbonate was previously determined on 22 of them ranging from 81.9% to 98.7% with an average of 87.3% (Fig. 3.8A; McFadden et al., 2008). The $\delta^{13}C$ values for the entire suite of samples range from 4.52‰ to -9.13‰ with an average of -4.55‰, while the $\delta^{18}O$ values range from 0.28‰ to -9.88‰ with an average of -6.01‰. respectively (Fig. 3.7B, C; Table 3.3). The pre-SE interval is characterized by an average $\delta^{13}C$ of +3.3‰ and an average $\delta^{18}O$ of -4.18‰. The SE interval is defined by an average $\delta^{13}C$ of -7.34‰ and an average $\delta^{18}O$ of -6.64‰ before climbing to an average $\delta^{13}C$ of -0.78‰ and an average $\delta^{18}O$ of -3.28‰ in the post-SE interval. The carbon and oxygen isotope trends are characterized by heavier values in the Member II/III transition before plummeting to the nadir in a ~5 m interval within which the C and O isotopes appear coupled. The low $\delta^{13}C$ and $\delta^{18}O$ values persist at the nadir for the remaining 35 m in Member III before climbing back over 25 m to pre-SE values into the shale dominated Member IV and the overlying Dengying Formation.

Elemental concentrations were calculated and plotted in figure 3.5 with numerical averages reported in Table 3.1 and the full data set in Appendix I Table A4. Both Li and P concentrations are elevated in the dolostone units before and after the SE relative to the limestone units during the SE. The average [Li] of the pre- and post-SE dolostone units is 1.83 ppm (n=30) while the limestones in the SE interval have an average [Li] of 0.1 ppm (Fig. 3.6B). The average [P] in the dolostone units is roughly 200 ppm, before falling to 13 ppm in the limestones (Fig. 3.5C). Strontium and Mn exhibit an inverse relationship where [Sr] are at a minimum in the dolostone

units prior to the SE before rising to a maximum of 210 ppm in the SE and then quickly falling back to a minimum in the post-SE interval (Fig. 3.6D). Manganese starts high in the pre-SE around 200 ppm before falling to roughly 90 ppm during the SE and rapidly rises back to pre-SE values in the post-SE interval (Fig. 3.6E). Aluminum and Rb were consistently below 250 ppm and 1 ppm, respectively (Fig., 3.6F, G). However, there were 8 samples that exhibited very high Al concentrations well above 250 ppm.

The average Li/carbonate in the Jiulongwan Section is 1.62 x 10^{-6} ppm/ppm with an average Li/carbonate for the pre-SE interval of 3.46 x 10^{-6} ppm/ppm, 1.15 x 10^{-6} ppm/ppm in the SE interval, and 2.0 x 10^{-6} ppm/ppm in the post-SE interval (Fig. 3.6B). The average CAP values for the Jiulongwan Section are 4.27 x 10^{-4} ppm/ppm with the highest values preceding the initial decline in $\delta^{13}C$ and the final recovery to post-SE $\delta^{13}C$ values. The average CAP values for the pre-SE, SE, and post-SE intervals are 3.95 x 10^{-4} ppm/ppm, 4.59 x 10^{-4} ppm/ppm, and 2.76 x 10^{-4} ppm/ppm, respectively (Fig. 3.6C). Both Sr/carbonate and Mn/carbonate show variability throughout the SE interval with the Sr/carbonate decreasing to a nadir of 1.2 x 10^{-4} ppm/ppm over a 50 m interval before rising to a short-lived maximum of 7.7 x 10^{-4} ppm/ppm after which the values subsequently decrease. The Mn/carbonate trend is opposite to the Sr/carbonate with the values gradually rising to roughly 0.001 ppm/ppm, followed by a notable decrease to roughly 2.5 x 10^{-4} ppm/ppm before rising to a maximum of 0.025 ppm/ppm in Member IV (Fig. 3.6D, E).

Lithium isotopes were measured on 32 samples spanning the entire SE interval with an average δ^7Li of 10.9‰ (average 2σ = ±0.28‰; Fig. 3.8E; Appendix I Table A5). The pre- and post-SE intervals are defined by heavier average δ^7Li values with the pre-SE interval δ^7Li composition of 13.1‰ (n=5; average 2σ = ±0.16‰; Table 3.3) and the post-SE interval δ^7Li value of 20.8‰ (n=4; average 2σ = ±0.25‰). The δ^7Li signal in the SE interval is very stable and

approximately 7‰ lighter than the pre-SE interval and 12‰ lighter than the post-SE interval (average δ^7Li = 8.7‰; n=23; average 2σ = 0.3‰).

Aluminum/carbonate and Rb/carbonate were plotted to assess potential detrital and clay influence on the δ^7Li values. The average Al/carbonate was 1.3 x 10^{-3} ppm/ppm with the highest values just before the falling limb and just above the climbing limb of the SE interval (Fig. 3.6F). The average Rb/carbonate was 7.7 x 10^{-7} ppm/ppm with the trend mirroring that of the Al/carbonate (Fig. 3.6G). Magnesium/Calcium and Mn/Sr ratios were calculated using the data obtained from the Li leach. Across the entire sample suite, the average Mg/Ca is 0.3, with a pre-SE average of 0.6, an average of 0.2 in the SE interval, and a post-SE average of 0.6. The average Mn/Sr for carbonates throughout the Jiuolongwan succession is 2.6. In the pre-SE interval, the Mn/Sr values reach a value of 5.41 with an average value of 1.79. In the SE interval, the Mn/Sr values reach up to 9.9 with an average value of 2.66 while the post-SE interval Mn/Sr values reach up to 7 with an average value of 3.34. Both the Mg/Ca and Mn/Sr values are at a maximum in the falling and climbing limbs of the SE while the SE interval is characterized by the lowest Mg/Ca and Mn/Sr (Fig. 3.7C, D). Consistent with the Mg/Ca and Mn/Sr, the Rb/Sr is highlighted by two notable peaks in the climbing and falling limbs of the SE. The average Rb/Sr for the pre- and post-SE are 5.0 x 10^{-4} and 1.4 x 10^{-3}, respectively, while the average Rb/Sr in the SE interval is 5.0 x 10^{-4} (Fig. 3.7E).

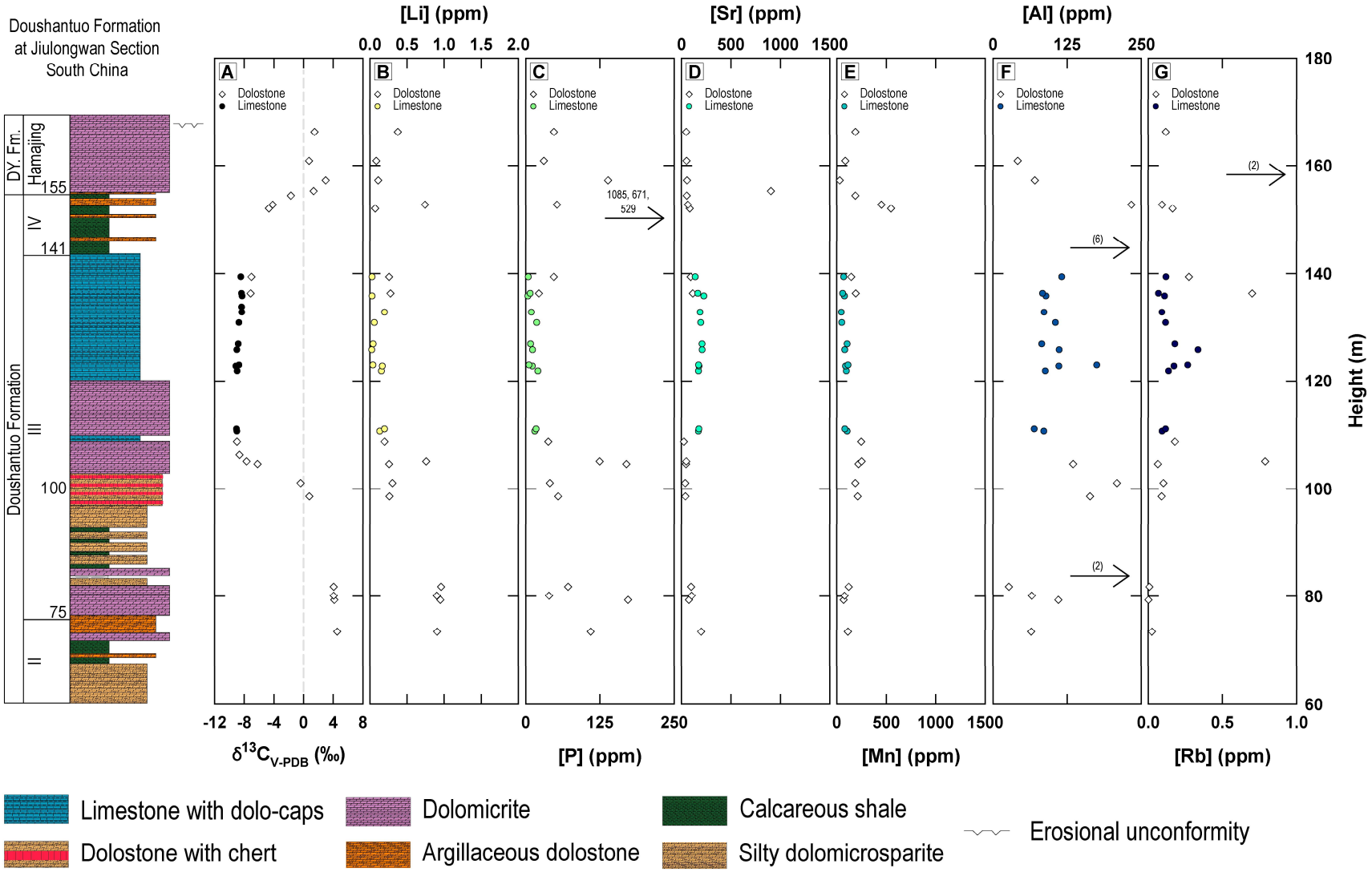


Figure 3.5: Stratigraphy and chemostratigraphy of the Doushantuo Formation at Jiulongwan Section. (B) Li concentrations are notably higher around 1.0 ppm in the dolostone intervals before and after the SE while the [Li] during the SE is at a nadir of roughly 0.2 ppm. (C) P broadly follow the Li concentrations, decreasing to a minimum in the SE interval before rising to pre-SE values in the post-SE interval. (D, E) Sr and Mn display an inverse trend where Sr values start at a minimum in the pre-SE before rising to a maximum during the SE while Mn starts at a maximum in the pre-SE and falls to a minimum during the SE. (F, G) Aluminum is elevated throughout the section with 8 samples falling off-axis while 2 samples plot off-axis for Rb (3 ppm and 1.3 ppm).

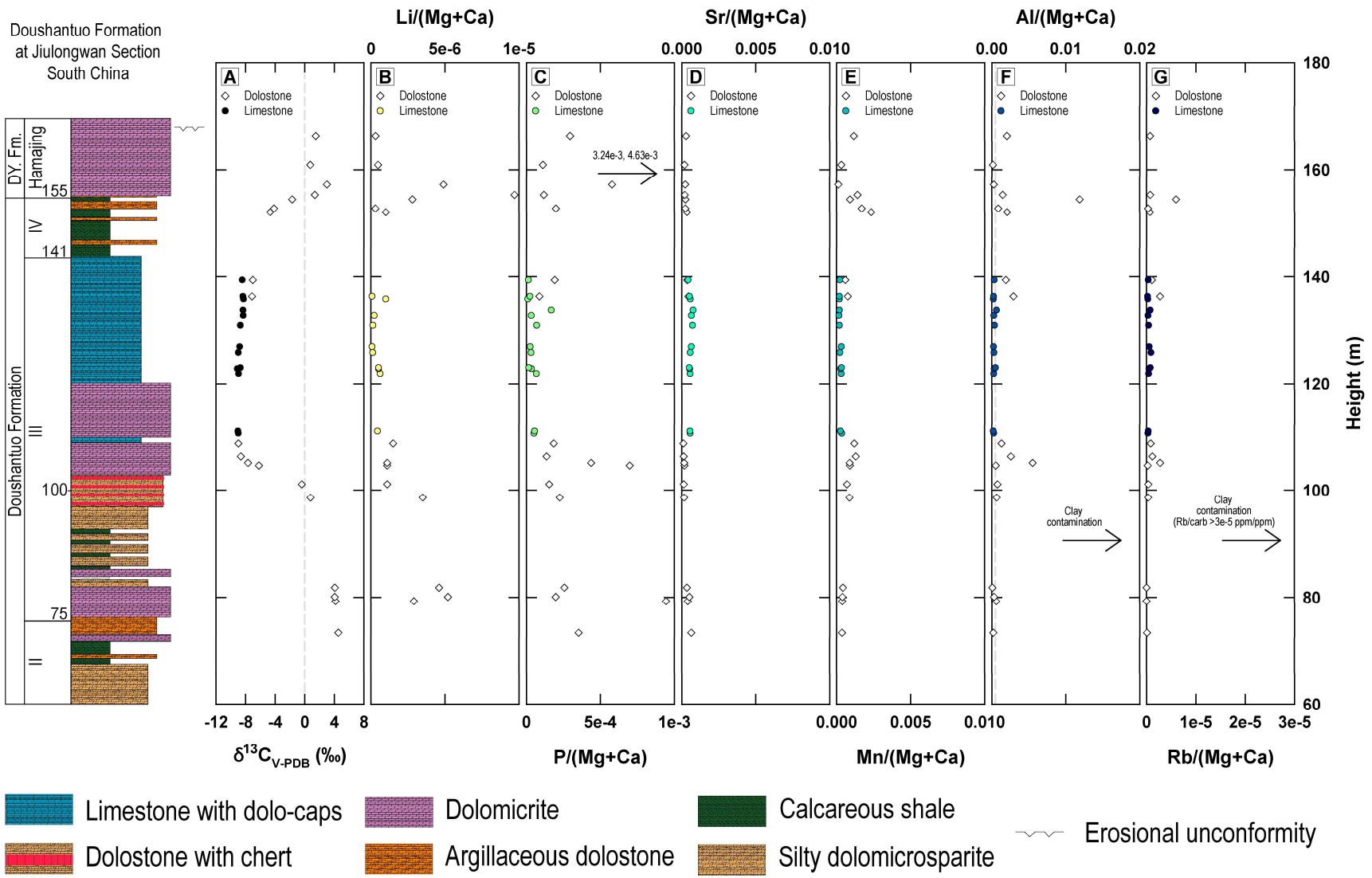


Figure 3.6: Stratigraphy and chemostratigraphy of the Doushantuo Formation at Jiulongwan Section. (B) Li/(Mg+Ca) ratios. (C) P/(Mg+Ca) or CAP ratios show a broad consistency with those reported in Dodd et al. (2023). (D) Sr/(Mg+Ca) ratios. (E) Mn/(Mg+Ca) ratios. (F) Al/(Mg+Ca) ratios, the stippled line represents the boundary beyond which aluminosilicates may have compromised the leachate. 8 samples from the dolostone section plot above the line. (G) Rb/(Mg+Ca) ratios are all consistently below the 3 x 10^{-5} ppm/ppm cutoff indicating a potential siliciclastic influence (Gan et al. *in-preparation*).

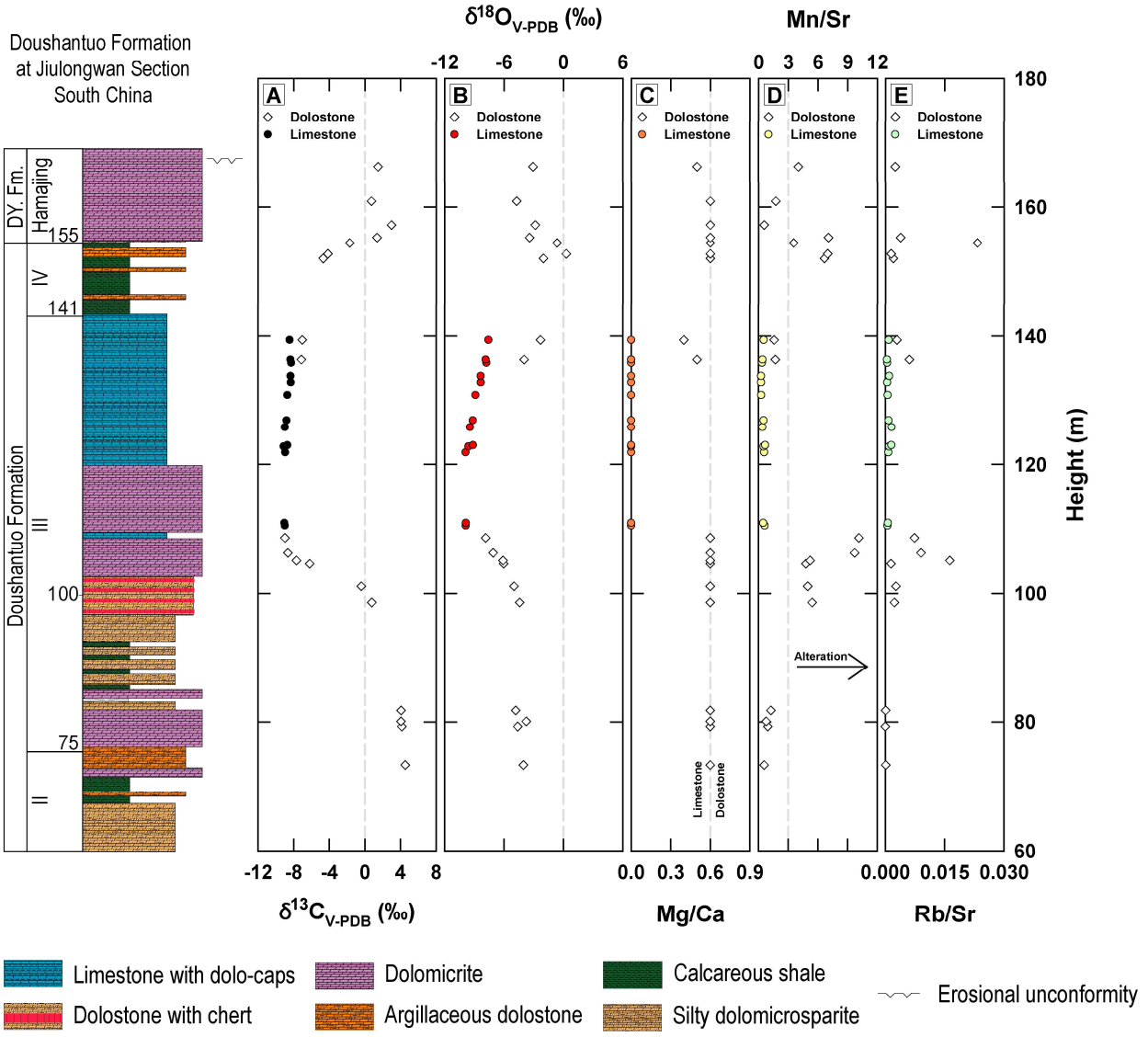


Figure 3.7: Stratigraphy and chemostratigraphy of the Doushantuo Formation at Jiulongwan Section. (A, B) Ultra low $\delta^{13}C$ and $\delta^{18}O$ values that are notably coupled (r^2=0.67, p<0.001). (C) Mg/Ca is elevated in the pre- and post-SE intervals, consistent with the dolostone units while the SE interval has low Mg/Ca, indicating limestone. (D) Mn/Sr is elevated in the pre- and post-SE intervals, consistent with the dolostone units while the SE interval has an Mn/Sr consistently below 3. (E) Rb/Sr is elevated in the dolostone units, attributable to a loss of Sr during the process of dolomitization.

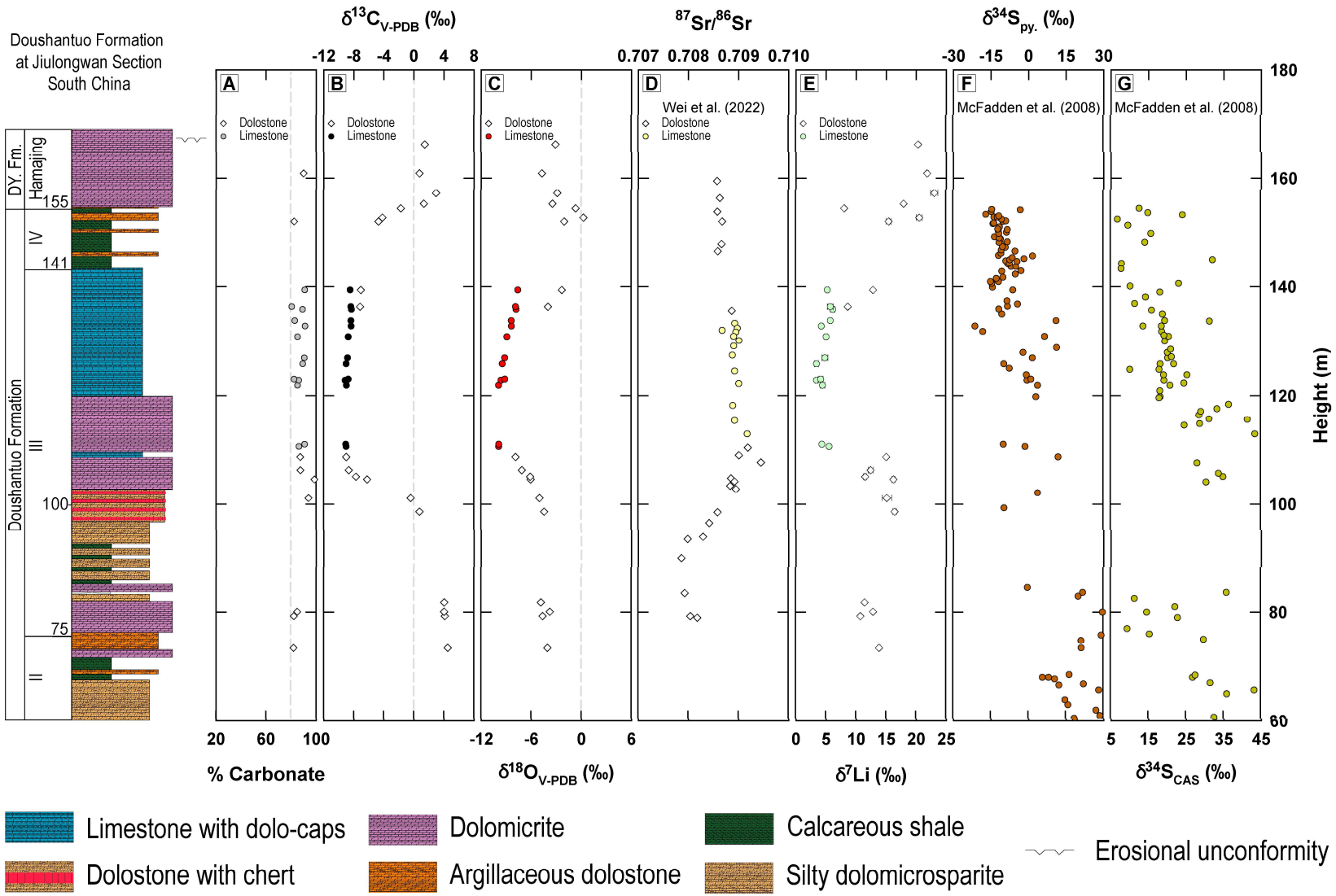


Figure 3.8: Stratigraphy and chemostratigraphy of the Doushantuo Formation at Jiulongwan Section. (A) % carbonate is >80% for the 22 samples it was determined on (McFadden et al., 2022). (B, C) Ultra low $\delta^{13}C$ and $\delta^{18}O$ values that are notably coupled (r^2=0.67, $p<0.001$) throughout the SE interval and decoupled in the intervals before and after the event. (D) $^{87}Sr/^{86}Sr$ normalized to this study (Wei et al., 2022). (E) $\delta^{7}Li$ trend of the entire SE interval. Dolostone units exhibit enrichment in ^{7}Li while the limestone samples are near crustal values. Associated uncertainties are ±0.3‰ based on replicate analyses. (F, G) $\delta^{34}S_{py.}$ and $\delta^{34}S_{CAS}$ values decrease throughout the SE interval, consistent with the growth of the sulfate reservoir (McFadden et al., 2008).

Table 3.1: Data table containing element concentration averages from the Li leach (Li, Mg, Al, P, Ca, Mn, Fe, Rb, and Sr) for both the Zhuya Group and Doushantuo Formation samples.

Succession	Formation	SE Stage	Height Range (m)	Li (ppm)	Mg (wt.%)	Al (wt. %)	P (ppm)	Ca (wt. %)	Mn (ppm)	Fe (wt. %)	Rb (ppm)	Sr (ppm)
Patom Uplift	Khopych	SE	403-567	0.58	0.24	0.01	22.79	20.63	169.90	0.22	0.08	878.42
	Khopych Reef		551-562	1.00	0.33	0.01	10.27	32.88	124.67	0.06	0.07	1286.61
	Alyanch		256-403	0.20	0.17	0.00	6.12	29.57	56.74	0.07	0.05	1072.81
	Nikol'skoe		0-256	0.46	0.37	0.01	19.20	27.07	669.98	0.15	0.11	448.57
Yangtze Block	Doushantuo/Dengying	Post-SE	82-93	0.19	8.27	0.01	72.24	14.22	102.64	0.02	0.12	51.28
	Doushantuo	SE	25-82	0.28	3.90	0.04	113.70	25.02	163.60	0.13	0.26	131.98
		Pre-SE	0-25	0.80	8.94	0.01	89.39	15.27	119.14	0.07	0.02	102.19

Table 3.2: Data table containing element ratio averages (Mg/Ca, Mn/Sr, Rb/Sr Li/(Mg+Ca), Al/(Mg+Ca), P/(Mg+Ca), Mn/(Mg+Ca), Rb/(Mg+Ca), and Sr/(Mg+Ca)) for both the Zhuya Group and Doushantuo Formation samples from the Li leach.

Succession	Formation	SE Stage	Mg/Ca	Mn/Sr	Rb/Sr	Li/(Mg+Ca)	Al/(Mg+Ca)	P/(Ca+Mg)	Mn/(Mg+Ca)	Rb/(Mg+Ca)	Sr/(Mg+Ca)
Patom Uplift	Khopych	SE	0.01	0.26	1.13E-04	2.84E-06	3.30E-04	1.28E-04	8.65E-04	3.53E-07	4.53E-03
	Khopych Reef		0.01	0.16	9.60E-05	2.39E-06	1.62E-04	3.19E-05	3.74E-04	2.09E-07	3.90E-03
	Alyanch		0.01	0.07	5.95E-05	7.32E-07	1.29E-04	3.51E-05	2.02E-04	1.64E-07	3.75E-03
	Nikol'skoe		0.01	2.67	3.11E-04	1.88E-06	4.18E-04	8.54E-05	2.52E-03	3.79E-07	1.65E-03
Yangtze Block	Doushantuo/Dengying	Post-SE	0.6	3.34	1.41E-03	2.00E-06	1.00E-03	2.76E-04	7.63E-04	3.42E-07	2.29E-04
	Doushantuo	SE	0.2	2.66	3.63E-03	1.15E-06	1.52E-03	4.59E-04	6.36E-04	9.93E-07	4.39E-04
		Pre-SE	0.6	1.79	5.03E-04	3.46E-06	3.84E-04	3.95E-04	4.92E-04	9.51E-08	4.15E-04

Table 3.3: Data table of averages for percent carbonate, isotopic averages (for $\delta^{13}C$, $\delta^{18}O$, $\delta^{7}Li$, $\delta^{7}Li_{SW}$, $\delta^{88}Sr$, and $^{87}Sr/^{86}Sr$) and average uncertainties for both the Zhuya Group and Doushantuo Formation.

Succession	Formation	SE Stage	Height Range (m)	% Carb.	$\delta^{13}C$ (‰)	$\delta^{18}O$(‰)	$\delta^{7}Li_{carb}$	$\delta^{7}Li_{SW}$	2σ	$\delta^{88}Sr$	2σ	$^{87}Sr/^{86}Sr$	2σ
Patom Uplift	Khopych	SE	403-567	78.6	-8.87	-9.21	8.5	13.5	0.2	0.38	0.01	0.7083	4.24E-06
	Khopych Reef		551-562	91.3	-8.34	-9.33	9.6	14.6	0.1	-	-	0.7084	3.89E-06
	Alyanch		256-403	95.3	-9.61	-9.51	9.5	14.5	0.2	0.37	0.01	0.7080	3.55E-06
	Nikol'skoe		0-256	81.2	-11.58	-10.75	4.9	9.9	0.2	0.29	0.03	0.7081	5.61E-06
Yangtze Block	Doushantuo/Dengying	Post-SE	82-93	89.9	-0.78	-3.28	20.8	21.0	0.3	-	-	-	-
	Doushantuo	SE	25-82	87.9	-7.34	-6.64	8.7	11.6	0.3	-	-	-	-
		Pre-SE	0-25	83.0	3.3	-4.18	13.1	13.1	0.2	-	-	-	-

3.5: Discussion

3.5.1: Diagenesis

Carbonate lithium isotope values can be utilized to estimate secular variations in seawater δ^7Li compositions during carbonate precipitation, as long as clay contamination and diagenesis are properly assessed (Murphy et al., 2022). There are many sedimentological indicators of diagenesis, although the most telltale sign is the erasure of primary sedimentary fabrics through extensive recrystallization often accompanied by an increase in crystal size (Land, 1970). However, alteration can occur despite the retention of primary fabrics, thus petrographic observations are often paired with geochemical data to better understand the style of diagenesis a rock might have undergone. Conventional geochemical indicators for post-depositional alteration include enriched δ^{18}O values, often accompanied by elevated Mg/Ca indicating dolomitization (Fritz and Smith, 1970; Fantle and Higgins, 2014), or depleted δ^{18}O values (<-10‰;) indicating influence from meteoric or high temperature fluids (Knauth and Kennedy, 2009; Derry, 2010), and elevated Mn/Sr values (>10), indicating marine or meteoric diagenesis (Jacobsen and Kaufman, 1999). By combining both petrographic observations with geochemical measurements, the fidelity of the primary seawater signal can be evaluated. The petrographic plates can be found in this chapter below, chapter 4, and Appendix II.

3.5.1.1: Patom Uplift

The domination of carbonates in the Zhuya Group is consistent with successions worldwide where the SE is notably rich in these shallow marine facies. The petrographic observations of the Zhuya Group revealed limestone samples consisting of fabric-retentive micrite and microspar. The Nikol'skoe Formation is characterized by microspar carbonates with higher siliciclastic and clay

abundances in the basal ~100 to 125 m before shifting to predominantly carbonate. The carbonate samples throughout the unit contain abundant ooids (avg. ~250 μm in diameter) with intraclastic cements (20% or less) that range from microspar to blocky sparite in the basal Nikol'skoe Formation (0-153 m), which are interpreted as penecontemporaneous cements.

The ooids present in the Nikol'skoe Formation are pristinely preserved with a characteristic radial internal fabric and a thin outer cortices. The radial internal structure and exceptional preservation of the Nikol'skoe Formation ooids suggests formation and deposition in a quieter environment like the deeper reaches of the shoreface where minimum wave agitation, coupled with carbonate supersaturation stimulated ooid growth (Fig. 3.9A, D; Davies, Bubela, and Ferguson, 1978). Moving up into the Alyanch and Khopych formations, carbonates persistently dominate through the entire section, although about 150 m into the unit, siliciclastic abundances increase. The ooids in the Khopych Formation increase in average size (~300-350 μm) and are surrounded by blocky intraclastic cements. The ooids appear to be bimineralic insofar as the inner cortex structure in almost 45% of the ooids have been recrystallized to some extent, but the original outer cortex has remained intact, many of which show finely laminated, concentric or tangential micritic fabrics. The first of the two ooid morphologies are micritic to microsparitic that gradually transition into blocky-micritic ooids beneath the reef complex (Fig. 3.9E, H). Above the reef complex the second ooid morphotype consists of blocky neomorphosed ooids (~65%), some of which appear to be bimineralic (although low in abundance representing <30% of all spheroidal allochems), and micritic to blocky-micritic ooids (Fig. 3.9I, L). The Khopych Formation ooids show clear signs of neomorphism and recrystallization of metastable aragonitic micrite and microspar ooids (Chatalov, 2005). During neomorphism of aragonite to low-Mg calcite under fluid-buffered conditions, carbonate δ^7Li is driven closer to seawater values, thus muting the offset

between primary carbonate sediments and seawater (Dellinger et al., 2020; Murphy et. al, 2022; Wei et al., 2023; Wei et al., 2024).

Following the petrographic analyses, 5 polished thin sections representative of Zhuya Group lithologies were mapped for elemental distributions relative to sedimentary textures to better understand the impact diagenesis and authigenic clay mineral formation may have had on the isotopic composition of the studied samples (figures 3.10 through 3.14). The 4x4 WDS stage maps show that Si, Mg, and Al co-occur throughout the Zhuya Group, indicating the presence of authigenic clay minerals. The high abundance of both clays and detrital material in the basal ~100 m of the Nikol'skoe Formation provides an explanation for the radiogenic Sr isotope compositions of samples at this level that are inconsistent with typical Ediacaran seawater. The co-occurrence of Sr with the clay mineral proxies in this interval suggests Sr was absorbed onto the surface of precipitating clays via ion exchange during carbonate cementation, driving the $^{87}Sr/^{86}Sr$ of the precipitating fluid to more radiogenic values that is reflected in the Sr isotope composition of the carbonates (Wahlberg et al., 1965; Başçetin and Atun, 2006; Wu et al., 2024). The manganese map revealed a preferential distribution in the intraclast cements, likely indicating cementation of allochems from anoxic porewater. In the Khopych Formation, the Mn maps reveal no clear trend, due to the very low concentrations while the Sr maps reveal higher concentrations within the carbonate cements, suggesting that the cement was penecontemporaneous and thus directly reflects the composition of seawater.

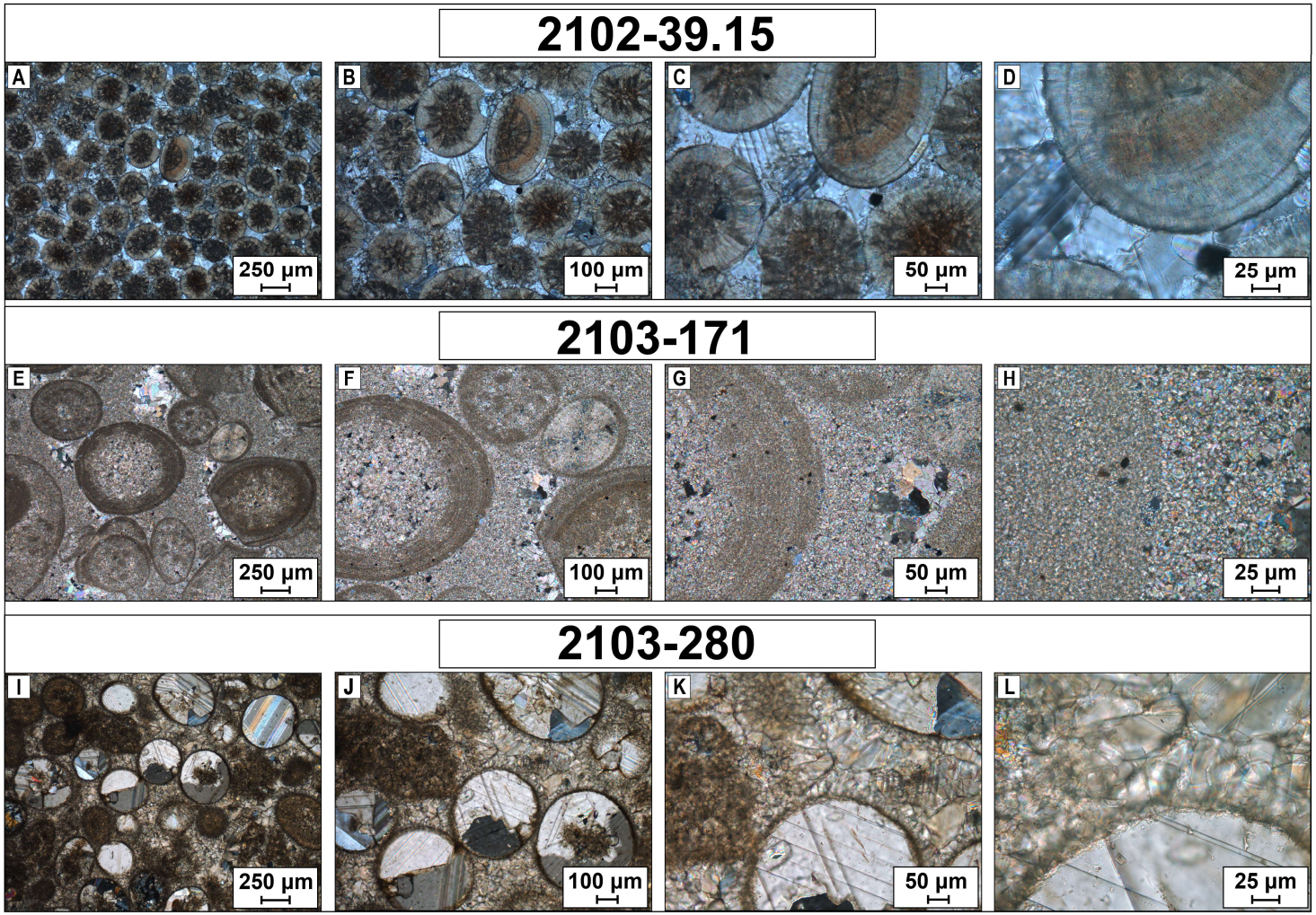


Figure 3.9: Three distinct ooid morphotypes present throughout the Zhuya Group. (A, D) Ooids approximately 250 µm in diameter in the Nikol'skoe Formation. The radial internal structure indicates high carbonate saturation paired with a slightly quieter environment permitted the development of a radial internal fabric (Davies et al., 1978). (E, H) Representative ooids from the basal Khopych Formation. The average diameter is 300 to 350 µm in diameter. The inner cortex in the ooids has been partially recrystallized, likely the result of neomorphism from an original aragonite mineralogy to low-Mg calcite. The tangential cortex indicates a high energy shoaling environment subject to constant agitation. (I, L) The final ooids from the Khopych Formation immediately above the reef complex that consist of blocky neomorphosed ooids, some of which were replaced by a singular grain, and bimineralic ooids with the inner nucleus retained and the inner cortex recrystallized. Samples are photographed under crossed-polarized light and at 5x, 10x, 20x, and 50x magnification from left to right.

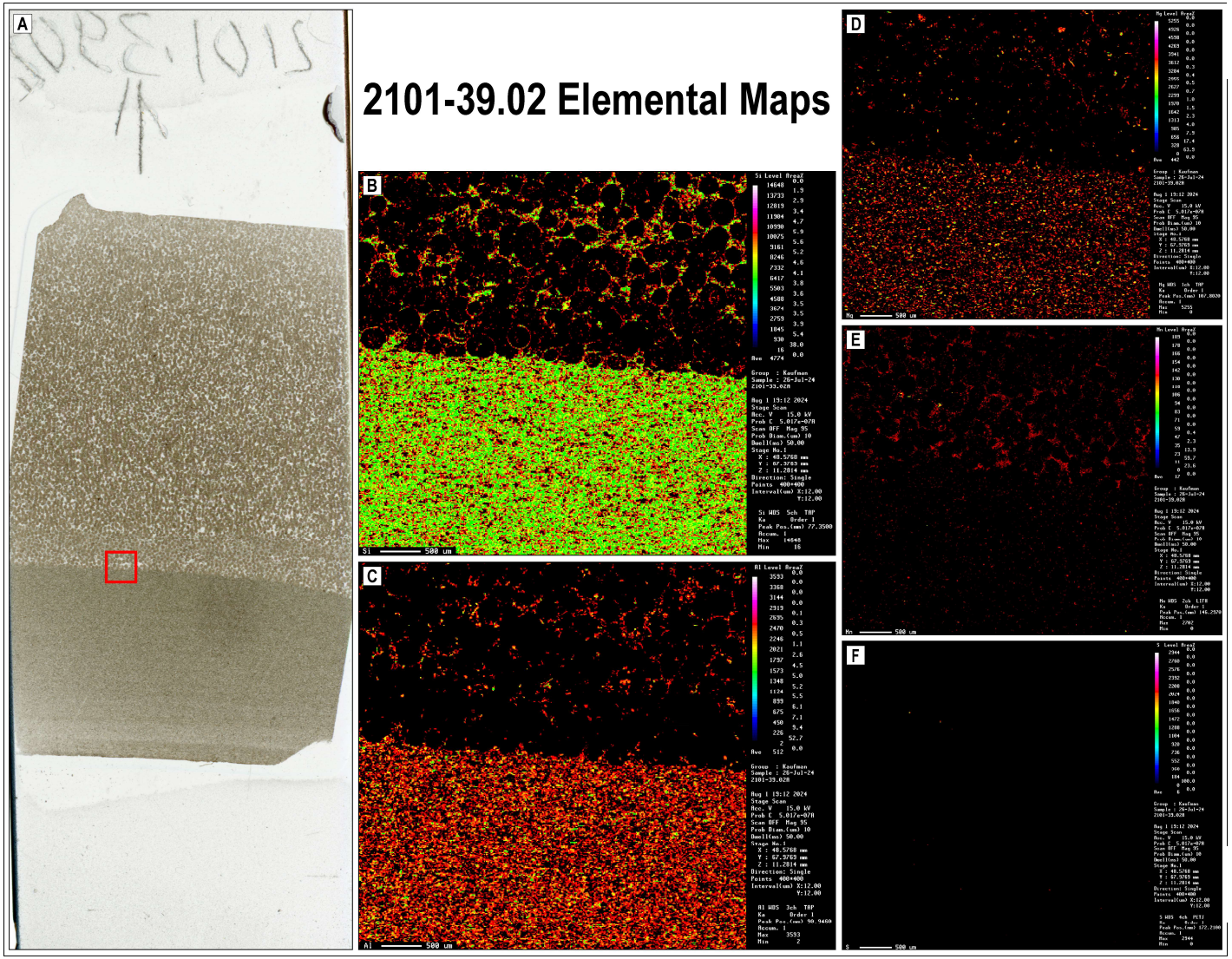


Figure 3.10: (A) Thin section scan of sample 2101-39.02 from the basal Nikol'skoe Formation. (B) Si maps reveal high density in the micritic half and heterogenous distribution in the intraclast cements of the ooid section. (C) Al has the same distribution as Si, suggesting a co-occurrence of aluminosilicate minerals. (D) The distribution of Mg broadly matches that of Si and Al indicating the presence of magnesian clay minerals, predominantly in the micrite. (E) Mn is concentrated in the intraclast cements, indicating transport of the ooids downslope where they were cemented under reduced conditions. (F) S map did not return any discernable information.

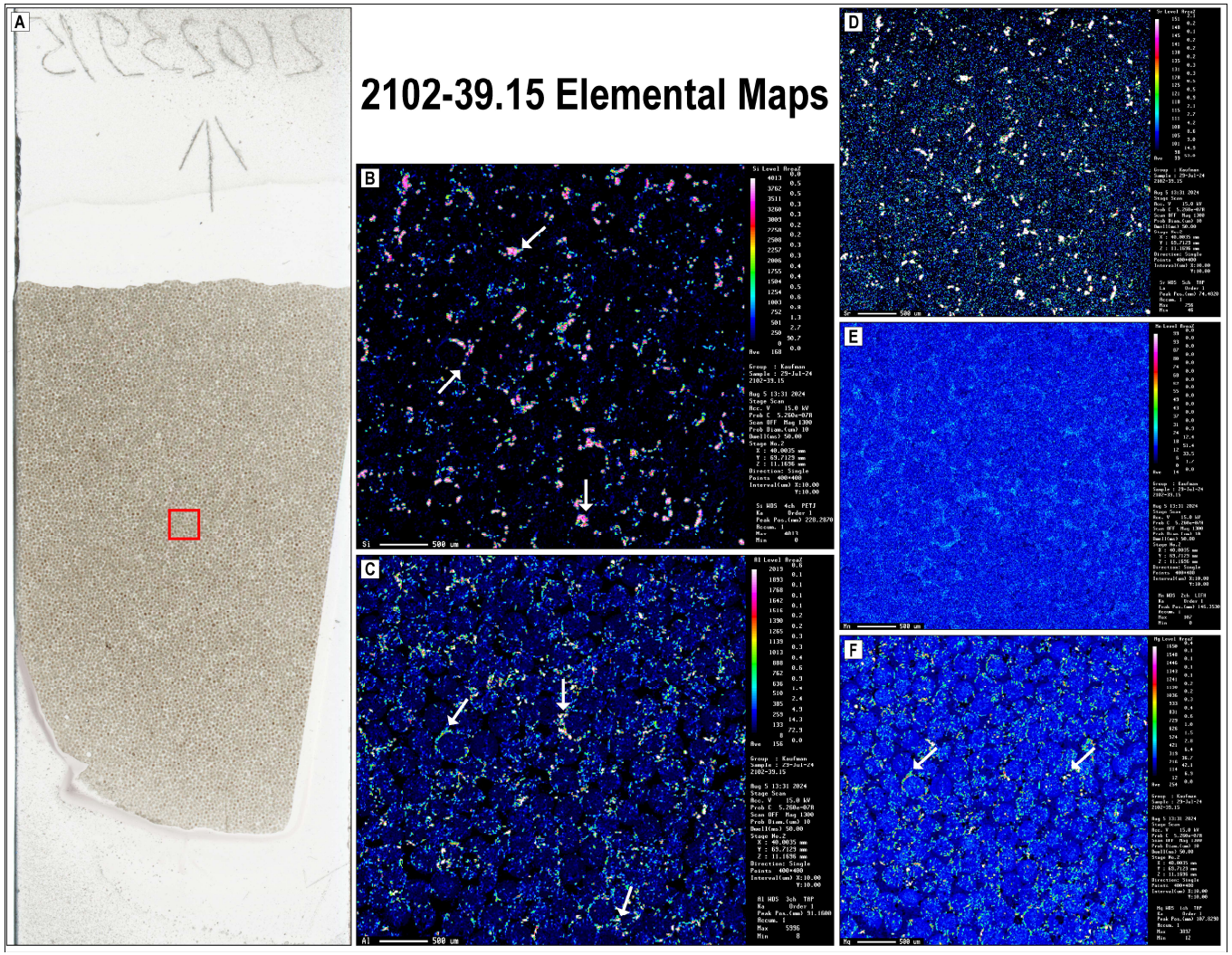


Figure 3.11: (A) Thin section scan of sample 2102-39.15 from the Nikol'skoe Formation. (B) Si maps reveal high density distributions primarily around the outer cortex of the ooids with some very high signatures indicating minor silicification (arrows point to high density points). (C) Al is distributed around the ooids, coincident with Si, but the ooids appear to contain minor amounts of Al inside the cortex. (D) The distribution of Mg matches that of Si and Al indicating the presence of magnesian clay minerals. The ooids appear to have higher Mg than the surrounding cements, though the co-occurrence with Al suggests authigenic clays are present (E) Mn is slightly more concentrated in the cements relative to the ooids, though the distribution is muted due to lower concentrations. (F) Sr is highly concentrated with Si, Mg, and Al, indicating that Sr may have absorbed onto the negatively charged surface of any clay minerals precipitating.

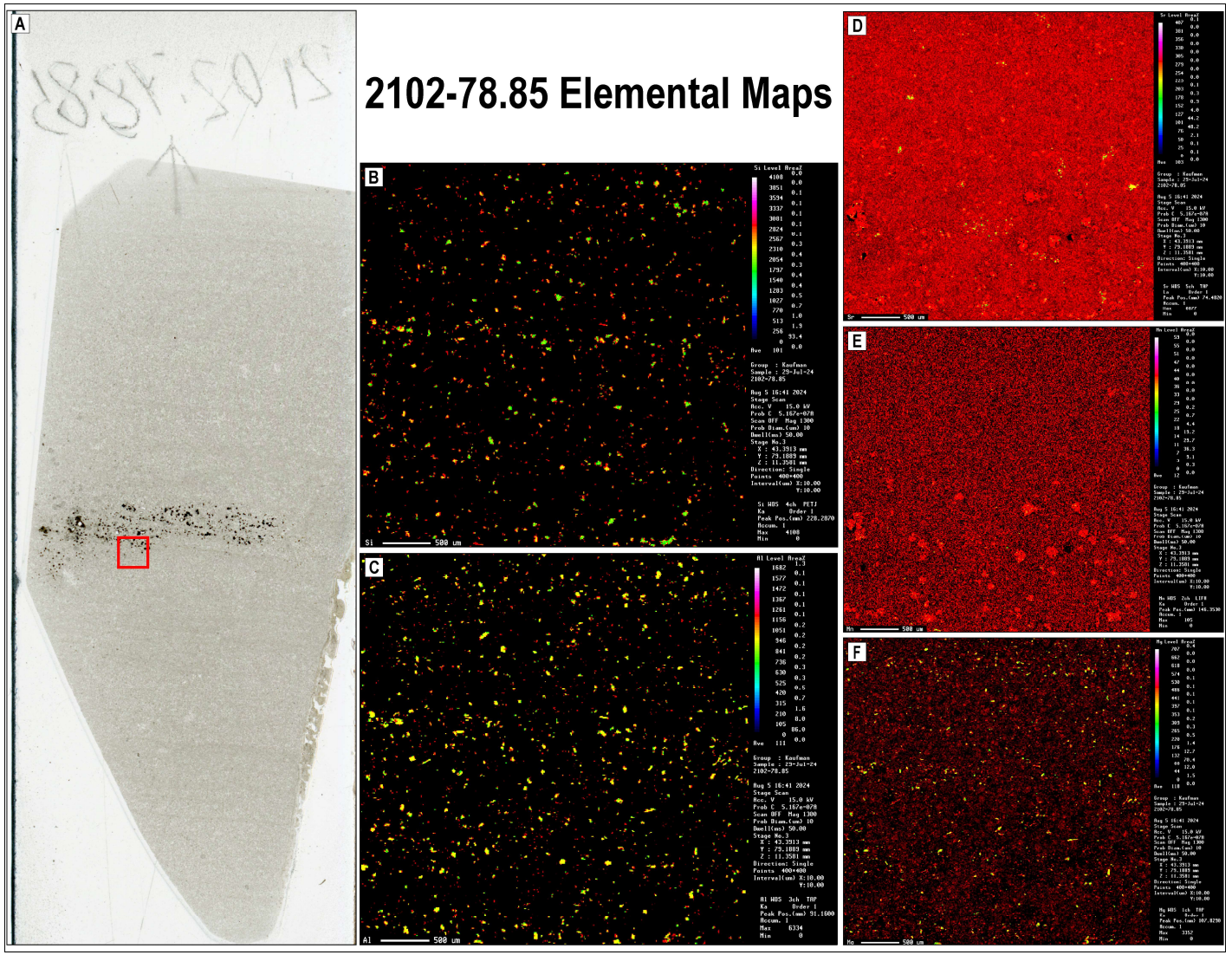


Figure 3.12: (A) Thin section scan of sample 2102-78.85 from the Nikol'skoe Formation. (B, D) Si, Al, and Mg maps reveal high density point distributions though the abundance is minor relative to the two underlying samples indicating a lack of abundant clay minerals present. (E, F) Mn and Sr are homogenously distributed throughout the map. Mn appears to be concentrated around the opaque phases consisting of pyrrhotite with pyrite rims.

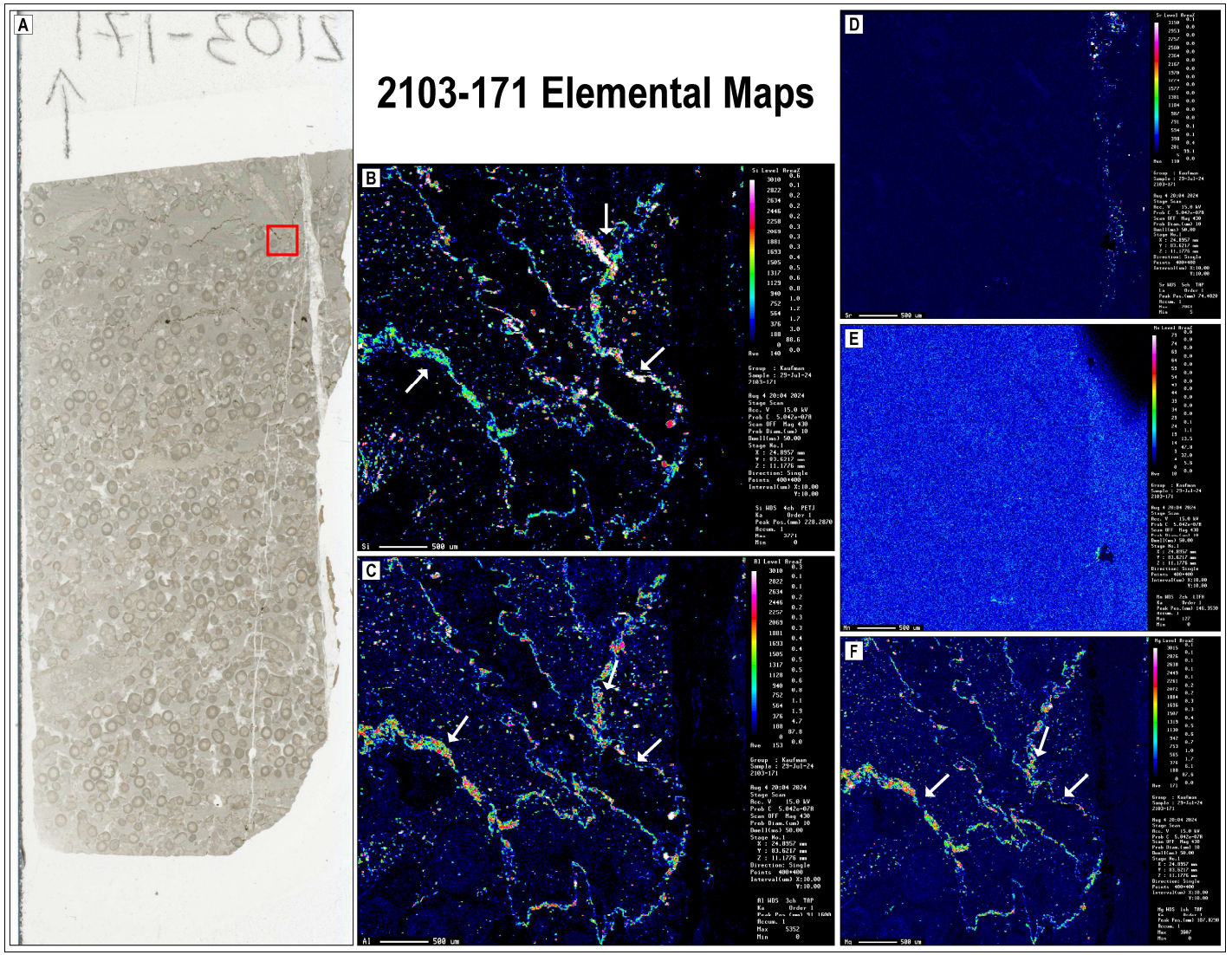


Figure 3.13: (A) Thin section scan of sample 2103-171 from the Khopych Formation. (B, C) Si, Al, and Mg maps reveal high concentration along the boundaries of the several stylolites (arrows indicate high concentration areas around the stylolites). (E, F) The Sr and Mn maps are relatively homogenous and thus cannot be interpreted.

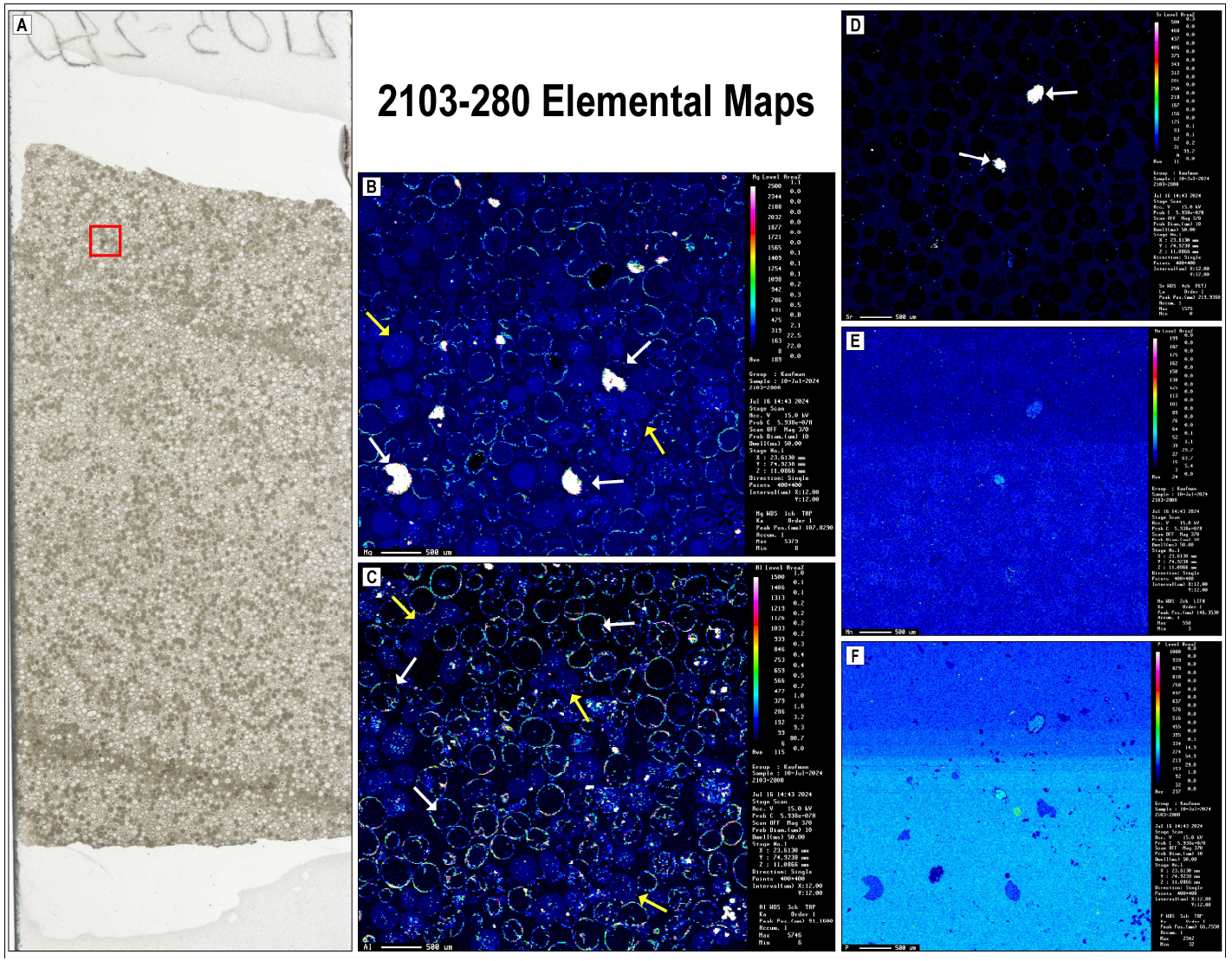


Figure 3.14: (A) Thin section scan of sample 2103-280 from the Khopych Formation. (B, C) Al and Mg maps reveal high concentration along the outer cortices of the ooids (white arrows point to neomorphosed single-crystal ooids and yellow arrows point to bimineralic ooids). (D) Sr is distributed primarily in the cements with two bright spots corresponding to a Sr-sulfide. (E, F) The Mn and P maps are fairly muted and do not exhibit a clear discernable distribution within a specific phase.

The petrographic findings indicate Zhuya Group samples generally preserve a primary δ^7Li seawater signature and are corroborated by the geochemical data from the Li leach solutions. The data from the Patom shows little to no correlation with conventional indicators of diagenesis (e.g., $\delta^{18}O$, Mn/Sr, Rb/Sr, Sr/Ca, and Mn/Ca) as well as ultrahigh [Sr] (Fig. 3.15A, I). The retention of Sr in the cements of the Alyanch and Khopych formations, despite deposition on a shallow carbonate shelf, suggests an early fluid-buffered style of diagenesis occurred, and altered the rocks with respect to seawater rather than meteoric fluids. The Mn/Sr values throughout the entire Zhuya Group are below 2, except for the basal Nikol'skoe Formation, which starts at a value of 8 and decreases to <3 at ~100 m. A conservative Mn/Sr cutoff of <3 was used to represent samples that are well-preserved because, while $\delta^{13}C$ values are more robust and have been shown to retain their primary signal at Mn/Sr values up to 10 (*cf.* Kaufman et al., 1993), Li and Sr isotopes have shown signs of alteration at lower Mn/Sr values (Ahm et al., 2018). Coincident with this interval of slightly elevated Mn/Sr, it is worth noting that the carbonates preserve radiogenic $^{87}Sr/^{86}Sr$ values that do not match globally established trends during this interval in Earth history. The high proportions of siliciclastic components in these samples may have influenced the carbonate Sr and Li isotopic values (Derry et al., 1992). For this reason, the lower ~100 m of the Patom should be interpreted with caution for both the δ^7Li and $^{87}Sr/^{86}Sr$ isotopic data and thus the interpretations focus on the low δ^7Li values recorded in the well-preserved limestone intervals from the upper ~500 m of the measured succession.

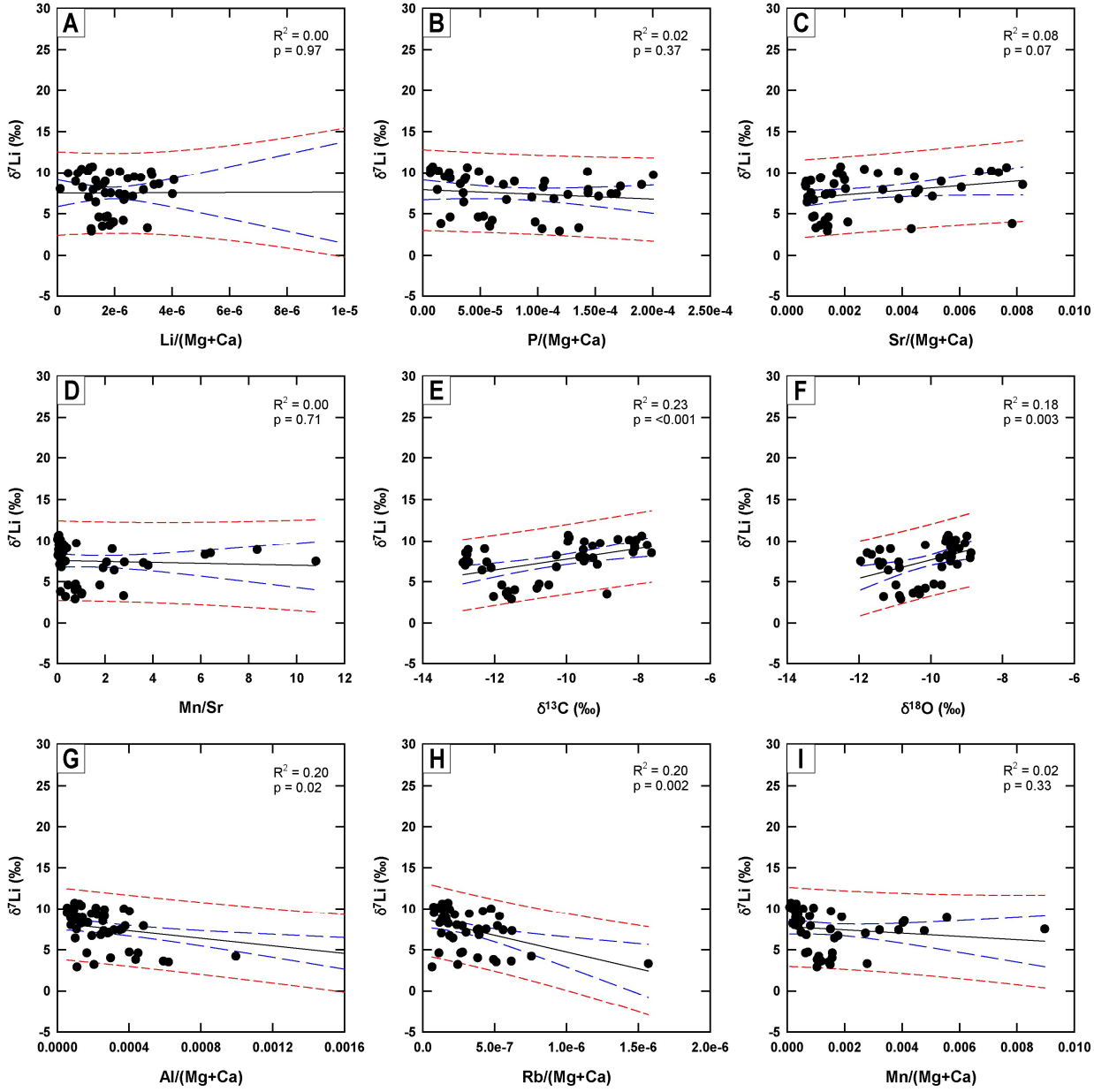


Figure 3.15: Cross-plots of δ^7Li versus other elemental ratios and conventional indicators of diagenesis for the Zhuya Group. (A) δ^7Li versus Li/(Mg+Ca). (B) δ^7Li versus P/(Mg+Ca). (C) δ^7Li versus Sr/(Mg+Ca). (D) δ^7Li versus Mn/Sr. (E) δ^7Li versus δ^{13}C. (F) δ^7Li versus δ^{18}O. (G) δ^7Li versus Al/(Mg+Ca). (H) δ^7Li versus Rb/(Mg+Ca). (I) δ^7Li versus Mg/(Mg+Ca). Note, black line is the regression line, blue stippled line is 95% confidence interval, and red stippled line is the 95% predicted confidence interval.

3.5.1.2: Doushantuo Formation

The diagenetic history of the Jiulongwan Section of the Doushantuo Formation reveals a drastically different style of preservation. The petrographic analyses revealed fabric-destructive dolomitization, characterized by euhedral dolomite spar (50-100 μm) in the samples that represent the falling and climbing limbs of the SE (Figs. 3.16). Conversely, the limestone samples in the nadir of SE interval consist of homogenous, fabric-retentive micrite (Appendix 2 Fig. A5). Insofar as dolomitization directly affects carbonate δ^7Li compositions, microsamples were collected and analyzed for two samples in the climbing limb of the SE that contained both limestone and dolomite fabrics (Fig. 3.17). Notably, the dolomite sub-samples exhibited heavier δ^7Li values (12.9‰ and 8.7‰) relative to the limestone sub-samples (5.3‰ and 5.8‰). This enrichment of δ^7Li is consistent with previous studies on the effect of dolomitization on carbonate δ^7Li values, where under both sediment- and fluid-buffered conditions, the δ^7Li is driven towards more ^{7}Li enriched compositions. This cm-scale comparison suggests that dolomitization and the formation of clay minerals in these carbonates resulted in higher δ^7Li values. With this view in mind, we focus on the limestones as reflecting depositional values rather than the trends defined by both limestone and dolomite in the Jiulongwan succession.

Four polished thin sections from the Jiulongwan carbonates were selected for elemental mapping to observe the distribution of common clay mineral elements (Fe, Al, Mg), and indicators of diagenesis (Sr, Mg, Mn). Two of the limestone samples did not yield any maps with discernable features due to the relatively homogenous microspar textures and absence of clay minerals. However, the two dolomite samples, one from the pre-SE interval, and the other from the climbing limb of the SE reveal elemental distributions that support the view that the dolostone δ^7Li values have been reset by the formation of authigenic clay minerals coincident with dolomitization. The

co-occurrence of Mg and Al in both samples indicates the presence of Mg-rich clays with sample SSFT-8.3 exhibiting interlayering of the clays with precipitated carbonate while the clays in HND-26.6 may have precipitated during dolomitization (Figures 3.18 and 3.19). Previous proto-dolomite precipitation experiments have revealed that under high carbonate saturation (~20 mM), illite, montmorillonite, and other negatively-charged clay minerals can serve as possible nucleation sites for dolomite (Liu et al., 2019). The sharp contrast between the limestone and dolostone portion of sample HND-26.6 suggests that the clay mineral horizon may have served as a template to form proto-dolomite, which after burial transformed into stoichiometric dolomite through dissolution and reprecipitation (Malone et al., 1996; Vasconcelos and McKenzie, 1997; Warren, 2000; Rodriguez-Blanco et al., 2015).

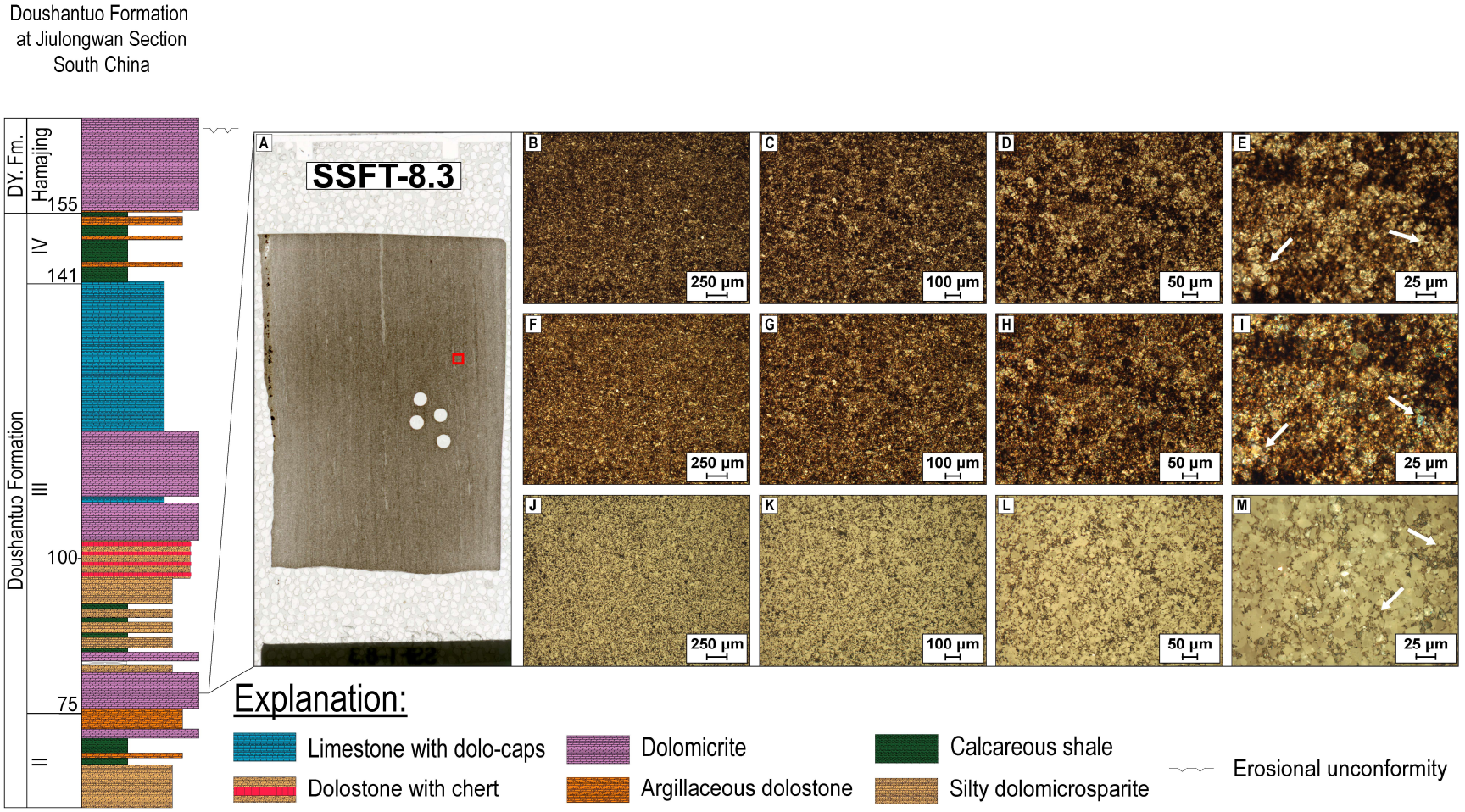


Figure 3.16: Plate of thin section photos from sample SSFT-8.3 from the Doushantuo Formation. (A) Thin section scan. (B, E) Plane-polarized light images of microspar with small, euhedral dolomite rhombs and clays (white arrows point to dolomite grains). (F, G) Crossed-polarized light images. (H, I) Reflected light images. Magnifications are 5x, 10x, 20x, and 50x from right to left, respectively.

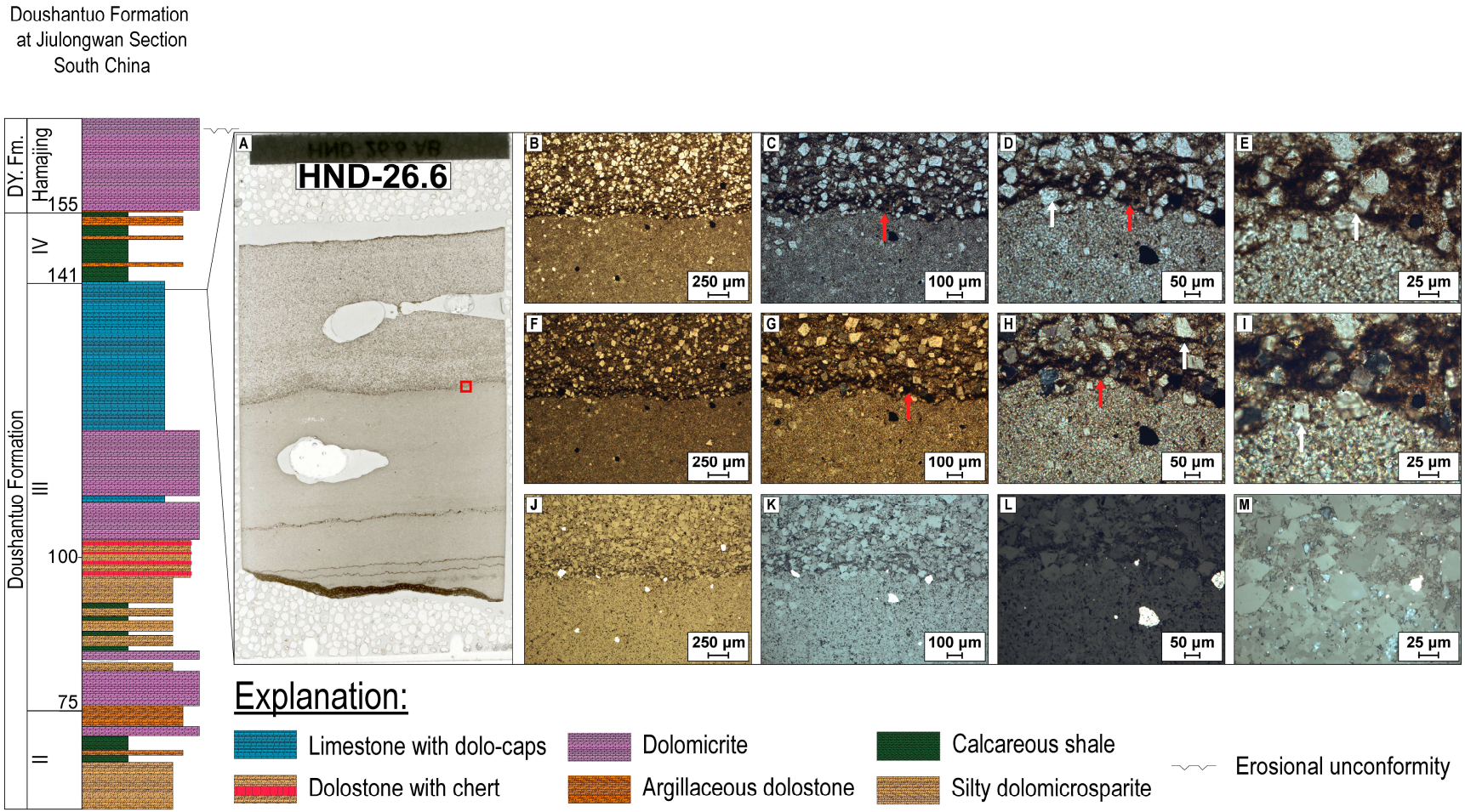


Figure 3.17: Plate of thin section photos from sample HND-26.6 from the Doushantuo Formation. (A) Thin section scan. (B, E) Plane-polarized light images of dolomite rhombs in the dolostone half (white arrows), clay horizon (red arrows), and the limestone half. (F, G) Crossed-polarized light images. (H, I) Reflected light images. Magnifications are 5x, 10x, 20x, and 50x from right to left, respectively.

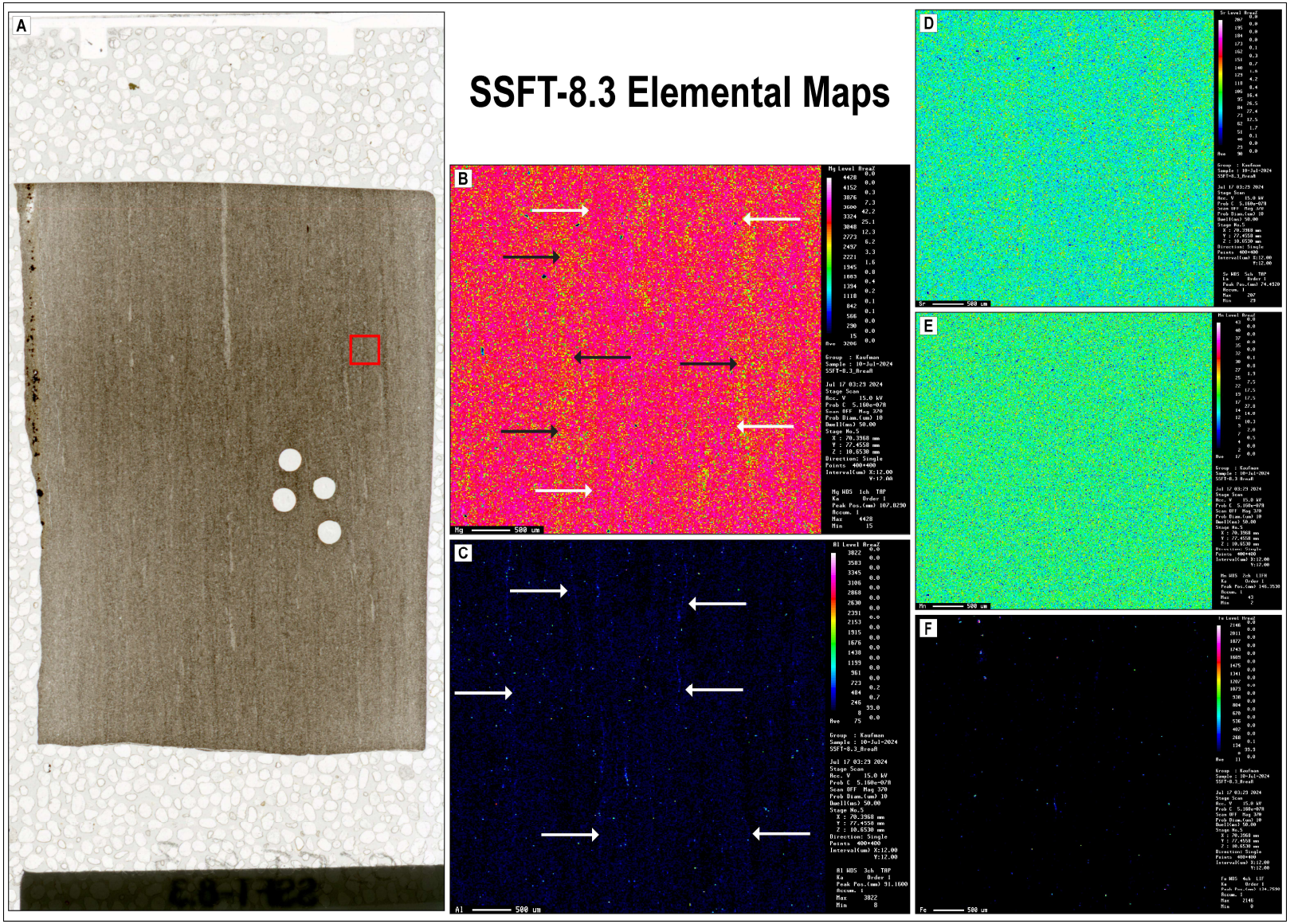


Figure 3.18: (A) Thin section scan of sample SSFT-8.3 from the Doushantuo Formation. (B, C) Al and Mg co-occur in interlayered regions of high and low density (white arrows point to high density regions and yellow arrows point to lower density regions). (D) Sr is relatively homogenously distributed but there is some faint interlayering similar to Al and Mg. (E, F) Mn and Fe are muted and thus cannot be reliably interpreted.

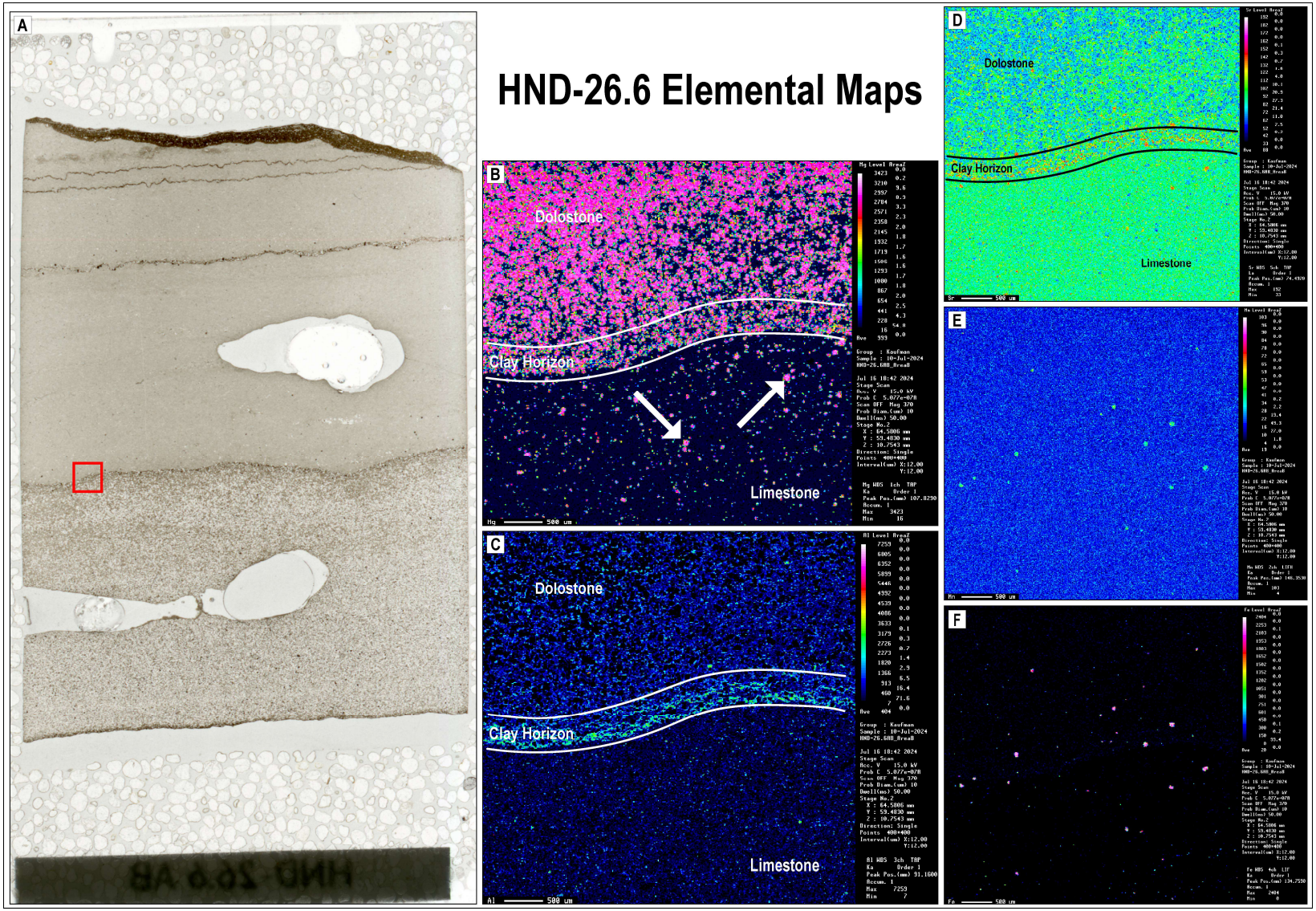


Figure 3.19: (A) Thin section scan of sample HND-26.6 from the Doushantuo Formation. (B, D) Al, Mg, and Sr maps reveal high concentration along the clay horizon separating the limestone from dolostone. Though there is a clear boundary, some small dolomite grains are present within the limestone. (E, F) The Mn and Fe maps are fairly muted and do not exhibit a clear discernable distribution within a specific phase.

The petrographic observations and elemental maps highlight the impact of authigenic clay mineral formation and dolomitization on the δ^7Li compositions of the Jiulongwan carbonates, suggesting that the limestones reflect depositional signals while the dolostones are ^{7}Li enriched to variable degrees due to the redistribution of ^{6}Li into authigenic clays. Nonetheless, conventional diagenetic indicators (e.g., Mn/Sr, Rb/Sr, Sr/carbonate, Mn/carbonate, and δ^{18}O) lack strong correlations with δ^7Li abundances (Fig. 3.20A-I). The Mn/Sr and Rb/Sr trends follow that of the Mg/Ca, highlighting the greater influence of dolomitization in the climbing and falling limbs of the SE, while the nadir of the excursion appears exceptionally well preserved based on the same geochemical screens. It is worth noting that the ^{87}Sr/^{86}Sr values from the Jiulongwan Section also do not match that of globally established Ediacaran seawater (Wei et al., 2022), this may be perhaps due to the restricted nature of the Jiulongwan Section from the open-ocean, although the consistency of other elemental and isotopic proxies refutes this view, or it may reflect differences in source rock with the weathering of basalts in the Patom Uplift or the weathering of the Huangling Granite in the Jiulongwan Section (Cui et al., 2015). More likely, the partial dolomitization of even the limestone samples provides an explanation for the more radiogenic Sr isotope compositions of the Doushantuo Formation relative to other SE successions worldwide.

Aside from the impact of diagenesis on the carbonate δ^7Li values, samples from both successions were screened for clay contamination during the leaching step, insofar as silicates are highly concentrated in [Li] (5 to 100 ppm) and Li/carbonate ratios (1.38×10^{-3} to 34.63×10^{-3} ppm/ppm) relative to carbonates (0 to 5 ppm) and (0.17×10^{-6} to 34.63×10^{-6} ppm/ppm; Liu et al., 2023). However, there is no evidence for clay contamination affecting the leachate, as there is a lack of correlation between δ^7Li and Li/(Mg + Ca), and the Li/(Mg + Ca) ratios range from 0 to 9.70×10^{-6} ppm/ppm, falling within the range of carbonates (*cf.* Gan et al., *in-preparation*).

Aluminum/carbonate ratios of the 78 samples from this study range from 0 to 11.9 x 10^{-3} ppm/ppm, 67 samples of which fall below the threshold value of 5.4 x 10^{-4} ppm/ppm used to indicate clay contamination (Kalderon-Asael et al., 2021; Wei et al., 2023), while 11 samples are slightly above the threshold value. Additionally, Rb/carbonate ratios for all 78 samples range from 0 to 6.0 x 10^{-6} ppm/ppm are below the proposed cutoff value of 3.0 x 10^{-5} ppm/ppm used to indicate clay contamination (Wei et al., 2023). It has been demonstrated that Rb is more sensitive to aluminosilicate contamination than Al (Korenaga, 2013; Sawaki et al., 2010), and thus, the combination of Al/carbonate and Rb/carbonate ratios suggest the leaching protocol was effective in minimizing contamination from clay minerals on the lithium isotope signals.

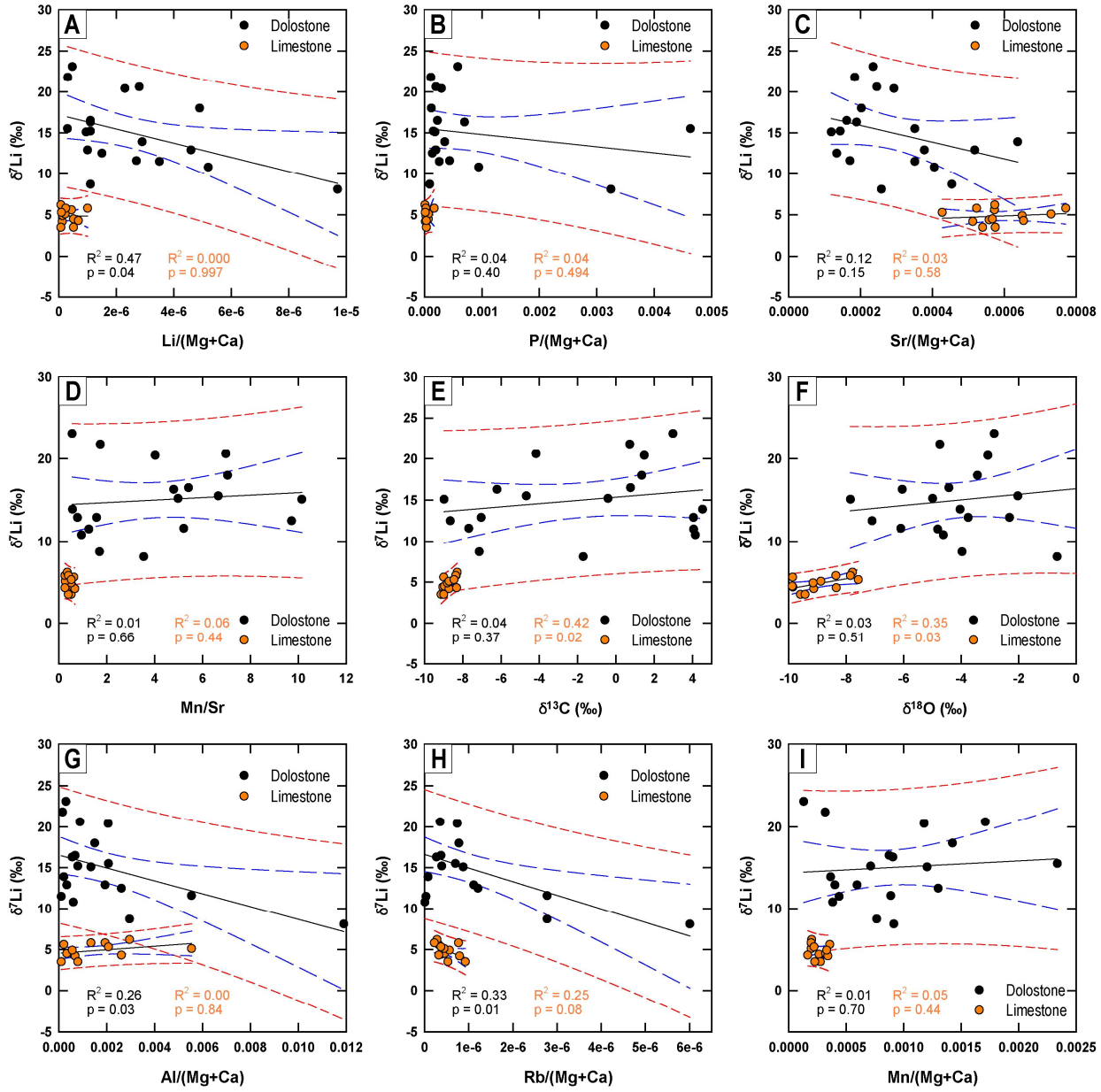


Figure 3.20: Cross-plots of δ^7Li versus other elemental ratios and conventional indicators of diagenesis for the Doushantuo Formation. (A) δ^7Li versus Li/(Mg+Ca). (B) δ^7Li versus P/(Mg+Ca). (C) δ^7Li versus Sr/(Mg+Ca). (D) δ^7Li versus Mn/Sr. (E) δ^7Li versus δ^{13}C. (F) δ^7Li versus δ^{18}O. (G) δ^7Li versus Al/(Mg+Ca). (H) δ^7Li versus Rb/(Mg+Ca). (I) δ^7Li versus Mg/(Mg+Ca). Note, orange represents dolostone and black represents limestone samples. Note, black line is the regression line, blue stippled line is 95% confidence interval, and red stippled line is the 95% predicted confidence interval.

3.5.2: An Alkalinity Anomaly

After properly quantifying the extent of diagenesis and detrital influence in the samples, the δ^7Li values of seawater can be reconstructed to analyze secular changes to the global Li cycle. A fractionation factor of 5 ± 5‰ is applied to limestone samples, based on prior experimental and modern carbonate studies (Marriott et al., 2004a; Marriott et al., 2004b; Pogge von Strandmann et al., 2013; Pogge von Strandmann et al., 2019; Gan et al., *in-preparation*)). For the dolostone samples in the Jiulongwan section, a fractionation factor of 0‰ is applied to samples with Mg/Ca = 0.6. In the Patom Uplift, the δ^7Li_{SW} values range from 7.9‰ to 15.7‰, while the Doushantuo Formation limestone samples range from 8.5‰ to 11.2‰ (± 5‰ for all limestone samples) and the dolostone samples range from 8.1‰ to 23.1‰ (Fig. 3.21).

Understanding the processes that exert control over Earth's carbon cycle on geological timescales is imperative in understanding the primary cause of major climatic perturbations throughout Earth's history. The weathering of silicate rocks, mid-ocean ridge hydrothermal alteration, and reverse weathering all exhibit first-order control over the δ^7Li composition of the ocean, which can be used to better understand Earth's surface processes during periods of major environmental changes (Murphy et al., 2022). δ^7Li values of concomitant seawater during non-steady state intervals, like the SE, provide a means of quantifying the underlying triggers of the perturbation. Assuming the dolostone samples reflect contemporaneous seawater chemistry, the high δ^7Li (~13.1‰) in the pre-SE interval suggests an incongruent weathering regime with an intermediate W/D ratio and clay mineral formation on land, resulting in a riverine flux with higher δ^7Li. This incongruent weathering regime would have been sustained through a warm, tropic-like climate that favored chemical weathering over physical weathering, promoting the highly fractionated carbonate δ^7Li values (Yin et al., 2023).

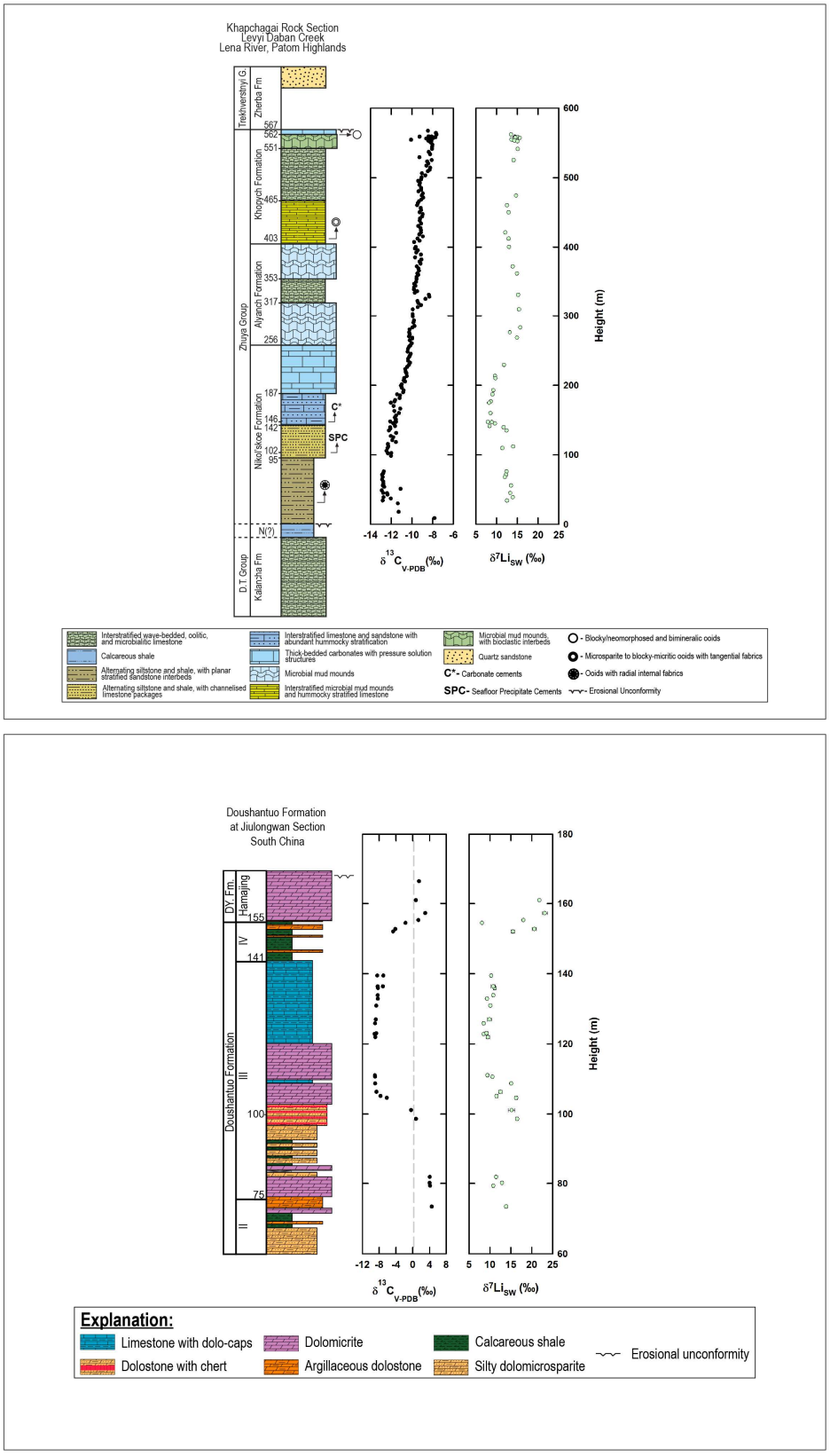


Figure 3.21: Stratigraphy and chemostratigraphy of the Zhuya Group and Doushantuo Formation. (Top) $\delta^{13}C$ and reconstructed seawater $\delta^{7}Li$ of the Zhuya Group. (Bottom) $\delta^{13}C$ and reconstructed seawater $\delta^{7}Li$ of the Doushantuo Formation.

The nadir of the δ^7Li excursion requires a combination of a high riverine flux with very light δ^7Li values, driven by intense weathering congruency on land, and either very rapid reverse weathering in the oceans or no reverse weathering at all. It has been postulated that prior to the advent of silica biomineralizers, the Precambrian oceans were highly saturated with respect to Si, which would have invoked the rapid formation of authigenic clays, driving a decrease in the fractionation of seawater Li isotopes (Tarhan et al., 2016). To get such low δ^7Li values, a shift towards a more congruent weathering regime characterized by either low W/D, which favors physical weathering over chemical weathering, or a high W/D, which favors chemical weathering over physical weathering, would have to occur. The latter scenario is unlikely as while it would result in low δ^7Li compositions, the signal would be buffered by hydrothermal fluids inducing a more stable δ^7Li signal (Yin et al., 2023). Furthermore, high W/D typically occurs in stable tundras or rainforests in the modern environment, which is unlikely to have occurred during the SE (*cf.* Gan et al., *in-preparation*). Therefore, the likely scenario is that the assembly of Gondwana and the physical weathering of freshly uplifted and exposed continental rock promoted a highly congruent (low W/D) weathering regime. This would have facilitated the intense dissolution of primary rock relative to secondary mineral formation, driving the δ^7Li of riverine waters towards more crustal values. An amplified weathering regime would have also delivered reactive silica to the already Si-rich oceans, prompting the rapid formation of authigenic clays, muting the fractionation between clay minerals and seawater during reverse weathering. Additionally, the buildup of DIC through continental weathering would have driven the supersaturation of $[CO_3^{2-}]$ and thus enhanced the alkalinity of the SE oceans, stimulating the rapid accumulation and deposition of massive carbonate platforms along continental margins.

The SE as an alkalinity anomaly is supported by numerous sedimentological indicators that are unique as they only occur during periods of high carbonate saturation (Fig. 1.5 on page 17; Gan et al., *in-preparation*). Throughout the Zhuya Group, large ooids (average 250-300 μm in diameter) of three different morphologies are preserved, as well as large grapestones, indicating precipitation under supersaturated conditions with respect to carbonate ion and increasingly agitated conditions, allowing the coated grains to remain in suspension (Fig., 3.9; Bathurst, 1975; Trower et al., 2017). In addition to the large ooids, aragonite seafloor precipitate fabrics are preserved in the middle Nikol'skoe Formation, similar to those of the Archean, some Neoproterozoic cap carbonate facies, and the basal Triassic (*cf.* Grotzinger and Knoll, 1995). Aragonite precipitate fabrics resemble 'blades of grass' growing out of the seafloor as their growth is seemingly based on the overgrowth of pre-existing crystal surfaces, which is thermodynamically favorable under supersaturated conditions (Bathurst, 1968). Furthermore, plate breccias and intraclasts are preserved at several stratigraphic intervals, the clasts of which appear to be composed of previously cemented seafloor that was ripped up, likely during a storm event or turbidites in this deep-water setting, and rapidly re-deposited. Lastly, the biomineralized remains of sponge-grade organisms in the Khopych Formation reef complex supports a biological response to the massive influx of salts and ions to the SE oceans. The stratigraphic distribution of the biomineralized organisms following the nadir of the SE suggests that the alkalinity anomaly may have forced the evolution of biomineralization in early metazoans due to the very high [CO_3^{2-}] in the SE oceans.

Concurrent with the sedimentological indicators of high carbonate saturation in the SE oceans, numerous geochemical indicators support the alkalinity anomaly, including preliminary $\delta^{88}Sr$ data from the Patom Uplift (*cf.* Gan et al., *in-preparation*). During carbonate precipitation,

the lighter ^{86}Sr is preferentially incorporated, driving residual seawater towards heavier $\delta^{88}Sr$, with the fractionation between carbonate and seawater growing with increasing precipitation rates (Böhm et al., 2012; Wang et al., 2023). Within the Patom Uplift, the $\delta^{88}Sr$ data is defined by a monotonous rise towards increasingly heavier values, with a prominent plateau starting around 300 m (Fig. 3.4 on page 50). However, if the SE reflects a global alkalinity anomaly characterized by supersaturated oceans with respect to carbonate, the expected rapid precipitation of carbonates under these conditions would likely drive the $\delta^{88}Sr$ of global seawater and concomitant carbonates towards heavier values, with authigenic carbonates formed in high alkalinity pore waters serving as the sink for the light Sr. Therefore, the interpretation of the $\delta^{88}Sr$ data in the Patom Uplift may have two potential explanations: 1.) Large-scale incorporation of authigenic carbonate resulted in depleted $\delta^{88}Sr$ in the Nikol'skoe Formation, that gradually decrease with stratigraphic height, or 2.) Local precipitation rates influenced the $\delta^{88}Sr$ values observed in the Nikol'skoe Formation up to 300 m where the plateau in $\delta^{88}Sr$ may reflect that of the global Ediacaran seawater, which became increasingly enriched in ^{88}Sr due to the rapid and widespread uptake of ^{86}Sr in precipitating carbonates early on in the SE. Coincident with the rising $\delta^{88}Sr$ values, the C and O isotopes display a clear covariation in the Patom Uplift (r^2=0.74; $p<0.001$; n=192), and the Doushantuo Formation (r^2=0.67; $p<0.001$; n=32), that has previously been attributed to meteoric and burial diagenesis (Fig. 3.22; Knauth and Kennedy, 2009; Derry, 2010). However, precipitation experiments on foraminifera by Spero et al. (1997) reveal that with increasing carbonate saturation and pH, a 'vital effect' is produced that drives the covariance and subsequent depletion of C and O isotopes. The depletion and covariation of the carbon and oxygen isotopes may reflect disequilibrium in the SE oceans that were promoted by elevated carbonate saturation, favoring rapid precipitation and elevated pH which drives an increase in isotopically light CO_3^{2-} in the calcifying solution

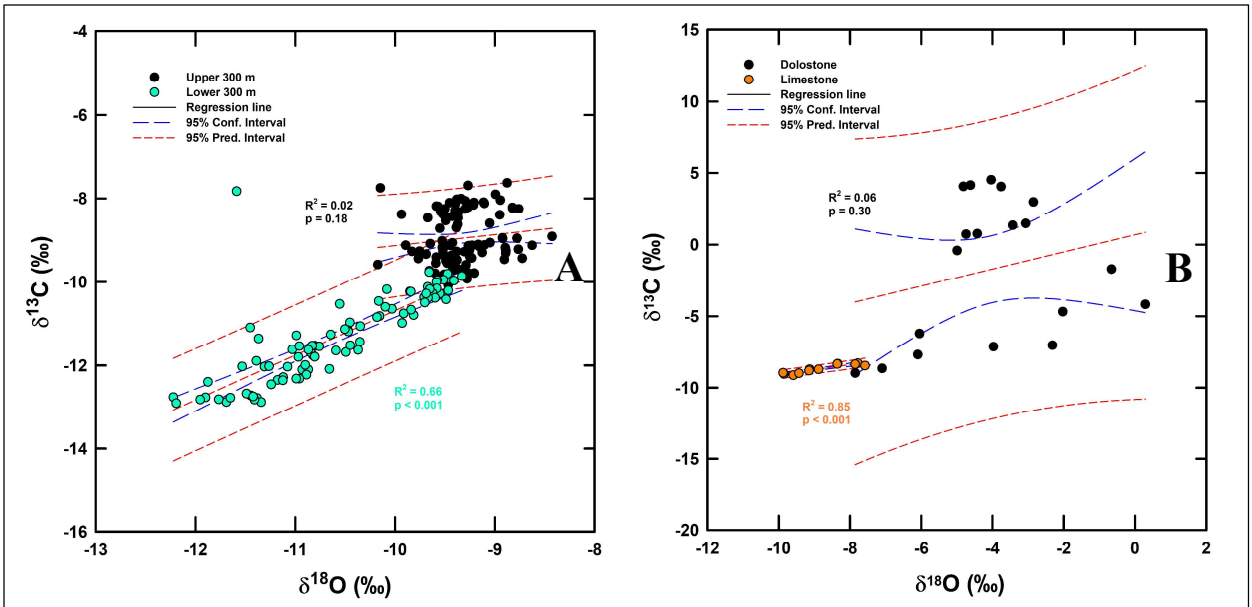


Figure 3.22: (A) Cross-plot of $\delta^{13}C$ versus $\delta^{18}O$ to highlight the coupling in the lower 300 m (r^2=0.66; p<0.001) of the Zhuya Group and de-coupling in the upper 300 m ((r^2=0.02; p=0.18). (B) Cross-plot of $\delta^{13}C$ versus $\delta^{18}O$ to highlight the coupling in the limestones (r^2=0.85; p<0.001) of the Doushantuo Formation and the decoupling in the dolostones (r^2=0.06; p=0.30).

(Usdowski and Hoefs, 1993; Zeebe, 1999, 2007; Erez, 2003; Grinstein et al., 2004; Bentov and Erez, 2006; Gabitov et al., 2012). The decoupling of the carbon and oxygen isotopes at 300 m coincident with the plateau in $\delta^{88}Sr$, may reflect the gradual transition towards equilibrium following the initial alkalinity event.

To drive a large-scale alkalinity anomaly, a combination of the following two processes must be in play: 1.) The widespread anaerobic respiration of DOC would drive a major increase in carbonate saturation, although the immediate effect of these processes is the dissolution of carbonate, followed by the precipitation of authigenic carbonate (Cui et al., 2017), and 2.) Intense congruent weathering, which would deliver blankets of sediments, salts, ions, oxidants, and nutrients to the oceans driving both seawater and carbonate δ^7Li towards more crustal values. The CAP values reported in Dodd et al. (2023) and from this study are consistent with elevated nutrient delivery in the early stages of the SE. An influx of key nutrients, like P, would be accompanied by an increase in primary productivity in the oceans. While increased productivity would aid in driving an alkalinity anomaly, the effects on redox would be more apparent (Cañadas et al., 2022;

Dodd et al., 2023), thus the latter scenario is likely the main driver of the alkalinity event, which is corroborated by the δ^7Li values measured on both the Patom Uplift and Jiulongwan sections.

3.6: Conclusions

Novel lithium isotope data from two widely separated Shuram Excursion successions reveal a pronounced shift from an incongruent weathering regime, consistent with secondary clay mineral formation and reverse weathering, to a congruent weathering regime defined by intense physical and chemical weathering paired with rapid reverse weathering, driving carbonate δ^7Li values towards the crustal average. This shift in weathering congruency provides substantial evidence that the SE was a global alkalinity anomaly driven by the supersaturation of carbonate in the Ediacaran oceans, prompting widespread precipitation and deposition of massive carbonate complexes along continental margins. Sedimentological indicators in the Patom Uplift support this weathering origin through the presence of massive ooids and grapestones, aragonite precipitate fabrics, vertical sheet crack cements, plate breccias, as well as evidence for early animal biomineralization. Consistent with the sedimentological indicators of carbonate supersaturation and rapid precipitation lie the coupling and subsequent decoupling of carbon and oxygen isotopes, as well as the novel yet preliminary δ^{88}Sr data from the Patom Uplift, suggesting widespread, rapid precipitation of carbonate during the SE. The alkalinity anomaly appears to be defined by the interval in which the carbon and oxygen isotopes are coupled, after which they decouple, signifying a return to steady state conditions, likely promoted by a decrease in weathering intensity and the slowing of reverse weathering in the oceans.

Chapter 4: A Multi-Proxy Redox Study of the Shuram Excursion in Siberia

4.1: Abstract

Uranium isotope evidence from a global distribution of Shuram Excursion (SE) successions reveal a pronounced positive shift in $\delta^{238}U$ values of approximately +0.4‰ in carbonates shortly after the onset of the negative carbon isotope excursion. High resolution stratigraphic uranium isotope analyses from a SE succession in Siberia are consistent with previous results from a regionally equivalent succession indicating ventilation of the basin. Global ventilation based on successions worldwide was conceivably driven by enhanced tectonic uplift and weathering during the middle Ediacaran Period associated with the assembly of Gondwana and a highly congruent weathering regime interpreted from $\delta^{7}Li$ compositions of SE limestones in Siberia and South China. Weathering fluxes from the continents would have accelerated the delivery of large quantities of oxidants, sediments, ions, salts, and nutrients to the oceans, stimulating the anaerobic oxidation of a large DOC reservoir. As the oxidation of the DOC pool continued, the mass release of ^{13}C-depleted DIC drove $\delta^{13}C$ values of coeval seawater to a minimum of -12‰ while the nutrient inventory built up in the oceans. The growth of the nutrient reservoir would have stimulated primary productivity resulting in an organic rain to the sediments accompanying enhanced sediment accumulation rates. In addition, the discovery of sponge-grade animals in the Siberian succession suggests an alternative path towards seawater oxygenation, with the metabolic activity of these simple animals that filter seawater, connecting the planktonic and benthic realms by consuming photosynthetic organic matter and thereby allowing oxygen to build up in the water column. Despite the global ventilation signal, the local redox architecture is

complex and oscillatory. High productivity on the distal slope likely formed an oxygen minimum wedge in the lower slope and shelf environments of the Zhuya Group while the upper slope environments remained oxidizing. The utilization of local and global redox proxies in an exceptionally well-preserved SE succession provides a unique opportunity to explore plausible connections between the tectonic, oceanographic, and biological worlds immediately prior to the appearance of the Ediacaran biota.

4.2: Introduction

The high oxygen demand for most complex eukaryotic organisms is what may have inhibited the appearance of macroscopic animals in the fossil record until the late Neoproterozoic Era (Nursall, 1959). Throughout much of the Precambrian, the oceans transiently shifted between ferruginous, resulting from the low levels of atmospheric oxygen and low levels of sulfate, and euxinic (Holland, 1982; Canfield et al., 2008), occasionally interspersed with brief periods of oxygenation (Frei et al., 2009; Partin et al., 2013). Prior to the advent of the first metazoans, a marked shift in the oxidation state of the oceans may have provided an environment conducive to the subsequent evolution and widely-accepted appearance of metazoan life during the Ediacaran Period (Berkner and Marshall, 1965; Knoll, 1992; Derry et al., 1992; Kaufman et al., 1993; Knoll, 2003). One of the key proteins that serve as the main component of metazoan extracellular matrices is collagen, a triple helical structured protein that binds cells and cellular components and requires oxygen from molecular O_2 for biosynthesis (Fujimoto and Tamiya, 1962; Prockop et al., 1963; Mills and Canfield, 2014). Previous studies to quantify the oxygen requirement for the initiation of collagen synthesis have cited the Michaelis-Menten kinetic value of 3×10^{-5}M O_2 (or 13% PAL or Present Atmospheric Level), where the reaction is only at half of the maximum rate, meaning that collagen synthesis can occur at lower O_2 levels, although the minimum threshold is still poorly

constrained (Towe, 1970; Mills and Canfield, 2014; Cole et al., 2020). Given the relatively low oxygen requirements for collagen synthesis, early metazoans were likely tolerant of low oxygen conditions (Cherry et al., 2022). Some simple animals, notably sponges, can survive under very low levels of oxygen, between 0.4-4.0% PAL (Mills et al., 2014). Previous molecular clock estimates have placed the appearance of sponges at nearly 800 Ma (Peterson et al., 2004; Peterson and Butterfield, 2005; Love et al., 2009; Maloof et al., 2010; Dohrmann and Wörheide, 2017; Xiao, 2020). If correct, their role in shaping the redox framework of the late Neoproterozoic may have been significant given their ability to filter massive amounts of water and sequester organic matter and metals, thereby clarifying the water column and allowing oxygen to build up in seawater. Transient oxygenation episodes during the late Neoproterozoic may have been stimulated by increased productivity and the potential evolution of early sponge-grade animals, brought about by enhanced nutrient delivery from the intense weathering of the continents. The lithium isotope evidence supports a highly congruent weathering regime on the continents during the assembly of Gondwana, resulting in the trafficking of key oxidants (like SO_4^{2-}, Fe^{2+}, NO_3^-) and critical nutrients (like P). The enhanced delivery of bio limiting nutrients would have driven an increase in primary productivity along continental margins, providing a mechanism for the oxidation of the large DOC pool in the Ediacaran oceans, thereby resulting in the negative shift in $\delta^{13}C$ as observed during the SE. The increased efficiency of organic matter export and burial during the SE, enhanced by the activity of sponge-grade animals, may have driven an ephemeral rise in molecular oxygen in the oceans that promoted their ventilation during the Shuram Excursion.

The redox architecture of the Ediacaran oceans was likely characterized by persistently ferruginous conditions in the deep ocean with perhaps a shallow oxic layer following the last of

the ‘Snowball Earth’ ice ages (Canfield et al., 2007). Based on pyrite morphology, trace metal abundances, iron-speciation analyses, and sulfur isotope signatures, Sahoo et al. (2016) suggested that the oxidation state of the Ediacaran Period was more dynamic with evidence for a major middle Ediacaran oxygenation event associated with the SE (see also Canfield et al., 2007; 2008; Xiao et al., 2016). Through this event sulfur isotope abundances reveal decreasing stratigraphic trends in both $\delta^{34}S_{pyrite}$ and $\delta^{34}S_{CAS}$ that are attributed to a growth in the sulfate reservoir via sulfide oxidation in the oceans and the delivery of sulfate from the continents via oxidative weathering processes (Fike et al., 2006; Kaufman et al., 2007; Shields et al., 2019). Furthermore, SE sulfate triple oxygen isotope data ($\Delta^{17}O$) from three separate paleocontinents reveals anomalous levels of ^{17}O depletion, the unique fingerprint of which is derived from atmospheric oxygen (Wang et al., 2023).

Redox-sensitive elements (RSEs) are excellent proxies for oceanic oxygenation because they are preferentially incorporated into reducing sediments. Under pervasive anoxia, the concentration of RSEs is muted and closer to the upper continental crust, evidenced by a drop in RSE concentration during Phanerozoic OAEs (Hetzel et al., 2009; Owens et al., 2012). Therefore, under more ventilated conditions, the concentration of RSEs hyperaccumulate in reducing sediments and the concentration of dissolved RSEs increases significantly, with carbonates effectively capturing this signal. During the SE, major enrichments are observed in redox-sensitive elements such as Mo, U, and V in black shales (Sahoo et al., 2016). Novel uranium isotope studies on several SE carbonate successions have revealed a stepwise shift of roughly +0.40‰ during the SE (Zhang et al., 2019; Li et al., 2020; Cao et al., 2020; Gong et al., 2023). Under expanded euxinic conditions the soluble U(VI) is reduced to the insoluble U(IV), which is preferentially enriched in

^{238}U and incorporated in reduced sediments, whereas under contracted euxinia, carbonate $\delta^{238}U$ shifts towards heavier values (Brennecka et al., 2011).

Despite a plethora of evidence in support of SE ventilation, recent $\varepsilon^{205}Tl$ data paired with muted RSE enrichments from shales within two SE successions suggest that the lack of Mn-oxide burial supports an ocean dominated by anoxic bottom waters. This data questions the extent, if any, of oceanic oxygenation during the SE (Ostrander et al., 2023). However, Tl isotopes are at best an indirect proxy for the extent of seafloor anoxia, and fluctuations in local redox conditions paired with very high sedimentation rates could drive the dilution of RSEs in mud rocks (Kunert and Kendall, 2023; Remírez et al. 2024). To further address the redox state of SE ocean water, this study presents high resolution stratigraphic U isotope, Ce anomaly, and trace element data on the exceptionally preserved Zhuya Group carbonates from the Patom Uplift in Siberia. Previous analyses of Patom Uplift carbonates by Zhang et al. (2019) revealed a positive shift in $\delta^{238}U$ values that is remarkably consistent with other SE-bearing successions, but the record was discontinuous. Samples from this study were collected from a different outcrop belt and sampled at roughly 3 m intervals from the nadir of the excursion through the climbing limb, just below an erosional unconformity at the top of the Khopych Formation that truncates the excursion. The objective of this study is to analyze the carbonate $\delta^{238}U$ from this exceptionally well-preserved succession, including in the reef complex where the biomineralized sponge-grade animal fossils were discovered. Furthermore, to evaluate the local redox conditions and how they may have partially influenced the carbonate $\delta^{238}U$ record, the use of cerium anomalies will be employed. Cerium is the only REE (besides Eu) that exists outside of the trivalent oxidation state. In the presence of oxygen, Ce(III) is oxidized to Ce(IV) and scavenged by Mn(oxyhydr)oxides, where it no longer participates in solid-solution exchange reactions, imparting a depletion in seawater relative to the

neighboring REE (German and Elderfield, 1990). By combining well-established global and local redox proxies, the argument on whether the SE represents a global oxygenation event or a globally synchronous authigenic event will be explored.

4.3: Results

The results of the geochemical measurements are presented graphically below and numerically in the form of averages in tables 4.1 and 4.2 and in tables A6 through A9 in Appendix I. Uranium concentrations start at <1 ppm at the base of the Nikol'skoe Formation and rapidly increase with stratigraphic height (Fig. 4.1B). The Alyanch and Khopych formations exhibit higher [U], averaging 4.5 ppm, relative to the Nikol'skoe Formation, which averages 2.1 ppm (Fig. 4.1B). The $\delta^{238}U$ values remain invariant averaging -0.24 ± 0.07‰ until the Khopych reef where there is a notable deviation in the U isotopes throughout the 8 m interval (Fig. 4.1C). The Y/Ho ratios of all samples across the Nikol'skoe, Alyanch, and Khopych formations are all greater than 36, averaging 51.3, with only four samples falling below the cutoff (Fig. 4.1D). For the first ~400 m, the Ce/Ce* is consistently >0.9. Above the 400 m mark, the Ce/Ce* data drops below 0.9 for ~100 m before reaching the reef complex where the Ce/Ce* shifts back to values >0.9 (Fig. 4.1E). The average Ce/Ce* is 1.21 across the entire stratigraphic interval. Manganese concentrations oscillate throughout the Zhuya Group starting with a sharp decline from a maximum in the basal Nikol'skoe Formation before reaching a nadir at the Nikol'skoe-Alyanch boundary. Concentrations rise in the Khopych Formation to approximately 300 ppm before declining in the upper Khopych Formation (Fig. 4.1F).

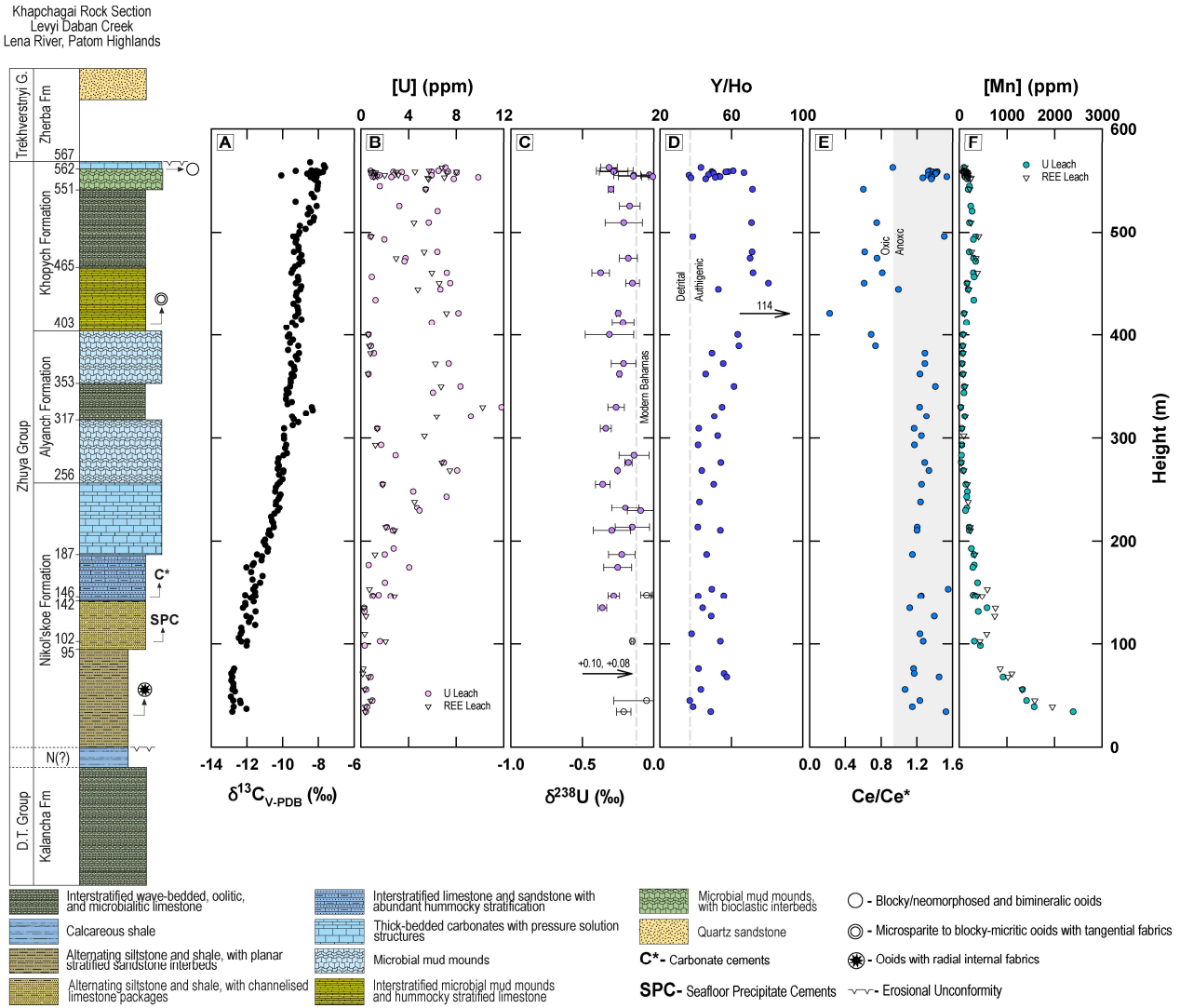


Figure 4.1: Zhuya Group chemostratigraphy. (A) Carbon isotopes measured relative to V-PDB. (B) High [U] signifies excellent preservation and a more aragonite-dominated mineralogy. (C) $\delta^{238}U$ values are consistently around -0.20‰, indicative of a global oceanic ventilation and a reduction in the euxinic reservoir. (D) Y/Ho consistently >36, indicative of an authigenic seawater signal. The Y/Ho may also be interpreted as the rocks having been deposited in an open marine setting, rather than a restricted basin. (E) Ce/Ce* highlights local redox variations with suboxic to anoxic conditions in the first ~400 m of the stratigraphic section, followed by a brief pulse of oxygenation for ~100 m, around 500 m conditions oscillate between anoxic and oxic before shifting back to anoxic in the upper ~30 m. (F) [Mn] exhibits a sharp decline from ~3000 ppm to ~100 ppm at the Nikol'skoe-Chencha Boundary, before slowly climbing to approximately 300 ppm in the middle Chencha Formation, then slowly declines to ~100 ppm.

Table 4.1: Data table of averages the U leach ($\delta^{238}U$ with average 2σ, Mn, Fe, Sr, Mo, Re, U, Mg/Ca, Mn/Sr, U/Al, Mo/(Mg+Ca), and U/(Mg+Ca)) for the Zhuya Group.

Succession	Formation	Height Range (m)	$\delta^{238}U$	2σ	[Mn] (ppm)	[Fe] (ppm)	[Sr] (ppm)	[Mo] (ppm)	[Re] (ppb)	[U] (ppm)	Mg/Ca	Mn/Sr	U/Al (ppm/wt.%)	Mo/(Mg+Ca)	U/(Mg+Ca)
Patom Uplift	Khopych	403-567	-0.24	0.06	241.84	0.17	1670.20	0.06	0.36	4.58	0.04	0.53	70.27	0.00	0.14
	Khopych Reef	551-562	-0.15	0.07	125.82	0.18	1883.39	0.09	0.28	4.07	0.01	0.16	124.53	0.00	0.11
	Alyanch	256-403	-0.24	0.06	72.63	0.15	1032.93	0.05	0.15	4.79	0.01	0.09	139.87	0.00	0.13
	Nikol'skoe	0-256	-0.25	0.08	546.20	0.14	663.35	0.07	0.35	2.09	0.02	1.12	31.69	0.00	0.08

Table 4.2: Data table of averages from the REE leach (Mn, Sr, U, Mg/Ca, Mn/Sr, Ce/Ce*, Y/Ho, Eu/Eu*, MREE/MREE*, and ∑REE) for the Zhuya Group.

Succession	Formation	Height Range (m)	[Mn] (ppm)	[Sr] (ppm)	[U] (ppm)	Mg/Ca	Mn/Sr	Ce/Ce*	Y/Ho	Eu/Eu*	MREE/MREE*	∑REE
Patom Uplift	Khopych	403-567	248.91	1809.28	5.03	0.01	0.39	0.78	68.62	1.11	0.97	1.21
	Khopych Reef	551-562	165.81	1549.62	3.83	0.01	0.20	1.38	51.58	0.98	1.02	2.72
	Alyanch	256-403	81.65	1035.07	4.19	0.01	0.09	1.19	52.17	1.15	1.06	0.42
	Nikol'skoe	0-256	846.39	582.60	1.21	0.01	2.88	1.26	46.63	1.23	1.33	2.16

4.4: Discussion

4.4.1: The Case for a Primary U Signal

On the global scale, uranium isotope values record both ocean oxygenation and deoxygenation events, provided they have not been exposed to post-depositional alteration (Brand and Veizer, 1980; Banner and Hanson, 1990; Jacobsen and Kaufman, 1999; Chen et al., 2018b; Zhang et al., 2020). Uranium is generally sediment-buffered when it comes to alteration due to the low concentrations of U in freshwater systems, although it can still be affected by diagenetic processes (Taylor and McLennan, 1985; Lau et al., 2017; Chen et al., 2018a.). Because U is a redox-sensitive element, the oxidation state of the altering fluid determines its mobility in fluids, thus exhibiting a major control on both the isotopic composition and the concentration of U in marine carbonates. Under reducing conditions, pore waters rich in decayed organic matter or dissolved sulfides can induce fractionation through the reduction of U(VI) to U(IV). This enrichment drives $\delta^{238}U$ towards heavier values in secondary minerals, although because U is immobile following reduction, if the system remains sediment-buffered, the original $\delta^{238}U$ signal may be preserved (Banner and Hanson et al., 1990; Romaniello et al., 2013; Higgins et al., 2018). Conversely, during sea-level low stands, carbonate sediments can be exposed to meteoric waters in both the vadose and phreatic zones, potentially altering the U isotope signal (Melim et al., 2002; Gill et al., 2008; Swart, 2015; Higgins et al., 2018; Zhang et al., 2020). Under oxic conditions, U reduction does not occur, therefore meteoric alteration should not inherently impart a positive fractionation in U isotopes. However, the dissolution and recrystallization of carbonates may alter the original U isotope signature through the preferential remobilization of isotopically enriched U(IV), resulting in lighter $\delta^{238}U$ values in oxic horizons while sediments at the oxic-anoxic

interface would be authigenically enriched in the isotopically heavy U(IV) (Chen et al., 2018a). Furthermore, the mineralogical transition from aragonite to calcite results in a major reduction in U concentration, but imparts a negligible fractionation in $\delta^{238}U$, unless the recrystallization occurs under anoxic conditions, in which case, authigenic enrichment of U(IV) imparts a significant fractionation (Gill et al. 2008; Hardisty et al., 2017; Chen et al., 2018a). The process of dolomitization, although not observed in the Patom Uplift samples, can also impart an appreciable, yet variable, fractionation in U isotopes. However, the consistency in $\delta^{238}U$ compositions between interbedded dolomites and limestones ranging in age from the modern Bahamas to the Permo-Triassic boundary to the Ediacaran suggests that early diagenetic dolomite can retain the U isotope signature of contemporaneous seawater (Romaniello et al., 2013; Brennecka et al., 2011; Lau et al., 2016; Zhang et al., 2019, 2020). Insofar as the U isotope composition of carbonates can be altered through a vast array of diagenetic processes, care should be taken to ensure that the samples selected reveal primary depositional fabrics and have minimal signs of secondary alteration.

The petrographic observations detailed in Chapter 3 highlight the excellent preservation of Zhuya Group limestones, however, there are signs of recrystallization in the Khopych Formation likely associated with the neomorphism of aragonite to low-Mg calcite. The preservation of the three different ooid morphologies that broadly consist with redox boundaries (detailed in subsequent subsections), aragonite seafloor precipitates, and the intraclasts of previously lithified seafloor are exemplary examples of the exceptional preservation of the Zhuya Group with representative samples highlighted in figures 4.2 through 4.5 and figures A1-A4 in Appendix 2. However, while petrographic screening can aid in identifying extensively altered samples, previous precipitation experiments have demonstrated that isotopic differences between abiotic and biogenic carbonates have minimal isotopic differences (<0.1‰), suggesting that $\delta^{238}U$ is not

significantly affected by carbonate mineralogy (Romaniello et al., 2013; Chen et al., 2016, 2018a; Livermore et al., 2020; Martin et al., 2023; Wei and Zhang, 2024). Conversely, early diagenesis of carbonate sediments, which may not be as apparent during petrographic observations, can shift the $\Delta^{238}U_{carbonate\text{-}seawater}$ = ~+0.24‰ to +0.27‰, further emphasizing the importance of quantifying the effects of early-stage diagenesis (Romaniello et al., 2013; Chen et al., 2018b; Tissot et al., 2018; Wei and Zhang, 2024). For this reason, additional geochemical tests are utilized to screen samples for alteration.

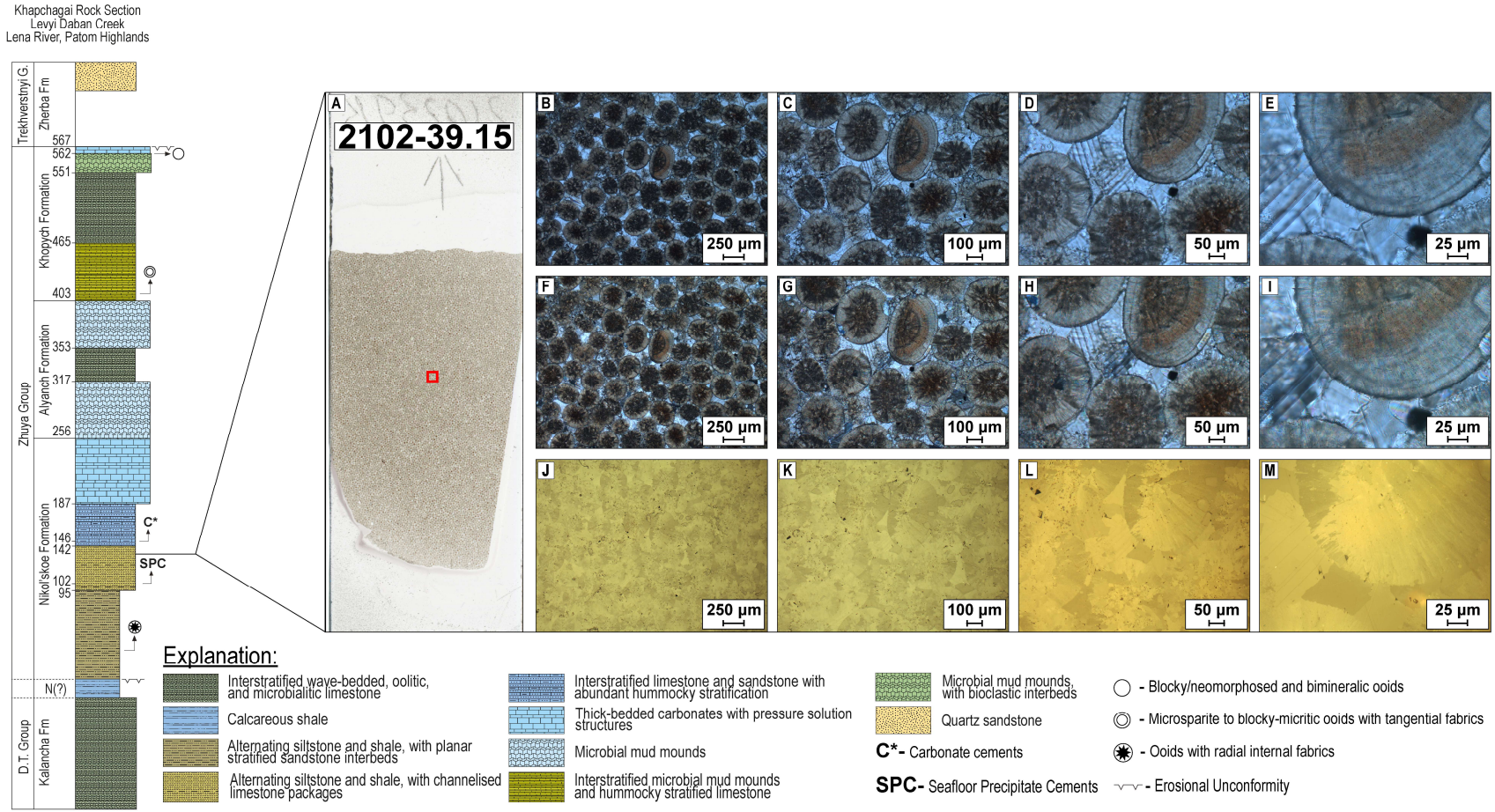


Figure 4.2: Plate of thin section photos from sample 2102-39.15 from the Patom Uplift. (A) Thin section scan. (B, E) Plane-polarized light images of representative ooids from the Nikol'skoe Formation with blocky intraclastic cements, highlighting the overall retention of original fabrics. (F, G) Crossed-polarized light images. (H, I) Reflected light images. Magnifications are 5x, 10x, 20x, and 50x from right to left, respectively.

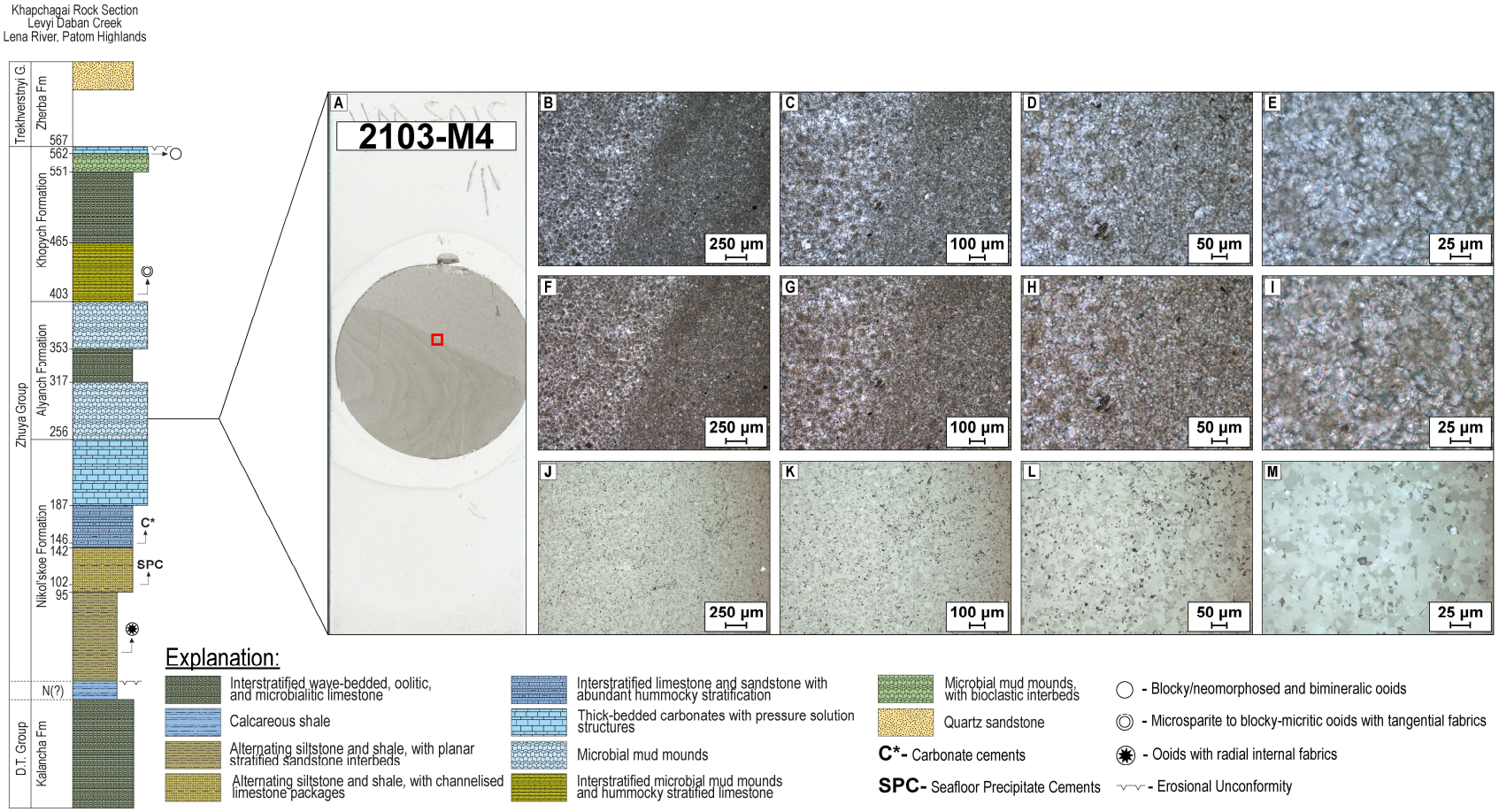


Figure 4.3: Plate of thin section photos from sample 2103-M4 from the Patom Uplift. (A) Thin section scan. (B, E) Plane-polarized light images of the boundary between the micrite and grainstone. (F, G) Crossed-polarized light images. (H, I) Reflected light images. Magnifications are 5x, 10x, 20x, and 50x from right to left, respectively.

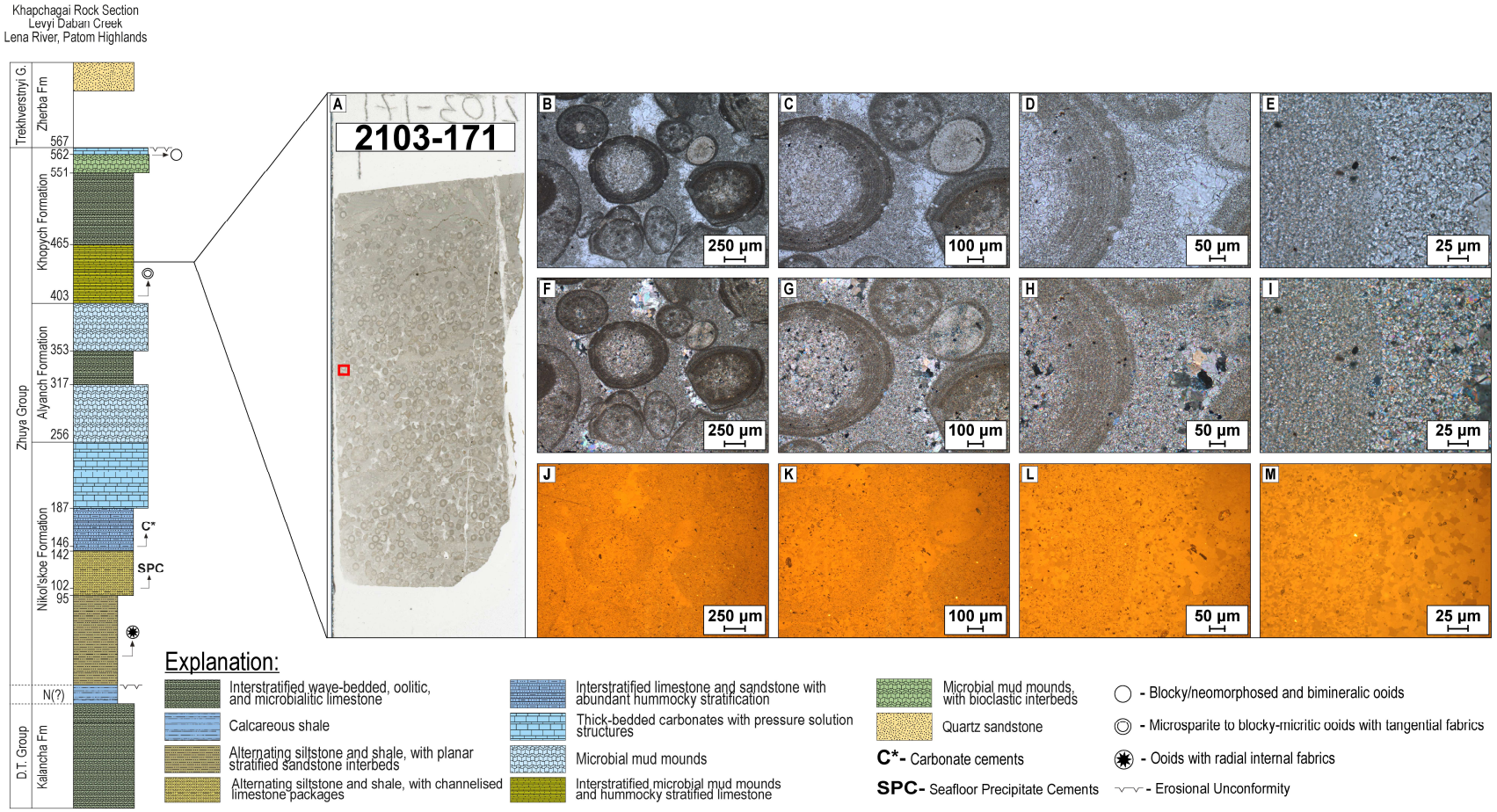


Figure 4.4: Plate of thin section photos from sample 2103-171 from the Patom Uplift. (A) Thin section scan. (B, E) Plane-polarized light images of representative ooids from the Khopych Formation below the reef complex. The ooids are roughly 300 µm in diameter with tangential fabrics and evidence of recrystallization, likely neomorphism of metastable aragonite to low-Mg Ca, though the primary depositional fabrics have been retained. (F, G) Crossed-polarized light images. (H, I) Reflected light images. Magnifications are 5x, 10x, 20x, and 50x from right to left, respectively.

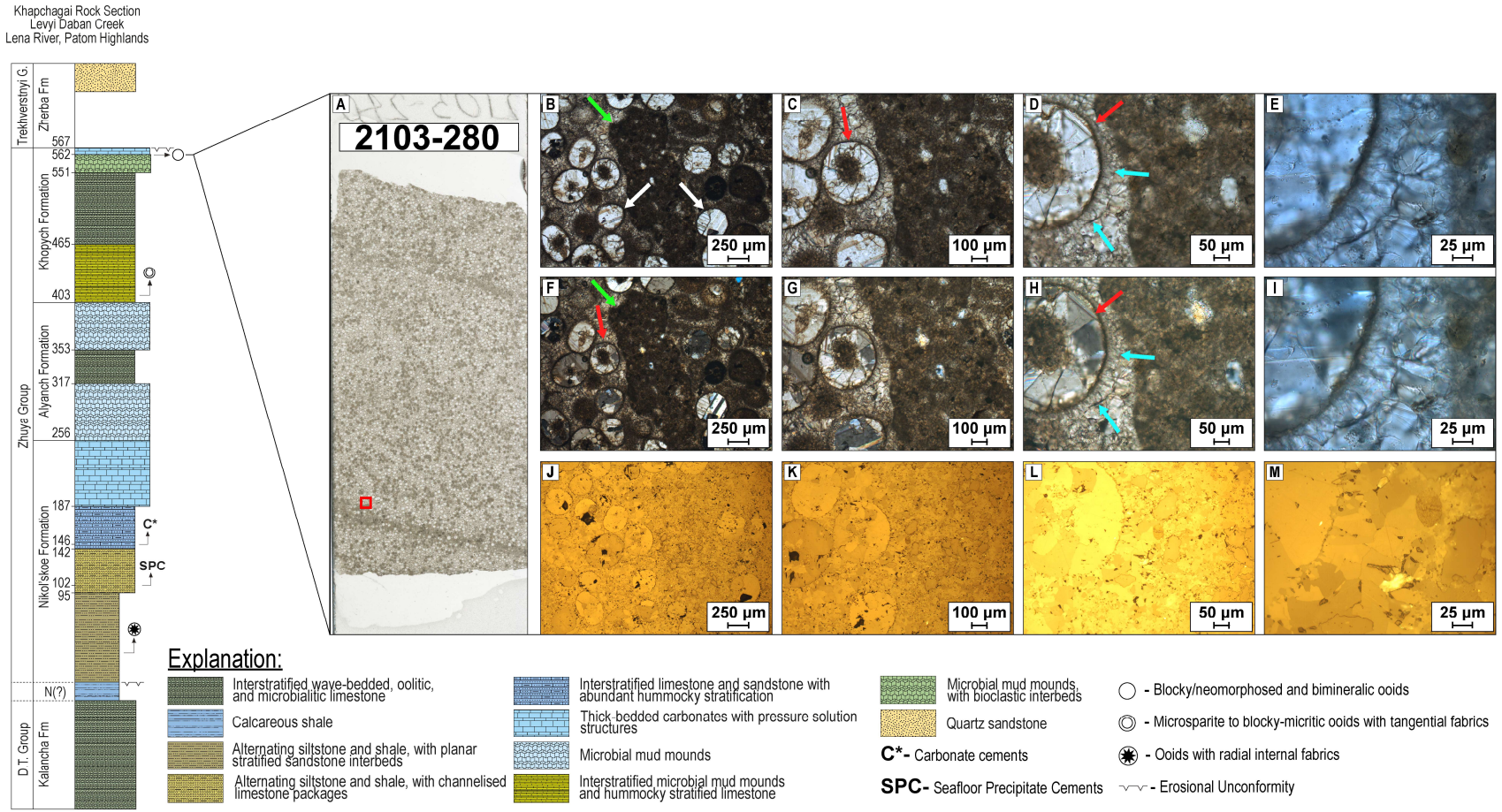


Figure 4.5: Plate of thin section photos from sample 2103-280 from the Patom Uplift. (A) Thin section scan. (B, E) Plane-polarized light images of the diverse ooid assemblage: Single crystal neomorphosed ooids (white arrows); bimineralic ooids (red arrows); and a large grapestone (green arrows). The 10x and 20x photos also highlight the dogtooth cements that surround some of the ooids (blue arrow). (F, G) Crossed-polarized light images. (H, I) Reflected light images. Magnifications are 5x, 10x, 20x, and 50x from right to left, respectively.

As a first pass to screening for post-depositional alteration, samples of secondary sheet crack cements (n=3) as well as samples with Mn/Sr>3 (n=5) were excluded to ensure only samples with minimal alteration were considered, although Higgins et al. (2018) demonstrated that even altered carbonates can have Mn/Sr<1. Furthermore, higher Mn and Fe concentrations can be a primary feature imparted in carbonate minerals from seawater given the lower oxygen and higher dissolved metal concentrations of Proterozoic seawater (Corsetti and Kaufman, 2003; Gilleaudeau and Kah, 2013) such that Mn/Sr might not be the most effective proxy in constraining alteration. $\delta^{238}U$ values were also compared to additional indicators of diagenesis (i.e., $\delta^{18}O$, $\delta^{13}C$, Mn/Sr, Mg/Ca, and [Mn]; see Figure 4.6A, E), but no statistically significant correlation was observed. Following the initial screening for diagenesis, a more extensive screening for authigenic enrichments in response to variable redox conditions was conducted. Because uranium responds to changes in redox, the most effective proxies to test whether the U isotope composition of the carbonates have been authigenically enriched during early diagenesis is through comparison with other redox-sensitive elements (i.e., Re and Mo). High concentrations of these elements may indicate the presence of sulfidic porewaters which are enriched in ^{238}U and thus have the ability to drive $\delta^{238}U$ towards heavier values. As such, the uranium isotope composition of the 32 samples that passed the initial screening were compared to redox sensitive element concentrations (U, Mo, Re, [U]/(Mg+Ca), and [Mo]/(Mg+Ca)) where no statistically significant correlation was observed, although the p-value for both [Mo] and [Re] is close to the cutoff of 0.05 (Fig. 4.6F-J). The lack of correlation between [U] and $\delta^{238}U$ has been noted in numerous studies and can be attributed to differences in carbonate speciation and mineralogy as uranium is partitioned more effectively into the orthorhombic lattice of aragonite, similar to Sr, whereas the trigonal lattice of calcite is less able to accommodate the large U cations (Chen et al., 2016; 2018b).

Lastly, $\delta^{238}U$ compositions can be influenced by detrital contributions from siliciclastic and clay minerals, imparting positive $\delta^{238}U$ signatures and further masking depositional carbonate $\delta^{238}U$ values. To assess the potential influence of detrital uranium on the carbonate signal, [Al] and U/Al (ppm/wt. %) were used as proxies for detrital influence, with no statistically significant correlation observed (Fig. 4.6K, L). Although minor diagenetic variability in [U] and $\delta^{238}U$ is unavoidable, the lack of statistically significant correlations between $\delta^{238}U$ and the various diagenetic proxies supports a primary $\delta^{238}U$ signal in the Patom Uplift carbonates. An offset representing the average $\Delta^{238}U_{carbonate\text{-}seawater}$ of $+0.27 \pm 0.14‰$ from modern carbonate studies was applied to the Patom Uplift carbonate $\delta^{238}U$ values to reconstruct the $\delta^{238}U_{seawater}$ during the SE (Chen et al., 2018b).

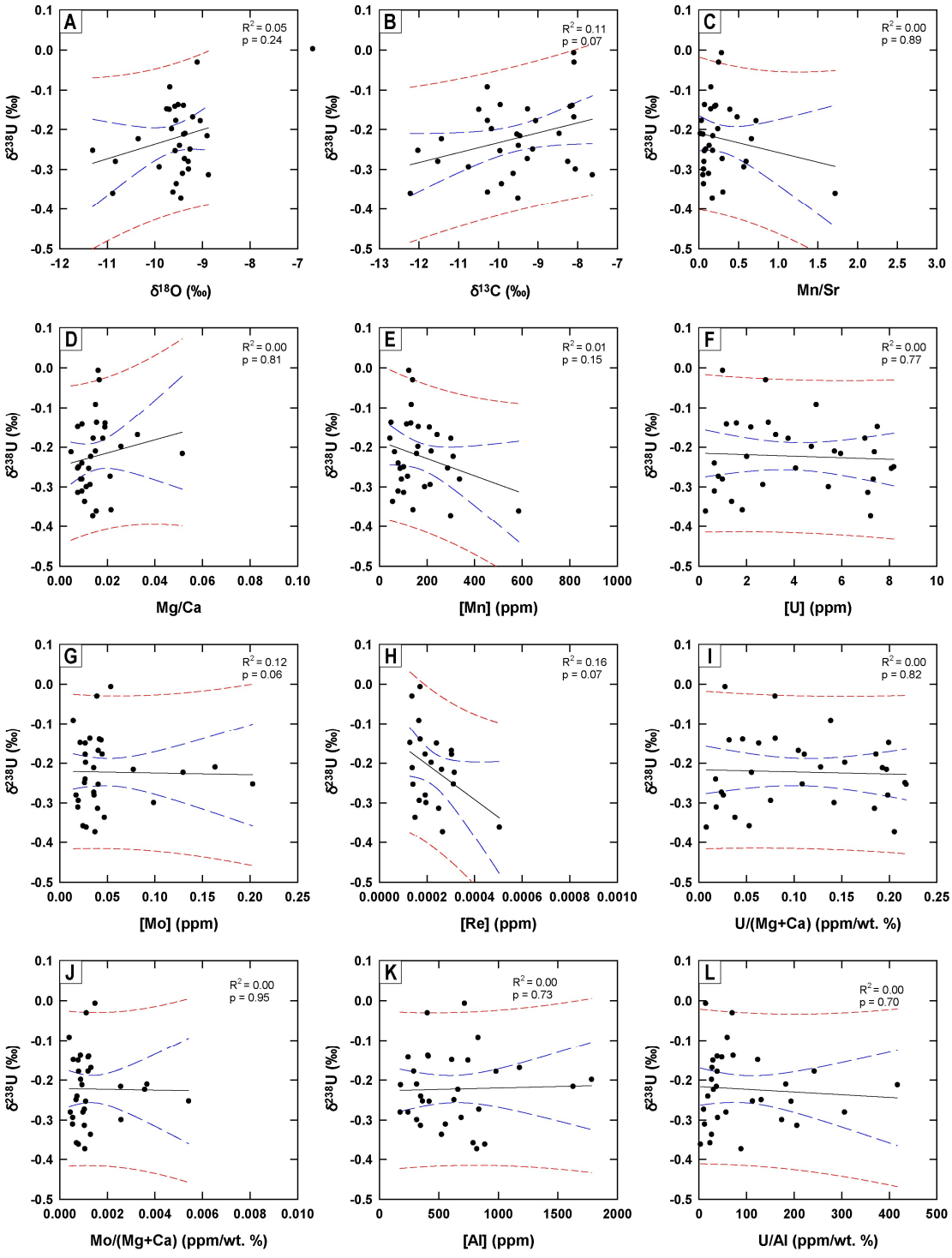


Figure 4.6: Cross-plots of $\delta^{238}U$ versus various proxies for diagenesis. (A) $\delta^{238}U$ versus $\delta^{18}O$. (B) $\delta^{238}U$ versus $\delta^{13}C$. (C) $\delta^{238}U$ versus Mn/Sr. (D) $\delta^{238}U$ versus Mg/Ca. (E) $\delta^{238}U$ versus [Mn]. (F) $\delta^{238}U$ versus [U]. (G) $\delta^{238}U$ versus [Mo]. (H) $\delta^{238}U$ versus [Re]. (I) $\delta^{238}U$ versus U/(Mg+Ca). (J) $\delta^{238}U$ versus Mo/(Mg+Ca). (K) $\delta^{238}U$ versus [Al]. (L) $\delta^{238}U$ versus U/Al. Note, black line is the regression line, blue stippled line is 95% confidence interval, and red stippled line is the 95% predicted confidence interval.

4.4.2: The Case for a Primary REE Signal

Cerium anomalies in carbonates have been effectively utilized in tracking local redox processes in both modern and ancient shallow-marine environments (German and Elderfield, 1990; Webb and Kamber, 2000; Nothdurft et al., 2004). Water column cerium anomalies are captured in carbonate sediments from trivalent REE incorporation into calcite at the Ca^{2+} site, with the charge balance likely maintained by the simultaneous incorporation of Na^{+} (Zhong and Mucci, 1995; Elzinga et al., 2002). In terms of susceptibility to diagenesis, numerous studies on both ancient carbonates and the modern Bahamas have emphasized that carbonates are able to retain the REY signature of the fluid from which they were initially precipitated, assuming late-stage alteration from oxidizing or reducing fluids with drastically different compositions is insignificant (Warren, 2000; Webb et al., 2009; Liu et al., 2019). The dissolution of primary marine carbonates drives the enrichment of REY in pore fluids, although the secondary carbonate minerals that precipitate should not deviate significantly from the original composition, unless precipitation occurs under a very high water to rock ratio or under drastically different compositions due to the structural incorporation of REE in the calcite (or aragonite) lattice (Liu et al., 2019; Tostevin, 2021).

Despite the robustness of carbonate REY signatures and their broad insensitivity to diagenetic modifications, the signal can be complicated by the unintentional addition of REY from non-carbonate phases during leaching. A comparison of leaching techniques by Tostevin et al. (2016) found that only pure (>85%) carbonates serve as effective REY archives. To ensure the carbonate REY phase is targeted, a sequential leach process is utilized to minimize overprinting of the carbonate REY phase by Fe-Mn(oxyhydr)oxides and clay minerals. Prior to data interpretations, samples were screened to ensure that the minimum weight percent carbonate (85%)

and Y/Ho (>36) criteria was met. Out of the 71 REY samples in this study, 5 fell below the 85% carbonate threshold while another 9 samples fell below the Y/Ho minimum of 36, with 5 samples measuring below the detection limit for Y. Following the screening, both Ce/Ce* and Y/Ho were compared to several proxies for detrital influence (Al, Zr, and Ti), Fe-Mn(oxyhydr)oxide interference (Mn and Fe), and MREE/MREE* was plotted against ΣREE to determine if MREE enrichment from Fe-Mn(oxyhydr)oxides had altered the carbonate REY signature (Fig. 4.7A-I; Wu et al., 2018). For all the REE data, a lack of statistically significant correlations with the diagenetic and contamination indicators verifies the leach technique was effective in only targeting the carbonate phase and preserving the depositional seawater signal. Further evidence of the effective preservation is in the REY spider plot in figure 4.8A where a slight La anomaly, slightly negative Ce/Ce* anomaly, and positive Y anomaly are preserved, indicating the retention of a seawater signal.

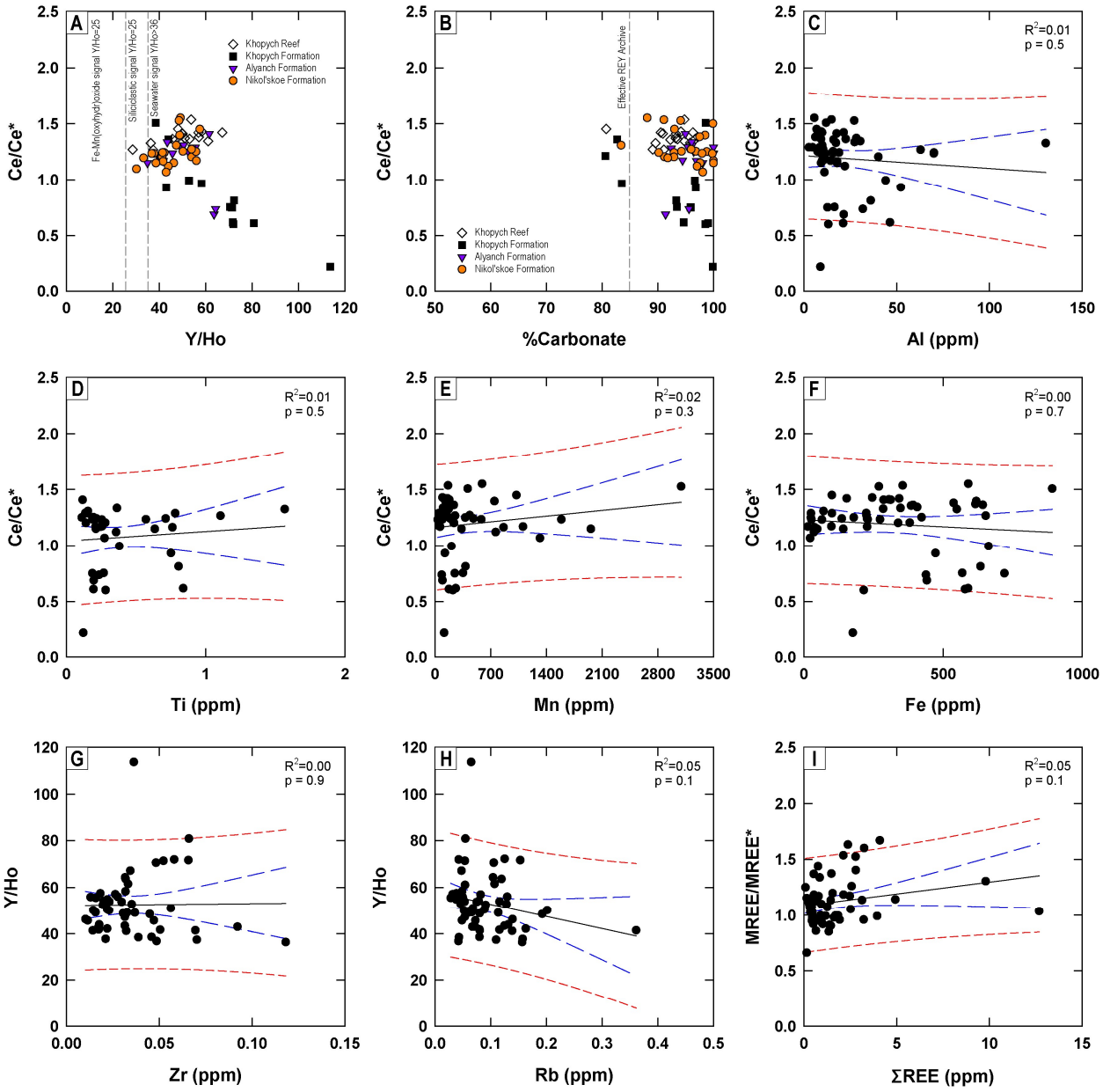


Figure 4.7: Cross-plots of Ce/Ce* and Y/Ho versus various proxies for alteration. (A) Ce/Ce* versus Y/Ho. (B) Ce/Ce* versus % carbonate. (C) Ce/Ce* versus [Al]. (D) Ce/Ce* versus [Ti]. (E) Ce/Ce* versus [Mn]. (F) Ce/Ce* versus [Fe]. (G) Y/Ho versus [Zr]. (H) Y/Ho versus [Rb]. (I) MREE/MREE* versus ∑REE. Note, black line is the regression line, blue stippled line is 95% confidence interval, and red stippled line is the 95% predicted confidence interval.

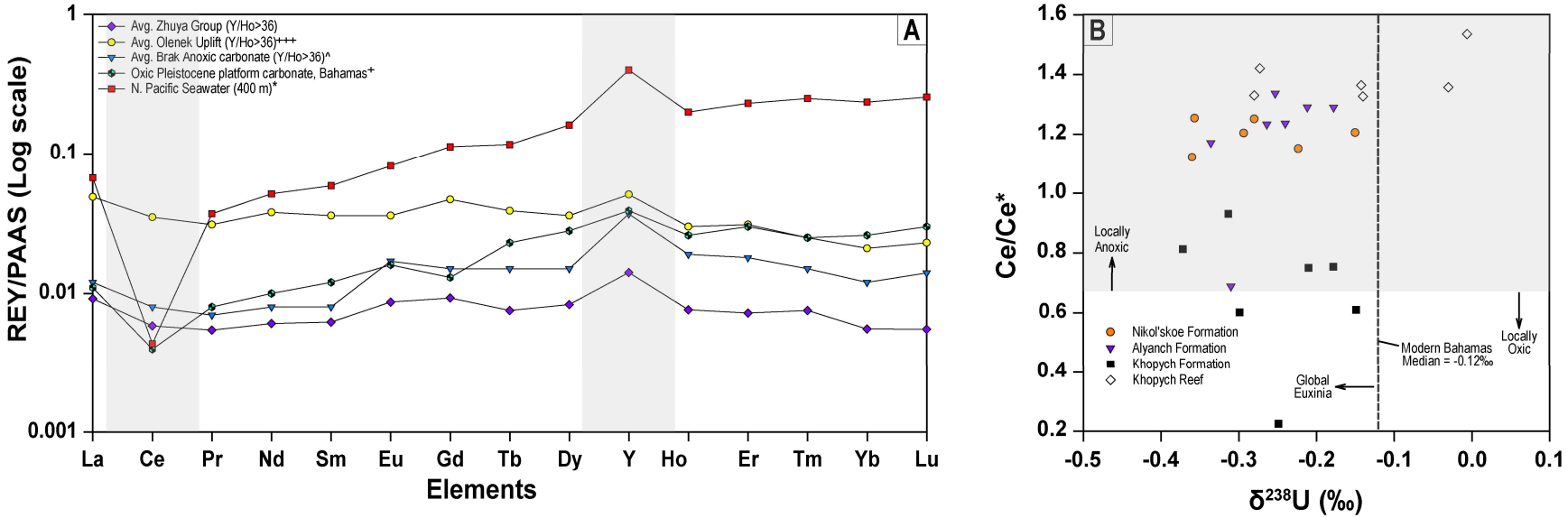


Figure 4.8: (A) REE Spider plot of the average Zhuya Group versus the average Olenek Uplift ($^{+++}$Cherry et al., 2022); Average Brak Section (Nama Group; $^{\wedge}$Tostevin et al., 2017); Average Pleistocene platform carbonate ($^{+}$Liu et al., 2019); and average N. Pacific Seawater from 400 m (*Alibo and Nozaki, 1999). (B) Ce/Ce* versus $\delta^{238}U$ divided by formation.

4.4.3: Global Redox Conditions

Based on the consistency amongst the $\delta^{238}U$ data from 6 geographically disparate SE successions (Doushantuo Formation at Jiulongwan and Siduping sections in South China, Patom Uplift of Siberia, Johnnie Formation in Death Valley, USA, Wonoka Formation of South Australia, and the Clemente Formation in NW Mexico), the SE represents a global ventilation event (Zhang et al., 2019; Li et al., 2020; Cao et al., 2020; Gong et al., 2023; Fig. 4.9). The step-wise increase in U isotope values occurs broadly coincident with the initial onset of the downturn in $\delta^{13}C$, although estimates place the maximum of the $\delta^{238}U$ increase approximately 0.8 ± 0.04 Myr after the onset of the negative CIE assuming sedimentation rates remained constant (Li et al., 2020). Grasping the timing of these events is important because in order to rapidly transition from a predominantly ferruginous ocean to near-modern levels of ventilation, oxygen has to build up both within these depositional basins and globally. During the SE, the remineralization of a massive DOC pool via anaerobic processes is purported to have driven the controversial negative carbon isotope anomaly (Rothman et al., 2003; Fike et al., 2006; Kaufman et al., 2007; McFadden et al., 2008; Grotzinger et al., 2011). However, to sustain the oxidation of the large DOC pool, a steady stream of oxidants (SO_4^{2-}, NO_3^-,

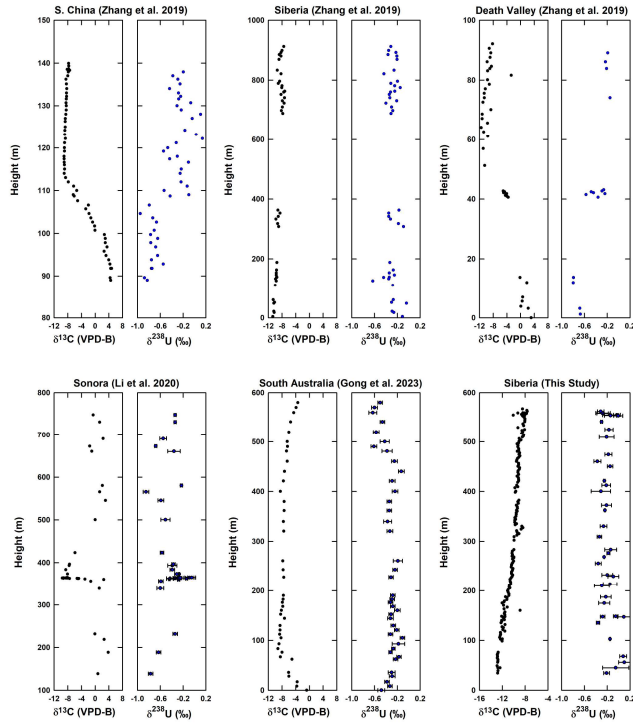


Figure 4.9: Global correlation between 6 different U isotope studies on 5 geographically distant SE successions. All of the successions exhibit a similar step-wise increase of roughly +0.4‰ towards a steady $\delta^{238}U$ signal of roughly -0.25‰ within the SE-interval before shifting back to near pre-SE values.

Mn(III/IV), or Fe(II)) is required. Prior studies combined with the novel Li isotope data presented in chapter 3 have revealed that throughout the SE, intense continental weathering associated with the suturing of Gondwana and the buildup of the Trans-Gondwanan super mountain range delivered the necessary materials to trigger the oxidation of the DOC pool. The remineralization of the DOC pool would have released organic-bound carbon and nutrients, which would aid in anaerobic processes and convert ^{13}C-depleted DOC to ^{13}C-depleted DIC that would be incorporated into carbonate sediments as primary precipitates and authigenic cements (Schrag et al., 2013; Cui et al., 2017). The release of nutrients would stimulate primary productivity, providing a mechanism for building up oxygen and ventilating the oceans.

The most efficient process to build up oxygen is through the sequestration and burial of organic matter and pyrite (Kasting and Canfield, 2012). While the first order control on organic carbon burial is sediment accumulation rate (Derry et al., 1992; Kaufman et al., 1993), the discovery of sponge-grade animals in the Khopych reef complex provides a potential biological mechanism for organic matter sequestration. Insofar as modern sponges are able to filter massive amounts of water, sequestering organic matter (both DOC and POC) as well as metals (which can be utilized in the metabolic reactions of their microbial symbionts), they promote the clarification of the water column (enhancing photosynthesis at depth) and link the pelagic and benthic realms through ecosystem engineering (Pile and Young, 2006; de Goeij et al., 2013; Cathalot et al., 2015). By removing the reduced product of photosynthesis, molecular oxygen could build up in the SE water column, thereby enhancing the activity of aerobic organisms and potentially explaining the ventilation of the SE oceans. In concert, the stimulation of primary productivity through weathering processes and of remineralization of a standing DOC pool by both aerobic and anaerobic microbes coupled with the increased efficiency of organic matter export by sponge-

grade animals would have allowed oxygen to build up in the oceans. Thus, the combined effects of weathering and biology are the likely drivers of a profound ventilation event as observed by the positive shift in U isotope data.

The ventilation of the SE oceans could be explained by intense congruent weathering on land, supported by the low δ^7Li data throughout the nadir of the SE from two distant successions, which would have delivered the necessary oxidants to stimulate the anaerobic conversion of DOC to DIC. The oxidation of the DOC pool would release: 1.) Organic-bound ^{13}C-depleted DIC, diluting the global DIC reservoir, which would be reflected by the profoundly negative $\delta^{13}C_{carb.}$ values; 2.) Key limiting nutrients like P and N, stimulating aerobic metabolisms and driving the production of ^{13}C-depleted CO_2, which would evade to the atmosphere providing a short-term feedback to further aid in weathering on land that would deliver isotopically light DIC to the oceans. As the DIC pool waxes and the DOC pool wanes, the δ^{13}C values would gradually recover towards pre-event values, and the shift towards a more incongruent weathering regime (evidenced by the gradual rise in δ^7Li values in the Zhuya Group) diminished the flux of continental material to the oceans. Once the large DOC pool had been largely exhausted, the gradual decline in sedimentation rates (evidenced by the steady and positive δ^{88}Sr signal) and OM export would restore the widespread anoxic conditions (Dodd et al., 2023).

4.4.4: Local Redox Conditions

While the U isotope evidence suggests that the global oceans were characterized by a stable, well-ventilated state, the redox architecture of local shelf environments remained dynamic. The pervasively positive Ce/Ce* values combined with elevated Mn concentrations suggests that low oxygen conditions favored the reductive dissolution of Ce(IV) and Mn(oxyhydr)oxides, promoting the incorporation of Ce and Mn^{2+} into carbonate allochems and cements. However, the

exact oxygen levels are relatively ambiguous insofar as Mn(IV) reduction can occur at dissolved oxygen levels of 10 μM up to possibly 100 μM O_2 (Klinkhammer and Bender, 1980; Trefry et al., 1984; Saager et al., 1989; German and Elderfield, 1990; Johnson et al., 1992). Cerium has a higher reduction potential thus the oxygen levels only provide a minimum estimate for dissolved O_2 (Tostevin, 2021). Despite evidence for locally anoxic to manganous conditions, the presence of the sponge-grade animals associated with the Khopych Formation reef complex supports the view that the shallow continental margin was a region of high primary productivity.

The geometry of the Zhuya Group has been interpreted as a rimmed platform defined by a barrier reef and a backreef lagoon (Fig. 4.10). The [Mn] and Ce/Ce* are at a maximum at the base of the outer slope in the shelf environment and with [Mn] gradually decreasing to a minimum moving up the ramp as the large microbial mud mounds appear above the Nikol'skoe-Alyanch boundary. Through the Alyanch Formation, the Ce/Ce* remains persistently positive until the Khopych Formation where a sudden negative Ce/Ce* indicates a brief period of oxygenation, followed by a positive Ce/Ce* in the reef complex and backreef lagoonal region. The anoxic and potentially manganous conditions in the Nikol'skoe and Alyanch Formations were likely formed via extensive primary productivity further up the slope in the reefal margin enhancing nutrient and organic matter loading and promoting the formation of an oxygen minimum zone (OMZ) at the base of the outer slope and shelf margins (Li et al., 2010; Wang et al., 2012; Ader et al., 2015; Cui et al., 2015; Cañadas et al. 2022). Above the OMZ in the Khopych Formation, the appearance of large, tangential ooids signifies the transition into an ooid shoal environment, indicating frequent wave agitation and the mixing oxygenated and anoxic water masses. Additionally, through the filtration efforts of the sponge-grade organisms on the proximal side of the reef, the clarification of the water column expanded the photic zone, which coupled with enhanced nutrient delivery,

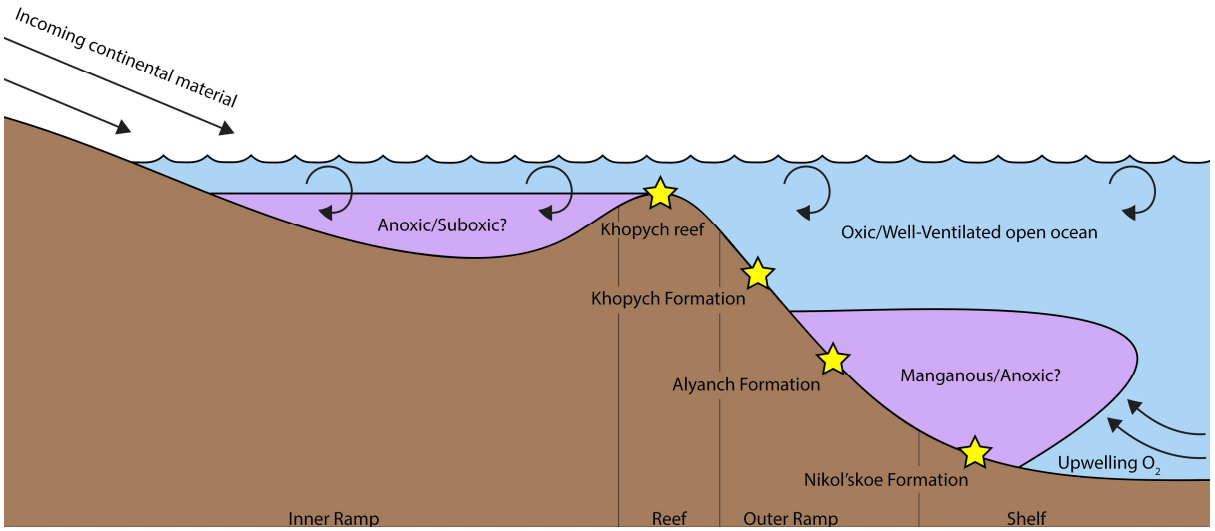


Figure 4.10: Cross-sectional interpretation of the local redox profile. The upwelling of ventilated waters coupled with the high productivity in the shallower ramp settings may have promoted the formation of a low oxygen wedge along the distal ramp and shelf settings, while enhanced organic matter loading in the restricted back lagoonal setting promoted suboxic to anoxic conditions.

likely enhancing photosynthesis in the water column. The reef complex is unique insofar as the strong positive Ce/Ce* indicates deposition under an anoxic water column. This dichotomy can be resolved by considering the proximal side of the reef complex forming a restricted back lagoon cut off from the open ocean where incoming nutrients stimulated eutrophication in the lagoonal setting. The general local redox profile of the Zhuya Group can be summed up by the REY profile in figure 4.9A. The relatively flat REY pattern is consistent with other anoxic platforms, although the general seawater REY signal is retained through the presence of a slight La anomaly, minor negative Ce anomaly, and the pronounced Y anomaly.

The time series Mn signal (figure 4.1F) partly corroborates the existence of an OMZ as it reflects the gradual transition from a deeper water environment to a shallow setting. This pattern is broadly consistent with Mn distribution in the modern ocean with elevated surface concentrations resulting from aeolian inputs and photo-reductive dissolution, the latter of which would be enhanced through the growth of the photic zone via the clarifying ability of sponges (Guieu et al., 1994; Shiller, 1997; Sunda and Huntsman, 1988; Lewis and Luther III, 2000). With

increasing depth, Mn concentrations decrease to a minimum due to particle scavenging, before increasing to a maximum in OMZs through OM recycling and reductive dissolution (Klinkhammer and Bender, 1980; Landing and Bruland, 1980, 1987; Martin et al., 1985; Saager et al., 1989; Lewis and Luther III, 2000).

4.4.5: Was the Shuram Excursion a True Oxygenation Event?

To evaluate the extent of oxygenated seafloor during the nadir of the SE and broadly co-occurring zenith of $\delta^{238}U$ values, the uranium isotope compositions from Zhuya Group carbonates were input into the 2-sink mass balance model detailed in Kipp and Tissot (2022). The model assumes that: 1.) conditions are at steady-state and riverine input is the sole source of U to the oceans at a constant $\delta^{238}U$ of -0.3‰; 2.) anoxic sediments account for 15% of the seawater U sink and the Δ_{anox} is +0.7‰; 3.) Δ_{other} is <0.05‰ and represents the combination of suboxic (42%), carbonate (28%), and other (15%) sinks. Because most carbonates are offset from seawater by an average of -0.27 ± 0.14‰, and the model is at steady-state and cannot go above a $\delta^{238}U_{seawater}$ of -0.3‰, offsets of -0.13‰, -0.27‰, and -0.41‰ were applied to the $\delta^{238}U_{carb.}$ of the Zhuya Group carbonates (Chen et al., 2018b). The results from the model are detailed in figure 4.11. Based on the offsets applied, the minimum $\delta^{238}U_{seawater}$ during the SE would have been -0.35‰, with model results suggesting that roughly 0.9% of the seafloor was occupied by anoxic

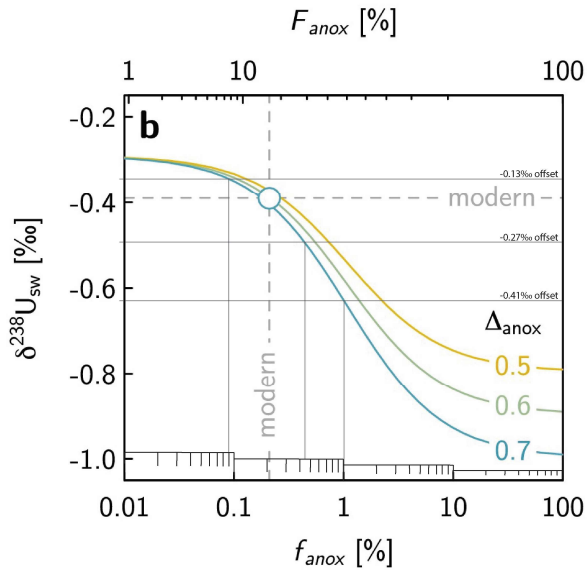


Figure 4.11: Results of the 2-sink model calculation. With the three offsets (-0.13‰, -0.27‰, and -0.41‰) applied to the average Zhuya Group $\delta^{238}U$ values, the minimum extent of seafloor anoxia is 0.09% and the maximum is 1%.

sediments. Conversely, the maximum $\delta^{238}U_{seawater}$ during the SE would have been -0.63‰, corresponding to roughly 1% of anoxic seafloor. The data presented herein shows remarkable consistency with that presented in Zhang et al. (2019) who estimated that the extent of anoxic seafloor in the pre-SE was 26-100% and <6% during the SE. However, with only two sinks, the suboxic seafloor area is not thoroughly represented and thus the model represents the absolute minimum extent of anoxic seafloor during the SE.

In order to resolve the seemingly conflicting $\delta^{238}U$ and Ce/Ce* anomaly data, the most parsimonious explanation is that during the SE, increased sedimentation rates coupled with an extremely efficient OM export mechanism drove the ventilation of the oceans. However, enhanced nutrient delivery along productive shelf margins increased OM loading, which paired with upwelling waters from the deeper ocean, promoted the formation of a low oxygen, potentially manganous wedge along the shelf margins. However, given the lack of appreciable organic material in these carbonate samples, this hypothesis is not easily testable. An alternative explanation for the persistently positive Ce/Ce* data is that while the overlying water column was well-ventilated, cementation occurred under the influence of reduced porewaters rich in dissolved Mn. The increasingly efficient export of OM, via the sponge sink and rapid sedimentation rates, may have restricted the redox boundary to the sediment-water interface. A restricted redoxcline would promote the dissolution of Fe-Mn(oxyhydr)oxides within the sediments, perhaps to oxidize the freshly buried organic matter, releasing Fe(II), Mn(II), and REE (notably Ce and the MREE), which were captured in precipitating carbonate cements, corroborated by the elemental map data reported in figure 3.11E which shows a higher density distribution of Mn in the cements rather than the allochems (Fig. 4.12; Tostevin et al., 2016; Cao et al., 2020). Thus, the rocks in the Nikol'skoe and Alyanch formations may reflect a mix of primary and early secondary cements,

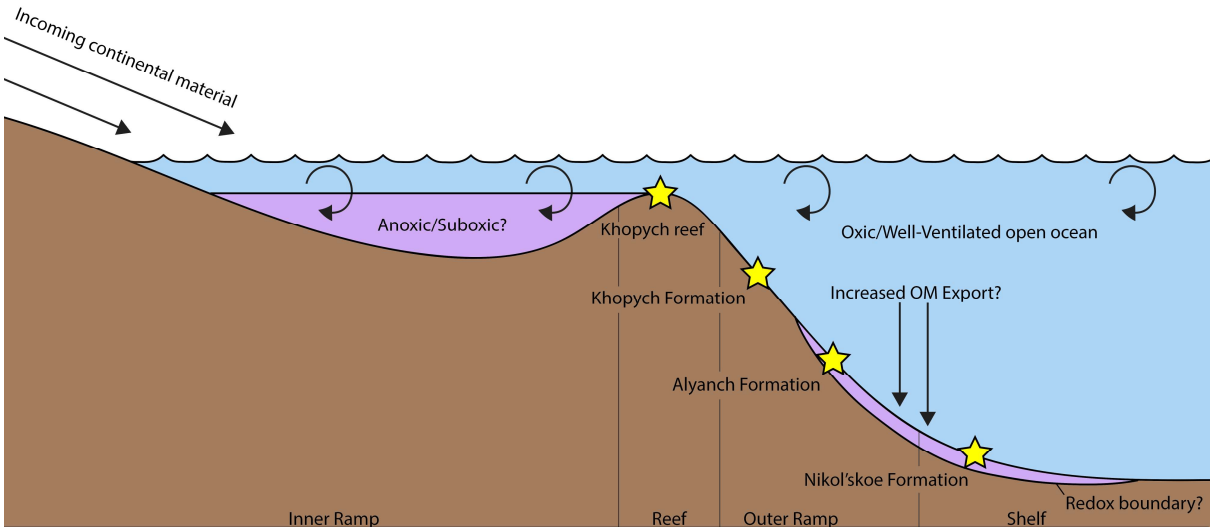


Figure 4.12: Alternate cross-sectional interpretation of the local redox profile where the increased export efficiency of organic matter restricted the redox boundary to the sediment-water interface, where cementation occurred under anoxic conditions. Further up in the Khopych Formation, the constant wave agitation likely aerated the sediments, efficiently capturing a primary seawater signal during cementation. The low oxygen back lagoon may still have been the result of enhanced organic matter loading and a general restriction from the open ocean.

although based on the preservation of characteristic seawater REE patterns, the overwhelming signal is that of seawater. Conversely, the shallower Khopych Formation, indicative of a higher energy environment, may have been aerated with oxic seawater through constant wave agitation, hence explaining the negative Ce/Ce*. Furthermore, if cementation occurred under reduced conditions, the U isotope composition could have been affected through the authigenic accumulation of U(IV), although even with the maximum offset applied, the mass-balance model indicates a major contraction of anoxic seafloor from 26-100% (*cf.* Zhang et al., 2019) to roughly 1%. The combination of model data, as well as the fidelity of $\delta^{238}U$ across several geographically disparate localities indicates that despite variations in local redox conditions, the U isotope data reflects a primary oceanographic signal.

4.5: Conclusions

Intense congruent weathering during the SE, evidenced by the novel $\delta^{7}Li$ isotope data presented in chapter 3, promoted the enhanced delivery of nutrients and oxidants, the latter of

which facilitated the anaerobic conversion of DOC to ^{13}C-depleted DIC and released organic-bound nutrients further building up the nutrient inventory of the oceans. The growth of the oceanic nutrient inventory stimulated widespread productivity and production of organic matter. The rapid sedimentation rates associated with the trafficking of salts, ions, and sediments, as well as a more efficient organic matter export mechanism through the metabolic activity of sponges, drove the ventilation of the SE oceans, prompting a transient shift towards near-modern $\delta^{238}U$ values. The measured carbonate uranium isotope values from one of the thickest SE successions are in good agreement with previous studies that suggest widespread oxidation of the middle Ediacaran oceans. However, insofar as carbonate U isotopes are typically offset from seawater $\delta^{238}U$ compositions, a correction factor of -0.27‰ was applied to the average $\delta^{238}U_{carb.}$ from the Zhuya Group to constrain $\delta^{238}U_{SW}$ for model calculations. Based on present-day parameters, the results from the 2-sink model indicate that the extent of anoxic seafloor during the SE is estimated at roughly 1% (compared to 0.05% today) when a maximum offset of -0.41‰ is applied.

While the global ocean was defined by a stable, ventilated signal, the local redox landscape remained dynamic and variable. Cerium anomaly data coupled with manganese concentrations reveal that lower slope and shelf margins were characterized by anoxic to manganous conditions, the distal and oolitic upper slope environments were well-oxygenated and highly productive, and the reefal unit and back lagoon were predominantly anoxic. The presence of sponge-grade organisms would have clarified the water column, increasing the depth of the photic zone, stimulating aerobic metabolisms in the oxic surficial layer, through which, the enhanced productivity would have enhanced organic matter loading and promoted the formation of oxygen minimum zones (OMZs) within the restricted back lagoon and along the distal slope and shelf margins. Alternatively, the increased export efficiency of OM via the ‘sponge-pump’ may have

spurred the contraction of the redox boundary to the sediment-water interface, which would dilute the primary seawater signal with that of anoxic porewaters captured during cementation. However, while the distal ramp and shelf environments captured the porewater signal, the constant sediment reworking in shallower ramp and rim settings may have efficiently captured an undiluted oxic seawater signal. This alternative hypothesis is supported by the elemental map data (presented in Chapter 3) which shows greater distribution of Mn in the cements rather than allochems.

Chapter 5: Research Conclusions

The multi-proxy approach to unveiling the potential drivers for one of the most enigmatic carbon isotope anomalies in Earth history has revealed that the nadir of the SE is consistent with a period of intense congruent weathering associated with episodes of collision and uplift during the assembly of Gondwana. The lithium isotope data from two SE successions reveals low, near crustal $\delta^7Li_{carb.}$ in the SE excursion interval, while the pre- and post-SE are complicated by the effects of dolomitization where the dolostones exhibit δ^7Li values approximately 5-8‰ heavier than their limestone counterparts. For this reason, the dolostones should be interpreted with caution. If one assumes that the dolostones reflect depositional seawater conditions, the higher δ^7Li could be attributed to higher rates of incongruent weathering of silicates on land, resulting in the formation of secondary terrestrial clay minerals and a riverine flux defined by an isotopically heavy dissolved δ^7Li load. Broadly coincident with the nadir of the negative $\delta^{13}C$ values, the low crustal δ^7Li values signify a more congruent weathering regime, characterized by the intense physical and chemical weathering of the continents paired with rapid reverse weathering. This period of highly congruent weathering would have supersaturated the oceans with respect to [CO_3^{2-}], invoking the anaerobic conversion of DOC to DIC, sparking the negative carbon isotope excursion, detailed visually in figure 5.1.

An enhanced flux of oxidants (like SO_4^{2-}, NO_3^-, and ferric iron) via intense silicate weathering would trigger the anaerobic conversion of DOC to ^{13}C-depleted DIC, some of which would be released back to the atmosphere via reverse weathering and while the concurrent nutrient flux would stimulate photosynthetic processes. Aerobic respiration would facilitate the release of$^{12}CO_2$ to the atmosphere through (a short term feedback) which would return to the oceans as isotopically light carbonate and bicarbonate ions, some of which would participate in reverse

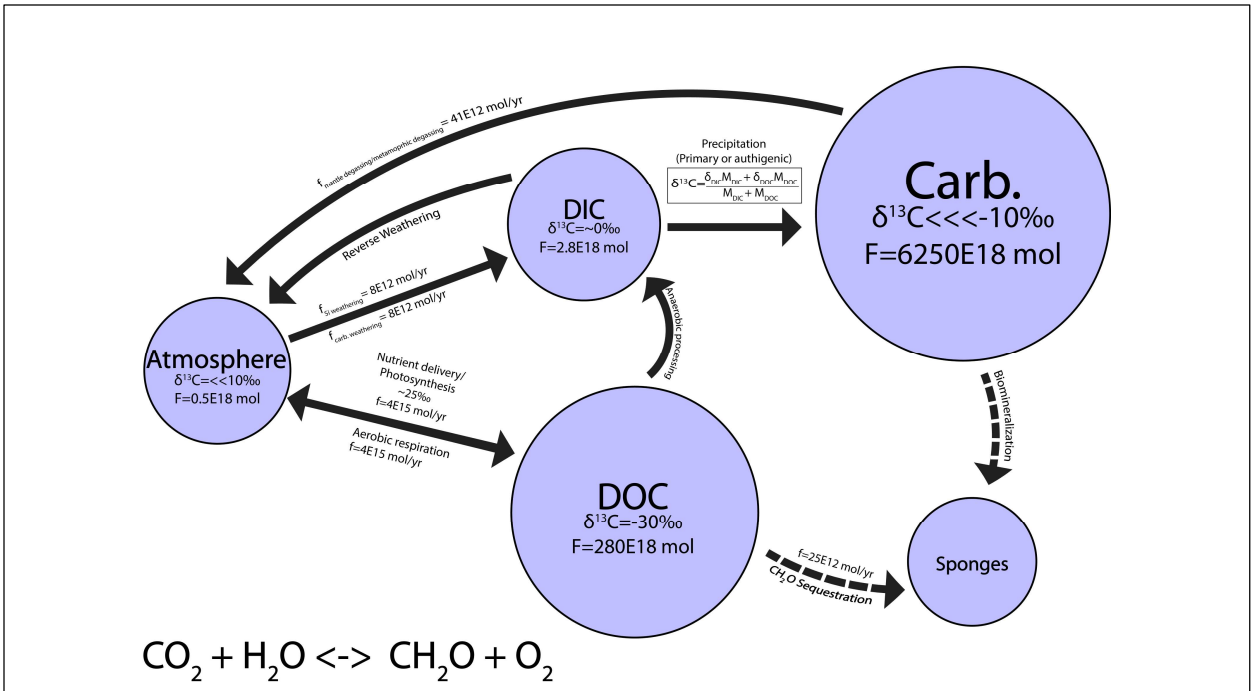


Figure 5.1: A synthesizing conceptual model, combining both the long-term and short-term carbon cycle, highlighting the various pathways in which the depleted $\delta^{13}C$ values preserved in SE-bearing strata could have been generated and promoted the subsequent environmental and biological changes observed throughout the anomaly. Each pathway is not mutually exclusive and was likely a combination of all components. Flux and reservoir values adapted from Wallman and Aloisi, (2012) and Shields and Mills, (2017).

weathering reactions, balancing the silicate weathering reactions. Furthermore, a fraction of the photosynthate produced would be sequestered via the 'sponge pump' driving an increase in O_2 and partially ventilating the oceans. By increasing the reservoir of ^{13}C-depleted DIC, the rapidly precipitating carbonates would inherit a $\delta^{13}C$ value reflecting a greater proportion of organic-derived DIC. Furthermore, the high concentration of carbonate ions in the ocean would have promoted the coupling of C/O isotopes, heavier $\delta^{88}Sr$, as well as the formation of giant ooids and grapestones, aragonite precipitates, seafloor plate breccias, and vertical sheet crack cements. A biological response to the forcing of intensified silicate weathering would have been to form a carbonate shell as a means of detoxifying to maintain homeostatic balance within their cells in response to the extremely high levels of salts and ions within the SE oceans.

Paired with the intense weathering episode, the growth of the nutrient inventory would have stimulated primary productivity, driving the widespread ventilation of the oceans through the

rapid organic matter burial via enhanced sedimentation rates, on top of the increasingly efficient biological export mechanism, driven by the filtering actions of sponges. The variable Ce/Ce* through the succession suggests that the local environments were characterized by dynamic and oscillating redox conditions. It is plausible that local primary productivity in the photic zone and shallow-slope settings would have promoted the formation of an oxygen minimum zone (OMZ) or wedge evidenced by the positive Ce/Ce* throughout the Nikol'skoe and Alyanch formations. This oxygen minimum wedge may have resulted in the dissolution of Mn(oxyhydr)oxides, formed in the overlying oxic waters, which were then incorporated into early precipitating carbonate cements. As the SE progressed, the gradual shift to a more incongruent weathering regime dampened the input of oxidants and nutrients, slowing the oxidation of the DOC pool and reducing organic matter burial, driving a gradual return of anoxia and a rebound in $\delta^{13}C$, $\delta^{7}Li$, and $\delta^{238}U$ compositions of carbonates.

These proxies provide an understanding of how extreme perturbations in the carbon cycle throughout Earth history pushed profound environmental and biological changes which may have implications for constraining future climatic changes brought about by anthropogenic forcings. During periods of high atmospheric pCO_2, the oceans absorb more CO_2 through air-sea gas exchange, resulting in the acidification of the oceans (Kump et al., 2009). Elevated levels of dissolved greenhouse gases in the oceans would drive a decrease in ocean pH, prompting a decrease in the carbonate saturation state and shallowing of the carbonate compensation depth, inhibiting the formation of new carbonates of both biogenic and abiogenic origin. Furthermore, the elevated atmospheric CO_2 levels would promote hot-house conditions stimulating increased weathering fluxes, allowing for the enhanced delivery of nutrients and subsequent eutrophication of the surface ocean, driving an increased flux of organic matter to the seafloor, which would be

subsequently oxidized, resulting in a notable decrease in dissolved O_2, promoting widespread anoxia, similar to that of OAE2 (Schlanger and Jenkyns, 1976; Schlanger et al., 1987; Arthur et al., 1987; Pearce et al., 2009) or other major positive carbon isotope excursions throughout Earth history.

However, despite the new geochemical data, several unanswered questions remain. 1.) Did an increase in productivity truly contribute to the ventilation of the oceans? 2.) Could the near-modern $\delta^{238}U$ values be the product of authigenic U(IV) enrichment? And 3.) Is there evidence for denitrification in the Nikol'skoe and Alyanch formations to corroborate the presence of an oxygen minimum zone?

To address the first question, because P is utilized by almost all living things as a key limiting nutrient, the lack of stable P isotopes hinders its ability to track productivity. For this reason, new proxies for productivity have been explored. One such proxy is the Cd isotope system, due to its coupling with PO_4^{3-} based on its nutrient like distribution where [Cd] is depleted in surface waters and progressively enriched in the deep ocean, suggesting preferential scavenging to aid in metabolic processes (de Baar et al., 1993). The isotopic distribution of Cd also shows similar trends where the $\delta^{114}Cd$ of the surface ocean is isotopically heavy, due to the preferential uptake of ^{110}Cd by phytoplankton during photosynthesis and gets increasingly depleted in ^{114}Cd with increasing depth (Sieber et al., 2019; Abouchami et al., 2011, 2014). If extensive primary productivity aided in the generation of the SE, and subsequent ventilation of the oceans, the $\delta^{114}Cd$ would reflect this period of enhanced productivity by exhibiting enrichments in ^{114}Cd during the event.

To address the second question, insofar as carbonate $\delta^{238}U$ values reflect an averaged signal between primary and authigenic cements, determining the offset to apply to $\delta^{238}U_{carb.}$ to reconstruct

seawater $\delta^{238}U$ is not an easy task as each geological unit has undergone a unique diagenetic history. Because U(VI) is sourced directly from seawater where it is incorporated into uranyl-bicarbonate complexes under oxic conditions and readily incorporated into the carbonate lattice, the isotopic composition should reflect a primary seawater $\delta^{238}U$ signal (Ku et al., 1977; Langmuir, 1978; Endrizzi et al., 2016; Chen et al., 2017; Chen et al., 2021). However, the incorporation of the isotopically heavy reduced species, U(IV), during syn- and post-depositional diagenetic processes can impose a large fractionation, overprinting the original $\delta^{238}U$ value. A new approach to quantifying the incorporation of U(IV) under reducing conditions is by comparing the fraction of U(IV) to the bulk rock U concentration, providing a rough approximation of the extent to which the $\delta^{238}U$ values were affected by the authigenic accumulation of the reduced U species (Wei and Zhang, 2024). To this end, the process of separating U(IV) from U(VI) via an anion exchange method has been successful in isolating U(IV) from U(VI) in geological samples from reef carbonates from the NK-1 drill core in the South China Sea (Yuan et al., 2023). Such analyses might be applied to future studies of the SE.

If the Nikol'skoe and Alyanch formations were deposited in an oxygen minimum zone, one of the dominant microbial processes that would be occurring is denitrification. Like P and C, N is a major constituent of life and thus exerts a strong control on primary productivity as a key limiting nutrient. The process of denitrification occurs under very specific oxygen levels and imparts a distinct isotopic fractionation (Ward, 2012). By utilizing N isotopic abundances in the Zhuya Group samples, the OMZ hypothesis might be effectively tested. However, in the event that the low abundance of organic matter in the samples inhibits the analysis of N isotopes, a selective elemental analysis to target different phases within the carbonate samples (ooids and cements) would be the next logical step. Insofar as bulk powders were used in the various

geochemical analyses, a component-specific analysis would elucidate the primary seawater signal from the authigenic background, which could provide a rough estimation of which component dominates the bulk rock elemental signatures.

While future studies are needed to resolve outstanding questions, the paired weathering and redox study of two globally disparate SE successions reveal new insights into the causes and consequences of the enigmatic carbon isotope anomaly. The amplification of congruent weathering on land, driven by the profound tectonic reconfiguration associated with the suturing of Gondwana, spurred the oxidation of a large DOC pool, promoted the supersaturation of the oceans with respect to carbonate, driving the rapid and widespread deposition of carbonates with unique sedimentary features along continental margins, and resulted in the gradual adaptation of animal biomineralization through the influx of salts and ions to the oceans. On top of that, the removal of newly formed organic matter to the highly efficient 'sponge pump' and the concomitant burial through rapid sedimentation rates stimulated the ventilation of the deep oceans for the duration of the SE. The consistency in elemental and isotopic data across widely separated successions supports the view that the SE was an oceanographic event, rather than a diagenetic insult. While the environmental effects of the SE are profound, the biological impact it had on the Ediacaran biota, which appeared shortly after the termination of the event, through the new adaptation of biomineralization, is very apparent. While the duration of the SE was short-lived in the geological sense (~10 Ma), this period of non-steady state conditions in the world oceans may have been responsible for lighting the fuse that would reach its crescendo with the Cambrian Explosion.

Appendix I

Table A1: Data table containing elemental concentrations from the Li leach (Li, Mg, Al, P, Ca, Mn, Fe, Rb, and Sr) for the Zhuya Group.

Sample	Height (m)	Formation	Li (ppm)	Mg (wt.%)	Al (wt. %)	P (ppm)	Ca (wt. %)	Mn (ppm)	Fe (wt. %)	Rb (ppm)	Sr (ppm)
2103-280	562.21	**Khopych**	0.59	0.20	0.00	33.45	17.36	84.71	0.28	0.03	1440.23
K2103.276.65	558.86	**Khopych Reef**	1.58	0.41	0.01	9.72	31.77	116.74	0.05	0.10	369.14
K2103.276.00	558.21		1.61	0.35	0.00	16.36	34.50	104.48	0.06	0.03	1285.20
K2103.275.75	557.96		0.77	0.19	0.00	5.51	28.70	85.81	0.06	0.02	1279.55
K2103.275.00	557.21		0.39	0.22	0.00	13.31	34.16	109.67	0.07	0.05	2627.16
K2103.272.55	554.76		1.18	0.40	0.00	10.83	32.79	133.50	0.04	0.04	542.27
K2103.271.10	553.31		0.86	0.45	0.01	8.39	34.64	133.94	0.05	0.08	406.30
2103-270	552.21		0.62	0.29	0.01	7.79	33.61	188.53	0.08	0.16	2496.64
2103-259	541.21	**Khopych**	0.57	0.26	0.00	25.11	17.25	161.35	0.27	0.03	1171.12
2103-244	525.21		1.27	0.37	0.01	11.38	31.00	247.77	0.08	0.17	629.04
2103-195	474.21		0.57	0.23	0.01	34.84	17.14	265.33	0.29	0.07	334.49
2103-181	460.21		0.32	0.19	0.01	24.81	17.05	260.70	0.27	0.08	770.69
2103-171	450.21		0.49	0.17	0.01	23.60	16.23	133.90	0.29	0.05	750.82
2103-143	421.21		0.43	0.16	0.00	24.91	16.11	79.93	0.28	0.05	823.19
2103-134	412.21		0.41	0.31	0.02	4.19	32.90	125.48	0.04	0.17	1107.82
2103-122	400.21	**Alyanch**	0.03	0.15	0.00	-0.19	31.39	82.53	0.03	0.07	641.84
2103-94	372.21		0.11	0.10	0.00	17.62	16.51	49.20	0.21	0.03	890.89
2103-84	362.21		0.13	0.16	0.00	2.22	34.02	76.45	0.02	0.04	592.79
2103-51	330.21		0.38	0.12	0.00	4.85	35.50	32.76	0.03	0.03	2534.46
2103-30	309.21		0.29	0.22	0.00	2.25	33.55	52.70	0.02	0.06	909.17
2103-4	283.21		0.24	0.16	0.01	3.29	33.53	42.31	0.02	0.06	664.38
2103-M4	276.21		0.15	0.15	0.00	17.76	16.80	32.83	0.23	0.03	1027.64
2103.2-83.17	268.55		0.29	0.26	0.00	1.13	35.23	85.13	0.03	0.04	1321.30
2103.2-70.00	255.38	**Nikol'skoe**	0.42	0.33	0.01	2.52	32.81	154.17	0.05	0.12	435.12
2103.2-44.00	229.38		0.40	0.26	0.00	19.27	16.63	113.01	0.27	0.07	657.42
2103.2-28.00	213.38		0.15	0.34	0.00	3.55	30.82	208.11	0.05	0.11	518.43
2102_114_35	210.23		0.38	0.32	0.00	4.92	29.55	210.51	0.05	0.10	328.04
2102-96.93	192.81		0.54	0.32	0.02	14.14	23.10	258.41	0.10	0.18	309.35
2102-91.15	187.03		0.28	0.22	0.00	13.96	14.04	223.55	0.22	0.05	301.62
2102-81.05	176.93		0.41	0.32	0.01	12.92	22.00	265.43	0.06	0.14	258.31
2102-78.85	174.73		0.19	0.19	0.00	16.64	15.83	240.52	0.23	0.04	692.93
2102-64.00	159.88		0.58	0.41	0.02	21.47	36.43	533.14	0.21	0.19	524.43
2102-51.35	147.23		0.52	0.44	0.00	52.49	43.69	459.80	0.08	0.03	620.77
K2102.51.00	146.88		0.66	0.35	0.02	5.53	34.97	370.30	0.05	0.17	2766.64
2102-49.20	145.08		0.55	0.42	0.01	18.34	37.66	600.13	0.07	0.04	337.72
2102-45.34	141.22		0.80	0.89	0.08	34.48	24.51	707.98	0.17	0.40	255.66
2102-43.71	139.59		0.74	0.54	0.01	23.22	31.35	565.70	0.07	0.06	295.74
2102-39.15	135.03		0.51	0.30	0.00	21.55	12.49	411.48	0.19	0.05	199.91
2102-13.86	109.74		0.35	0.42	0.01	12.25	33.89	624.95	0.06	0.08	255.98
2102.1-10.13	76.01		0.35	0.34	0.01	26.15	15.62	619.92	0.24	0.09	221.16
2102.1-5.35	71.23		0.37	0.34	0.00	20.01	15.50	756.86	0.23	0.10	210.25
2101-67.85	67.85		0.33	0.34	0.01	28.92	30.13	830.71	0.16	0.04	218.88
2101-55.80	55.8		0.53	0.35	0.00	4.58	26.90	1160.09	0.03	0.07	194.58
2101-45.03	45.03		0.45	0.35	0.01	55.04	31.64	1289.64	0.11	0.04	208.85
2101.39.02	39.02		0.64	0.35	0.01	18.33	31.32	1915.08	0.77	0.18	237.81
2101-34.17	34.17		0.54	0.38	0.00	11.30	31.84	2890.08	0.03	0.12	267.57

Table A2: Data table containing elemental ratios from the Li leach (X/(Mg+Ca)) from the Li leach (Mg/Ca, Mn/Sr, Rb/Sr, Li, Al, P, Mn, Rb, Sr) for the Zhuya Group.

Sample	Height (m)	Formation	Mg/Ca	Mn/Sr	Rb/Sr	Li/(Mg+Ca)	Al/(Mg+Ca)	P/(Ca+Mg)	Mn/(Mg+Ca)	Rb/(Mg+Ca)	Sr/(Mg+Ca)
2103-280	562.21	**Khopych**	0.01	0.06	2.01E-05	3.37E-06	2.53E-04	1.90E-04	4.82E-04	1.65E-07	8.20E-03
K2103.276.65	558.86	**Khopych Reef**	0.01	0.31	2.75E-04	2.91E-06	1.90E-04	3.75E-05	3.69E-04	3.23E-07	1.17E-03
K2103.276.00	558.21		0.01	0.08	2.50E-05	2.18E-06	5.50E-05	4.87E-05	2.92E-04	9.70E-08	3.87E-03
K2103.275.75	557.96		0.01	0.07	1.77E-05	2.68E-06	5.44E-05	1.91E-05	2.97E-04	7.84E-08	4.43E-03
K2103.275.00	557.21		0.01	0.04	1.77E-05	1.14E-06	1.22E-04	3.87E-05	3.19E-04	1.35E-07	7.64E-03
K2103.272.55	554.76		0.01	0.25	8.02E-05	3.54E-06	1.18E-04	3.26E-05	4.02E-04	1.31E-07	1.63E-03
K2103.271.10	553.31		0.01	0.33	1.91E-04	2.46E-06	2.22E-04	2.39E-05	3.82E-04	2.22E-07	1.16E-03
2103-270	552.21		0.01	0.08	6.46E-05	1.83E-06	3.71E-04	2.30E-05	5.56E-04	4.75E-07	7.36E-03
2103-259	541.21	**Khopych**	0.02	0.14	2.53E-05	3.27E-06	2.15E-04	1.43E-04	9.21E-04	1.69E-07	6.69E-03
2103-244	525.21		0.01	0.39	2.66E-04	4.06E-06	2.63E-04	3.63E-05	7.90E-04	5.34E-07	2.01E-03
2103-195	474.21		0.01	0.79	2.17E-04	3.30E-06	4.02E-04	2.01E-04	1.53E-03	4.18E-07	1.93E-03
2103-181	460.21		0.01	0.34	9.84E-05	1.86E-06	3.61E-04	1.44E-04	1.51E-03	4.40E-07	4.47E-03
2103-171	450.21		0.01	0.18	6.01E-05	3.00E-06	3.78E-04	1.44E-04	8.17E-04	2.75E-07	4.58E-03
2103-143	421.21		0.01	0.10	5.96E-05	2.63E-06	2.89E-04	1.53E-04	4.91E-04	3.01E-07	5.06E-03
2103-134	412.21		0.01	0.11	1.56E-04	1.25E-06	4.80E-04	1.26E-05	3.78E-04	5.20E-07	3.34E-03
2103-122	400.21	**Alyanch**	0.00	0.13	1.16E-04	1.01E-07	7.60E-05	-6.04E-07	2.62E-04	2.37E-07	2.03E-03
2103-94	372.21		0.01	0.06	3.01E-05	6.38E-07	1.40E-04	1.06E-04	2.96E-04	1.61E-07	5.36E-03
2103-84	362.21		0.00	0.13	7.53E-05	3.78E-07	9.27E-05	6.50E-06	2.24E-04	1.31E-07	1.73E-03
2103-51	330.21		0.00	0.01	1.05E-05	1.07E-06	9.52E-05	1.36E-05	9.20E-05	7.47E-08	7.12E-03
2103-30	309.21		0.01	0.06	6.12E-05	8.45E-07	1.34E-04	6.65E-06	1.56E-04	1.65E-07	2.69E-03
2103-4	283.21		0.00	0.07	9.43E-05	1.23E-06	9.61E-05	8.64E-06	1.33E-04	1.76E-07	1.86E-03
2103-M4	276.21		0.01	0.03	2.92E-05	8.81E-07	1.32E-04	1.05E-04	1.94E-04	1.77E-07	6.06E-03
2103.2-83.17	268.55		0.01	0.08	5.91E-05	7.13E-07	2.63E-04		2.61E-04	1.87E-07	3.17E-03
2103.2-70.00	255.38	**Nikol'skoe**									
2103.2-44.00	229.38		0.02	0.17	1.01E-04	2.34E-06	2.42E-04	1.14E-04	6.69E-04	3.92E-07	3.89E-03
2103.2-28.00	213.38		0.01	0.45	1.84E-04	1.67E-06	4.50E-04	2.38E-05	6.42E-04	2.64E-07	1.44E-03
2102_114_35	210.23		0.01	0.77	2.91E-04	1.75E-06	4.01E-04	5.29E-05	7.25E-04	2.76E-07	9.48E-04
2102-96.93	192.81		0.01	0.84	5.73E-04	2.30E-06	9.95E-04	6.04E-05	1.10E-03	7.56E-07	1.32E-03
2102-91.15	187.03		0.02	0.74	1.81E-04	1.96E-06	2.97E-04	9.79E-05	1.57E-03	3.82E-07	2.11E-03
2102-81.05	176.93		0.01	1.03	5.32E-04	1.82E-06	5.91E-04	5.79E-05	1.19E-03	6.16E-07	1.16E-03
2102-78.85	174.73		0.01	0.35	5.63E-05	1.18E-06	2.05E-04	1.04E-04	1.50E-03	2.43E-07	4.33E-03
2102-64.00	159.88		0.01	1.02	3.59E-04	1.57E-06	6.19E-04	5.83E-05	1.45E-03	5.11E-07	1.42E-03
2102-51.35	147.23		0.01	0.74	4.56E-05	1.19E-06	1.10E-04	1.19E-04	1.04E-03	6.41E-08	1.41E-03
K2102.51.00	146.88		0.01	0.13	6.28E-05	1.88E-06	4.37E-04	1.57E-05	1.05E-03	4.92E-07	7.83E-03
2102-49.20	145.08		0.01	1.78	1.27E-04	1.45E-06	1.64E-04	4.82E-05	1.58E-03	1.12E-07	8.87E-04
2102-45.34	141.22		0.04	2.77	1.56E-03	3.14E-06	3.07E-03	1.36E-04	2.79E-03	1.57E-06	1.01E-03
2102-43.71	139.59		0.02	1.91	2.01E-04	2.32E-06	1.92E-04	7.28E-05	1.77E-03	1.87E-07	9.28E-04
2102-39.15	135.03		0.02	2.06	2.42E-04	4.01E-06	3.15E-04	1.69E-04	3.22E-03	3.78E-07	1.56E-03
2102-16.10	111.98		0.01	2.29	1.88E-04	1.34E-06	1.09E-04	5.81E-05	1.90E-03	1.56E-07	8.30E-04
2102-13.86	109.74		0.01	2.38	3.02E-04	1.34E-06	9.99E-05	3.56E-05	1.65E-03	2.10E-07	6.94E-04
2102.1-10.13	76.01		0.02	2.80	4.03E-04	2.16E-06	3.48E-04	1.64E-04	3.88E-03	5.59E-07	1.39E-03
2102.1-5.35	71.23		0.02	3.60	4.68E-04	2.35E-06	2.59E-04	1.26E-04	4.78E-03	6.21E-07	1.33E-03
2101-67.85	67.85		0.01	3.80	1.80E-04	1.09E-06	2.81E-04	9.49E-05	2.73E-03	1.29E-07	7.18E-04
2101-55.80	55.8		0.01	6.40	2.30E-04	1.58E-06	8.63E-05	7.01E-05	4.09E-03	1.47E-07	6.39E-04
2101-45.03	45.03		0.01	6.17	1.80E-04	1.41E-06	1.70E-04	1.72E-04	4.03E-03	1.18E-07	6.53E-04
2101.39.02	39.02		0.01	8.34	2.09E-04	1.67E-06	7.48E-05	7.98E-05	5.56E-03	1.39E-07	6.67E-04
2101-34.17	34.17		0.01	10.80	4.66E-04	1.67E-06	1.08E-04	3.51E-05	8.97E-03	3.87E-07	8.30E-04

Table A3: Data table of isotopic data ($\delta^{13}C$, $\delta^{18}O$, $\delta^{7}Li$, $\delta^{7}Li_{sw}$, $\delta^{88}Sr$, $^{87}Sr/^{86}Sr$ and associated uncertainties) for the Zhuya Group. Note, red means interpret with caution.

Sample	Height (m)	Formation	$\delta^{13}C$ (‰)	$\delta^{18}O$(‰)	$\delta^{7}Li_{carb}$	$\delta^{7}Li_{SW}$	2σ	$\delta^{88}Sr$	2σ	$^{87}Sr/^{86}Sr$	2σ
2103-280	562.21	Khopych	-7.63	-8.88	8.5	13.5	0.1	0.38	0.01	0.7084	4.79E-06
K2103.276.65	558.86	Khopych Reef	-9.27	-9.38	9.4	14.4	0.2			0.7084	9.70E-06
K2103.276.00	558.21		-8.25	-9.30	10.1	15.1	0.1			0.7084	2.76E-06
K2103.275.75	557.96		-7.75	-10.15	9.5	14.5	0.0			0.7084	2.70E-06
K2103.275.00	557.21		-7.90	-8.99	10.6	15.6	0.2			0.7084	2.13E-06
K2103.272.55	554.76		-8.14	-9.40	8.6	13.6	0.1			0.7084	2.57E-06
K2103.271.10	553.31		-8.10	-9.45	9.3	14.3	0.1			0.7085	2.29E-06
2103-270	552.21		-8.19	-9.57	10	15	0.0			0.7084	5.05E-06
2103-259	541.21	Khopych	-8.06	-9.30	10.1	15.1	0.1	0.32	0.02	0.7084	4.26E-06
2103-244	525.21		-8.10	-9.21	9.1	14.1	0.1				
2103-195	474.21		-9.06	-9.05	9.7	14.7	0.3	0.42	0.01	0.7082	3.44E-06
2103-181	460.21		-9.51	-9.45	7.5	12.5	0.2	0.33	0.01	0.7082	3.34E-06
2103-171	450.21		-9.26	-9.75	7.9	12.9	0.2	0.40	0.01	0.7082	4.49E-06
2103-143	421.21		-9.14	-9.26	7.1	12.1	0.2	0.40	0.01	0.7082	6.89E-06
2103-134	412.21		-9.46	-8.90	7.9	12.9	0.1	0.42	0.01	0.7081	2.49E-06
2103-122	400.21	Alyanch	-9.63	-9.42	8	13	0.2				
2103-94	372.21		-9.53	-9.40	8.9	13.9	0.4	0.37	0.01	0.7081	4.71E-06
2103-84	362.21		-9.50	-9.48	9.9	14.9	0.2	0.39	0.01	0.7081	3.56E-06
2103-51	330.21		-8.56	-9.47	10.2	15.2	0.3			0.7080	3.14E-06
2103-30	309.21		-9.92	-9.55	10.4	15.4	0.2			0.7080	3.56E-06
2103-4	283.21		-9.95	-9.51	10.7	15.7	0.0	0.35	0.01	0.7080	2.60E-06
2103-M4	276.21		-10.28	-9.56	8.2	13.2	0.2	0.36	0.01	0.7080	3.30E-06
2103.2-83.17	268.55		-9.96	-9.58	9.9	14.9	0.1	0.36	0.01	0.7080	4.01E-06
2103.2-70.00	255.38	Nikol'skoe	-10.28	-9.62				0.41	0.01	0.7080	5.29E-06
2103.2-44.00	229.38		-10.28	-9.69	6.8	11.8	0.4	0.29	0.01	0.7080	4.63E-06
2103.2-28.00	213.38		-10.49	-9.70	4.6	9.6	0.1				
2102_114_35	210.23		-10.76	-9.91	4.7	9.7	0.1				
2102-96.93	192.81		-10.82	-10.15	4.2	9.2	0.1				
2102-91.15	187.03		-11.44	-10.35	4	9	0.1	0.529	0.01	0.7080	9.42E-06
2102-81.05	176.93		-11.68	-10.49	3.6	8.6	0.1				
2102-78.85	174.73		-12.03	-11.31	3.2	8.2	0.1	0.19	0.06	0.7082	4.13E-06
2102-64.00	159.88		-8.87	-10.31	3.5	8.5	0.2				
2102-51.35	147.23		-11.53	-10.83	2.9	7.9	0.2				
K2102.51.00	146.88		-11.63	-10.37	3.8	8.8	0.4				
2102-49.20	145.08		-11.80	-10.97	4.6	9.6	0.1				
2102-45.34	141.22		-11.63	-10.87	3.3	8.3	0.1				
2102-43.71	139.59		-12.10	-10.87	**6.7**	**11.7**	**0.3**				
2102-39.15	135.03		-12.22	-10.89	**7.4**	**12.4**	**0.4**	0.364	0.01	**0.7083**	**4.58E-06**
2102-16.10	111.98		-12.28	-11.12	**9**	**14**	**0.2**				
2102-13.86	109.74		-12.35	-11.18	**6.4**	**11.4**	**0.1**				
2102.1-10.13	76.01		-12.72	-11.45	**7.4**	**12.4**	**0.3**	0.267	0.01	**0.7088**	**8.18E-06**
2102.1-5.35	71.23		-12.88	-11.34	**7.3**	**12.3**	**0.1**	0.29	0.01	**0.7089**	**6.90E-06**
2101-67.85	67.85		-12.82	-11.41	**7**	**12**	**0.5**				
2101-55.80	55.8		-12.81	-11.77	**8.5**	**13.5**	**0.1**	0.02	0.01	**0.7093**	**6.48E-06**
2101-45.03	45.03		-12.77	-11.65	**8.3**	**13.3**	**0.2**				
2101.39.02	39.02		-12.74	-11.42	**8.9**	**13.9**	**0.1**	0.217	0.01	**0.7095**	**7.43E-06**
2101-34.17	34.17		-12.82	-11.95	**7.5**	**12.5**	**0.2**				

Table A4: Data table containing elemental concentrations from the Li leach (Li, Mg, Al, P, Ca, Mn, Fe, Rb, and Sr) for the Doushantuo Formation.

Sample	Height (m)	Formation	Member	Li (ppm)	Mg (wt.%)	Al (wt. %)	P (ppm)	Ca (wt. %)	Mn (ppm)	Fe (wt. %)	Rb (ppm)	Sr (ppm)
SSFT-2.4	73.4	**Doushantuo**	**II**	0.90	11.56	0.01	109.53	19.50	113.15	0.06	0.03	198.02
SSFT-8.3	79.3		**III**	0.95	6.66	0.01	172.19	11.59	69.83	0.04	0.00	74.01
SSFT-9.1a	80.1			0.90	7.18	0.01	39.22	12.58	79.52	0.06	0.00	102.32
SSFT-10.8	81.8			0.96	10.09	0.00	71.48	17.71	122.04	0.05	0.01	97.62
SSFT-27.6	98.6			0.26	9.21	0.02	54.54	14.95	211.16	0.13	0.09	39.00
SSFT-30.1	101.1			0.30	10.18	0.02	40.76	16.27	188.53	0.08	0.10	37.89
SSFT-33.6a	104.6			0.26	9.28	0.01	169.80	15.04	220.39	0.12	0.07	45.96
SSFT-34.1a	105.1			0.76	10.52	0.16	124.50	17.93	252.78	0.26	0.79	48.49
SSFT-37.7a	108.7			0.20	7.79	0.03	38.14	12.87	248.59	0.31	0.18	24.50
SFFT-39.6	110.6			0.13	0.21	0.01	15.50	29.63	106.61	0.03	0.09	171.03
SSFT-40.0	111			0.20	0.24	0.01	17.64	31.45	83.69	0.03	0.12	176.83
HND-9.1	121.9			0.16	0.23	0.01	20.54	30.26	98.06	0.04	0.14	172.90
HND-10.0	122.8			0.17	0.28	0.01	11.28	32.66	90.79	0.05	0.17	177.81
HND-10.2	123			0.04	0.41	0.02	5.57	33.38	115.02	0.10	0.27	173.20
HND-13.0	125.8			0.02	0.30	0.01	11.56	36.15	82.63	0.09	0.34	209.61
HND-14.1	126.9			0.04	0.26	0.01	8.27	31.88	106.31	0.06	0.18	208.92
HND-18.05a	130.85			0.06	0.22	0.01	18.66	26.59	52.32	0.10	0.12	195.80
HND-20.0	132.8			0.20	0.22	0.01	9.54	28.64	47.72	0.05	0.09	188.63
HND-23.05a	135.85			0.03	0.28	0.01	3.82	39.28	79.04	0.09	0.11	226.92
HND-23.55a	136.35			-0.08	0.23	0.01	7.65	31.39	61.46	0.07	0.07	165.38
HND-23.55b	136.35			0.28	7.86	0.07	22.33	17.42	193.44	0.90	0.70	114.78
HND-26.6a	139.4			0.03	0.20	0.01	4.48	32.34	71.79	0.02	0.12	139.03
HND-26.6b	139.4			0.26	7.37	0.05	47.40	17.37	147.00	0.22	0.28	93.44
HND-39.2	152		**IV**	0.07	8.42	0.05	1085.65	15.03	548.02	0.05	0.16	82.33
HND-39.9	152.7			0.74	9.77	0.02	52.76	16.67	452.23	0.05	0.09	64.83
HND-41.6	154.4	**Dengying**	**Hamajing**	2.01	7.56	0.25	671.75	13.13	189.25	0.10	1.24	53.41
HND-42.45	155.25			21.88	165.71	0.67	529.20	281.31	6368.75	0.96	3.48	904.10
HND-44.4	157.2			0.11	8.98	0.01	138.76	14.99	31.24	0.02		56.38
HND-48.1A	160.9			0.08	10.17	0.00	30.44	17.21	86.93	0.01		50.30
HND-53.5	166.3			0.38	5.65	0.03	47.53	10.46	189.76	0.03	0.12	47.18

Table A5: Data table of isotopic data ($\delta^{13}C$, $\delta^{18}O$, $\delta^{7}Li$, $\delta^{7}Li_{SW}$, and associated uncertainties) and elemental ratio data (X/(Mg+Ca)) from the Li leach (Mg/Ca, Mn/Sr, Rb/Sr, Li, Al, P, Mn, Rb, and Sr) for the Doushantuo Formation.

Sample	Height (m)	Formation	Member	% Carb.	$\delta^{13}C$	$\delta^{18}O$	$\delta^{7}Li_{carb}$	$\delta^{7}Li_{SW}$	2σ	Mg/Ca	Mn/Sr	Rb/Sr	Li/(Mg+Ca)	Al/(Mg+Ca)	P/(Mg+Ca)	Mn/(Mg+Ca)	Rb/(Mg+Ca)	Sr/(Mg+Ca)
SSFT-2.4	73.4	Doushantuo	II	82.0	4.3	-4.1	13.9	13.9	0.2	0.6	0.57	1.28E-04	2.90E-06	2.08E-04	3.53E-04	3.64E-04	8.18E-08	6.37E-04
SSFT-8.3	79.3		III	82.2	3.9	-4.8	10.8	10.8	0.1	0.6	0.94	2.38E-05	5.20E-06	6.04E-04	9.43E-04	3.83E-04	9.64E-09	4.06E-04
SSFT-9.1a	80.1			84.9	3.9	-3.6	12.9	12.9	0.1	0.6	0.78	-4.26E-05	4.60E-06	3.32E-04	1.99E-04	4.02E-04	-2.21E-08	5.18E-04
SSFT-10.8	81.8				3.9	-4.2	11.5	11.5	0.1	0.6	1.25	9.36E-05	3.50E-06	9.75E-05	2.57E-04	4.39E-04	3.29E-08	3.51E-04
SSFT-27.6	98.6				0.5	-4.2	16.5	16.5	0.3	0.6	5.41	2.31E-03	1.10E-06	6.77E-04	2.26E-04	8.74E-04	3.73E-07	1.61E-04
SSFT-30.1	101.1			94.0	-0.7	-4.9	15.2	15.2	0.8	0.6	4.98	2.73E-03	1.10E-06	7.91E-04	1.54E-04	7.13E-04	3.91E-07	1.43E-04
SSFT-33.6a	104.6			98.7	-6.3	-5.8	16.3	16.3	0.3	0.6	4.80	1.44E-03	1.10E-06	5.57E-04	6.98E-04	9.06E-04	2.72E-07	1.89E-04
SSFT-34.1a	105.1				-7.7	-5.7	11.6	11.6	0.3	0.6	5.21	1.63E-02	2.70E-06	5.54E-03	4.37E-04	8.88E-04	2.78E-06	1.70E-04
SSFT-35.3	106.3			87.6	-8.7	-6.8	12.5	12.5	0.4	0.6	9.72	9.04E-03	1.50E-06	2.61E-03	1.37E-04	1.30E-03	1.21E-06	1.34E-04
SSFT-37.7a	108.7			87.4	-8.9	-7.5	15.1	15.1	0.1	0.6	10.15	7.39E-03	9.50E-07	1.34E-03	1.85E-04	1.20E-03	8.76E-07	1.19E-04
SFFT-39.6	110.6			86.3	-8.9	-10	5.6	10.6	0.2	0	0.62	5.54E-04	4.40E-07	2.88E-04	5.19E-05	3.57E-04	3.17E-07	5.73E-04
SSFT-40.0	111			91.0	-8.9	-9.9	4.4	9.4	0.2	0	0.47	6.71E-04	6.20E-07	2.21E-04	5.57E-05	2.64E-04	3.74E-07	5.58E-04
HND-9.1	121.9			85.3	-9.1	-10	4.5	9.5	0.4	0	0.57	7.99E-04	5.10E-07	2.90E-04	6.74E-05	3.22E-04	4.53E-07	5.67E-04
HND-10.0	122.8			86.2	-9	-9.9	3.5	8.5	0.2	0	0.51	9.83E-04	5.10E-07	3.38E-04	3.43E-05	2.76E-04	5.31E-07	5.40E-04
HND-10.2	123			82.5	-8.8	-9.6	4.2	9.2	0.4	0	0.66	1.54E-03	1.20E-07	5.18E-04	1.65E-05	3.40E-04	7.92E-07	5.13E-04
HND-13.0	125.8			89.4	-8.7	-9.5	3.5	8.5	0.3	0	0.39	1.61E-03	6.80E-08	3.07E-04	3.17E-05	2.27E-04	9.25E-07	5.75E-04
HND-14.1	126.9			90.7	-8.7	-9.3	4.9	9.9	0.5	0	0.51	8.68E-04	1.30E-07	2.57E-04	2.58E-05	3.31E-04	5.64E-07	6.50E-04
HND-18.05a	130.85			85.2	-8.6	-8.9	5.1	10.1	0.2	0	0.27	6.06E-04	2.20E-07	3.94E-04	6.96E-05	1.95E-04	4.42E-07	7.30E-04
HND-20.0	132.8			91.3	-8.2	-8.2	4.3	9.3	0.2	0	0.25	4.96E-04	6.80E-07	2.99E-04	3.30E-05	1.65E-04	3.24E-07	6.54E-04
HND-21.0	133.8			83.0	-8.4	-8.4	5.8	10.8	0.2	0	0.25	9.99E-04	1.00E-06	6.58E-04	1.69E-04	1.96E-04	7.70E-07	7.71E-04
HND-23.05a	135.85			89.2	-8.5	-5	6.2	11.2	0.4	0	0.35	4.91E-04	7.10E-08	2.27E-04	9.66E-06	2.00E-04	2.82E-07	5.74E-04
HND-23.55a	136.35			80.6	-8.2	-7.7	5.8	10.8	0.5	0	0.40	4.27E-04	-2.40E-07	2.65E-04	2.42E-05	1.94E-04	2.23E-07	5.23E-04
HND-23.55b	136.35				-6.9	-3.7	8.7		0.2	0.5	1.70	6.11E-03	1.10E-06	2.95E-03	8.83E-05	7.65E-04	2.78E-06	4.54E-04
HND-26.6a	139.4			91.0	-8.3	-7.5	5.3	10.3	0.2	0	0.52	8.71E-04	8.70E-08	3.57E-04	1.38E-05	2.21E-04	3.72E-07	4.27E-04
HND-26.6b	139.4				-6.8	-2.3	12.9		0.1	0.4	1.57	2.95E-03	1.00E-06	1.93E-03	1.92E-04	5.94E-04	1.12E-06	3.78E-04
HND-39.2	152		IV	82.5	-4.9	-2.3	15.5	15.5	0.4	0.6	6.66	1.99E-03	3.00E-07	2.07E-03	4.63E-03	2.34E-03	7.00E-07	3.51E-04
HND-39.9	152.7				-4.1	0.8	20.6	20.6	0.5	0.6	6.98	1.44E-03	2.80E-06	8.83E-04	2.00E-04	1.71E-03	3.54E-07	2.45E-04
HND-41.6	154.4	Dengying	Hamajing		-1.6	-0.5	8.1	8.1	0.1	0.6	3.54	2.33E-02	9.70E-06	1.19E-02	3.25E-03	9.14E-04	6.00E-06	2.58E-04
HND-42.45	155.25				0.7	-3.8	18	18	0.1	0.6	7.04	3.85E-03	4.90E-06	1.50E-03	1.18E-04	1.42E-03	7.78E-07	2.02E-04
HND-44.4	157.2				3.5	-2.2	23.1	23.1	0.6	0.6	0.55	-2.95E-04	4.70E-07	2.96E-04	5.79E-04	1.30E-04	-6.93E-08	2.35E-04
HND-48.1A	160.9			89.9	-8.7	-4.6	21.8	21.8	0.2	0.6	1.73	-4.63E-04	3.10E-07	1.53E-04	1.11E-04	3.18E-04	-8.51E-08	1.84E-04
HND-53.5	166.3				1.4	-2.5	20.4		0.1	0.5	4.02	2.54E-03	2.30E-06	2.06E-03	2.95E-04	1.18E-03	7.43E-07	2.93E-04

Table A6: Data table containing elemental concentrations from the U leach (Li, Mg, Al, P, Ca, V, Cr, Mn, Fe, Rb, Sr, Zr, Mo, Re, Th, and U) for the Zhuya Group.

Sample	Height (m)	Formation	% Carbonate	Li (ppm)	Mg (wt. %)	Al (wt. %)	P (ppm)	Ca (wt. %)	V (ppm	Cr (ppm)	Mn (ppm)	Fe (wt. %)	Rb (ppm)	Sr (ppm)	Zr (ppm)	Mo (ppm)	Re (ppb)	Th (ppm)	U (ppm)
2103-280	562.21	**Khopych**	96.80	1.84	0.29	0.03	69.84	38.20	1.24	1.81	101.57	0.16	0.26	2064.49	1.25	0.04	0.25	0.26	7.10
K2103.276.75	558.96	**Khopych Reef**	94.80	1.49	0.34	0.04	58.90	38.74	3.22	4.56	96.33	0.22	0.31	4773.04	0.75	0.04	0.21	0.21	6.52
K2103.276.65	557.86		90.55	3.05	0.72	0.08	125.09	33.88	7.33	4.59	118.22	0.25	0.73	404.00	1.25	0.04		0.47	0.82
K2103.276.00	558.21		95.80	1.46	0.32	0.02	73.28	36.60	1.03	1.47	92.22	0.13	0.26	1465.69	0.86	0.04	0.19	0.26	7.32
K2103.275.90	558.11		94.14	1.60	0.33	0.04	157.18	35.77	1.20	1.79	85.10	0.21	0.34	1345.15	1.26	0.03		0.34	5.94
K2103.275.75	557.96		97.21	0.80	0.21	0.02	31.29	38.48	1.63	1.58	99.35	0.14	0.17	1681.51	0.29	0.04		0.07	2.73
K2103.275.50	557.71		69.31	5.19	0.63	0.18	309.65	25.68	4.70	8.21	136.51	0.39	1.33	985.50	3.99	0.33	0.43	1.11	3.44
K2103.275.15	557.36		90.91	2.46	0.54	0.06	94.20	32.81	2.26	2.34	122.48	0.16	0.56	495.31	0.85	0.03	0.16	0.48	1.03
K2103.275.00	557.21		96.31	0.93	0.29	0.02	53.01	42.13	0.95	1.48	107.66	0.16	0.24	9457.63	0.98	0.21	0.28	0.21	8.04
K2103.274.00	556.21		93.26	1.84	0.51	0.04	62.99	34.02	2.52	2.23	120.99	0.13	0.45	418.41	0.71	0.09	0.13	0.35	0.88
2103-273	555.21		92.27	1.71	0.57	0.04	67.44	34.49	2.45	2.45	139.59	0.15	0.39	564.40	1.21	0.04	0.14	0.31	2.80
K2103.272.55	554.76		89.60	1.82	0.64	0.04	83.78	33.57	1.66	2.39	131.84	0.17	0.37	622.50	1.04	0.04	0.17	0.32	1.57
K2103.272.30	554.51		89.10	2.85	0.41	0.05	1752.01	33.18	3.60	5.95	176.56	0.24	0.35	587.49	3.79	0.26	1.23	1.63	5.93
K2103.271.60	553.81		96.76	1.17	0.34	0.02	50.07	36.07	1.05	1.86	114.11	0.15	0.27	578.64	0.31	0.04		0.09	1.16
K2103.271.10	553.31		94.78	2.72	0.57	0.07	85.83	35.67	1.43	1.86	123.08	0.17	0.61	434.55	0.44	0.05	0.17	0.22	0.99
K2103.270.75	552.96		80.73	2.25	0.40	0.06	171.94	30.24	2.76	4.42	127.32	0.18	0.60	921.19	1.49	0.02	0.17	0.57	2.56
K2103.270.50	552.71		93.21	1.60	0.37	0.04	77.58	35.41	1.80	3.28	135.71	0.18	0.32	1178.45	1.41	0.02	0.13	0.30	9.86
2103-270	552.21		91.10	1.37	0.37	0.04	95.74	37.72	1.81	3.81	164.00	0.16	0.36	6409.14	0.76	0.03	0.18	0.33	3.78
K2103.269.00	551.21		93.53	1.14	0.32	0.02	87.34	35.57	1.38	2.52	173.73	0.13	0.23	1578.48	1.09	0.24	0.27	0.33	7.80
2103-262	544.21	**Khopych**	56.30	5.92	1.51	0.30	301.46	18.51	9.14	8.84	214.00	0.00	2.25	296.10	2.78	0.10	0.55	1.06	1.59
2103-259	541.21		98.56	1.51	0.42	0.03	55.27	37.90	1.87	2.78	189.75	0.18	0.26	3319.95	0.80	0.10	0.20	0.18	5.44
2103-244	525.21		83.50	3.19	0.98	0.12	135.77	29.88	2.85	4.45	242.20	0.27	1.06	503.52	1.12	0.04	0.30	0.66	3.22
2103-239	520.21		82.67	2.72	0.84	0.12	151.50	30.30	3.32	4.88	273.62	0.28	1.04	336.12	1.96	0.07		0.87	6.44
2103-228	509.21		95.90	1.42	0.66	0.03	93.52	43.89	1.85	3.50	217.48	0.24	0.26	14204.38	0.98	0.16		0.19	5.70
2103-214	495.21		98.59	1.54	0.37	0.04	124.77	36.49	1.63	2.74	342.40	0.21	0.24	262.45	0.52	0.02		0.41	0.81
2103-211	492.21		52.80	6.61	1.45	0.29	402.82	17.16	7.31	7.10	298.47	0.00	2.09	305.98	3.06	0.09	0.51	1.29	1.97
2103-201	480.21		94.67	1.77	0.48	0.07	72.99	35.15	1.82	3.84	211.28	0.18	0.63	575.83	0.93	0.03		0.38	6.42
2103-195	474.21		93.44	2.80	0.60	0.10	131.13	33.25	4.54	6.12	300.04	0.26	0.80	416.98	0.88	0.03	0.30	0.63	3.75
2103-192	471.21		58.00	4.84	2.22	0.32	285.43	17.17	6.87	9.60	347.43	0.00	2.85	247.33	2.50	0.08	0.50	1.29	3.66
2103-181	460.21		93.29	1.98	0.48	0.08	91.02	34.64	2.91	5.01	299.04	0.24	0.82	1781.90	1.09	0.04	0.27	0.50	7.22
2103-177	456.21		66.50	3.54	1.61	0.19	248.90	22.43	4.41	6.03	315.42	0.00	1.84	357.84	1.78	0.05	0.47	1.06	0.91
2103-171	450.21		99.05	1.49	0.28	0.06	46.83	37.31	2.14	3.28	163.04	0.25	0.37	1095.62	0.81	0.02	0.13	0.19	7.50
2103-165	444.21		96.65	3.07	0.50	0.11	94.88	36.34	1.96	4.07	186.63	0.31	0.60	1119.79	0.78			0.42	6.67
2103-155	433.85		50.30	5.42	1.73	0.26	446.73	15.57	6.49	7.55	307.30	0.00	2.13	305.90	3.24	0.06	0.51	1.35	1.22
2103-143	421.21		99.91	2.25	0.30	0.06	75.00	37.53	2.21	5.58	101.62	0.23	0.53	1199.14	1.07	0.03		0.22	8.19
2103-134	412.21		80.60	4.96	1.48	0.16	210.53	28.74	4.68	6.82	155.73	0.38	1.39	894.32	2.46	0.08	0.26	0.79	5.95
2103-122	400.21	**Alyanch**	91.40	1.27	0.33	0.06	82.18	35.21	1.69	3.17	78.19	0.00	0.65	651.13	0.70	0.02		0.26	0.65
2103-111	389.21		95.63	1.29	0.59	0.06	54.46	35.80	1.22	3.06	71.08	0.16	0.56	604.12	0.67			0.25	0.84
2103-104	382.21		95.41	0.91	0.62	0.04	49.62	36.19	1.41	3.08	74.12	0.18	0.46	586.72	0.57	0.18		0.25	1.09
2103-94	372.21		100.00	0.51	0.18	0.02	29.85	38.06	0.88	4.72	63.32	0.05	0.24	1269.06	0.50	0.04	0.14	0.12	7.37
2103-84	362.21		99.91	0.87	0.34	0.03	33.46	36.54	1.54	3.74	78.67	0.09	0.47	612.79	0.37	0.03		0.19	0.65
2103-72	350.21		92.40	2.68	0.70	0.09	156.72	34.49	2.21	4.88	107.08	0.24	0.77	1170.44	1.72	0.03		0.52	8.37
2103-66	344.21		90.85	1.51	0.79	0.06	95.30	35.49	2.32	7.69	101.56	0.25	0.65	765.42	1.12	0.05		0.38	6.05
2103-51	330.21		100.00	0.76	0.13	0.02	35.10	39.27	0.82	2.02	34.04	0.09	0.26	2732.36	0.50	0.04	0.12	0.10	11.80
2103-42	321.21		96.19	1.44	0.59	0.06	103.00	36.19	2.18	4.35	116.29	0.25	0.63	1031.24	1.42	0.05		0.39	9.24
2103-30	309.21		96.96	1.84	0.37	0.05	63.99	35.99	2.39	4.41	55.24	0.16	0.62	952.61	0.68	0.05	0.15	0.32	1.38
2103-14	293.21		94.46	1.62	0.67	0.06	84.15	35.48	2.24	4.32	58.09	0.17	0.60	743.16	0.98	0.04		0.38	1.70
2103-4	283.21		98.08	1.00	0.55	0.04	63.51	35.85	1.60	5.27	48.53	0.10	0.52	684.50	0.69	0.03		0.25	2.92
2103-M4	276.21		100.00	1.45	0.52	0.03	46.05	36.99	1.66	5.37	43.72	0.12	0.43	1383.69	0.41	0.04	0.19	0.16	6.97
2103.2-83.17	268.55		96.10	1.55	0.45	0.04	62.11	36.71	1.59	7.16	86.91	0.18	0.62	1273.82	1.03	0.04	0.14	0.31	8.09
2103.2-70.00	255.38	**Nikol'skoe**	94.26	1.67	0.73	0.08	73.89	33.79	2.22	4.51	140.78	0.21	1.10	466.66	0.72	0.02		0.43	1.82
2103.2-63.00	248.38		73.10	4.10	1.08	0.16	274.19	25.96	3.95	9.36	173.89	0.00	1.48	809.89	2.40	0.04	0.27	0.92	4.40
2103.2-58.00	243.38		91.10	1.83	0.79	0.08	128.39	33.73	2.18	4.87	158.86	0.23	0.74	953.78	1.81	0.04		0.62	7.20
2103.2-47.00 (2)	232.38		83.40	2.98	0.77	0.18	156.60	30.06	4.43	8.28	161.56	0.32	1.75	679.13	2.36	0.03	0.22	0.96	4.72
2103.2-44.00	229.38		96.85	1.67	0.53	0.08	97.01	35.06	2.75	5.12	133.98	0.21	0.79	889.81	1.29	0.01	0.17	0.59	4.93
2103.2-28.00	213.38		91.20	1.41	0.65	0.07	94.77	34.06	1.59	3.71	209.92	0.20	0.76	538.58	1.03	0.03	0.24	0.47	2.18
2102-114.35	210.23		92.90	1.45	0.45	0.07	159.12	35.23	1.60	9.80	212.88	0.15	0.82	376.46	0.69	0.02	0.17	0.48	2.69
2102-96.93	192.81		62.70	2.92	0.89	0.20	322.84	22.02	5.05	8.02	256.42	0.00	1.64	312.89	2.91	0.02	0.45	1.21	2.75
2102-91.15	187.03		97.63	1.11	0.47	0.07	60.46	35.84	3.04	4.12	309.69	0.23	0.86	468.32	0.60	0.13	0.31	0.38	2.00
2102-81.05	176.93		74.30	2.60	0.71	0.16	214.35	26.35	3.84	6.74	316.53	0.00	1.68	337.78	1.81	0.04	0.36	0.98	0.65

Table A6 cont'd: Data table containing elemental concentrations from the U leach (Li, Mg, Al, P, Ca, V, Cr, Mn, Fe, Rb, Sr, Zr, Mo, Re, Th, and U) for the Zhuya Group

Sample	Height (m)	Formation	% Carbonate	Li (ppm)	Mg (wt. %)	Al (wt. %)	P (ppm)	Ca (wt. %)	V (ppm	Cr (ppm)	Mn (ppm)	Fe (wt. %)	Rb (ppm)	Sr (ppm)	Zr (ppm)	Mo (ppm)	Re (ppb)	Th (ppm)	U (ppm)
2102-78.85	174.73	**Nikol'skoe**	99.90	0.66	0.28	0.04	48.35	37.17	1.77	5.26	286.46	0.18	0.49	1657.57	0.36	0.20	0.31	0.23	4.06
2102-64.00	159.88		75.10	2.31	0.67	0.14	226.77	27.45	3.34	6.54	388.00	0.28	1.33	1012.59	1.20	0.05	0.43	0.84	2.02
K2102.52.00	147.88		91.80	1.25	0.49	0.07	71.11	34.54	4.75	2.28	294.64	0.12	0.90	528.00	0.44	0.04	0.31	0.27	1.49
2102-51.35	147.23		98.80	0.67	0.35	0.02	58.93	38.09	0.75	0.76	336.58	0.05	0.27	565.70	0.40	0.02		0.10	0.99
K2102.51.00	146.88		90.17	2.36	0.46	0.18	109.17	34.75	6.23	4.59	340.94	0.27	1.79	3484.42	0.92	0.05	0.21	0.44	2.50
2102-39.15	135.03		97.05	1.84	0.54	0.09	217.99	34.93	2.63	11.36	585.59	0.19	0.66	341.02	0.64	0.03	0.50	0.60	0.27
2102-35.50	131.38		43.30	3.89	0.81	0.27	396.26	14.38	5.86	7.53	401.56	0.00	2.50	147.19	2.46	0.05	0.72	1.51	0.30
K2102.6.60a	102.48		96.00	0.69	0.34	0.03	43.84	37.06	1.54	1.54	318.90	0.09	0.41	870.33	0.71	0.03	0.14	0.22	1.60
2102-2.44	98.32		51.10	3.57	0.76	0.27	384.02	17.36	5.09	7.03	444.02	0.00	2.57	164.69	2.51	0.03	0.54	1.51	0.33
2101-67.85	67.85		93.00	0.61	0.45	0.02	108.01	37.43	1.29	2.01	923.09	0.12	0.29	304.06	0.60	0.07		0.33	0.82
2101-55.80	55.8		98.10	1.21	0.48	0.03	182.33	36.52	2.23	3.56	1330.14	0.10	0.45	275.69	0.48	0.17	0.63	0.57	0.44
2101-45.03	45.03		99.81	0.83	0.45	0.02	195.47	36.93	1.72	2.36	1414.95	0.11	0.31	262.64	0.99	0.42		0.65	0.96
2101-39.02	39.02		100.00	1.59	0.57	0.07	322.24	31.34	2.64	4.46	1575.63	0.20	1.08	251.66	1.76	0.17		1.16	0.52
2101-34.17	34.17		94.11	2.23	0.80	0.10	356.96	31.32	3.03	5.67	2393.70	0.22	1.39	221.50	1.43	0.04		1.27	0.42

Table A7: Data table containing % carbonate, isotopic data ($\delta^{13}C$, $\delta^{18}O$, $\delta^{238}U$ and associated uncertainties) and elemental ratios from the U leach (Mg/Ca, Mn/Sr, Sr/Ca, Rb/Sr, U/Th, U/Al, Mo/(Mg+Ca), U/(Mg+Ca), Sr/(Mg+Ca), Mn/(Mg+Ca)) for the Zhuya Group.

Sample	Height (m)	Formation	$\delta^{13}C$	$\delta^{18}O$	% Carbonate	$\delta^{238}U$	2σ	Mg/Ca	Mn/Sr	Sr/Ca	Rb/Sr	U/Th	U/Al (ppm/wt.%)	Mo/(Mg+Ca)	U/(Mg+Ca)	Sr/(Mg+Ca)	Mn/(Mg+Ca)
2103-285	567.21	**Khopych**	-9.46	-9.67	96.25												
2103-282	564.21		-7.69	-9.27	98.26												
2103-280	562.21		-7.63	-8.88	96.8	-0.31	0.06	0.01	0.05	54.05	0.00	27.83	205.83	0.00	0.18	53.64	2.64
2103-277	559.21		-9.39	-8.95	85.45												
K2103.276.75	558.96	**Khopych Reef**	-9.12	-9.10	94.8			0.01	0.02	123.22	0.00	31.06	185.84	0.00	0.17	122.14	2.47
K2103.276.65	557.86		-9.27	-9.38	90.55	-0.27	0.13	0.02	0.29	11.92	0.00	1.76	9.79	0.00	0.02	11.68	3.42
K2103.276.00	558.21		-8.25	-9.30	95.8	-0.28	-0.10	0.01	0.06	40.05	0.00	28.46	305.85	0.00	0.20	39.70	2.50
K2103.275.90	558.11		-8.00	-9.34	94.14			0.01	0.06	37.61	0.00	17.71	152.82	0.00	0.16	37.26	2.36
K2103.275.75	557.96		-7.75	-10.15	97.21			0.01	0.06	43.70	0.00	38.67	144.88	0.00	0.07	43.46	2.57
K2103.275.50	557.71		-8.32	-9.36	69.31			0.02	0.14	38.38	0.00	3.11	19.43	0.01	0.13	37.47	5.19
K2103.275.15	557.36		-8.21	-9.27	90.91			0.02	0.25	15.10	0.00	2.17	16.57	0.00	0.03	14.85	3.67
K2103.275.00	557.21		-7.90	-8.99	96.31			0.01	0.01	224.51	0.00	38.98	347.44	0.01	0.19	222.99	2.54
K2103.274.00	556.21		-9.62	-9.37	93.26			0.01	0.29	12.30	0.00	2.51	19.86	0.00	0.03	12.12	3.50
2103-273	555.21		-8.09	-9.11	92.27	-0.03	0.06	0.02	0.25	16.36	0.00	9.11	69.77	0.00	0.08	16.10	3.98
K2103.272.55	554.76		-8.14	-9.40	89.6	-0.14	0.14	0.02	0.21	18.54	0.00	4.93	38.32	0.00	0.05	18.20	3.85
K2103.272.30	554.51		-10.08	-9.47	89.1			0.01	0.30	17.71	0.00	3.63	116.30	0.01	0.18	17.49	5.26
K2103.271.60	553.81		-8.19	-9.58	96.76	-0.14	0.11	0.01	0.20	16.04	0.00	13.53	47.96	0.00	0.03	15.89	3.13
K2103.271.10	553.31		-8.10	-9.45	94.78	-0.01	0.08	0.02	0.28	12.18	0.00	4.52	13.91	0.00	0.03	11.99	3.40
K2103.270.75	552.96		-8.43	-9.43	80.73			0.01	0.14	30.46	0.00	4.51	44.06	0.00	0.08	30.06	4.15
K2103.270.50	552.71		-8.22	-8.82	93.21			0.01	0.12	33.28	0.00	32.42	267.69	0.00	0.28	32.93	3.79
2103-270	552.21		-8.19	-9.57	91.1			0.01	0.03	169.91	0.00	11.57	105.93	0.00	0.10	168.26	4.31
K2103.269.00	551.21		-8.24	-8.82	93.53			0.01	0.11	44.37	0.00	23.85	335.42	0.01	0.22	43.97	4.84
2103-268	550.21	**Khopych**	-8.16	-9.21	51.77												
2103-265	547.21		-8.02	-9.38	92.39												
2103-262	544.21		-8.04	-8.95	56.3			0.08	0.72	16.00	0.01	1.49	5.34	0.01	0.08	14.79	10.69
2103-259	541.21		-8.06	-9.30	98.56	-0.30	0.02	0.01	0.06	87.60	0.00	30.22	173.67	0.00	0.14	86.64	4.95
2103-255	536.835		-8.38	-9.93	59.04												
2103-252	533.46		-8.25	-9.50	81.79												
2103-248	529.21		-9.28	-9.52	81.97												
2103-244	525.21		-8.10	-9.21	83.5	-0.17	0.07	0.03	0.48	16.85	0.00	4.86	27.38	0.00	0.10	16.32	7.85
2103-242	523.21		-8.53	-9.49	88.16												
2103-239	520.21		-8.42	-9.50	82.67			0.03	0.81	11.09	0.00	7.38	52.89	0.00	0.21	10.79	8.79
2103-236	517.21		-8.59	-9.05	70.92												
2103-233	514.21		-8.25	-8.76	60.67												
2103-230	511.21		-8.29	-9.40	64.33												
2103-228	509.21		-8.47	-9.37	95.9	-0.21	0.13	0.01	0.02	323.67	0.00	30.39	182.37	0.00	0.13	318.90	4.88
2103-225	506.21		-9.04	-9.52	92.51												
2103-222	503.21		-8.72	-9.55	66.97												
2103-219	500.21		-9.06	-9.42	74.55												
2103-216	497.21		-9.12	-9.23	68.3												
2103-214	495.21		-9.41	-9.59	98.59			0.01	1.30	7.19	0.00	1.98	19.52	0.00	0.02	7.12	9.29
2103-211	492.21		-9.24	-9.25	52.8			0.08	0.98	17.83	0.01	1.53	6.70	0.00	0.11	16.44	16.04
2103-209	489.41		-9.28	-9.38	89.66												
2103-206	485.21		-9.12	-9.17	78.71												
2103-203	482.21		-9.11	-9.10	60.05												
2103-201	480.21		-9.37	-9.43	94.67			0.01	0.37	16.38	0.00	16.93	92.34	0.00	0.18	16.16	5.93
2103-198	477.21		-8.95	-8.92	74.49												
2103-195	474.21		-9.06	-9.05	93.44	-0.18	0.06	0.02	0.72	12.54	0.00	5.95	38.25	0.00	0.11	12.32	8.86
2103-192	471.21		-8.91	-8.43	58			0.13	1.40	14.40	0.01	2.82	11.44	0.00	0.19	12.75	17.91
2103-189	468.21		-9.10	-9.17	83.74												
2103-187	466.21		-9.31	-8.89	53.45												
2103-184	463.21		-9.43	-8.72	59.13												
2103-181	460.21		-9.51	-9.45	93.29	-0.37	0.06	0.01	0.17	51.43	0.00	14.52	88.22	0.00	0.21	50.73	8.51
2103-177	456.21		-9.15	-9.16	66.5			0.07	0.88	15.95	0.01	0.87	4.78	0.00	0.04	14.89	13.12
2103-174	453.21		-9.12	-9.89	96.88												
2103-171	450.21		-9.26	-9.75	99.05	-0.15	0.05	0.01	0.15	29.36	0.00	40.08	123.39	0.00	0.20	29.14	4.34
2103-168	447.21		-8.96	-8.92	55.35												
2103-165	444.21		-9.01	-9.53	96.65			0.01	0.17	30.81	0.00	15.81	60.76	0.00	0.18	30.39	5.07
2103-162	441.21		-9.22	-8.76	61.71												
2103-159	438.21		-9.25	-8.89	64.75												
2103-155	433.85		-9.12	-8.63	50.3			0.11	1.00	19.65	0.01	0.91	4.64	0.00	0.07	17.68	17.76
2103-152	430.37		-9.39	-9.25	76.88												
2103-149	427.21		-9.18	-8.89	68.62												
2103-146	424.21		-9.13	-9.26	96.19												
2103-143	421.21		-9.14	-9.26	99.91	-0.25	0.01	0.01	0.08	31.95	0.00	36.45	130.78	0.00	0.22	31.70	2.69
2103-140	418.21		-9.29	-9.13	85.82												
2103-137	415.21		-8.95	-8.78	74.93												
2103-134	412.21		-9.46	-8.90	80.6	-0.22	0.08	0.05	0.17	31.12	0.00	7.50	36.58	0.00	0.20	29.59	5.15
2103-131	409.21		-9.27	-9.30	82.4												
2103-129	407.21		-9.79	-9.21	95.02												
2103-126	404.21																
2103-122	400.21	**Alyanch**	-9.63	-9.42	91.4	-0.31	0.17	0.01	0.12	18.49	0.00	2.50	11.68	0.00	0.02	18.32	2.20
2103-120	398.21		-9.71	-9.41	95.66												
2103-117	395.21		-9.42	-9.23	95.77												
2103-114	392.21		-9.58	-10.17	93.89												
2103-111	389.21		-9.13	-9.44	95.63			0.02	0.12	16.88	0.00	3.35	14.21		0.02	16.60	1.95
2103-107	385.21		-9.70	-9.36	97.57												
2103-104	382.21		-9.09	-9.65	95.41			0.02	0.13	16.21	0.00	4.44	27.38	0.00	0.03	15.94	2.01
2103-101	379.21		-9.27	-9.83	95.16												
2103-98	376.21		-9.17	-9.53	94												
2103-94	372.21		-9.53	-9.40	100	-0.21	0.09	0.00	0.05	33.34	0.00	61.95	417.00	0.00	0.19	33.19	1.66
2103-91	369.21		-9.37	-9.42	90.72												
2103-88	366.21		-9.33	-9.69	94.52												
2103-84	362.21		-9.50	-9.48	99.91	-0.24	0.01	0.01	0.13	16.77	0.00	3.38	18.62	0.00	0.02	16.62	2.13
2103-82	360.21		-9.38	-9.50	94.96												
2103-79	357.21		-9.55	-9.48	91.92												
2103-76	354.21		-9.55	-9.59	94.68												
2103-72	350.21		-9.59	-9.29	92.4			0.02	0.09	33.94	0.00	16.21	97.96	0.00	0.24	33.27	3.04
2103-69	347.21		-9.78	-9.27	90.87												
2103-66	344.21		-9.66	-9.38	90.85			0.02	0.13	21.57	0.00	15.92	107.79	0.00	0.17	21.09	2.80
2103-64	342.21		-9.79	-9.60													
2103-60	338.21		-9.82	-9.51													
2103-57	335.21		-9.49	-9.49													
2103-55	333.21		-9.73	-9.66													
2103-51	330.21		-8.37	-9.52	100	-0.26	0.06	0.00	0.01	69.58	0.00	123.70	538.04	0.00	0.30	69.35	0.86
2103-48	327.21		-8.32	-9.54													

Table A7 cont'd: Data table containing % carbonate, isotopic data ($\delta^{13}C$, $\delta^{18}O$, $\delta^{238}U$ and associated uncertainties) and elemental ratios from the U leach (Mg/Ca, Mn/Sr, Sr/Ca, Rb/Sr, U/Th, U/Al, Mo/(Mg+Ca), U/(Mg+Ca), Sr/(Mg+Ca), Mn/(Mg+Ca)) for the Zhuya Group.

Sample	Height (m)	Formation	$\delta^{13}C$	$\delta^{18}O$	% Carbonate	$\delta^{238}U$	2σ	Mg/Ca	Mn/Sr	Sr/Ca	Rb/Sr	U/Th	U/Al (ppm/wt.%)	Mo/(Mg+Ca)	U/(Mg+Ca)	Sr/(Mg+Ca)	Mn/(Mg+Ca)
2103-45	324.21	Alyanch	-8.70	-9.38													
2103-42	321.21		-9.48	-9.38	96.19			0.02	0.11	28.50	0.00	23.40	161.44	0.00	0.25	28.04	3.16
2103-39	318.21		-9.39	-9.40													
2103-36	315.21		-9.13	-9.49													
2103-33	312.21		-9.44	-9.77													
2103-30	309.21		-9.92	-9.55	96.96	-0.34	0.04	0.01	0.06	26.47	0.00	4.36	26.35	0.00	0.04	26.20	1.52
2103-27	306.21																
2103-23	302.21		-9.93	-9.28	96.45												
2103-20	299.21		-9.92	-9.47													
2103-17	296.21																
2103-14	293.21		-9.80	-9.47	94.46			0.02	0.08	20.94	0.00	4.48	30.17	0.00	0.05	20.55	1.61
2103-11	290.21		-9.86	-9.33													
2103-7	285.21		-9.76	-9.66													
2103-4	283.21		-9.95	-9.51	98.08	-0.14	0.10	0.02	0.07	19.09	0.00	11.60	71.72	0.00	0.08	18.80	1.33
2103-1	280.21		-10.23	-9.85													
2103-M4	276.21		-10.28	-9.56	100	-0.18	0.03	0.01	0.03	37.40	0.00	43.48	242.31	0.00	0.19	36.89	1.17
2103-M7	273.21		-10.21	-9.59													
2103-M10	270.21		-10.28	-9.55													
2103.2-83.17	268.55		-9.96	-9.58	96.1	-0.25	0.00	0.01	0.07	34.70	0.00	26.01	193.52	0.00	0.22	34.29	2.34
2103.2-81.70	267.08		-9.97	-9.41													
2103.2-79.10	264.48		-10.21	-9.47													
2103.2-75.00	260.38		-10.01	-9.58													
2103.2-72.00	257.38		-10.16	-9.58													
2103.2-70.00	255.38	Nikol'skoe	-10.28	-9.62	94.26	-0.36	0.05	0.02	0.30	13.81	0.00	4.24	23.16	0.00	0.05	13.52	4.08
2103.2-67.00	252.38		-10.38	-9.60	70.2												
2103.2-63.00	248.38		-10.42	-9.49	73.1			0.04	0.21	31.20	0.00	4.77	27.02	0.00	0.16	29.95	6.43
2103.2-60.00 (2)	245.38		-10.12	-9.67	86.92												
2103.2-58.00	243.38		-10.18	-10.08	91.1			0.02	0.17	28.28	0.00	11.60	89.66	0.00	0.21	27.63	4.60
2103.2-56.00	241.38		-10.24	-9.84	84.27												
2103.2-53.00	238.38		-10.37	-9.71	92.91												
2103.2-50.00	235.38		-10.38	-9.67	86.24												
2103.2-47.00 (2)	232.38		-10.17	-9.65	83.4	-0.20	0.10	0.03	0.24	22.59	0.00	4.90	26.48	0.00	0.15	22.03	5.24
2103.2-44.00	229.38		-10.28	-9.69	96.85	-0.09	0.09	0.02	0.15	25.38	0.00	8.32	59.48	0.00	0.14	25.01	3.77
2103.2-41.00	226.38		-10.46	-10.16	95.2												
2103.2-37.90	223.28		-10.65	-10.03	88.13												
2103.2-34.00	219.38		-10.60	-10.10													
2103.2-32.00	217.38		-10.53	-10.55													
2103.2-28.00	213.38		-10.49	-9.70	91.2	-0.15	0.12	0.02	0.39	15.81	0.00	4.65	29.32	0.00	0.06	15.52	6.05
2102-114.35	210.23		-10.76	-9.91	92.9	-0.29	0.13	0.01	0.57	10.69	0.00	5.58	39.10	0.00	0.08	10.55	5.97
2102-111.00	206.88		-10.79	-9.81													
2102-109.55	205.43		-10.67	-9.84													
2102-105.45	201.33		-10.99	-9.93													
2102-103.50	199.38		-11.06	-10.35													
2102-100.50	196.38		-10.97	-10.45	78.3												
2102-96.93	192.81		-10.82	-10.15	62.7			0.04	0.82	14.21	0.01	2.27	13.74	0.00	0.12	13.65	11.19
2102-94.00	189.88		-10.84	-10.18	70.81												
2102-91.15	187.03		-11.44	-10.35	97.63	-0.22	0.09	0.01	0.66	13.07	0.00	5.23	30.41	0.00	0.06	12.90	8.53
2102-89.40	185.28		-11.16	-10.47	61.75												
2102-85.67	181.55		-11.19	-10.47	79.22												
2102-82.80	178.68		-11.62	-11.03	72.6												
2102-81.05	176.93		-11.68	-10.49	74.3			0.03	0.94	12.82	0.00	0.66	3.98	0.00	0.02	12.48	11.70
2102-78.85	174.73		-12.03	-11.31	99.9	-0.25	0.10	0.01	0.17	44.59	0.00	17.54	112.43	0.01	0.11	44.26	7.65
2102-74.30	170.18		-11.76	-10.82	84.57												
2102-70.47	166.35		-11.13	-10.50	46.32												
2102-67.13	163.01		-11.69	-10.85													
2102-64.00	159.88		-11.26	-10.64	75.1			0.02	0.38	36.89	0.00	2.40	14.68	0.00	0.07	36.01	13.80
2102-60.50	156.38		-11.54	-10.80	68.74												
2102-57.80	153.68		-11.65	-10.59	88.1												
2102-54.88	150.76		-11.55	-10.76	57.12												
K2102.52.00	147.88		-12.10	-10.93	91.8	-0.05	0.04	0.01	0.56	15.29	0.00	5.58	22.60	0.00	0.04	15.07	8.41
2102-51.35	147.23		-11.53	-10.83	98.8	-0.28	0.04	0.01	0.59	14.85	0.00	9.74	56.72	0.00	0.03	14.71	8.76
K2102.51.00	146.88		-11.63	-10.37	90.17	0.09	0.11	0.01	0.10	100.26	0.00	5.70	13.55	0.00	0.07	98.95	9.68
2102-49.20	145.08		-11.80	-10.97													
2102-45.34	141.22		-11.63	-10.87													
2102-43.71	139.59		-12.10	-10.87													
2102-41.85	137.73		-12.09	-10.66	96.33												
2102-39.15	135.03		-12.22	-10.89	97.05	-0.36	0.03	0.02	1.72	9.76	0.00	0.46	3.10	0.00	0.01	9.61	16.51
2102-35.50	131.38		-11.52	-10.45	43.3			0.08	2.73	10.23	0.02	0.20	1.12	0.00	0.02	9.69	26.43
2102-31.10	126.98		-12.03	-11.08	98.5												
2102-29.30	125.18		-11.79	-10.81	82.16												
2102-25.23	121.11		-11.89	-11.39	51.88												
2102-22.40	118.28		-11.54	-10.96													
2102-19.60	115.48		-12.32	-10.96													
2102-16.10	111.98		-12.28	-11.12	97.54												
2102-13.86	109.74		-12.35	-11.18	97.97												
2102-9.86	105.74		-12.48	-11.24	97.82												
K2102.6.60a	102.48		-11.98	-10.90	96	-0.15	0.01	0.01	0.37	23.48	0.00	7.45	58.84	0.00	0.04	23.27	8.53
2102-6.34	102.22		-12.32	-10.99	81.79												
2102-2.44	98.32		-12.02	-11.26	51.1			0.04	2.70	9.48	0.02	0.22	1.20	0.00	0.02	9.09	24.50
2102.1-10.13	76.01		-12.72	-11.45	100												
2102.1-7.55	73.43		-12.78	-11.38	100												
2102.1-5.35	71.23		-12.88	-11.34	100												
2101-67.85	67.85		-12.82	-11.41	93	0.08	0.06	0.01	3.04	8.12	0.00	2.53	37.82	0.00	0.02	8.03	24.37
2101-64.45	64.45		-12.87	-11.69	90.12												
2101-61.51	61.51		-12.76	-11.90	100												
2101-58.16	58.16		-12.76	-12.22	96												
2101-55.80	55.8		-12.81	-11.77	98.1	0.10	0.10	0.01	4.82	7.55	0.00	0.77	13.22	0.00	0.01	7.45	35.95
2101-53.84	53.84		-12.67	-11.49	77												
2101-50.96	50.96		-11.09	-11.45	32												
2101-48.78	48.78		-12.90	-12.19	96												
2101-45.03	45.03		-12.77	-11.65	99.81	-0.05	0.23	0.01	5.39	7.11	0.00	1.49	40.40	0.01	0.03	7.03	37.85
2101-44.83	44.83		-12.39	-11.88	95.29												
2101-42.56	42.56		-12.36	-11.12	59												
2101-39.02	39.02		-12.74	-11.42	100			0.02	6.26	8.03	0.00	0.45	7.16	0.01	0.02	7.89	49.37
2101-36.96	36.96		-12.03	-11.53	54												
2101-34.17	34.17		-12.82	-11.95	94.11	-0.21	0.05	0.03	10.81	7.07	0.01	0.33	4.10	0.00	0.01	6.90	74.52

Table A7 cont'd: Data table containing % carbonate, isotopic data ($\delta^{13}C$, $\delta^{18}O$, $\delta^{238}U$ and associated uncertainties) and elemental ratios from the U leach (Mg/Ca, Mn/Sr, Sr/Ca, Rb/Sr, U/Th, U/Al, Mo/(Mg+Ca), U/(Mg+Ca), Sr/(Mg+Ca), Mn/(Mg+Ca)) for the Zhuya Group.

Sample	Height (m)	Formation	$\delta^{13}C$	$\delta^{18}O$	% Carbonate	$\delta^{238}U$	2σ	Mg/Ca	Mn/Sr	Sr/Ca	Rb/Sr	U/Th	U/Al (ppm/wt.%)	Mo/(Mg+Ca)	U/(Mg+Ca)	Sr/(Mg+Ca)	Mn/(Mg+Ca)
2101-30.00	30	**Nikol'skoe**	-11.36	-11.37	48												
2101-17.80	17.8		-11.28	-10.99	42												
2101-8.95	8.95		-7.83	-11.59	28												

Table A8: Data table containing % carbonate and elemental concentrations from the REE leach (Li, Mg, Al, Ca, Ti, Mn, Fe, Rb, Sr, Zr, and U) for the Zhuya Group. Note red means interpret with caution.

Sample	Height (m)	Formation	% Carbonate	Li (ppm)	Mg (wt. %)	Al (wt. %)	Ca (wt. %)	Ti (ppm)	Mn (ppm)	Fe (wt. %)	Rb (ppm)	Sr (ppm)	Zr (ppm)	U (ppm)
2103-280	562.21	Khopych	96.80	0.92	0.29	0.01	40.05	0.75	122.74	0.05	0.07	2196.58	0.09	6.80
K2103.276.75	558.96	Khopych Reef	94.80		0.27	0.00	43.31		127.65	0.04	0.05	2856.61		5.73
K2103.276.65	557.86		90.55		0.44	0.00	41.05		155.86	0.03	0.08	453.25		0.86
K2103.276.00	558.21		95.80		0.38	0.00	45.32		130.98	0.03	0.06	1682.89	0.04	8.02
K2103.275.90	558.11		94.14		0.29	0.00	34.13		93.04	0.02	0.05	1203.27	0.03	4.53
K2103.275.75	557.96		97.21		0.25	0.00	45.64		137.06	0.05	0.03	1931.09	0.03	2.96
K2103.275.15	557.36		90.91		0.48	0.00	37.40		164.96	0.03	0.06	530.89		1.22
K2103.275.00	557.21		96.31		0.24	0.00	45.91		139.95	0.02	0.05	3883.24	0.03	7.20
K2103.274.00	556.21		93.26		0.52	0.00	39.68		178.05	0.03	0.05	448.13	0.02	1.07
K2103.273.00	555.21		92.27		0.43	0.00	41.63		188.77	0.04	0.05	618.37	0.03	3.15
K2103.272.55	554.76		89.60		0.43	0.01	39.93	1.57	169.47	0.05	0.16	634.14	0.12	1.99
K2103.272.30	554.51		89.10		0.45	0.00	43.07		265.56	0.02	0.07	707.22	0.06	2.91
K2103.271.60	553.81		96.76		0.37	0.00	40.87		158.62	0.06	0.05	562.29		1.37
K2103.271.10	553.31		94.78		0.46	0.00	38.77		163.02	0.04	0.07	427.65	0.03	1.08
K2103.270.75	552.96		80.73		0.38	0.01	39.77		192.54	0.06	0.11	1135.92	0.05	3.39
K2103.270.50	552.71		93.21		0.38	0.00	41.19		193.79	0.06	0.07	1273.29	0.06	7.00
K2103.270.00	552.21		91.10		0.39	0.01	49.65	1.11	251.04	0.07	0.11	5453.71	0.07	5.61
K2103.269.00	551.21		93.53		0.34	0.00	42.14		234.95	0.04	0.05	1285.47	0.05	5.68
2103-259	541.21	Khopych	98.56	0.73	0.35	0.00	38.98	0.28	223.02	0.02	0.04	1580.31	0.06	5.46
2103-244	525.21		83.50	1.65	1.00	0.00	34.01	0.56	296.86	0.08	0.22	539.09	0.05	3.20
2103-239	520.21		82.67	0.88	0.44	0.00	37.01		342.52	0.06	0.18	392.86	0.09	4.87
2103-228	509.21		95.90	0.67	0.65	0.00	42.67	0.19	247.71	0.07	0.05	8696.03	0.05	4.45
2103-214	495.21		98.59	0.79	0.29	0.00	38.23		409.63	0.09	0.04	263.78	0.04	0.87
2103-201	480.21		94.67	1.14	0.50	0.00	38.84	0.84	260.13	0.06	0.15	604.29	0.07	5.31
2103-195	474.21		93.44	0.98	0.39	0.00	35.19	0.27	350.80	0.06	0.11	410.29	0.05	2.96
2103-181	460.21		93.29	0.71	0.37	0.00	38.91	0.81	382.18	0.06	0.12	1096.01		5.95
2103-171	450.21		99.05	0.62	0.22	0.00	36.29	0.19	173.91	0.06	0.05	999.16	0.07	6.57
2103-165	444.21		96.65	1.15	0.38	0.00	36.43	0.38	205.63	0.07	0.13	1135.26	0.04	4.78
2103-143	421.21		99.91	0.62	0.22	0.00	37.40	0.12	113.37	0.02	0.06	1111.11	0.04	7.19
2103-134	412.21		80.60	1.72	1.10	0.02	35.41	4.06	166.67	0.08	0.40	1069.63	0.14	6.15
2103-122	400.21	Alyanch Formation	91.40	0.46	0.33	0.00	37.80	0.20	93.29	0.04	0.12	656.66	0.03	0.62
2103-111	389.21		95.63	0.47	0.43	0.00	37.56	0.23	82.99	0.04	0.10	596.29	0.03	0.71
2103-104	382.21		95.41	0.30	0.44	0.00	38.35	0.14	85.68	0.02	0.07	588.71	0.02	0.80
2103-94	372.21		100.00	0.18	0.13	0.00	35.09	0.78	66.38	0.00	0.03	1013.36	0.02	6.25
2103-84	362.21		99.91	0.26	0.29	0.00	37.91	0.19	91.97	0.02	0.07	568.78	0.01	0.59
2103-72	350.21		94.96	0.54	0.37	0.00	37.24	0.12	123.42	0.03	0.11	1234.23	0.03	6.73
2103-66	344.21		92.40	0.34	0.31	0.00	38.83		109.39	0.03	0.14	753.51	0.08	6.00
2103-51	330.21		100.00	0.27	0.12	0.00	37.88	0.25	33.38	0.01	0.04	2496.35	0.02	10.22
2103-42	321.21		96.19	0.36	0.23	0.00	37.80	0.15	127.27	0.01	0.09	1071.61	0.02	6.36
2103-30	309.21		96.96	0.49	0.30	0.00	36.94	0.25	62.47	0.02	0.08	894.89	0.02	1.38
2103-23	302.21		96.45	0.47	0.40	0.00	38.84	0.11	96.42	0.02	0.09	1177.52	0.02	5.33
2103-14	293.21		94.46	0.42	0.28	0.00	35.27	0.26	53.55	0.01	0.08	712.13	0.01	1.21
2103-4	283.21		98.08	0.27	0.22	0.00	36.49	0.28	46.41	0.01	0.09	617.63	0.03	2.45
2103-M4	276.21		100.00	0.31	0.50	0.00	35.13	0.15	46.43	0.01	0.08	1219.96	0.02	6.80
2103.2-83.17	268.55		96.10	0.60	0.41	0.00	36.80	0.36	98.26	0.03	0.12	1225.43	0.03	7.47
2103.2-70.00	255.38	Nikol'skoe	94.26	0.65	0.53	0.00	37.39	0.19	170.38	0.04	0.20	473.95	0.01	1.83
2103.2-58.00	243.38		91.10	0.60	0.50	0.00	39.51		192.73	0.05	0.11	1001.27	0.10	8.69

Table A8 cont'd: Data table containing % carbonate and elemental concentrations from the REE leach (Li, Mg, Al, Ca, Ti, Mn, Fe, Rb, Sr, Zr, and U) for the Zhuya Group. Note red means interpret with caution.

Sample	Height (m)	Formation	% Carbonate	Li (ppm)	Mg (wt. %)	Al (wt. %)	Ca (wt. %)	Ti (ppm)	Mn (ppm)	Fe (wt. %)	Rb (pm)	Sr (ppm)	Zr (ppm)	U (ppm)
2103.2-53.00	238.38	Nikol'skoe	92.91	0.64	0.35	0.00	37.50	0.22	189.36	0.01	0.16	795.41	0.02	4.50
2103.2-47.00(2)	232.38		83.40	1.06	0.61	0.00	35.20	0.31	188.98	0.06	0.35	755.67	0.03	4.26
2103.2-44.00	229.38		96.85	0.54	0.35	0.00	40.24		164.19	0.06	0.14	931.84	0.07	7.19
2103.2-28.00	213.38		91.20	0.56	0.36	0.00	35.37	0.28	232.89	0.04	0.14	526.34	0.03	2.08
2102-114.35	210.23		92.90	0.71	0.37	0.00	35.71	0.14	237.61	0.03	0.12	354.03	0.02	2.84
2102-91.15	187.03		97.63	0.46	0.41	0.00	36.25	0.21	331.51	0.01	0.14	454.11	0.01	1.18
2102-78.85	174.73		99.90	0.24	0.22	0.00	38.21		347.96	0.02	0.06	1143.86	0.05	5.74
2102-57.80	153.68		88.10	0.53	0.46	0.00	37.28		591.28	0.06	0.11	309.41	0.03	0.72
K2102.52.00	147.88		91.80		0.53	0.02	43.34	2.48	443.94	0.03	0.29	616.25	0.09	2.14
2102-51.35	147.23		98.80	0.44	0.32	0.00	36.00	0.19	378.82	0.00	0.05	514.56	0.01	1.06
K2102.51.00	146.88		90.17		0.39	0.01	45.94	0.71	481.58	0.02	0.36	4039.10	0.07	2.82
2102-39.15	135.03		97.05	1.04	0.50	0.00	39.20	0.36	761.50	0.00	0.13	359.17	0.02	0.26
2102-31.10	126.98		98.50	0.42	0.36	0.00	37.33		746.41	0.06	0.08	286.91	0.03	0.43
2102-16.10	111.98		97.54	0.49	0.38	0.00	36.28		635.88	0.01	0.08	279.62	0.02	0.24
2102-13.86	109.74		97.97	0.46	0.39	0.01	34.70	0.57	579.98	0.03	0.16	255.84	0.02	0.31
K2102.6.60a	102.48		96.00		0.38	0.00	41.51		434.32	0.02	0.05	828.57	0.02	2.07
2102.1-10.13	76.01		100.00	0.48	0.42	0.00	36.34	0.76	860.34	0.00	0.12	297.83	0.05	0.19
2102.1-5.35	71.23		100.00	0.44	0.43	0.00	37.06	0.21	1105.62	0.00	0.13	292.15	0.03	0.16
2101-67.85	67.85		93.00	0.31	0.34	0.00	36.19		1023.16	0.01	0.04	280.68	0.02	0.64
2101-55.80	55.8		98.10	0.52	0.38	0.00	33.93	0.27	1318.43	0.00	0.07	237.83	0.02	0.31
2101-45.03	45.03		99.81	0.45	0.38	0.00	36.50		1586.80	0.00	0.04	245.22	0.05	0.80
2101-42.56	42.56		59.00	4.53	0.99	0.40	22.83	9.44	2193.44	0.56	1.87	170.28	0.12	0.42
2101-39.02	39.02		100.00	0.57	0.36	0.00	36.84	0.63	1957.91	0.00	0.08	271.29	0.05	0.37
2101-34.17	34.17		94.11	0.94	0.55	0.00	36.69		3093.56	0.03	0.19	247.02	0.04	0.35

Table A9: Data table containing elemental ratios from the REE leach (Mn/Sr, Mg/Ca, Sr/Ca, Mn/Fe, Y/Ho, Ce/Ce*, Eu/Eu*, MREE/MREE*, Nd/Yb, and ∑REE) for the Zhuya Group. Note red means interpret with caution.

Sample	Height (m)	Formation	Mn/Sr	Mg/Ca	Sr/Ca	Mn/Fe	Y/Ho	Ce/Ce*	Eu/Eu*	MREE/MREE*	Nd/Yb	∑REE
2103-280	562.21	Khopych	0.06	0.01	54.85	0.25	42.95	0.93	1.12	1.17	1.10	2.48
K2103.276.75	558.96	Khopych Reef	0.04	0.01	65.95	0.31	61.06	1.34	0.93	1.17	1.28	0.80
K2103.276.65	557.86		0.34	0.01	11.04	0.45	56.89	1.42	1.04	0.90	1.39	1.46
K2103.276.00	558.21		0.08	0.01	37.14	0.45	49.08	1.33	0.92	1.05	1.06	2.52
K2103.275.90	558.11		0.08	0.01	35.25	0.37	58.32	1.43	1.08	0.99	1.10	1.17
K2103.275.75	557.96		0.07	0.01	42.31	0.25	57.07	1.38	1.04	1.00	1.42	1.85
K2103.275.15	557.36		0.31	0.01	14.19	0.53	49.79	1.41	0.97	0.98	1.22	1.63
K2103.275.00	557.21		0.04	0.01	84.59	0.87	67.13	1.42	0.86	0.99	1.52	3.95
K2103.274.00	556.21		0.40	0.01	11.29	0.56	50.06	1.41	0.99	0.95	0.99	0.81
K2103.273.00	555.21		0.31	0.01	14.86	0.49	47.19	1.36	0.98	0.91	1.02	1.39
K2103.272.55	554.76		0.27	0.01	15.88	0.31	36.31	1.33	1.03	1.14	1.22	3.14
K2103.272.30	554.51		0.38	0.01	16.42	1.23	28.50	1.27	1.08	1.29	1.81	0.46
K2103.271.60	553.81		0.28	0.01	13.76	0.25	53.03	1.36	0.85	1.12	0.93	0.45
K2103.271.10	553.31		0.38	0.01	11.03	0.46	53.75	1.54	0.84	0.97	0.97	0.83
K2103.270.75	552.96		0.17	0.01	28.56	0.32	48.10	1.45	0.99	0.93	1.61	6.14
K2103.270.50	552.71		0.15	0.01	30.92	0.31	51.01	1.37	0.96	0.96	1.09	3.23
K2103.270.00	552.21		0.05	0.01	109.85	0.38	37.35	1.27	1.13	1.14	1.15	4.93
K2103.269.00	551.21		0.18	0.01	30.50	0.59	45.70	1.36	1.02	1.04	1.41	12.68
2103-259	541.21	Khopych	0.14	0.01	40.54	0.94	71.89	0.60	1.19	1.00	1.29	0.91
2103-244	525.21		0.55	0.03	15.85	0.37	58.16	0.97	1.03	1.04	1.07	2.35
2103-239	520.21		0.87	0.01	10.61	0.57	43.93	1.36	1.00	1.03	0.71	2.90
2103-228	509.21		0.03	0.02	203.81	0.33	71.34	0.75	1.35	1.13	1.32	1.45
2103-214	495.21		1.55	0.01	6.90	0.46	38.43	1.51	1.02	0.97	0.52	0.79
2103-201	480.21		0.43	0.01	15.56	0.42	71.63	0.62	1.10	0.92	1.09	1.02
2103-195	474.21		0.85	0.01	11.66	0.59	70.56	0.75	1.07	0.85	0.85	1.35
2103-181	460.21		0.35	0.01	28.17	0.58	72.18	0.81	1.11	1.00	0.96	1.71
2103-171	450.21		0.17	0.01	27.54	0.29	80.78	0.61	1.07	0.93	1.38	0.98
2103-165	444.21		0.18	0.01	31.17	0.30	52.78	0.99	1.03	1.07	1.10	1.27
2103-143	421.21		0.10	0.01	29.71	0.57	113.69	0.22	1.07	0.66	0.74	0.16
2103-134	412.21		0.16	0.03	30.21	0.20	40.27	1.21	1.02	1.01	1.60	6.72
2103-122	400.21	Alyanch	0.14	0.01	17.37	0.20	63.58	0.69	1.10	0.98	1.28	0.46
2103-111	389.21		0.14	0.01	15.88	0.18	64.26	0.74	1.16	0.92	1.01	0.51
2103-104	382.21		0.15	0.01	15.35	0.35	49.19	1.29	0.99	1.03	0.87	0.36
2103-94	372.21		0.07	0.00	28.88	1.57	55.52	1.29	1.42	1.32		
2103-84	362.21		0.16	0.01	15.00	0.36	45.67	1.24	1.01	1.11	1.05	0.27
2103-72	350.21		0.10	0.01	33.14	0.40	61.52	1.41	0.98	0.86	0.85	0.65

Table A9 cont'd: Data table containing elemental ratios from the REE leach (Mn/Sr, Mg/Ca, Sr/Ca, Mn/Fe, Y/Ho, Ce/Ce*, Eu/Eu*, MREE/MREE*, Nd/Yb, and ∑REE) for the Zhuya Group. Note red means interpret with caution.

Sample	Height (m)	Formation	Mn/Sr	Mg/Ca	Sr/Ca	Mn/Fe	Y/Ho	Ce/Ce*	Eu/Eu*	MREE/MREE*	Nd/Yb	∑REE
2103-66	344.21	Alyanch	0.15	0.01	19.41	0.32		1.28	1.24	1.05	0.63	
2103-51	330.21		0.01	0.00	65.90	0.41	54.87	1.23	1.98	1.25	1.08	0.09
2103-42	321.21		0.12	0.01	28.35	1.45	50.49	1.31	0.99	1.03	0.85	0.46
2103-30	309.21		0.07	0.01	24.23	0.25	41.76	1.17	1.03	1.07	1.08	0.42
2103-23	302.21		0.08	0.01	30.32	0.48	52.41	1.25	1.14	0.95	1.00	0.44
2103-14	293.21		0.08	0.01	20.19	0.46	41.36	1.17	1.04	1.07	1.02	0.32
2103-4	283.21		0.08	0.01	16.93	0.30	34.88	1.15	1.08	1.18	1.25	0.51
2103-M4	276.21		0.04	0.01	34.73	0.41	54.17	1.29	1.05	1.15	0.89	0.16
2103.2-83.17	268.55		0.08	0.01	33.30	0.27	43.42	1.34	1.08	1.10	1.08	0.95
2103.2-70.00	255.38	Nikol'skoe	0.36	0.01	12.68	0.38	50.16	1.25	1.04	1.07	0.82	0.33
2103.2-58.00	243.38		0.19	0.01	25.34	0.36		1.53	1.09	0.90	0.57	
2103.2-53.00	238.38		0.24	0.01	21.21	1.21	42.14	1.24	1.08	1.13	1.00	0.64
2103.2-47.00(2)	232.38		0.25	0.02	21.47	0.31	47.28	1.31	0.96	1.01	1.07	1.76
2103.2-44.00	229.38		0.18	0.01	23.16	0.30		1.25	1.01	1.04	0.69	
2103.2-28.00	213.38		0.44	0.01	14.88	0.58	41.19	1.21	1.10	1.20	1.09	1.55
2102-114.35	210.23		0.67	0.01	9.91	0.66	53.92	1.20	1.13	1.13	0.88	0.40
2102-91.15	187.03		0.73	0.01	12.53	2.06	46.20	1.15	1.17	1.18	0.88	0.55
2102-78.85	174.73		0.30	0.01	29.94	2.11		1.50	4.60	1.03	0.56	
2102-57.80	153.68		1.91	0.01	8.30	1.01	49.11	1.55	0.98	0.96	0.61	1.93
K2102.52.00	147.88		0.72	0.01	14.22	1.38	33.23	1.20	1.10	1.53	1.21	4.53
2102-51.35	147.23		0.74	0.01	14.29	9.12	55.82	1.25	1.46	1.37	1.06	0.54
K2102.51.00	146.88		0.12	0.01	87.92	2.07	41.43	1.24	1.36	1.37	1.24	1.49
2102-39.15	135.03		2.12	0.01	9.16	13.70	43.90	1.12	1.14	1.53	1.16	2.13
2102-31.10	126.98		2.60	0.01	7.69	1.22	48.77	1.40	1.11	1.19	0.66	2.14
2102-16.10	111.98		2.27	0.01	7.71	4.45		1.38	0.92	1.14	0.63	
2102-13.86	109.74		2.27	0.01	7.37	1.98	37.71	1.24	1.11	1.40	1.22	2.80
K2102.6.60a	102.48		0.52	0.01	19.96	1.89	53.90	1.27	1.43	1.34	0.93	0.86
2102.1-10.13	76.01		2.89	0.01	8.20	15.46	41.65	1.16	1.25	1.60	1.30	3.25
2102.1-5.35	71.23		3.78	0.01	7.88	35.02	55.97	1.17	1.48	1.52	1.16	2.79
2101-67.85	67.85		3.65	0.01	7.76	9.85	57.44	1.45	1.13	1.26	0.80	2.58
2101-55.80	55.80		5.54	0.01	7.01	34.34	42.93	1.07	1.45	1.63	1.16	2.38
2101-45.03	45.03		6.47	0.01	6.72	47.98	36.72	1.23	1.37	1.44	0.89	0.77
2101-42.56	42.56		12.88	0.05	7.46	0.38	30.15	1.10	1.13	1.78	1.08	140.43
2101-39.02	39.02		7.22	0.01	7.36	40.46	38.55	1.15	1.56	1.67	1.12	4.10
2101-34.17	34.17		12.52	0.02	6.73	11.45	48.49	1.53	0.98	1.30	0.93	9.80

Appendix II

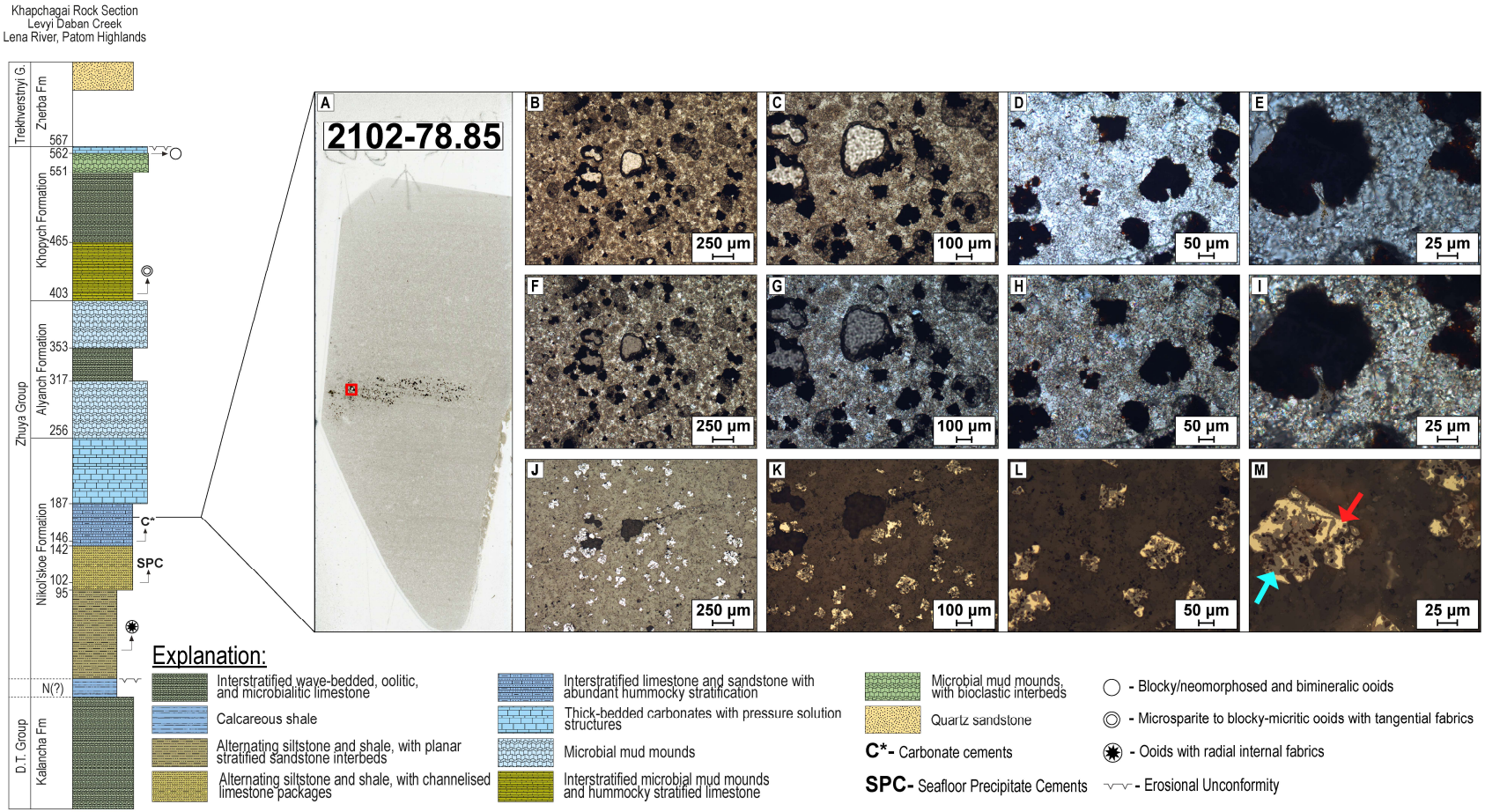


Figure A1: Plate of thin section photos from sample 2102-78.85 from the Patom Uplift. (A) Thin section scan. (B, E) Plane-polarized light images of microspar with the interspersed opaque phases. (F, G) Crossed-polarized light images. (H, I) Reflected light images highlighting the presence of pyrrhotite (blue arrow) with pyrite rims (red arrow) indicating that pyritization was abruptly ended through a lack of sufficient sulfide. Magnifications are 5x, 10x, 20x, and 50x from right to left, respectively.

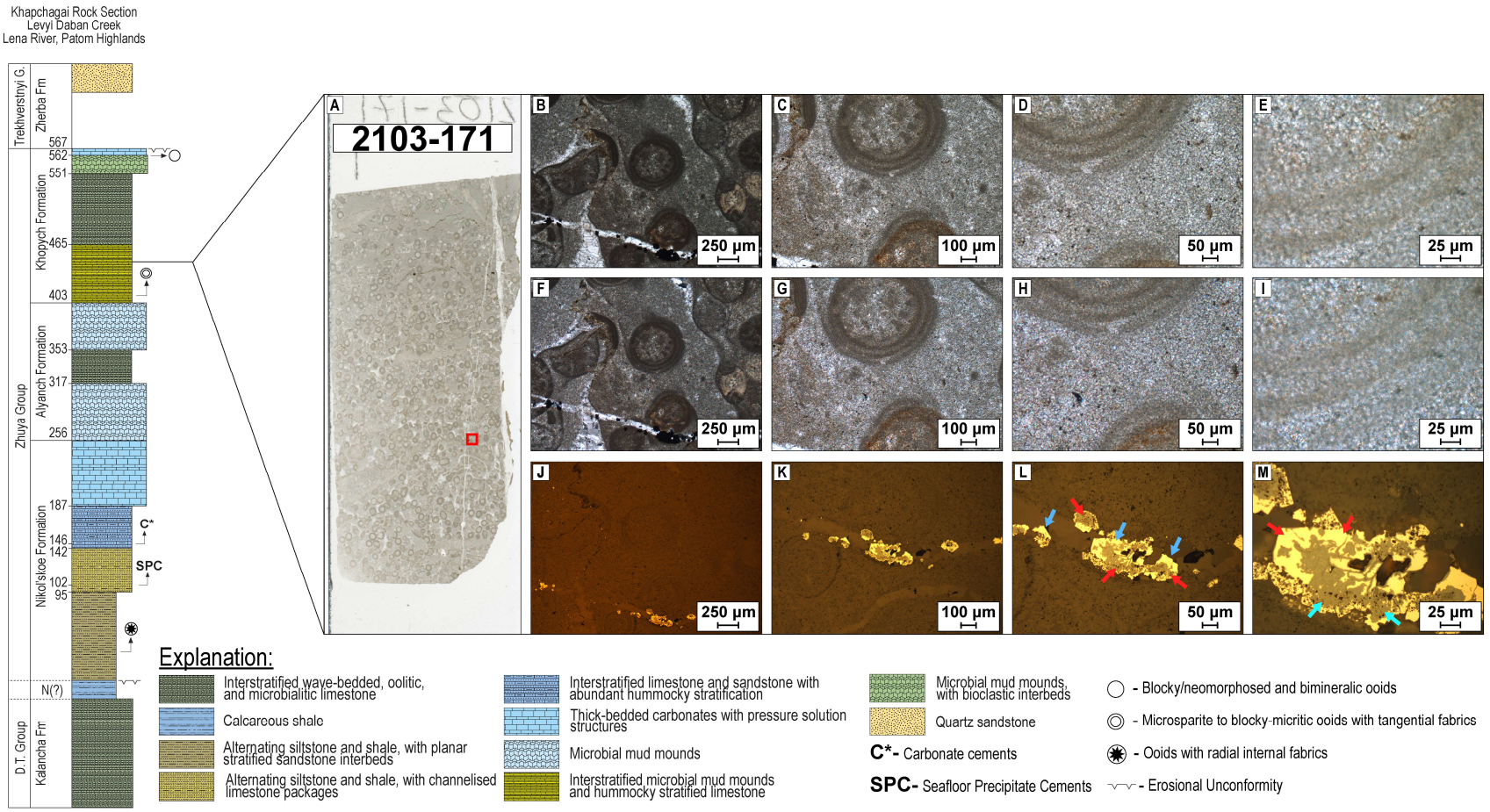


Figure A2: Plate of thin section photos of an alternate view of sample 2103-171 from the Patom Uplift. (A) Thin section scan. (B, E) Plane-polarized light images. (F, G) Crossed-polarized light images. (H, I) Reflected light images (red arrows point to pyrrhotite and the blue arrows point to the pyrite rims). Magnifications are 5x, 10x, 20x, and 50x from right to left, respectively.

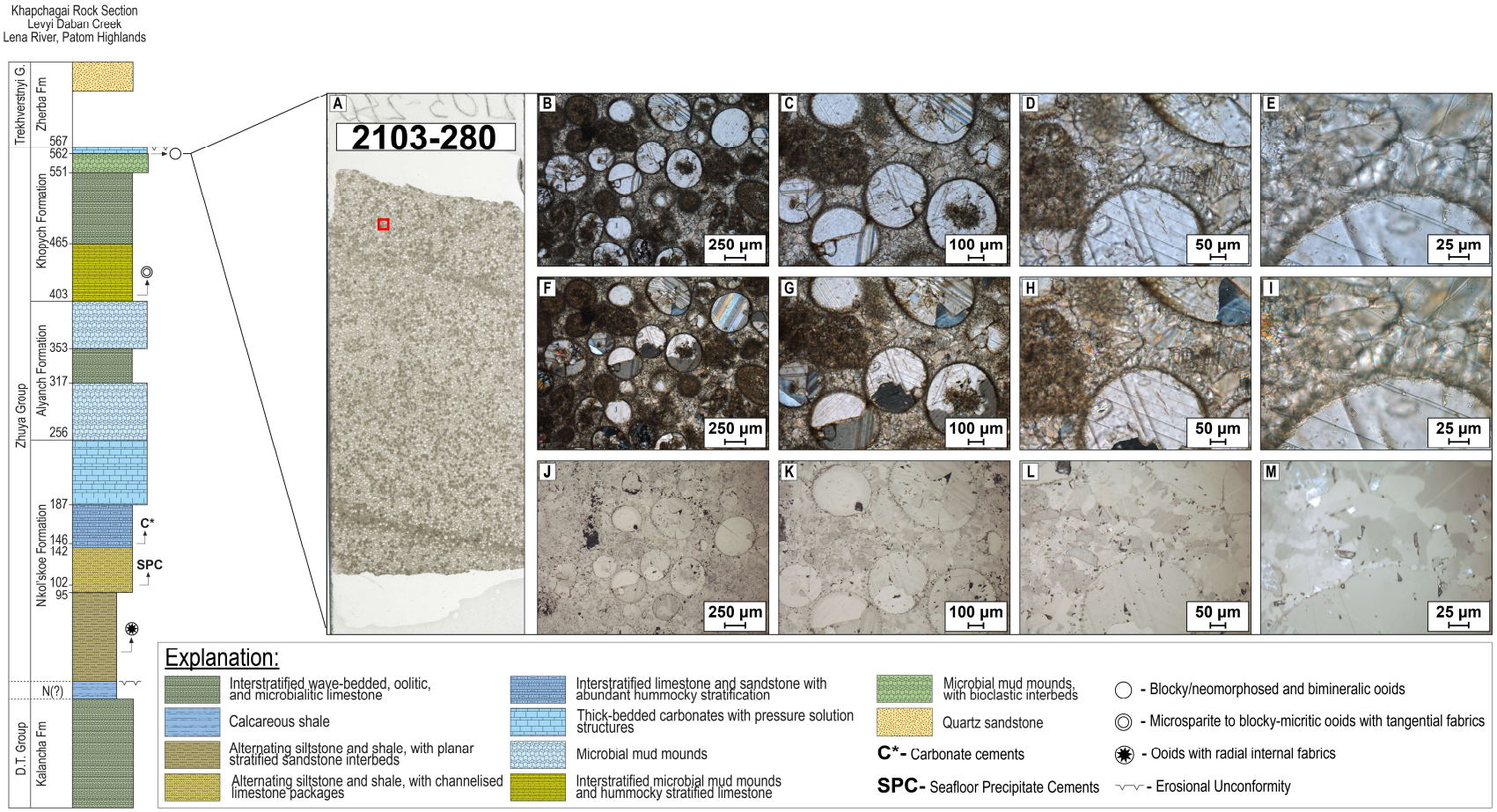


Figure A3: Plate of thin section photos of an alternate view of sample 2103-280 from the Patom Uplift. (A) Thin section scan. (B, E) Plane-polarized light images. (F, G) Crossed-polarized light images. (H, I) Reflected light images. Magnifications are 5x, 10x, 20x, and 50x from right to left, respectively.

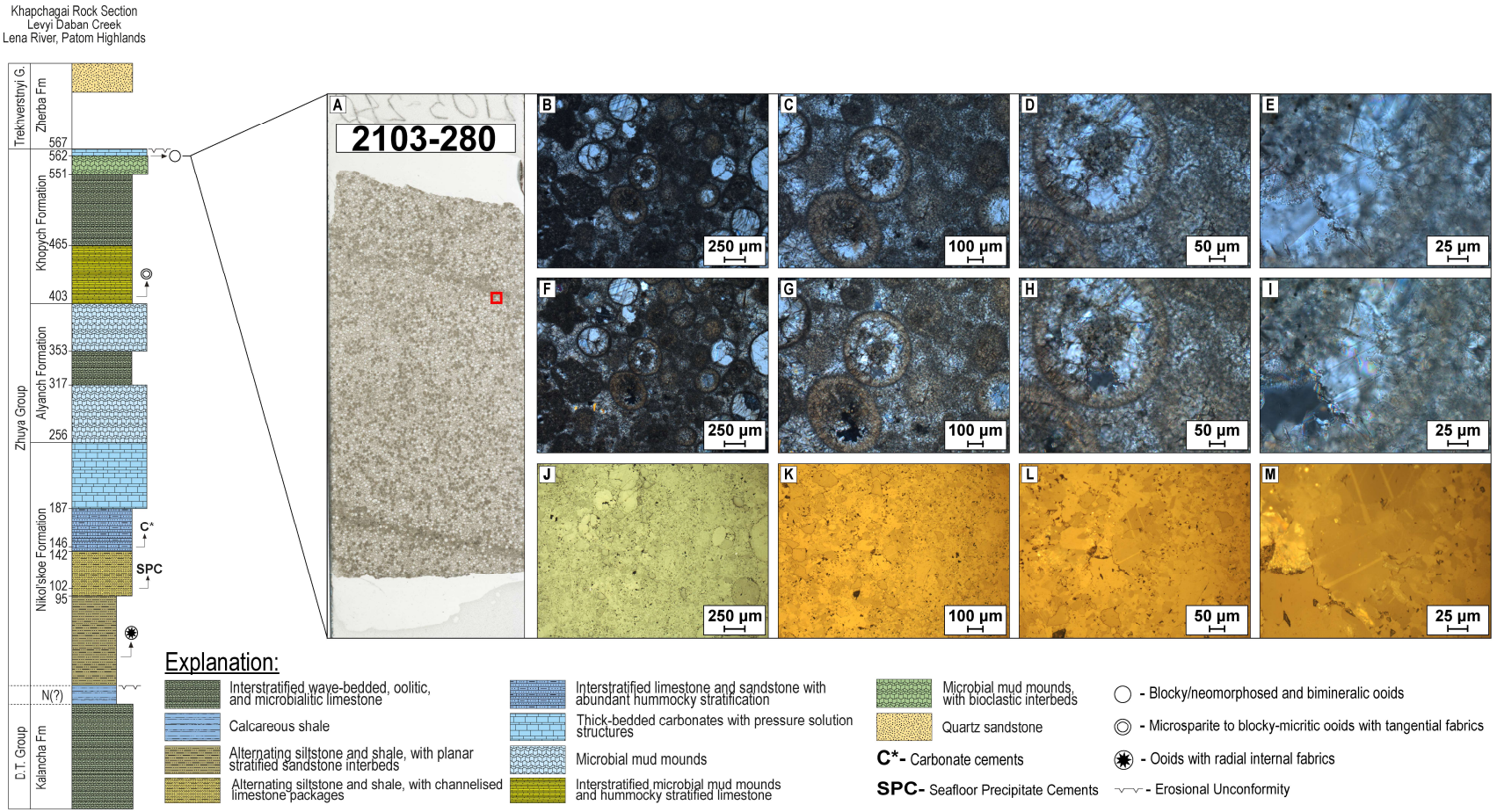


Figure A4: Plate of thin section photos of an alternate view of sample 2103-280 from the Patom Uplift. (A) Thin section scan. (B, E) Plane-polarized light images. (F, G) Crossed-polarized light images. (H, I) Reflected light images. Magnifications are 5x, 10x, 20x, and 50x from right to left, respectively.

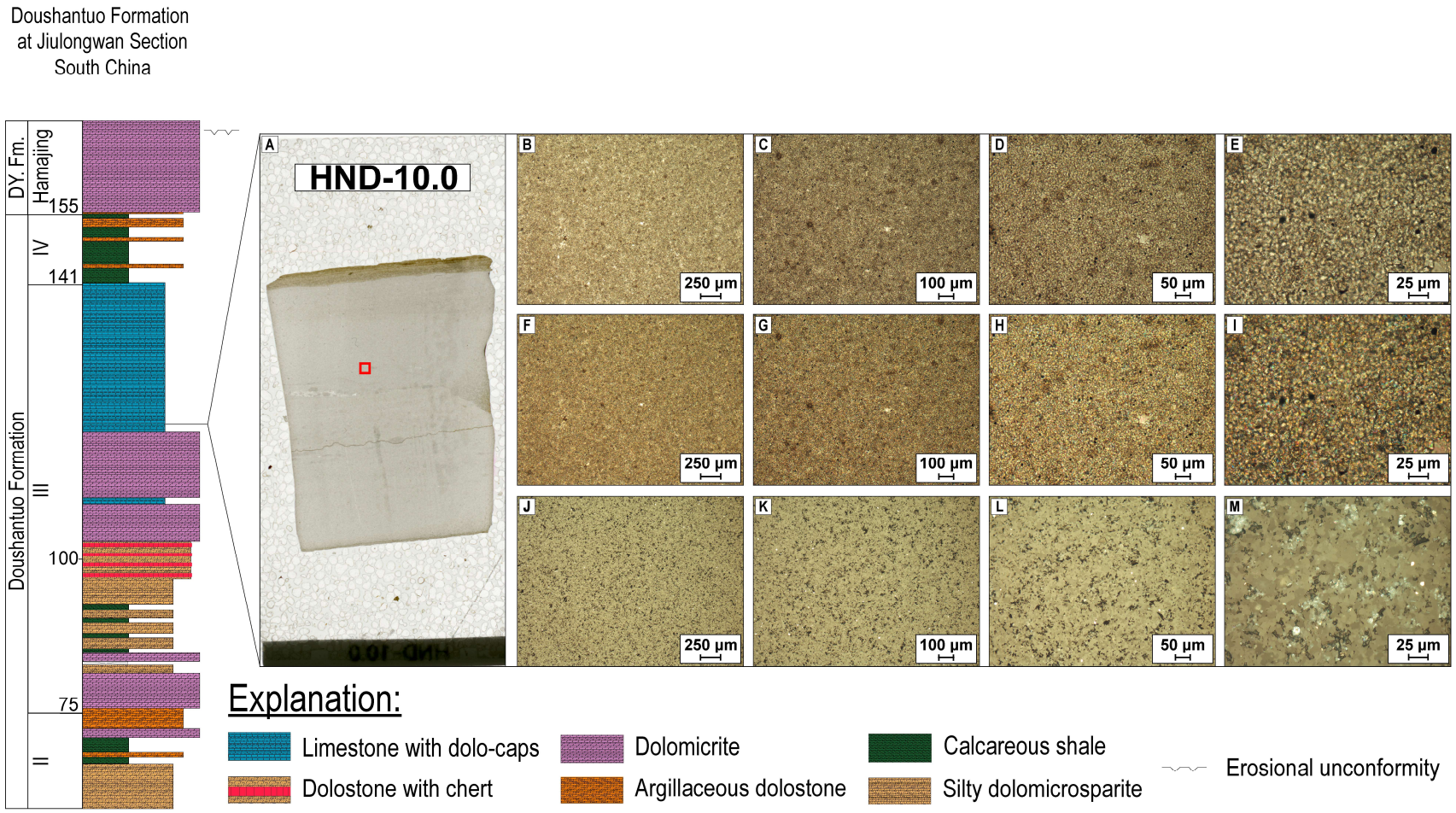


Figure A5: Plate of thin section photos of sample HND-10.0 from the Doushantuo Formation. (A) Thin section scan. (B, E) Plane-polarized light images. (F, G) Crossed-polarized light images. (H, I) Reflected light images. Magnifications are 5x, 10x, 20x, and 50x from right to left, respectively.

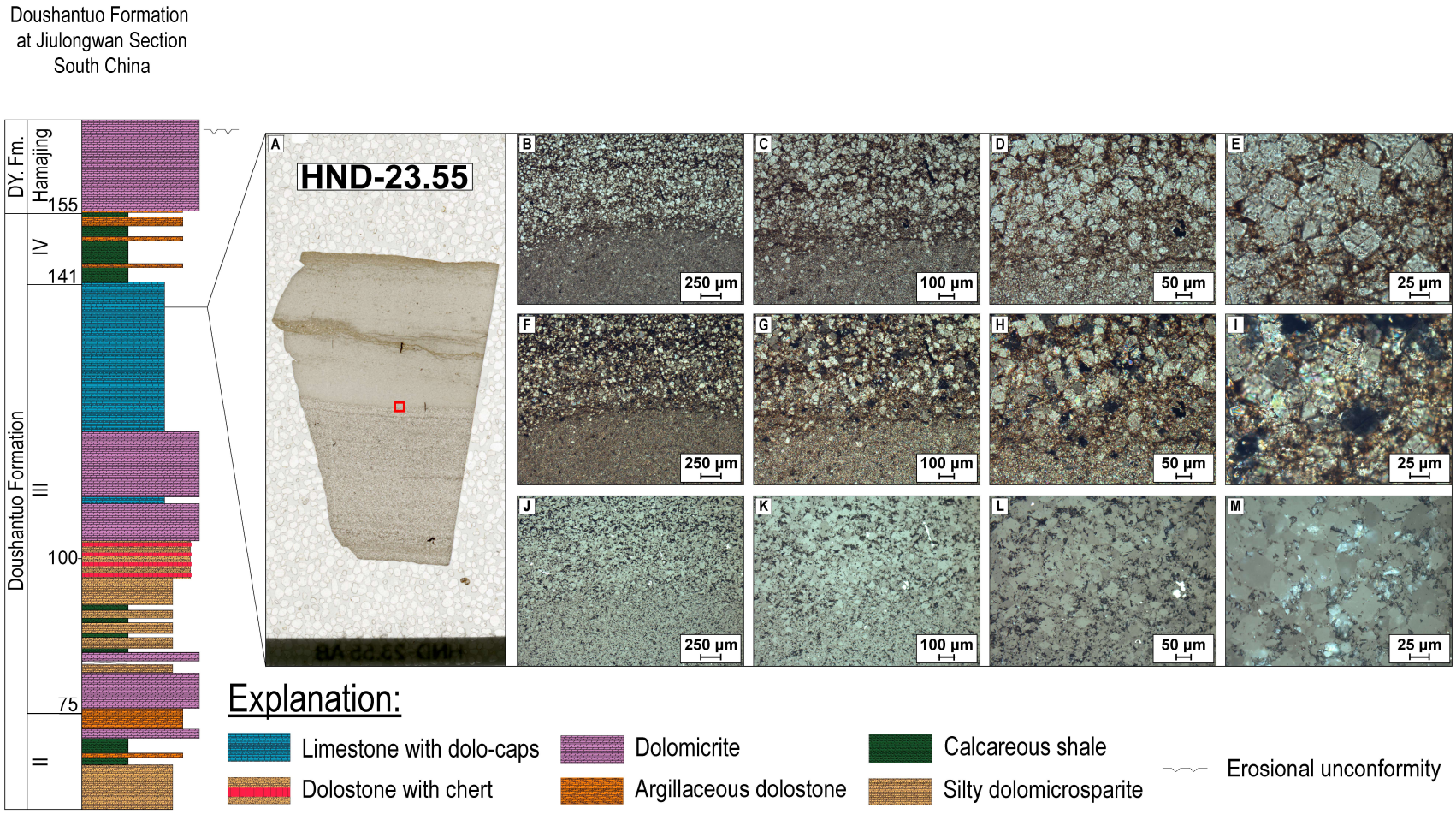


Figure A6: Plate of thin section photos of sample HND-23.55 from the Doushantuo Formation at the dolostone-limestone boundary. (A) Thin section scan. (B, E) Plane-polarized light images. (F, G) Crossed-polarized light images. (H, I) Reflected light images. Magnifications are 5x, 10x, 20x, and 50x from right to left, respectively.

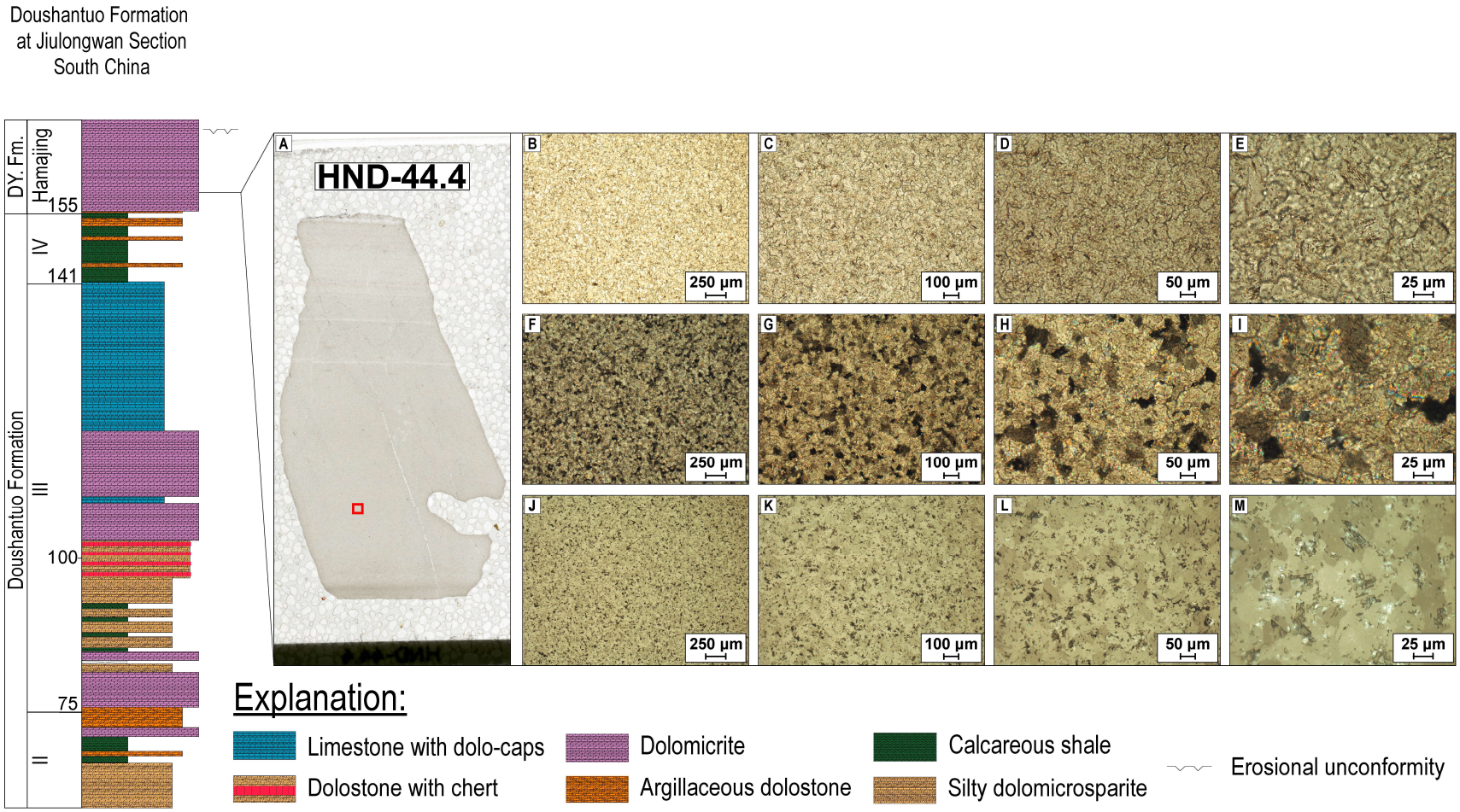


Figure A7: Plate of thin section photos of sample HND-44.4 from the Doushantuo Formation. (A) Thin section scan. (B, E) Plane-polarized light images. (F, G) Crossed-polarized light images. (H, I) Reflected light images. Magnifications are 5x, 10x, 20x, and 50x from right to left, respectively.

Bibliography

Abouchami, W., Galer, S. J. G., de Baar, H. J. W., Alderkamp, A. C., Middag, R., Laan, P., Feldmann, H., & Andreae, M. O. (2011). Modulation of the Southern Ocean cadmium isotope signature by Ocean Circulation and primary productivity. *Earth and Planetary Science Letters*, *305*(1–2), 83–91. https://doi.org/10.1016/j.epsl.2011.02.044

Abouchami, W., Galer, S. J. G., de Baar, H. J. W., Middag, R., Vance, D., Zhao, Y., Klunder, M., Mezger, K., Feldmann, H., & Andreae, M. O. (2014). Biogeochemical cycling of cadmium isotopes in the Southern Ocean along the Zero meridian. *Geochimica et Cosmochimica Acta*, *127*, 348–367. https://doi.org/10.1016/j.gca.2013.10.022

Ader, M., Thomazo, C., Sansjofre, P., Busigny, V., Papineau, D., Laffont, R., Cartigny, P., & Halverson, G. P. (2015). Interpretation of the nitrogen isotopic composition of Precambrian sedimentary rocks: Assumptions and perspectives. *Chemical Geology*, *429*, 93–110. https://doi.org/10.1016/j.chemgeo.2016.02.010

Ahm, A.-S. C., Bjerrum, C. J., Blättler, C. L., Swart, P. K., & Higgins, J. A. (2018). Quantifying early marine diagenesis in shallow-water carbonate sediments. *Geochimica et Cosmochimica Acta*, *236*, 140–159. https://doi.org/10.1016/j.gca.2018.02.042

Alibo, D. S., & Nozaki, Y. (1999). Rare earth elements in seawater: Particle Association, shale-normalization, and CE oxidation. *Geochimica et Cosmochimica Acta*, *63*(3–4), 363–372. https://doi.org/10.1016/s0016-7037(98)00279-8

Allan, J. R., & Matthews, R. K. (1982). Isotope signatures associated with early meteoric diagenesis. *Sedimentology*, *29*(6), 797–817. https://doi.org/10.1111/j.1365-3091.1982.tb00085.x

An, Z., Jiang, G., Tong, J., Tian, L., Ye, Q., Song, H., & Song, H. (2015). Stratigraphic position of the Ediacaran miaohe biota and its constrains on the age of the upper Doushantuo $\delta^{13}C$ anomaly in the Yangtze Gorges area, South China. *Precambrian Research*, *271*, 243–253. https://doi.org/10.1016/j.precamres.2015.10.007

Arthur, M. A., Schlanger, S. O., & Jenkyns, H. C. (1987). The Cenomanian-turonian oceanic anoxic event, ii. Palaeoceanographic controls on organic-matter production and preservation. *Geological Society, London, Special Publications*, *26*(1), 401–420. https://doi.org/10.1144/gsl.sp.1987.026.01.25

Banner, J. L., & Hanson, G. N. (1990). Calculation of simultaneous isotopic and trace element variations during water-rock interaction with applications to carbonate diagenesis. *Geochimica et Cosmochimica Acta*, *54*(11), 3123–3137. https://doi.org/10.1016/0016-7037(90)90128-8

Barnes, C. E., & Cochran, J. K. (1993). Uranium geochemistry in estuarine sediments: Controls on removal and release processes. *Geochimica et Cosmochimica Acta*, *57*(3), 555–569. https://doi.org/10.1016/0016-7037(93)90367-6

Başçetin, E., & Atun, G. (2006). Adsorption behavior of strontium on binary mineral mixtures of montmorillonite and kaolinite. *Applied Radiation and Isotopes*, *64*(8), 957–964. https://doi.org/10.1016/j.apradiso.2006.03.008

Basu, A., Sanford, R. A., Johnson, T. M., Lundstrom, C. C., & Löffler, F. E. (2014). Uranium isotopic fractionation factors during u(vi) reduction by bacterial isolates. *Geochimica et Cosmochimica Acta*, *136*, 100–113. https://doi.org/10.1016/j.gca.2014.02.041

Bathurst, R. G. (1968). Precipitation of oöids and other aragonite fabrics in Warm Seas. *Recent Developments in Carbonate Sedimentology in Central Europe*, 1–10. https://doi.org/10.1007/978-3-642-88052-0_1

Bathurst, R. G. C. . (1975). *Carbonate sediments and their diagenesis*. Elsevier.

Bentov, S., & Erez, J. (2006). Impact of biomineralization processes on the MG content of foraminiferal shells: A biological perspective. *Geochemistry, Geophysics, Geosystems*, *7*(1). https://doi.org/10.1029/2005gc001015

Bergmann, Kristin Diane (2013) *Constraints on the Carbon Cycle and Climate During the Early Evolution of Animals.* Dissertation (Ph.D.), California Institute of Technology. doi:10.7907/KFJX-7S28. https://resolver.caltech.edu/CaltechTHESIS:06102013-045943358

Berkner, L. V., & Marshall, L. C. (1965). On the origin and rise of oxygen concentration in the Earth's atmosphere. *Journal of the Atmospheric Sciences*, *22*(3), 225–261. https://doi.org/10.1175/1520-0469(1965)022<0225:otoaro>2.0.co;2

Berner, R. A., Lasaga, A. C., & Garrels, R. M. (1983). The carbonate-silicate geochemical cycle and its effect on atmospheric carbon dioxide over the past 100 million years. *American Journal of Science*, *283*(7), 641–683. https://doi.org/10.2475/ajs.283.7.641

Bigeleisen, J. (1996). Nuclear size and shape effects in chemical reactions. isotope chemistry of the heavy elements. *Journal of the American Chemical Society*, *118*(15), 3676–3680. https://doi.org/10.1021/ja954076k

Blank, J. G., Delaney, J. R., & Marais, D. J. D. (1993). The concentration and isotopic composition of carbon in basaltic glasses from the Juan de Fuca Ridge, Pacific Ocean. *Geochimica Et Cosmochimica Acta*, *57*(4), 875–887. https://doi.org/10.1016/0016-7037(93)90175-v

Boag, T. H., Stockey, R. G., Elder, L. E., Hull, P. M., & Sperling, E. A. (2018). Oxygen, temperature and the deep-marine stenothermal cradle of Ediacaran evolution. *Proceedings*

of the Royal Society B: Biological Sciences, *285*(1893), 20181724. https://doi.org/10.1098/rspb.2018.1724

Böhm, F., Eisenhauer, A., Tang, J., Dietzel, M., Krabbenhöft, A., Kisakürek, B., & Horn, C. (2012). Strontium isotope fractionation of planktic foraminifera and inorganic calcite. *Geochimica et Cosmochimica Acta*, *93*, 300–314. https://doi.org/10.1016/j.gca.2012.04.038

Brand, U., & Veizer, J. (1980). Chemical diagenesis of a multicomponent carbonate system--1: Trace elements. *SEPM Journal of Sedimentary Research*, *Vol. 50*. https://doi.org/10.1306/212f7bb7-2b24-11d7-8648000102c1865d

Brennecka, G. A., Herrmann, A. D., Algeo, T. J., & Anbar, A. D. (2011). Rapid expansion of oceanic anoxia immediately before the end-Permian mass extinction. *Proceedings of the National Academy of Sciences*, *108*(43), 17631–17634. https://doi.org/10.1073/pnas.1106039108

Bristow, T. F., & Kennedy, M. J. (2008). Carbon isotope excursions and the oxidant budget of the Ediacaran atmosphere and Ocean. *Geology*, *36*(11), 863. https://doi.org/10.1130/g24968a.1

Broecker, W. S. (1970). A boundary condition on the evolution of atmospheric oxygen. *Journal of Geophysical Research*, *75*(18), 3553–3557. https://doi.org/10.1029/jc075i018p03553

Broecker, W. S., & Peng, T.-H. (1982). *Tracers in the sea*. Columbia University.

Brown, S. T., Basu, A., Ding, X., Christensen, J. N., & DePaolo, D. J. (2018). Uranium isotope fractionation by abiotic reductive precipitation. *Proceedings of the National Academy of Sciences*, *115*(35), 8688–8693. https://doi.org/10.1073/pnas.1805234115

Burns, S.J.; Matter, Albert (1993). *Carbon isotopic record of the Latest Proterozoic from Oman.* Eclogae Geologicae Helvetiae, 86(2), pp. 595-607. Birkhäuser 10.5169/seals-167254

Burns, S. J., Haudenschild, U., & Matter, A. (1994). The strontium isotopic composition of carbonates from the late precambrian (~ 560-540 ma) Huqf Group of Oman. *Chemical Geology*, *111*(1–4), 269–282. https://doi.org/10.1016/0009-2541(94)90094-9

Busch, J. F., Hodgin, E. B., Ahm, A.-S. C., Husson, J. M., Macdonald, F. A., Bergmann, K. D., Higgins, J. A., & Strauss, J. V. (2022). Global and local drivers of the Ediacaran Shuram Carbon Isotope Excursion. *Earth and Planetary Science Letters*, *579*, 117368. https://doi.org/10.1016/j.epsl.2022.117368

Calver, C. R. (2000). Isotope stratigraphy of the Ediacaran (Neoproterozoic III) of the Adelaide Rift Complex, Australia, and the overprint of water column stratification. *Precambrian Research*, *100*(1–3), 121–150. https://doi.org/10.1016/s0301-9268(99)00072-8

Cañadas, F., Papineau, D., Leng, M. J., & Li, C. (2022). Extensive primary production promoted the recovery of the Ediacaran Shuram Excursion. *Nature Communications*, *13*(1). https://doi.org/10.1038/s41467-021-27812-5

Canfield, D. E., Poulton, S. W., & Narbonne, G. M. (2007). Late-Neoproterozoic deep-ocean oxygenation and the rise of Animal Life. *Science*, *315*(5808), 92–95. https://doi.org/10.1126/science.1135013

Canfield, Donald E., Poulton, S. W., Knoll, A. H., Narbonne, G. M., Ross, G., Goldberg, T., & Strauss, H. (2008). Ferruginous conditions dominated later Neoproterozoic deep-water chemistry. *Science*, *321*(5891), 949–952. https://doi.org/10.1126/science.1154499

Cao, C., Liu, X.-M., Bataille, C. P., & Liu, C. (2020). What do Ce anomalies in marine carbonates really mean? A perspective from leaching experiments. *Chemical Geology*, *532*, 119413. https://doi.org/10.1016/j.chemgeo.2019.119413

Cao, M., Daines, S. J., Lenton, T. M., Cui, H., Algeo, T. J., Dahl, T. W., Shi, W., Chen, Z.-Q., Anbar, A., & Zhou, Y.-Q. (2020). Comparison of Ediacaran platform and slope $\delta^{238}U$ Records in South China: Implications for global-ocean oxygenation and the origin of the Shuram Excursion. *Geochimica et Cosmochimica Acta*, *287*, 111–124. https://doi.org/10.1016/j.gca.2020.04.035

Cao, C., Bataille, C. P., Song, H., Saltzman, M. R., Tierney Cramer, K., Wu, H., Korte, C., Zhang, Z., & Liu, X.-M. (2022). Persistent late Permian to early Triassic warmth linked to enhanced reverse weathering. *Nature Geoscience*, *15*(10), 832–838. https://doi.org/10.1038/s41561-022-01009-x

Cao, C., Liu, X.-M., Wang, X.-K., & Chen, J. (2023). Effective use of limestones to reconstruct seawater Li isotope compositions - a community standard proposal. *Chemical Geology*, *626*, 121441. https://doi.org/10.1016/j.chemgeo.2023.121441

Cathalot, C., Van Oevelen, D., Cox, T. J., Kutti, T., Lavaleye, M., Duineveld, G., & Meysman, F. J. (2015). Cold-water coral reefs and adjacent sponge grounds: Hotspots of benthic respiration and organic carbon cycling in the Deep Sea. *Frontiers in Marine Science*, *2*. https://doi.org/10.3389/fmars.2015.00037

Chatalov, A. (2005). Monomineralic carbonate ooid types in the Triassic sediments from Northwestern Bulgaria. *Geologica Balcanica*, *35*(1–2), 63–91. https://doi.org/10.52321/geolbalc.35.1-2.63

Chen, Z., Zhou, C., Xiao, S., Wang, W., Guan, C., Hua, H., & Yuan, X. (2014). New Ediacara fossils preserved in marine limestone and their ecological implications. *Scientific Reports*, *4*(1). https://doi.org/10.1038/srep04180

Chen, X., Romaniello, S. J., Herrmann, A. D., Wasylenki, L. E., & Anbar, A. D. (2016). Uranium isotope fractionation during coprecipitation with aragonite and calcite.

Geochimica et Cosmochimica Acta, *188*, 189–207. https://doi.org/10.1016/j.gca.2016.05.022

Chen, X., Romaniello, S. J., & Anbar, A. D. (2017). Uranium isotope fractionation induced by aqueous speciation: Implications for U isotopes in marine $CaCO_3$ as a paleoredox proxy. *Geochimica et Cosmochimica Acta*, *215*, 162–172. https://doi.org/10.1016/j.gca.2017.08.006

Chen, X., Romaniello, S. J., Herrmann, A. D., Samankassou, E., & Anbar, A. D. (2018a). Biological effects on uranium isotope fractionation ($^{238}U/^{235}U$) in primary biogenic carbonates. *Geochimica et Cosmochimica Acta*, *240*, 1–10. https://doi.org/10.1016/j.gca.2018.08.028

Chen, X., Romaniello, S. J., Herrmann, A. D., Hardisty, D., Gill, B. C., & Anbar, A. D. (2018b). Diagenetic effects on uranium isotope fractionation in carbonate sediments from the Bahamas. *Geochimica et Cosmochimica Acta*, *237*, 294–311. https://doi.org/10.1016/j.gca.2018.06.026

Chen, X., Romaniello, S. J., McCormick, M., Sherry, A., Havig, J. R., Zheng, W., & Anbar, A. D. (2021). Anoxic depositional overprinting of $^{238}U/^{235}U$ in calcite: When do carbonates tell Black Shale Tales? *Geology*, *49*(10), 1193–1197. https://doi.org/10.1130/g48949.1

Cherry, L. B., Gilleaudeau, G. J., Grazhdankin, D. V., Romaniello, S. J., Martin, A. J., & Kaufman, A. J. (2022). A diverse Ediacara assemblage survived under low-oxygen conditions. *Nature Communications*, *13*(1). https://doi.org/10.1038/s41467-022-35012-y

Chumakov, N. M., Pokrovsky, B. G., & Melezhik, V. A. (2011). Chapter 27 the glaciogenic Bol'shoy Patom Formation, Lena River, Central Siberia. *Geological Society, London, Memoirs*, *36*(1), 309–316. https://doi.org/10.1144/m36.27

Cloud, P. E. (1968). Atmospheric and hydrospheric evolution on the Primitive Earth. *Science*, *160*(3829), 729–736. https://doi.org/10.1126/science.160.3829.729

Cole, D. B., Mills, D. B., Erwin, D. H., Sperling, E. A., Porter, S. M., Reinhard, C. T., & Planavsky, N. J. (2020). On the co-evolution of surface oxygen levels and animals. *Geobiology*, *18*(3), 260–281. https://doi.org/10.1111/gbi.12382

Condon, D., Zhu, M., Bowring, S., Wang, W., Yang, A., & Jin, Y. (2005). U-Pb ages from the Neoproterozoic Doushantuo Formation, China. *Science*, *308*(5718), 95–98. https://doi.org/10.1126/science.1107765

Corsetti, F. A., & J. Kaufman, A. (2003). Stratigraphic investigations of carbon isotope anomalies and neoproterozoic ice ages in Death Valley, California. *Geological Society of America Bulletin*, *115*(8), 916–932. https://doi.org/10.1130/b25066.1

Craig, H. (1953). The geochemistry of the stable carbon isotopes. *Geochimica et Cosmochimica Acta*, *3*(2–3), 53–92. https://doi.org/10.1016/0016-7037(53)90001-5

Cui, H., Kaufman, A. J., Xiao, S., Zhu, M., Zhou, C., & Liu, X.-M. (2015). Redox architecture of an Ediacaran Ocean Margin: Integrated chemostratigraphic ($\delta^{13}C$–$\delta^{34}S$–$^{87}Sr/^{86}Sr$–Ce/Ce*) correlation of the Doushantuo Formation, South China. *Chemical Geology*, *405*, 48–62. https://doi.org/10.1016/j.chemgeo.2015.04.009

Cui, H., Kaufman, A. J., Xiao, S., Zhou, C., & Liu, X.-M. (2017). Was the Ediacaran Shuram excursion a globally synchronized early diagenetic event? insights from methane-derived authigenic carbonates in the uppermost Doushantuo Formation, South China. *Chemical Geology*, *450*, 59–80. https://doi.org/10.1016/j.chemgeo.2016.12.010

Cui, H., Kaufman, A. J., Zou, H., Kattan, F. H., Trusler, P., Smith, J., Yu. Ivantsov, A., Rich, T. H., Al Qubsani, A., Yazedi, A., Liu, X.-M., Johnson, P., Goderis, S., Claeys, P., & Vickers-Rich, P. (2020). Primary or secondary? A dichotomy of the strontium isotope anomalies in the Ediacaran carbonates of Saudi Arabia. *Precambrian Research*, *343*, 105720. https://doi.org/10.1016/j.precamres.2020.105720

Davies, P. J., Bubela, B., & Ferguson, J. (1978). The formation of Ooids. *Sedimentology*, *25*(5), 703–730. https://doi.org/10.1111/j.1365-3091.1978.tb00326.x

de Baar, H. J. W., Bacon, M. P., Brewer, P. G., & Bruland, K. W. (1985). Rare earth elements in the Pacific and Atlantic Oceans. *Geochimica Et Cosmochimica Acta*, *49*(9), 1943–1959. https://doi.org/10.1016/0016-7037(85)90089-4

de Baar, H. J. W. (1991). On cerium anomalies in the Sargasso Sea. *Geochimica Et Cosmochimica Acta*, *55*(10), 2981–2983. https://doi.org/10.1016/0016-7037(91)90463-f

de Baar, H. J. W., Saager, P. M., Nolting, R. F., & van der Meer, J. (1994). Cadmium versus Phosphate in the World Ocean. *Marine Chemistry*, *46*(3), 261–281. https://doi.org/10.1016/0304-4203(94)90082-5

de Goeij, J. M., van Oevelen, D., Vermeij, M. J., Osinga, R., Middelburg, J. J., de Goeij, A. F., & Admiraal, W. (2013). Surviving in a marine desert: The sponge loop retains resources within coral reefs. *Science*, *342*(6154), 108–110. https://doi.org/10.1126/science.1241981

DeCarlo, E. H., & Green, W. J. (2002). Rare earth elements in the water column of Lake Vanda, McMurdo Dry Valleys, Antarctica. *Geochimica Et Cosmochimica Acta*, *66*(8), 1323–1333. https://doi.org/10.1016/s0016-7037(01)00861-4

Dellinger, M., Gaillardet, J., Bouchez, J., Calmels, D., Louvat, P., Dosseto, A., Gorge, C., Alanoca, L., & Maurice, L. (2015). Riverine Li Isotope Fractionation in the Amazon River basin controlled by the weathering regimes. *Geochimica et Cosmochimica Acta*, *164*, 71–93. https://doi.org/10.1016/j.gca.2015.04.042

Dellinger, M., Hardisty, D. S., Planavsky, N. J., Gill, B. C., Kalderon-Asael, B., Asael, D., Croissant, T., Swart, P. K., & West, A. J. (2020). The effects of diagenesis on lithium isotope ratios of shallow marine carbonates. *American Journal of Science*, *320*(2), 150–184. https://doi.org/10.2475/02.2020.03

Derry, L. A., Kaufman, A. J., & Jacobsen, S. B. (1992). Sedimentary cycling and environmental change in the Late Proterozoic: Evidence from stable and radiogenic isotopes. *Geochimica et Cosmochimica Acta*, *56*(3), 1317–1329. https://doi.org/10.1016/0016-7037(92)90064-p

Derry, L. A. (2010). A burial diagenesis origin for the Ediacaran Shuram–Wonoka carbon isotope anomaly. *Earth and Planetary Science Letters*, *294*(1-2), 152–162. https://doi.org/10.1016/j.epsl.2010.03.022

Ding, Y., Sun, W., Liu, S., Xie, J., Tang, D., Zhou, X., Zhou, L., Li, Z., Song, J., Li, Z., Xu, H., Tang, P., Liu, K., Li, W., & Chen, D. (2022). Low oxygen levels with high redox heterogeneity in the late ediacaran shallow ocean: Constraints from I/(Ca + Mg) and Ce/Ce* of the Dengying Formation, South China. *Geobiology*, *20*(6), 790–809. https://doi.org/10.1111/gbi.12520

Dodd, M. S., Shi, W., Li, C., Zhang, Z., Cheng, M., Gu, H., Hardisty, D. S., Loyd, S. J., Wallace, M. W., vS. Hood, A., Lamothe, K., Mills, B. J., Poulton, S. W., & Lyons, T. W. (2023). Uncovering the Ediacaran phosphorus cycle. *Nature*, *618*(7967), 974–980. https://doi.org/10.1038/s41586-023-06077-6

Dohrmann, M., & Wörheide, G. (2017). Dating early animal evolution using phylogenomic data. *Scientific Reports*, *7*(1). https://doi.org/10.1038/s41598-017-03791-w

Elzinga, E. J., Reeder, R. J., Withers, S. H., Peale, R. E., Mason, R. A., Beck, K. M., & Hess, W. P. (2002). EXAFS study of rare-earth element coordination in calcite. *Geochimica et Cosmochimica Acta*, *66*(16), 2875–2885. https://doi.org/10.1016/s0016-7037(02)00888-8

Emrich, K., Ehhalt, D. H., & Vogel, J. C. (1970). Carbon isotope fractionation during the precipitation of calcium carbonate. *Earth and Planetary Science Letters*, *8*(5), 363–371. https://doi.org/10.1016/0012-821x(70)90109-3

Endrizzi, F., Leggett, C. J., & Rao, L. (2016). Scientific basis for efficient extraction of uranium from seawater. I: Understanding the chemical speciation of uranium under seawater conditions. *Industrial & Engineering Chemistry Research*, *55*(15), 4249–4256. https://doi.org/10.1021/acs.iecr.5b03679

Erez, J. (2003). The source of ions for biomineralization in Foraminifera and their implications for paleoceanographic proxies. *Reviews in Mineralogy and Geochemistry*, *54*(1), 115–149. https://doi.org/10.2113/0540115

Evans, M. N., Selmer, K. J., Breeden, B. T., Lopatka, A. S., & Plummer, R. E. (2016). Correction algorithm for online continuous flow δ^{13}C and δ^{18}O carbonate and cellulose

stable isotope analyses. *Geochemistry, Geophysics, Geosystems*, *17*(9), 3580–3588. https://doi.org/10.1002/2016gc006469

Fantle, M. S., & DePaolo, D. J. (2007). CA isotopes in carbonate sediment and pore fluid from ODP Site 807A: The $Ca^{2+}_{aq.}$–calcite equilibrium fractionation factor and calcite recrystallization rates in pleistocene sediments. *Geochimica et Cosmochimica Acta*, *71*(10), 2524–2546. https://doi.org/10.1016/j.gca.2007.03.006

Fantle, M. S., & Higgins, J. (2014). The effects of diagenesis and dolomitization on Ca and MG isotopes in marine platform carbonates: Implications for the geochemical cycles of Ca and mg. *Geochimica et Cosmochimica Acta*, *142*, 458–481. https://doi.org/10.1016/j.gca.2014.07.025

Farquhar, G. (1989). Carbon isotope discrimination and photosynthesis. *Annual Review of Plant Physiology and Plant Molecular Biology*, *40*(1), 503–537. https://doi.org/10.1146/annurev.arplant.40.1.503

Faure, G. *Principles of Isotope Geology. Second edition*. United States.

Fike, D., Grotzinger, J., Pratt, L. *et al.* Oxidation of the Ediacaran Ocean. *Nature* 444, 744–747 (2006). https://doi.org/10.1038/nature05345

Frei, R., Gaucher, C., Poulton, S. W., & Canfield, D. E. (2009). Fluctuations in precambrian atmospheric oxygenation recorded by Chromium Isotopes. *Nature*, *461*(7261), 250–253. https://doi.org/10.1038/nature08266

Fritz, P., & Smith, D. G. W. (1970). The isotopic composition of Secondary Dolomites. *Geochimica et Cosmochimica Acta*, *34*(11), 1161–1173. https://doi.org/10.1016/0016-7037(70)90056-6

Fujimoto, D., & Tamiya, N. (1962). Incorporation of 18O from air into hydroxyproline by Chick Embryo. *Biochemical Journal*, *84*(2), 333–335. https://doi.org/10.1042/bj0840333

Gabitov, R. I., Watson, E. B., & Sadekov, A. (2012). Oxygen isotope fractionation between calcite and fluid as a function of growth rate and temperature: An in-situ study. *Chemical Geology*, *306–307*, 92–102. https://doi.org/10.1016/j.chemgeo.2012.02.021

Gan, T., Gilleaudeau, G., **Pedersen, M.,** Doerrler, A., Maximenko, V., Grazhdankin, D., Hellmann, J., Nana Yobo, L., Xiao, S., Liu, X. M., Kaufman, A. (*in-preparation*). Intense continental weathering during the Ediacaran Shuram Excursion

German, C. R., & Elderfield, H. (1990). Application of the CE anomaly as a paleoredox indicator: The ground rules. *Paleoceanography*, *5*(5), 823–833. https://doi.org/10.1029/pa005i005p00823

Gill, B. C., Lyons, T. W., & Frank, T. D. (2008). Behavior of carbonate-associated sulfate during meteoric diagenesis and implications for the sulfur isotope paleoproxy. *Geochimica et Cosmochimica Acta*, *72*(19), 4699–4711. https://doi.org/10.1016/j.gca.2008.07.001

Gilleaudeau, G. J., & Kah, L. C. (2013). Carbon Isotope Records in a Mesoproterozoic Epicratonic Sea: Carbon cycling in a low-oxygen world. *Precambrian Research*, *228*, 85–101. https://doi.org/10.1016/j.precamres.2013.01.006

Goldstein, S. J., & Jacobsen, S. B. (1987). The Nd and Sr isotopic systematics of river-water dissolved material: Implications for the sources of nd and sr in seawater. *Chemical Geology: Isotope Geoscience Section*, *66*(3–4), 245–272. https://doi.org/10.1016/0168-9622(87)90045-5

Gong, Z., Wei, G., Fakhraee, M., Alcott, L. J., Jiang, L., Zhao, M., & Planavsky, N. J. (2023). Revisiting marine redox conditions during the Ediacaran Shuram Carbon Isotope Excursion. *Geobiology*, *21*(4), 407–420. https://doi.org/10.1111/gbi.12547

Grinstein, M., Bentov, S., Koller-Rink, S., De Beer, D., Erez, J., 2004. Direct microelectrodes measurements at the calcification site of foraminifera. EOS Trans. AGU, Fall Meet. San Francisco. #B21B-0864 (abstr.)

Grotzinger, J. P., & Knoll, A. H. (1995). Anomalous carbonate precipitates: Is the Precambrian the key to the Permian? *PALAIOS*, *10*(6), 578. https://doi.org/10.2307/3515096

Grotzinger, J. P., Fike, D. A., & Fischer, W. W. (2011). Enigmatic origin of the largest-known carbon isotope excursion in Earth's history. *Nature Geoscience*, *4*(5), 285–292. https://doi.org/10.1038/ngeo1138

Guieu, C., Duce, R., & Arimoto, R. (1994). Dissolved input of manganese to the ocean: Aerosol source. *Journal of Geophysical Research: Atmospheres*, *99*(D9), 18789–18800. https://doi.org/10.1029/94jd01120

Guo, Q., Strauss, H., Kaufman, A. J., Schröder, S., Gutzmer, J., Wing, B., Baker, M. A., Bekker, A., Jin, Q., Kim, S.-T., & Farquhar, J. (2009). Reconstructing Earth's surface oxidation across the Archean-proterozoic transition. *Geology*, *37*(5), 399–402. https://doi.org/10.1130/g25423a.1

Hardisty, D. S., Lu, Z., Bekker, A., Diamond, C. W., Gill, B. C., Jiang, G., Kah, L. C., Knoll, A. H., Loyd, S. J., Osburn, M. R., Planavsky, N. J., Wang, C., Zhou, X., & Lyons, T. W. (2017). Perspectives on Proterozoic surface ocean redox from iodine contents in ancient and recent carbonate. *Earth and Planetary Science Letters*, *463*, 159–170. https://doi.org/10.1016/j.epsl.2017.01.032

Hathorne, E., & James, R. (2006). Temporal record of lithium in seawater: A tracer for silicate weathering? *Earth and Planetary Science Letters*, *246*(3–4), 393–406. https://doi.org/10.1016/j.epsl.2006.04.020

Hayes, J. M., (1983) Geochemical evidence bearing on the origin of aerobiosis, a speculative hypothesis.

Hetzel, A., Böttcher, M. E., Wortmann, U. G., & Brumsack, H.-J. (2009). Paleo-redox conditions during OAE 2 reflected in demerara rise sediment geochemistry (ODP leg 207). *Palaeogeography, Palaeoclimatology, Palaeoecology*, *273*(3–4), 302–328. https://doi.org/10.1016/j.palaeo.2008.11.005

Higgins, J. A., Blättler, C. L., Lundstrom, E. A., Santiago-Ramos, D. P., Akhtar, A. A., Crüger Ahm, A.-S., Bialik, O., Holmden, C., Bradbury, H., Murray, S. T., & Swart, P. K. (2018). Mineralogy, early marine diagenesis, and the chemistry of shallow-water carbonate sediments. *Geochimica et Cosmochimica Acta*, *220*, 512–534. https://doi.org/10.1016/j.gca.2017.09.046

Holland, H. D. (1982). *The chemical evolution of the atmosphere and Oceans Heinrich D. Holland*. Princeton University Press.

Cosmochimica Acta, *160*, 243–266. https://doi.org/10.1016/j.gca.2015.03.012

Husson, J. M., Maloof, A. C., & Schoene, B. (2012). A syn-depositional age for Earth's deepest $\delta^{13}C$ excursion required by isotope conglomerate tests. *Terra Nova*, *24*(4), 318–325. https://doi.org/10.1111/j.1365-3121.2012.01067.x

Husson, J. M., Higgins, J. A., Maloof, A. C., & Schoene, B. (2015). Ca and Mg isotope constraints on the origin of Earth's deepest $\delta^{13}C$ excursion. *Geochimica et*

Ishikawa, T., Ueno, Y., Komiya, T., Sawaki, Y., Han, J., Shu, D., Li, Y., Maruyama, S., & Yoshida, N. (2008). Carbon Isotope Chemostratigraphy of a Precambrian/cambrian boundary section in the Three gorge area, South China: Prominent global-scale isotope excursions just before the Cambrian explosion. *Gondwana Research*, *14*(1–2), 193–208. https://doi.org/10.1016/j.gr.2007.10.008

Isson, T. T., & Planavsky, N. J. (2018). Reverse weathering as a long-term stabilizer of marine ph and planetary climate. *Nature*, *560*(7719), 471–475. https://doi.org/10.1038/s41586-018-0408-4

Jacobsen, S. B., & Kaufman, A. J. (1999). The sr, C and O isotopic evolution of Neoproterozoic seawater. *Chemical Geology*, *161*(1–3), 37–57. https://doi.org/10.1016/s0009-2541(99)00080-7

Jiang, G., Sohl, L. E., & Christie-Blick, N. (2003). Neoproterozoic stratigraphic comparison of the lesser Himalaya (India) and Yangtze Block (south China): Paleogeographic implications. *Geology*, *31*(10), 917. https://doi.org/10.1130/g19790.1

Jiang, G., Kennedy, M. J., Christie-Blick, N., Wu, H., & Zhang, S. (2006). Stratigraphy, sedimentary structures, and textures of the late Neoproterozoic Doushantuo cap carbonate

in South China. *Journal of Sedimentary Research*, *76*(7), 978–995. https://doi.org/10.2110/jsr.2006.086

Jiang, G., Shi, X., Zhang, S., Wang, Y., & Xiao, S. (2011). Stratigraphy and paleogeography of the Ediacaran Doushantuo Formation (ca. 635–551MA) in South China. *Gondwana Research*, *19*(4), 831–849. https://doi.org/10.1016/j.gr.2011.01.006

Jiang, Ganqing, Wang, X., Shi, X., Xiao, S., Zhang, S., & Dong, J. (2012). The origin of decoupled carbonate and organic carbon isotope signatures in the early Cambrian (ca. 542–520 Ma) Yangtze Platform. *Earth and Planetary Science Letters*, *317–318*, 96–110. https://doi.org/10.1016/j.epsl.2011.11.018

Johnson, K. S., Berelson, W. M., Coale, K. H., Coley, T. L., Elrod, V. A., Fairey, W. R., Iams, H. D., Kilgore, T. E., & Nowicki, J. L. (1992). Manganese flux from continental margin sediments in a transect through the oxygen minimum. *Science*, *257*(5074), 1242–1245. https://doi.org/10.1126/science.257.5074.1242

Kalderon-Asael, B., Katchinoff, J. A., Planavsky, N. J., Hood, A. v., Dellinger, M., Bellefroid, E. J., Jones, D. S., Hofmann, A., Ossa, F. O., Macdonald, F. A., Wang, C., Isson, T. T., Murphy, J. G., Higgins, J. A., West, A. J., Wallace, M. W., Asael, D., & Pogge von Strandmann, P. A. (2021). A lithium-isotope perspective on the evolution of carbon and Silicon Cycles. *Nature*, *595*(7867), 394–398. https://doi.org/10.1038/s41586-021-03612-1

Kasting, J. F., & Canfield, D. E. (2012). The global oxygen cycle. *Fundamentals of Geobiology*, 93–104. https://doi.org/10.1002/9781118280874.ch7

Kaufman, A. J., Jacobsen, S. B., & Knoll, A. H. (1993). The Vendian record of SR and C isotopic variations in seawater: Implications for tectonics and Paleoclimate. *Earth and Planetary Science Letters*, *120*(3–4), 409–430. https://doi.org/10.1016/0012-821x(93)90254-7

Kaufman, A. J., & Knoll, A. H. (1995). Neoproterozoic variations in the C-isotopic composition of seawater: Stratigraphic and biogeochemical implications. *Precambrian Research*, *73*(1-4), 27–49. https://doi.org/10.1016/0301-9268(94)00070-8

Kaufman, Alan J., Knoll, A. H., Semikhatov, M. A., Grotzinger, J. P., Jacobsen, S. B., & Adams, W. (1996). Integrated chronostratigraphy of Proterozoic–Cambrian boundary beds in the western Anabar Region, Northern Siberia. *Geological Magazine*, *133*(5), 509–533. https://doi.org/10.1017/s0016756800007810

Kaufman, A. J., Jiang, G., Christie-Blick, N., Banerjee, D. M., & Rai, V. (2006). Stable isotope record of the terminal neoproterozoic krol platform in the Lesser Himalayas of Northern India. *Precambrian Research*, *147*(1–2), 156–185. https://doi.org/10.1016/j.precamres.2006.02.007

Kaufman, Alan J., Corsetti, F. A., & Varni, M. A. (2007). The effect of rising atmospheric oxygen on carbon and sulfur isotope anomalies in the neoproterozoic johnnie formation, Death Valley, USA. *Chemical Geology*, *237*(1–2), 47–63. https://doi.org/10.1016/j.chemgeo.2006.06.023

Kaufman, A.J., Lindsay-Kaufman, A., Lojacono-Evans, B., Doerrler, A., Piccoli, P., Pedersen, M., Gan, T., Rohrback, R., Schiffbauer, J.D., Selly, T., Maloof, A.C., Manzuk, R.A., Wilcots, J., Gilleaudeau, G.J., Goderis, S., Bykova, N.V., and Grazhdankin, D.V. (2023) The Cryogenian emergence of sponge-grade animals and their environmental consequences. *Geological Society of America Abstracts with Programs*. Vol. 55, No. 6, 2023 doi: 10.1130/abs/2023AM-393813 © Copyright 2023 The Geological Society of America

Kendall, B., Komiya, T., Lyons, T. W., Bates, S. M., Gordon, G. W., Romaniello, S. J., Jiang, G., Creaser, R. A., Xiao, S., McFadden, K., Sawaki, Y., Tahata, M., Shu, D., Han, J., Li, Y., Chu, X., & Anbar, A. D. (2015). Uranium and molybdenum isotope evidence for an episode of widespread ocean oxygenation during the late Ediacaran Period. *Geochimica et Cosmochimica Acta*, *156*, 173–193. https://doi.org/10.1016/j.gca.2015.02.025

Kipp, M. A., & Tissot, F. L. H. (2022). Inverse methods for consistent quantification of seafloor anoxia using uranium isotope data from marine sediments. *Earth and Planetary Science Letters*, *577*, 117240. https://doi.org/10.1016/j.epsl.2021.117240

Kısakűrek, B., James, R. H., & Harris, N. B. W. (2005). Li and δ^7Li in Himalayan rivers: Proxies for silicate weathering? *Earth and Planetary Science Letters*, *237*(3–4), 387–401. https://doi.org/10.1016/j.epsl.2005.07.019

Klinkhammer, G. P., & Bender, M. L. (1980). The distribution of manganese in the Pacific Ocean. *Earth and Planetary Science Letters*, *46*(3), 361–384. https://doi.org/10.1016/0012-821x(80)90051-5

Knauth, L. P., & Kennedy, M. J. (2009). The late Precambrian greening of the Earth. *Nature*, *460*(7256), 728–732. https://doi.org/10.1038/nature08213

Knoll, A. H. (1992). Biological and biogeochemical preludes to the Ediacaran Radiation. *Topics in Geobiology*, 53–84. https://doi.org/10.1007/978-1-4899-2427-8_3

Knoll, A., Grotzinger, J., Kaufman, A., & Kolosov, P. (1995). Integrated approaches to terminal Proterozoic stratigraphy: An example from the Olenek Uplift, Northeastern Siberia. *Precambrian Research*, *73*(1–4), 251–270. https://doi.org/10.1016/0301-9268(94)00081-2

Knoll, A. H. (2003). *Life on a young planet*. Princeton University Press.

Kolesnikov, A. V., Rud'ko, S. V., & Fedonkin, M. A. (2024). Life on the way out of Shuram Excursion: New locality of Ediacaran Biota in the Ura Uplift of the Southern Siberian platform. *Gondwana Research*, *125*, 359–367. https://doi.org/10.1016/j.gr.2023.08.021

Korenaga, J. (2013). Initiation and evolution of plate tectonics on earth: Theories and observations. *Annual Review of Earth and Planetary Sciences*, *41*(1), 117–151. https://doi.org/10.1146/annurev-earth-050212-124208

Ku, T.-L., Mathieu, G. G., & Knauss, K. G. (1977). Uranium in open ocean: Concentration and isotopic composition. *Deep Sea Research*, *24*(11), 1005–1017. https://doi.org/10.1016/0146-6291(77)90571-9

Kump, L., Bralower, T., & Ridgwell, A. (2009). Ocean acidification in deep time. *Oceanography*, *22*(4), 94–107. https://doi.org/10.5670/oceanog.2009.100

Kunert, A., & Kendall, B. (2023). Global Ocean redox changes before and during the Toarcian Oceanic anoxic event. *Nature Communications*, *14*(1). https://doi.org/10.1038/s41467-023-36516-x

Land, L. S. (1990). Phreatic versus vadose meteoric diagenesis of limestones: Evidence from a fossil water table. *Carbonate Diagenesis*, 185–195. https://doi.org/10.1002/9781444304510.ch15

Landing, W. M., & Bruland, K. W. (1980). Manganese in the North Pacific. *Earth and Planetary Science Letters*, *49*(1), 45–56. https://doi.org/10.1016/0012-821x(80)90149-1

Landing, W. M., & Bruland, K. W. (1987). The contrasting biogeochemistry of iron and manganese in the Pacific Ocean. *Geochimica et Cosmochimica Acta*, *51*(1), 29–43. https://doi.org/10.1016/0016-7037(87)90004-4

Langmuir, D. (1977). *Uranium Solution-Mineral Equilibria at Low Temperatures with Applications to Sedimentary Ore Deposits*. https://doi.org/10.2172/6774931

Lau, K. V., Maher, K., Altiner, D., Kelley, B. M., Kump, L. R., Lehrmann, D. J., Silva-Tamayo, J. C., Weaver, K. L., Yu, M., & Payne, J. L. (2016). Marine anoxia and delayed Earth system recovery after the end-Permian extinction. *Proceedings of the National Academy of Sciences*, *113*(9), 2360–2365. https://doi.org/10.1073/pnas.1515080113

Lau, K. V., Macdonald, F. A., Maher, K., & Payne, J. L. (2017). Uranium isotope evidence for temporary ocean oxygenation in the aftermath of the Sturtian Snowball Earth. *Earth and Planetary Science Letters*, *458*, 282–292. https://doi.org/10.1016/j.epsl.2016.10.043

Lemarchand, D., Wasserburg, G. J., & Papanastassiou, D. A. (2004). Rate-controlled calcium isotope fractionation in synthetic calcite. *Geochimica et Cosmochimica Acta*, *68*(22), 4665–4678. https://doi.org/10.1016/j.gca.2004.05.029

Lewis, B. L., & Luther III, G. W. (2000). Processes controlling the distribution and cycling of manganese in the oxygen minimum zone of the Arabian Sea. *Deep Sea Research Part II: Topical Studies in Oceanography*, *47*(7–8), 1541–1561. https://doi.org/10.1016/s0967-0645(99)00153-8

Li, C., Love, G. D., Lyons, T. W., Fike, D. A., Sessions, A. L., & Chu, X. (2010). A stratified redox model for the Ediacaran Ocean. *Science*, *328*(5974), 80–83. https://doi.org/10.1126/science.1182369

Li, C., Planavsky, N. J., Shi, W., Zhang, Z., Zhou, C., Cheng, M., Tarhan, L. G., Luo, G., & Xie, S. (2015). Ediacaran marine redox heterogeneity and early animal ecosystems. *Scientific Reports*, *5*(1). https://doi.org/10.1038/srep17097

Li, Z., Cao, M., Loyd, S. J., Algeo, T. J., Zhao, H., Wang, X., Zhao, L., & Chen, Z.-Q. (2020). Transient and stepwise ocean oxygenation during the late Ediacaran Shuram Excursion: Insights from carbonate $\delta^{238}U$ of northwestern Mexico. *Precambrian Research*, *344*, 105741. https://doi.org/10.1016/j.precamres.2020.105741

Linnemann U, Ovtcharova M, Schaltegger U, et al. New high-resolution age data from the Ediacaran–Cambrian boundary indicate rapid, ecologically driven onset of the Cambrian explosion. *Terra Nova*. 2019; 31: 49–58. https://doi.org/10.1111/ter.12368

Liu, X., & Byrne, R. H. (1995). Comparative carbonate complexation of yttrium and gadolinium at 25 °C and 0.7 mol DM−3 ionic strength. *Marine Chemistry*, *51*(3), 213–221. https://doi.org/10.1016/0304-4203(95)00067-4

Liu, X.-F., Liu, X.-M., Wang, X.-K., Zhai, S., & Liu, X. (2023). Dolostone as a reliable tracer of seawater lithium isotope composition. *Communications Earth & Environment*, *4*(1). https://doi.org/10.1038/s43247-023-00711-x

Liu, X.-M., Hardisty, D. S., Lyons, T. W., & Swart, P. K. (20199). Evaluating the fidelity of the cerium paleoredox tracer during variable carbonate diagenesis on the Great Bahamas Bank. *Geochimica et Cosmochimica Acta*, *248*, 25–42. https://doi.org/10.1016/j.gca.2018.12.028

Livermore, B. D., Dahl, T. W., Bizzarro, M., & Connelly, J. N. (2020). Uranium isotope compositions of biogenic carbonates – implications for U uptake in shells and the application of the paleo-ocean oxygenation proxy. *Geochimica et Cosmochimica Acta*, *287*, 50–64. https://doi.org/10.1016/j.gca.2020.07.005

Love, G. D., Grosjean, E., Stalvies, C., Fike, D. A., Grotzinger, J. P., Bradley, A. S., Kelly, A. E., Bhatia, M., Meredith, W., Snape, C. E., Bowring, S. A., Condon, D. J., & Summons, R. E. (2009). Fossil steroids record the appearance of Demospongiae during the Cryogenian period. *Nature*, *457*(7230), 718–721. https://doi.org/10.1038/nature07673

Mackenzie, F. T., & Kump, L. R. (1995). Reverse weathering, Clay Mineral Formation, and Oceanic Element Cycles. *Science*, *270*(5236), 586–586. https://doi.org/10.1126/science.270.5236.586

Malone, M. J., Baker, P. A., & Burns, S. J. (1996). Recrystallization of dolomite: An experimental study from. *Geochimica et Cosmochimica Acta*, *60*(12), 2189–2207. https://doi.org/10.1016/0016-7037(96)00062-2

Maloof, A. C., Rose, C. V., Beach, R., Samuels, B. M., Calmet, C. C., Erwin, D. H., Poirier, G. R., Yao, N., & Simons, F. J. (2010). Possible animal-body fossils in pre-Marinoan limestones from South Australia. *Nature Geoscience*, *3*(9), 653–659. https://doi.org/10.1038/ngeo934

Marriott, C. S., Henderson, G. M., Crompton, R., Staubwasser, M., & Shaw, S. (2004a). Effect of mineralogy, salinity, and temperature on Li/Ca and Li isotope composition of calcium carbonate. *Chemical Geology*, *212*(1–2), 5–15. https://doi.org/10.1016/j.chemgeo.2004.08.002

Marriott, C.S., Henderson. G.M., Belshaw, N.S., Tudhope, A.W. (2004b). Temperature dependence of δ^7Li, δ^{44}Ca and Li/Ca during growth of calcium carbonate. *Earth and Planetary Science Letters*, *222*(2), 615–624. https://doi.org/10.1016/s0012-821x(04)00149-9

Martin, J. H., Knauer, G. A., & Broenkow, W. W. (1985). Vertex: The lateral transport of manganese in the Northeast Pacific. *Deep Sea Research Part A. Oceanographic Research Papers*, *32*(11), 1405–1427. https://doi.org/10.1016/0198-0149(85)90056-1

Martin, A. N., Markowska, M., Chivas, A. R., & Weyer, S. (2023). Assessing the reliability of Modern Marine Stromatolites as archives for the uranium isotope paleoredox proxy. *Geochimica et Cosmochimica Acta*, *345*, 75–89. https://doi.org/10.1016/j.gca.2023.01.011

McFadden, K. A., Huang, J., Chu, X., Jiang, G., Kaufman, A. J., Zhou, C., Yuan, X., & Xiao, S. (2008). Pulsed oxidation and biological evolution in the Ediacaran Doushantuo Formation. *Proceedings of the National Academy of Sciences*, *105*(9), 3197–3202. https://doi.org/10.1073/pnas.0708336105

Meert, J. G. (2003). A synopsis of events related to the Assembly of Eastern Gondwana. *Tectonophysics*, *362*(1–4), 1–40. https://doi.org/10.1016/s0040-1951(02)00629-7

Melezhik, V. A., Pokrovsky, B. G., Fallick, A. E., Kuznetsov, A. B., & Bujakaite, M. I. (2009). Constraints on ^{87}Sr/^{86}Sr of late Ediacaran seawater: Insight from Siberian High-SR Limestones. *Journal of the Geological Society*, *166*(1), 183–191. https://doi.org/10.1144/0016-76492007-171

Melim, L. A., Westphal, H., Swart, P. K., Eberli, G. P., & Munnecke, A. (2002). Questioning carbonate diagenetic paradigms: Evidence from the neogene of the Bahamas. *Marine Geology*, *185*(1–2), 27–53. https://doi.org/10.1016/s0025-3227(01)00289-4

Mills, D. B., & Canfield, D. E. (2014). Oxygen and animal evolution: Did a rise of atmospheric oxygen “trigger” the origin of animals? *BioEssays*, *36*(12), 1145–1155. https://doi.org/10.1002/bies.201400101

Mills, D. B., Ward, L. M., Jones, C., Sweeten, B., Forth, M., Treusch, A. H., & Canfield, D. E. (2014). Oxygen requirements of the earliest animals. *Proceedings of the National Academy of Sciences*, *111*(11), 4168–4172. https://doi.org/10.1073/pnas.1400547111

Minguez, D., & Kodama, K. P. (2017). Rock magnetic chronostratigraphy of the Shuram Carbon Isotope Excursion: Wonoka Formation, Australia: Reply. *Geology*, *45*(10). https://doi.org/10.1130/g39648y.1

Misra, S., & Froelich, P. N. (2012). Lithium isotope history of Cenozoic seawater: Changes in silicate weathering and reverse weathering. *Science*, *335*(6070), 818–823. https://doi.org/10.1126/science.1214697

Moczydłowska, M., & Nagovitsin, K. E. (2011). Ediacaran radiation of organic-walled microbiota recorded in the Ura Formation, Patom Uplift, East Siberia. *Precambrian Research*, *198–199*, 1–24. https://doi.org/10.1016/j.precamres.2011.12.010

Möller, P., & Bau, M. (1993). Rare-earth patterns with positive cerium anomaly in alkaline waters from Lake Van, Turkey. *Earth and Planetary Science Letters*, *117*(3–4), 671–676. https://doi.org/10.1016/0012-821x(93)90110-u

Murphy, J. G., Ahm, A.-S. C., Swart, P. K., & Higgins, J. A. (2022). Reconstructing the lithium isotopic composition (δ^7Li) of seawater from shallow marine carbonate sediments. *Geochimica et Cosmochimica Acta*, *337*, 140–154. https://doi.org/10.1016/j.gca.2022.09.019

Narbonne, G.M., Xiao, S., Shields, G. A., & Gehling, J. G. (2012). The Ediacaran Period. *The Geologic Time Scale*, 413–435. https://doi.org/10.1016/b978-0-444-59425-9.00018-4

Nelson, L. L., Ahm, A.-S. C., Macdonald, F. A., Higgins, J. A., & Smith, E. F. (2021). Fingerprinting local controls on the Neoproterozoic carbon cycle with the isotopic record of Cryogenian carbonates in the Panamint Range, California. *Earth and Planetary Science Letters*, *566*, 116956. https://doi.org/10.1016/j.epsl.2021.116956

Nielsen, L. C., Druhan, J. L., Yang, W., Brown, S. T., & DePaolo, D. J. (2011). Calcium isotopes as tracers of biogeochemical processes. *Advances in Isotope Geochemistry*, 105–124. https://doi.org/10.1007/978-3-642-10637-8_7

Nomura, M., Higuchi, N., & Fujii, Y. (1996). Mass dependence of uranium isotope effects in the U(IV)−U(VI) exchange reaction. *Journal of the American Chemical Society*, *118*(38), 9127–9130. https://doi.org/10.1021/ja954075s

Nothdurft, L. D., Webb, G. E., & Kamber, B. S. (2004). Rare Earth Element Geochemistry of Late devonian reefal carbonates, Canning Basin, Western Australia: Confirmation of a seawater ree proxy in ancient limestones. *Geochimica et Cosmochimica Acta*, *68*(2), 263–283. https://doi.org/10.1016/s0016-7037(03)00422-8

Nozaki, Y., Zhang, J., & Amakawa, H. (1997). The fractionation between Y and Ho in the marine environment. *Earth and Planetary Science Letters*, *148*(1–2), 329–340. https://doi.org/10.1016/s0012-821x(97)00034-4

Nursall, J. R. (1959). Oxygen as a prerequisite to the origin of the metazoa. *Nature*, *183*(4669), 1170–1172. https://doi.org/10.1038/1831170b0

Osburn, M. R., Owens, J., Bergmann, K. D., Lyons, T. W., & Grotzinger, J. P. (2015). Dynamic changes in sulfate sulfur isotopes preceding the Ediacaran Shuram Excursion. *Geochimica et Cosmochimica Acta*, *170*, 204–224. https://doi.org/10.1016/j.gca.2015.07.039

Ostrander, C. M., Bjerrum, C. J., Ahm, A. C., Stenger, S. R., Bergmann, K. D., El-Ghali, M. A., Harthi, A. R., Aisri, Z., & Nielsen, S. G. (2023). Widespread seafloor anoxia during generation of the Ediacaran Shuram Carbon Isotope Excursion. *Geobiology*, *21*(5), 556–570. https://doi.org/10.1111/gbi.12557

Owens, J. D., Lyons, T. W., Li, X., Macleod, K. G., Gordon, G., Kuypers, M. M., Anbar, A., Kuhnt, W., & Severmann, S. (2012). Iron Isotope and Trace Metal Records of iron cycling in the proto-north atlantic during the cenomanian-turonian oceanic anoxic event (OAE-2). *Paleoceanography*, *27*(3). https://doi.org/10.1029/2012pa002328

Park, R., & Epstein, S. (1961). Metabolic fractionation of C^{13} & C^{12} in plants. *Plant Physiology*, *36*(2), 133–138. https://doi.org/10.1104/pp.36.2.133

Partin, C. A., Lalonde, S. V., Planavsky, N. J., Bekker, A., Rouxel, O. J., Lyons, T. W., & Konhauser, K. O. (2013). Uranium in iron formations and the rise of atmospheric oxygen. *Chemical Geology*, *362*, 82–90. https://doi.org/10.1016/j.chemgeo.2013.09.005

Pearce, M. A., Jarvis, I., & Tocher, B. A. (2009). The cenomanian–turonian boundary event, OAE2 and palaeoenvironmental change in Epicontinental Seas: New insights from the dinocyst and geochemical records. *Palaeogeography, Palaeoclimatology, Palaeoecology*, *280*(1–2), 207–234. https://doi.org/10.1016/j.palaeo.2009.06.012

Pelechaty, S. M., Grotzinger, J. P., Kashirtsev, V. A., & Zhernovsky, V. P. (1996). Chemostratigraphic and sequence stratigraphic constraints on Vendian-Cambrian Basin Dynamics, Northeast Siberian Craton. *The Journal of Geology*, *104*(5), 543–563. https://doi.org/10.1086/629851

Pelechaty, S. M. (1998). Integrated chronostratigraphy of the Vendian System of Siberia: Implications for a global stratigraphy. *Journal of the Geological Society*, *155*(6), 957–973. https://doi.org/10.1144/gsjgs.155.6.0957

Penniston-Dorland, S. C., Bebout, G. E., Pogge von Strandmann, P. A. E., Elliott, T., & Sorensen, S. S. (2012). Lithium and its isotopes as tracers of subduction zone fluids and metasomatic processes: Evidence from the Catalina Schist, California, USA. *Geochimica et Cosmochimica Acta*, *77*, 530–545. https://doi.org/10.1016/j.gca.2011.10.038

Penniston-Dorland, S., Liu, X.-M. & Rudnick, R. L. Lithium isotope geochemistry. Rev. Mineral. Geochem. 82, 165–217 (2017).

Peterson, K. J., Lyons, J. B., Nowak, K. S., Takacs, C. M., Wargo, M. J., & McPeek, M. A. (2004). Estimating metazoan divergence times with a molecular clock. *Proceedings of the National Academy of Sciences*, *101*(17), 6536–6541. https://doi.org/10.1073/pnas.0401670101

Peterson, K. J., & Butterfield, N. J. (2005). ORIGIN OF THE EUMETAZOA: Testing ecological predictions of molecular clocks against the Proterozoic Fossil Record. *Proceedings of the National Academy of Sciences*, *102*(27), 9547–9552. https://doi.org/10.1073/pnas.0503660102

Petrov, P. Yu. (2018). Postglacial deposits of the Dal'Nyaya Taiga group: Early Vendian in the URA uplift, Siberia. communication 1. Barakun Formation. *Lithology and Mineral Resources*, *53*(5), 417–429. https://doi.org/10.1134/s0024490218050073

Pile, A. J., & Young, C. M. (2006). The natural diet of a hexactinellid sponge: Benthic–pelagic coupling in a deep-sea microbial food web. *Deep Sea Research Part I: Oceanographic Research Papers*, *53*(7), 1148–1156. https://doi.org/10.1016/j.dsr.2006.03.008

Pogge von Strandmann, P. A. E., Burton, K. W., James, R. H., van Calsteren, P., & Gislason, S. R. (2010). Assessing the role of climate on uranium and lithium isotope behaviour in rivers draining a basaltic terrain. *Chemical Geology*, *270*(1–4), 227–239. https://doi.org/10.1016/j.chemgeo.2009.12.002

Pogge von Strandmann, P. A., Jenkyns, H. C., & Woodfine, R. G. (2013). Lithium isotope evidence for enhanced weathering during oceanic anoxic event 2. *Nature Geoscience*, *6*(8), 668–672. https://doi.org/10.1038/ngeo1875

Pogge von Strandmann, P. A. E., Schmidt, D. N., Planavsky, N. J., Wei, G., Jones, C. L. C., & Baumann, K.-H. (2019). Assessing bulk carbonates as archives for seawater Li Isotope ratios. *Chemical Geology*, *530*, 119338. https://doi.org/10.1016/j.chemgeo.2019.119338

Pogge von Strandmann, P. A., Jones, M. T., West, A. J., Murphy, M. J., Stokke, E. W., Tarbuck, G., Wilson, D. J., Pearce, C. R., & Schmidt, D. N. (2021). Lithium isotope evidence for enhanced weathering and erosion during the paleocene-eocene thermal maximum. *Science Advances*, *7*(42). https://doi.org/10.1126/sciadv.abh4224

Pogge von Strandmann, P. A. E., Liu, X., Liu, C.-Y., Wilson, D. J., Hammond, S. J., Tarbuck, G., Aristilde, L., Krause, A. J., & Fraser, W. T. (2022). Lithium isotope behaviour during basalt weathering experiments amended with organic acids. *Geochimica et Cosmochimica Acta*, *328*, 37–57. https://doi.org/10.1016/j.gca.2022.04.032

Pokrovskii, B. G., Melezhik, V. A., & Bujakaite, M. I. (2006). Carbon, oxygen, strontium, and sulfur isotopic compositions in late Precambrian rocks of the Patom Complex, central

Siberia: Communication 1. results, isotope stratigraphy, and dating problems. *Lithology and Mineral Resources*, *41*(5), 450–474. https://doi.org/10.1134/s0024490206050063

Pokrovsky, B. G., & Bujakaite, M. I. (2015). Geochemistry of C, O, and Sr isotopes in the Neoproterozoic carbonates from the southwestern Patom paleobasin, southern middle Siberia. *Lithology and Mineral Resources*, *50*(2), 144–169. https://doi.org/10.1134/s0024490215010046

Pourret, O., Davranche, M., Gruau, G., & Dia, A. (2008). New insights into cerium anomalies in organic-rich alkaline waters. *Chemical Geology*, *251*(1–4), 120–127. https://doi.org/10.1016/j.chemgeo.2008.03.002

Prockop, D., Kaplan, A., & Udenfriend, S. (1963). Oxygen-18 studies on the conversion of proline to collagen hydroxyproline. *Archives of Biochemistry and Biophysics*, *101*(3), 499–503. https://doi.org/10.1016/0003-9861(63)90509-5

Rademacher, L. K., Lundstrom, C. C., Johnson, T. M., Sanford, R. A., Zhao, J., & Zhang, Z. (2006). Experimentally determined uranium isotope fractionation during reduction of hexavalent U by bacteria and zero valent iron. *Environmental Science & Technology*, *40*(22), 6943–6948. https://doi.org/10.1021/es0604360

Remírez, M. N., Gilleaudeau, G. J., Gan, T., Kipp, M. A., Tissot, F. L., Kaufman, A. J., & Parente, M. (2024). Carbonate uranium isotopes record global expansion of marine anoxia during the Toarcian Oceanic anoxic event. *Proceedings of the National Academy of Sciences*, *121*(27). https://doi.org/10.1073/pnas.2406032121

Rodriguez-Blanco, J. D., Shaw, S., & Benning, L. G. (2015). A route for the direct crystallization of Dolomite. *American Mineralogist*, *100*(5–6), 1172–1181. https://doi.org/10.2138/am-2015-4963

Romaniello, S. J., Herrmann, A. D., & Anbar, A. D. (2013). Uranium concentrations and 238U/235U isotope ratios in modern carbonates from the Bahamas: Assessing a novel paleoredox proxy. *Chemical Geology*, *362*, 305–316. https://doi.org/10.1016/j.chemgeo.2013.10.002

Rooney, A. D., Cantine, M. D., Bergmann, K. D., Gómez-Pérez, I., Al Baloushi, B., Boag, T. H., Busch, J. F., Sperling, E. A., & Strauss, J. V. (2020). Calibrating the coevolution of Ediacaran life and environment. *Proceedings of the National Academy of Sciences*, *117*(29), 16824–16830. https://doi.org/10.1073/pnas.2002918117

Rothman, D. H., Hayes, J. M., & Summons, R. E. (2003). Dynamics of the Neoproterozoic carbon cycle. *Proceedings of the National Academy of Sciences*, *100*(14), 8124–8129. https://doi.org/10.1073/pnas.0832439100

Rud‘ko, S. V., Kuznetsov, A. B., Yu. Petrov, P., Sitkina, D. R., & Kaurova, O. K. (2021). Pb-Pb dating of the Dal’nyaya Taiga group in the Ura Uplift of southern Siberia: Implications for

correlation of C-isotopic and biotic events in the Ediacaran. *Precambrian Research*, *362*, 106285. https://doi.org/10.1016/j.precamres.2021.106285

Saager, P. M., De Baar, H. J. W., & Burkill, P. H. (1989). Manganese and iron in Indian Ocean Waters. *Geochimica et Cosmochimica Acta*, *53*(9), 2259–2267. https://doi.org/10.1016/0016-7037(89)90348-7

Sahoo, S. K., Planavsky, N. J., Jiang, G., Kendall, B., Owens, J. D., Wang, X., Shi, X., Anbar, A. D., & Lyons, T. W. (2016). Oceanic oxygenation events in the anoxic Ediacaran Ocean. *Geobiology*, *14*(5), 457–468. https://doi.org/10.1111/gbi.12182

Saltzman, M. R., & Thomas, E. (2012). Carbon isotope stratigraphy. *The Geologic Time Scale*, 207–232. https://doi.org/10.1016/b978-0-444-59425-9.00011-1

Sawaki, Y., Ohno, T., Tahata, M., Komiya, T., Hirata, T., Maruyama, S., Windley, B. F., Han, J., Shu, D., & Li, Y. (2010). The Ediacaran radiogenic Sr isotope excursion in the Doushantuo Formation in the Three Gorges Area, South China. *Precambrian Research*, *176*(1–4), 46–64. https://doi.org/10.1016/j.precamres.2009.10.006

Schauble, E. A. (2007). Role of nuclear volume in driving equilibrium stable isotope fractionation of mercury, thallium, and other very heavy elements. *Geochimica et Cosmochimica Acta*, *71*(9), 2170–2189. https://doi.org/10.1016/j.gca.2007.02.004

Schlanger, S., & Jenkyns, H. (1976). Cretaceous Oceanic Anoxic Events: Causes and Consequences. Geologie En Mijnbouw, 55(3-4), 179–184.

Schlanger, S. O., Arthur, M. A., Jenkyns, H. C., & Scholle, P. A. (1987). The Cenomanian-turonian oceanic anoxic event, I. Stratigraphy and distribution of organic carbon-rich beds and the marine $\delta^{13}C$ excursion. *Geological Society, London, Special Publications*, *26*(1), 371–399. https://doi.org/10.1144/gsl.sp.1987.026.01.24

Schmitt, R. da, Fragoso, R. de, & Collins, A. S. (2018). Suturing Gondwana in the Cambrian: The orogenic events of the final amalgamation. *Regional Geology Reviews*, 411–432. https://doi.org/10.1007/978-3-319-68920-3_15

Schrag, D. P., Higgins, John. A., Macdonald, F. A., & Johnston, D. T. (2013). Authigenic carbonate and the history of the global carbon cycle. *Science*, *339*(6119), 540–543. https://doi.org/10.1126/science.1229578

Segessenman, D. C., & Peters, S. E. (2023). Macrostratigraphy of the Ediacaran system in North America. *Laurentia: Turning Points in the Evolution of a Continent*, 399–424. https://doi.org/10.1130/2022.1220(21)

Sergeev, V. N., Knoll, A. H., & Vorob'Eva, N. G. (2011). Ediacaran microfossils from the URA formation, Baikal-Patom Uplift, siberia: Taxonomy and biostratigraphic significance. *Journal of Paleontology*, *85*(5), 987–1011. https://doi.org/10.1666/11-022.1

Shields, G. A., & Mills, B. J. (2017). Tectonic controls on the long-term carbon isotope mass balance. *Proceedings of the National Academy of Sciences*, *114*(17), 4318–4323. https://doi.org/10.1073/pnas.1614506114

Shields, G. A., Mills, B. J., Zhu, M., Raub, T. D., Daines, S. J., & Lenton, T. M. (2019). Unique Neoproterozoic carbon isotope excursions sustained by coupled evaporite dissolution and Pyrite Burial. *Nature Geoscience*, *12*(10), 823–827. https://doi.org/10.1038/s41561-019-0434-3

Shiller, A. M. (1997). Manganese in surface waters of the Atlantic Ocean. *Geophysical Research Letters*, *24*(12), 1495–1498. https://doi.org/10.1029/97gl01456

Sieber, M., Conway, T. M., de Souza, G. F., Obata, H., Takano, S., Sohrin, Y., & Vance, D. (2019). Physical and biogeochemical controls on the distribution of dissolved cadmium and its isotopes in the Southwest Pacific Ocean. *Chemical Geology*, *511*, 494–509. https://doi.org/10.1016/j.chemgeo.2018.07.021

Simkiss, K. (1977). Biomineralization and detoxification. *Calcified Tissue Research*, *24*(1), 199–200. https://doi.org/10.1007/bf02223316

Sperling, E. A., Wolock, C. J., Morgan, A. S., Gill, B. C., Kunzmann, M., Halverson, G. P., Macdonald, F. A., Knoll, A. H., & Johnston, D. T. (2015). Statistical analysis of Iron Geochemical Data Suggests Limited late Proterozoic oxygenation. *Nature*, *523*(7561), 451–454. https://doi.org/10.1038/nature14589

Spero, H. J., Bijma, J., Lea, D. W., & Bemis, B. E. (1997). Effect of seawater carbonate concentration on foraminiferal carbon and oxygen isotopes. *Nature*, *390*(6659), 497–500. https://doi.org/10.1038/37333

Squire, R., Campbell, I., Allen, C., & Wilson, C. (2006). Did the Transgondwanan Supermountain trigger the explosive radiation of animals on earth? *Earth and Planetary Science Letters*, *250*(1–2), 116–133. https://doi.org/10.1016/j.epsl.2006.07.032

Starkey, H. C. (1982). *The role of clays in fixing lithium*. United States Government Printing Office ; For sale by the Distribution Branch, U.S. Geological Survey.

Stirling, C. H., Andersen, M. B., Warthmann, R., & Halliday, A. N. (2015). Isotope fractionation of 238U and 235U during biologically-mediated uranium reduction. *Geochimica Et Cosmochimica Acta*, *163*, 200–218. https://doi.org/10.1016/j.gca.2015.03.017

Stylo, M., Neubert, N., Wang, Y., Monga, N., Romaniello, S. J., Weyer, S., & Bernier-Latmani, R. (2015). Uranium isotopes fingerprint biotic reduction. *Proceedings of the National Academy of Sciences*, *112*(18), 5619–5624. https://doi.org/10.1073/pnas.1421841112

Sunda, W. G., & Huntsman, S. A. (1988). Effect of sunlight on redox cycles of manganese in the southwestern Sargasso Sea. *Deep Sea Research Part A. Oceanographic Research Papers*, *35*(8), 1297–1317. https://doi.org/10.1016/0198-0149(88)90084-2

Swart, P. K., & Kennedy, M. J. (2012). Does the global stratigraphic reproducibility of $\delta^{13}C$ in Neoproterozoic carbonates require a marine origin? A pliocene–pleistocene comparison. *Geology*, *40*(1), 87–90. https://doi.org/10.1130/g32538.1

Swart, P. K. (2015). The geochemistry of carbonate diagenesis: The past, present and future. *Sedimentology*, *62*(5), 1233–1304. https://doi.org/10.1111/sed.12205

Tang, J., Dietzel, M., Böhm, F., Köhler, S. J., & Eisenhauer, A. (2008). Sr^{2+}/Ca^{2+} and $^{44}Ca/^{40}Ca$ fractionation during inorganic calcite formation: II. Ca isotopes. *Geochimica et Cosmochimica Acta*, *72*(15), 3733–3745. https://doi.org/10.1016/j.gca.2008.05.033

Tarhan, L. G., Hood, A. v.S., Droser, M. L., Gehling, J. G., & Briggs, D. E. G. (2016). Exceptional preservation of soft-bodied Ediacara biota promoted by silica-rich oceans. *Geology*, *44*(11), 951–954. https://doi.org/10.1130/g38542.1

Taylor, S. R., & McLennan, S. M. (1985). *The continental crust, its composition and Evolution: An examination of the geochemical record preserved in Sedimentary Rocks*. Blackwell Scientific.

Teng, F.-Z., McDonough, W. F., Rudnick, R. L., Dalpé, C., Tomascak, P. B., Chappell, B. W., & Gao, S. (2004). Lithium isotopic composition and concentration of the upper continental crust. *Geochimica et Cosmochimica Acta*, *68*(20), 4167–4178. https://doi.org/10.1016/j.gca.2004.03.031

Tissot, F. L. H., & Dauphas, N. (2015). Uranium isotopic compositions of the crust and ocean: Age corrections, U budget and global extent of modern anoxia. *Geochimica Et Cosmochimica Acta*, *167*, 113–143. https://doi.org/10.1016/j.gca.2015.06.034

Tissot, F. L. H., Chen, C., Go, B. M., Naziemiec, M., Healy, G., Bekker, A., Swart, P. K., & Dauphas, N. (2018). Controls of eustasy and diagenesis on the $^{238}U/^{235}U$ of carbonates and evolution of the seawater ($^{234}U/^{238}U$) during the last 1.4 myr. *Geochimica et Cosmochimica Acta*, *242*, 233–265. https://doi.org/10.1016/j.gca.2018.08.022

Tostevin, R., Shields, G. A., Tarbuck, G. M., He, T., Clarkson, M. O., & Wood, R. A. (2016). Effective use of cerium anomalies as a redox proxy in carbonate-dominated marine settings. *Chemical Geology*, *438*, 146–162. https://doi.org/10.1016/j.chemgeo.2016.06.027

Tostevin, R., Clarkson, M. O., Gangl, S., Shields, G. A., Wood, R. A., Bowyer, F., Penny, A. M., & Stirling, C. H. (2019). Uranium isotope evidence for an expansion of anoxia in terminal Ediacaran Oceans. *Earth and Planetary Science Letters*, *506*, 104–112. https://doi.org/10.1016/j.epsl.2018.10.045

Tostevin, Rosalie. (2021). *Cerium Anomalies and Paleoredox*. https://doi.org/10.1017/9781108847223

Towe, K. M. (1970). Oxygen-collagen priority and the early metazoan fossil record. *Proceedings of the National Academy of Sciences*, *65*(4), 781–788. https://doi.org/10.1073/pnas.65.4.781

Trefry, J. H., Presley, B. J., Keeney-Kennicutt, W. L., & Trocine, R. P. (1984a). Distribution and chemistry of manganese, iron, and suspended particulates in Orca Basin. *Geo-Marine Letters*, *4*(2), 125–130. https://doi.org/10.1007/bf02277083

Trower, E. J., Lamb, M. P., & Fischer, W. W. (2017). Experimental evidence that ooid size reflects a dynamic equilibrium between rapid precipitation and abrasion rates. *Earth and Planetary Science Letters*, *468*, 112–118. https://doi.org/10.1016/j.epsl.2017.04.004

Urey, H. C., Lowenstam, H. A., Epstein, S., & McKinney, C. R. (1951). Measurement of paleotemperatures and temperatures of the Upper Cretaceous of England, Denmark, and the Southeastern United States. *Geological Society of America Bulletin*, *62*(4), 399. https://doi.org/10.1130/0016-7606(1951)62[399:mopato]2.0.co;2

Usdowski, E., & Hoefs, J. (1993). Oxygen isotope exchange between carbonic acid, bicarbonate, carbonate, and water: A re-examination of the data of McCrea (1950) and an expression for the overall partitioning of oxygen isotopes between the carbonate species and water. *Geochimica et Cosmochimica Acta*, *57*(15), 3815–3818. https://doi.org/10.1016/0016-7037(93)90159-t

Valley, J. W. (2001). Stable isotope thermometry at high temperatures. *Reviews in Mineralogy and Geochemistry*, *43*(1), 365–413. https://doi.org/10.2138/gsrmg.43.1.365

Van Cappellen, P., & Ingall, E. D. (1996). Redox stabilization of the atmosphere and oceans by phosphorus-limited marine productivity. *Science*, *271*(5248), 493–496. https://doi.org/10.1126/science.271.5248.493

Vasconcelos, C., & McKenzie, J. A. (1997). Microbial mediation of modern dolomite precipitation and diagenesis under anoxic conditions (Lagoa Vermelha, Rio de Janeiro, Brazil). *SEPM Journal of Sedimentary Research*, *Vol. 67*. https://doi.org/10.1306/d4268577-2b26-11d7-8648000102c1865d

Veizer, J., Ala, D., Azmy, K., Bruckschen, P., Buhl, D., Bruhn, F., Carden, G. A. F., Diener, A., Ebneth, S., Godderis, Y., Jasper, T., Korte, C., Pawellek, F., Podlaha, O. G., & Strauss, H. (1999). $^{87}Sr/^{86}Sr$, $\delta^{13}C$ and $\delta^{18}O$ evolution of Phanerozoic seawater. *Chemical Geology*, *161*(1–3), 59–88. https://doi.org/10.1016/s0009-2541(99)00081-9

Vorob'eva, N. G., & Petrov, P. Yu. (2020). Microbiota of the Barakun Formation and biostratigraphic characteristics of the Dal'nyaya Taiga group: Early Vendian of the Ura

uplift (eastern siberia). *Stratigraphy and Geological Correlation*, *28*(4), 365–380. https://doi.org/10.1134/s0869593820040103

Wahlberg, J. S., Baker, J. H., Vernon, R. W., & Dewar, R. S. (1965). *Exchange adsorption of strontium on clay minerals*. United States Department of the Interior, Geological Survey.

Wallmann, K., & Aloisi, G. (2012). The global carbon cycle: Geological processes. *Fundamentals of Geobiology*, 20–35. https://doi.org/10.1002/9781118280874.ch3

Wang, H., Peng, Y., Li, C., Cao, X., Cheng, M., & Bao, H. (2023). Sulfate triple-oxygen-isotope evidence confirming oceanic oxygenation 570 million years ago. *Nature Communications*, *14*(1). https://doi.org/10.1038/s41467-023-39962-9

Wang, J., Chen, D., Yan, D., Wei, H., & Xiang, L. (2012). Evolution from an anoxic to oxic deep ocean during the Ediacaran–Cambrian transition and implications for bioradiation. *Chemical Geology*, *306–307*, 129–138. https://doi.org/10.1016/j.chemgeo.2012.03.005

Wang, J., Tarhan, L. G., Jacobson, A. D., Oehlert, A. M., & Planavsky, N. J. (2023). The evolution of the Marine Carbonate Factory. *Nature*, *615*(7951), 265–269. https://doi.org/10.1038/s41586-022-05654-5

Ward, B. (2012). The global nitrogen cycle. *Fundamentals of Geobiology*, 36–48. https://doi.org/10.1002/9781118280874.ch4

Warren, J. (2000). Dolomite: Occurrence, evolution and economically important associations. *Earth-Science Reviews*, *52*(1–3), 1–81. https://doi.org/10.1016/s0012-8252(00)00022-2

Webb, Gregory E., & Kamber, B. S. (2000). Rare earth elements in Holocene Reefal Microbialites: A new shallow seawater proxy. *Geochimica et Cosmochimica Acta*, *64*(9), 1557–1565. https://doi.org/10.1016/s0016-7037(99)00400-7

Webb, G. E., Nothdurft, L. D., Kamber, B. S., Kloprogge, J. T., & Zhao, J. (2009). Rare earth element geochemistry of Scleractinian coral skeleton during meteoric diagenesis: A sequence through neomorphism of aragonite to calcite. *Sedimentology*, *56*(5), 1433–1463. https://doi.org/10.1111/j.1365-3091.2008.01041.x

Wei, G.-Y., Wang, J., Planavsky, N. J., Zhao, M., Bolton, E. W., Jiang, L., Asael, D., Wei, W., & Ling, H.-F. (2022). On the origin of Shuram Carbon Isotope Excursion in South China and its implication for Ediacaran atmospheric oxygen levels. *Precambrian Research*, *375*, 106673. https://doi.org/10.1016/j.precamres.2022.106673

Wei, G.-Y., Zhang, F., Yin, Y.-S., Lin, Y.-B., Pogge von Strandmann, P. A. E., Cao, M., Li, N., Xiong, G., Chen, X., Fan, C., Xu, C., Tan, F., Zhang, X., Yang, H., Ling, H.-F., & Shen, S.-Z. (2023). A 13 million-year record of Li isotope compositions in island carbonates: Constraints on bulk inorganic carbonate as a global seawater Li Isotope Archive. *Geochimica et Cosmochimica Acta*, *344*, 59–72. https://doi.org/10.1016/j.gca.2023.01.013

Wei, G.-Y., & Zhang, F. (2024). Pristine or altered, what can early diagenesis tell us in shallow-water carbonates? *Earth and Planetary Science Letters*, *641*, 118806. https://doi.org/10.1016/j.epsl.2024.118806

Weldeghebriel, M. F., & Lowenstein, T. K. (2023). Seafloor hydrothermal systems control long-term changes in seawater [Li^+]: Evidence from fluid inclusions. *Science Advances*, *9*(30). https://doi.org/10.1126/sciadv.adf1605

Wu, H.-P., Jiang, S.-Y., Palmer, M. R., Wei, H.-Z., & Yang, J.-H. (2018). Positive cerium anomaly in the Doushantuo cap carbonates from the Yangtze Platform, South China: Implications for intermediate water column manganous conditions in the aftermath of the Marinoan Glaciation. *Precambrian Research*, *320*, 93–110. https://doi.org/10.1016/j.precamres.2018.10.019

Wu, N., Zhang, J., Mao, H., Zhang, G., & Zhao, Z. (2024). Geochemical behavior of stable strontium isotopes during continental weathering process: A Review. *Geosystems and Geoenvironment*, *3*(2), 100144. https://doi.org/10.1016/j.geogeo.2022.100144

Xiao, S., Narbonne, G. M., Zhou, C., Laflamme, M., Grazhdankin, D. V., Moczydlowska-Vidal, M., & Cui, H. (2016). Towards an ediacaran time scale: Problems, protocols, and prospects. *Episodes*, *39*(4), 540–555. https://doi.org/10.18814/epiiugs/2016/v39i4/103886

Xiao, S. (2020). Ediacaran sponges, animal biomineralization, and skeletal reefs. *Proceedings of the National Academy of Sciences*, *117*(35), 20997–20999. https://doi.org/10.1073/pnas.2014393117

Yang, C., Li, X.-H., Zhu, M., & Condon, D. J. (2016). Sims U–Pb zircon geochronological constraints on upper ediacaran stratigraphic correlations, South China. *Geological Magazine*, *154*(6), 1202–1216. https://doi.org/10.1017/s0016756816001102

Yin, Y.-S., Wei, G.-Y., Pogge von Strandmann, P. A. E., Lechte, M. A., Hohl, S. V., Lin, Y.-B., Li, D., Chen, T., Yang, T., Zhang, F., Isson, T. T., Zhang, H., Cai, Y., & Ling, H.-F. (2023). Widespread clay authigenesis and highly congruent silicate weathering in the Marinoan Aftermath. *Earth and Planetary Science Letters*, *623*, 118423. https://doi.org/10.1016/j.epsl.2023.118423

Yuan, Y., Chen, T., Zhang, F., Liu, Y., Xiong, G., Wei, G.-Y., Dahl, T. W., Yan, W., Ling, H.-F., Cheng, H., & Shen, S.-Z. (2023). Substantial incorporation of isotopically heavy reduced u species into marine carbonate sediments. *Geochimica et Cosmochimica Acta*, *358*, 27–37. https://doi.org/10.1016/j.gca.2023.07.023

Zeebe, R. E. (1999). An explanation of the effect of seawater carbonate concentration on foraminiferal oxygen isotopes. *Geochimica et Cosmochimica Acta*, *63*(13–14), 2001–2007. https://doi.org/10.1016/s0016-7037(99)00091-5

Zeebe, R. E. (2007). An expression for the overall oxygen isotope fractionation between the sum of dissolved inorganic carbon and water. *Geochemistry, Geophysics, Geosystems*, *8*(9). https://doi.org/10.1029/2007gc001663

Zhang, F., Xiao, S., Kendall, B., Romaniello, S. J., Cui, H., Meyer, M., Gilleaudeau, G. J., Kaufman, A. J., & Anbar, A. D. (2018). Extensive marine anoxia during the terminal Ediacaran Period. *Science Advances*, *4*(6). https://doi.org/10.1126/sciadv.aan8983

Zhang, F., Xiao, S., Romaniello, S. J., Hardisty, D., Li, C., Melezhik, V., Pokrovsky, B., Cheng, M., Shi, W., Lenton, T. M., & Anbar, A. D. (2019). Global marine redox changes drove the rise and fall of the Ediacara biota. *Geobiology*, *17*(6), 594–610. https://doi.org/10.1111/gbi.12359

Zhang, F., Lenton, T. M., del Rey, Á., Romaniello, S. J., Chen, X., Planavsky, N. J., Clarkson, M. O., Dahl, T. W., Lau, K. V., Wang, W., Li, Z., Zhao, M., Isson, T., Algeo, T. J., & Anbar, A. D. (2020). Uranium isotopes in marine carbonates as a global ocean paleoredox proxy: A critical review. *Geochimica et Cosmochimica Acta*, *287*, 27–49. https://doi.org/10.1016/j.gca.2020.05.011

Zhong, S., & Mucci, A. (1995). Partitioning of rare earth elements (REEs) between calcite and seawater solutions at 25°C and 1 atm, and high dissolved REE concentrations. *Geochimica et Cosmochimica Acta*, *59*(3), 443–453. https://doi.org/10.1016/0016-7037(94)00381-u

Zhou, C., Xie, G., McFadden, K., Xiao, S., & Yuan, X. (2007). The diversification and extinction of Doushantuo-Pertatataka acritarchs in South China: Causes and biostratigraphic significance. *Geological Journal*, *42*(3–4), 229–262. https://doi.org/10.1002/gj.1062

Zhu, M.-Y., Babcock, L. E., & Peng, S.-C. (2006). Advances in Cambrian stratigraphy and paleontology: Integrating correlation techniques, paleobiology, taphonomy and Paleoenvironmental Reconstruction. *Palaeoworld*, *15*(3–4), 217–222. https://doi.org/10.1016/j.palwor.2006.10.016